

UNIVERSITY OF BIRMINGHAM

ESTABLISHING CONTINUOUS PLANAR LASER-INDUCED FLUORESCENCE TO EVALUATE STATIC MIXERS IN CONJUNCTION WITH PARTICLE TRACKING COMPUTATIONAL FLUID DYNAMICS

by

THOMAS ROBINSON

A thesis submitted to the University of Birmingham for the degree of DOCTOR OF ENGINEERING

School of Chemical Engineering
College of Engineering and Physical Sciences
University of Birmingham

November 2024

UNIVERSITY OF
BIRMINGHAM

University of Birmingham Research Archive

e-theses repository

This unpublished thesis/dissertation is copyright of the author and/or third parties. The intellectual property rights of the author or third parties in respect of this work are as defined by The Copyright Designs and Patents Act 1988 or as modified by any successor legislation.

Any use made of information contained in this thesis/dissertation must be in accordance with that legislation and must be properly acknowledged. Further distribution or reproduction in any format is prohibited without the permission of the copyright holder.

Contents

Abstract xix

Acknowledgements xx

1 Introduction **1**

1.1 State-of-the-Art and Business Case 3

1.2 Aims and Objectives 6

1.3 Thesis Layout 7

2 Literature Review **10**

2.1 Introduction 10

2.2 Fluid Fundamentals 11

2.2.1 General Rheology 11

2.2.2 Rheological Data 14

2.2.3 Laminar Flow 16

2.2.4 Turbulent Flow 18

2.3 Mixing Theory 19

2.3.0.1 Coefficient of Variance 20

2.3.1 Striation Thickness 23

2.3.2 Areal Fraction Method 24

2.3.2.1 CG Number 26

2.3.3 Mixing Criteria 28

2.4 Static Mixer Energy Loss 30

2.5 Methods of Mixing Measurement 32

2.5.1 Planar Laser-Induced Fluorescence (PLIF) 32

2.5.2 Computational Fluid Dynamics (CFD) 38

2.6 Conclusions 44

3 The Development of a Novel Test Facility for Continuous PLIF 46

3.1 Introduction 46

3.2 Hardware 47

3.2.1 Test Rig Principle 47

3.2.2 Main Testing Rig 50

3.2.2.1 Principle 50

3.2.2.2 Design 53

3.2.2.3 Optics 57

3.2.2.4 PLIF Hardware 58

3.2.3 Auxiliary Rig 61

3.2.3.1 Overview 61

3.2.3.2 Temperature Control 65

3.2.3.3 On-line Viscometer 65

3.2.3.4 Filtration 67

3.2.3.5 Data Acquisition 68

3.2.3.6 Control Input/Output 71

3.3 Software, Data and Industry 4.0 72

3.3.1 Modbus 73

3.3.2 DASYLab® 74

3.3.3 Control Principle 77

3.3.4 Insight 4G™ 77

3.3.5 SQLite Data Storage 78

3.4 Image Post-Processing 79

3.5 Rig Commissioning 83

3.5.1 Image Calibration 83

3.5.1.1 Principle 83

3.5.1.2 Method 84

3.5.1.3 Results 85

3.6 Test Rig Fluid Parameter Capabilities . . . 88
3.6.1 Viscosity Control . . . 88
3.6.2 Velocity Control . . . 89
3.6.3 Resultant Reynolds Range and Testing Parameters . . . 90
3.6.4 Conclusions . . . 92

4 Low Reynolds Laminar Static Mixer Testing 94
4.1 Introduction . . . 94
4.2 Materials and Methods . . . 94
4.2.1 Test Fluids . . . 95
4.2.2 Test Parameters . . . 96
4.2.3 Tested Static Mixer Geometries . . . 98
4.2.3.1 SMX™ . . . 98
4.2.3.2 SMX™ plus . . . 98
4.2.3.3 CALGAVIN Static Mixer . . . 100
4.3 Results and Discussion . . . 101
4.3.1 Pressure Drop . . . 101
4.3.2 Planar Laser-Induced Fluorescence (PLIF) Results . . . 108
4.3.3 Coefficient of Variance . . . 120
4.3.4 CG Number . . . 123
4.3.5 Mixing Efficiency . . . 136
4.3.5.1 Length efficiency . . . 136
4.3.5.2 Energy Loss Efficiency . . . 137
4.4 Conclusion and Next Steps . . . 139

5 Boundary Separation in Laminar Static Mixing 141
5.1 Introduction . . . 141
5.2 Materials and Methods . . . 142
5.2.1 Test Fluids . . . 143
5.3 Results and Discussion . . . 146

5.3.1 Pressure Drop . . . 146
5.3.2 PLIF Results . . . 150
5.3.3 Coefficient of Variance . . . 166
5.3.4 CALGAVIN Mixing Number . . . 170
5.3.5 Mixing Efficiency . . . 173
5.4 Mixing Results Across Glycerol Mass Fractions . . . 174
5.5 Conclusion and Next Steps . . . 183
5.6 Conclusion and Next Steps . . . 183

6 Computational Fluid Dynamics in Laminar Mixing 186
6.1 Introduction . . . 186
6.2 Materials and Methods . . . 187
6.2.1 Numerical Theory . . . 187
6.2.2 Modelling and Simulation Environment . . . 187
6.2.3 Application Model . . . 188
6.2.4 Numerical Model . . . 190
6.2.5 Meshing and Mesh Independence . . . 195
6.3 Passive Scalar Mixing . . . 197
6.4 Particle Tracking Mixing Evaluation . . . 201
6.5 Conclusions and Next Steps . . . 208

7 Conclusions 211

8 Further Work 216

Bibliography 219

List of Figures

2.1 Nov Kenics Static Mixer 11

2.2 Sulzer SMX plus Static Mixer 11

2.3 CoV in Three Demonstrational Mixing Examples (Kukukova et al., 2009) 22

2.4 Bar Graph Showing Discrete Areal Intensity Distributions for each Experiment (Alberini et al., 2014) 25

2.5 Left – Original 2048x2048 pixel Planar Laser-Induced Fluorescence (PLIF) image. Middle – Planar Laser-Induced Fluorescence (PLIF) image downsampled to 128x128 pixels. Right – Planar Laser-Induced Fluorescence (PLIF) image downsampled to 8x8 pixels 29

2.6 Excitation and Re-emission Ranges for Rhodamine 6G with Respect to Planar Laser-Induced Fluorescence (PLIF) (Baj et al., 2016) 38

3.1 Process and Instrumentation Diagram (P&ID) of Continuous Planar Laser-Induced Fluorescence (PLIF) Test Facility 49

3.2 Main Planar Laser-Induced Fluorescence (PLIF) Testing Section on Lidded Optical Table 50

3.3 Custom Soldered Copper Fins on RTD 51

3.4 Dye Injection Tube in Central (Left) and Wall (Right) Injection Positioning 52

3.5 Mixing Testing Section. Top: Top View of Test Section. Bottom: Side View of Test Section. 53

3.6 Cross-section of the PLIF Test Section 54

3.7 Custom Male (Left) and Female (Right) Tri-clamp Compatible Fittings 55

3.8 Planar Laser Optical System. Top: Top View of Optics Depicting Laser Light Propagation from Plano-Convex Lens. Bottom: Side View of Optics Depicting Laser Light Propagation from Plano-Concave Lens 58
3.9 CAD model of PLIF System Layout 59
3.10 Planar Laser-Induced Fluorescence (PLIF) Testing Auxiliary Rig 62
3.11 Electrical Wall Box Housing Dat Acquisition and Input/Output Hardware and Wiring 70
3.12 DASYLab® Module and Wiring for the Planar Laser-Induced Fluorescence (PLIF) Test Rig 75
3.13 DASYLab® Control Display for the Planar Laser-Induced Fluorescence (PLIF) Test Rig 77
3.14 PLIF Images of Test Section Flooded with Rhodamine 6G Concentrations of 0.0 mg L^{-1} (Top Left), 0.1 mg L^{-1} (Top Right), 0.3 mg L^{-1} (Bottom Left) and 0.5 mg L^{-1} (Bottom Right) 86
3.15 Rhodamine 6G Concentration to Mean Planar Laser-Induced Fluorescence (PLIF) Image Intensity 87
3.16 Temperature Dependence on Rhodamine 6G Fluorescence Luminance . 87

4.1 Temperature Viscosity Curve for 99.8 wt.% Glycerol 96
4.2 Temperature Density Curve for 99.8 wt.% Glycerol 96
4.3 Technical Drawing of SMX™ Static Mixer Insert 99
4.4 Technical Drawing of SMX™ plus Static Mixer Insert 100
4.5 Normalised Friction Factor over Reynolds Number for SMX™ Static Mixer Insert 102
4.6 Normalised Friction Factor over Reynolds Number for SMX™ plus Static Mixer Insert 102
4.7 Normalised Friction Factor over Reynolds Number for CALGAVIN Static Mixer Insert 103
4.8 Friction Factor over Reynolds Number for the High Shear Static Mixer Designs: SMX™, SMX™ plus and the CALGAVIN Static Mixer 103

4.9 Experimental Fanning friction factor for the SMX™ insert compared to literature. (Thakur et al., 2003) 106
4.10 All Captured CALGAVIN Static Mixer PLIF Images for 99.8 wt .% Glycerol Solution with Each being the Average of 100 Images 111
4.11 All Captured Sulzer ™ Static Mixer PLIF Images for 99.8 wt .% Glycerol Solution with Each being the Average of 100 images 112
4.12 All Captured Sulzer ™ plus Static Mixer PLIF Images for 99.8 wt .% Glycerol Solution with Each being the Average of 100 images 113
4.13 Sequential Planar Laser-Induced Fluorescence (PLIF) images 0.25 seconds after each other for four units of a CALGAVIN Static Mixer at a Reynolds number of 7.57 114
4.14 Planar Laser-Induced Fluorescence (PLIF) Mixing images for the tested lengths of the SMX™ Static Mixer at a Reynolds number of 3.74 ± 3.95 115
4.15 Planar Laser-Induced Fluorescence (PLIF) Mixing images for the tested lengths of the SMX™ plus Static Mixer at a Reynolds number of 4.85 ± 2.92116
4.16 Planar Laser-Induced Fluorescence (PLIF) Mixing images for the tested lengths of the CALGAVIN Static Mixer at a Reynolds number of 6.44 ± 4.51 - Part A 117
4.17 Planar Laser-Induced Fluorescence (PLIF) Mixing images for the tested lengths of the CALGAVIN Static Mixer at a Reynolds number of 6.44 ± 4.51 - Part B 118
4.18 Planar Laser-Induced Fluorescence (PLIF) Imagery at the outlet of a SMX™ at $0.002\,\mathrm{m\,s^{-1}}$ 119
4.19 The influence of Reynolds Number on Coefficient of Variance (CoV) for each tested length of the SMX™ Static Mixer 121
4.20 The influence of Reynolds Number on Coefficient of Variance (CoV) for each tested length of the SMX™ plus Static Mixer 121
4.21 The influence of Reynolds Number on Coefficient of Variance (CoV) for each tested length of the CALGAVIN Static Mixer 122

4.22 Reference Chart for Understanding CG Number 126
4.23 Example of the Affect on CG Number and CoV when Incorrect Ratios of Mixture Components are Introduced 127
4.24 Histogram of Planar Laser-Induced Fluorescence (PLIF) images for the SMX™ Static Mixer with Calculation Curves for CG Number 129
4.25 Histogram of Planar Laser-Induced Fluorescence (PLIF) images for the SMX™ plus Static Mixer with Calculation Curves for CG Number . . . 130
4.26 Histogram of Planar Laser-Induced Fluorescence (PLIF) images for the CALGAVIN Static Mixer with Calculation Curves for CG Number . . . 131
4.27 Histogram of Planar Laser-Induced Fluorescence (PLIF) images for the CALGAVIN Static Mixer with Calculation Curves for CG Number in Log Scale 132
4.28 Histogram of Planar Laser-Induced Fluorescence (PLIF) images for the CALGAVIN Static Mixer with Calculation Curves for CG Number in Log Scale 133
4.29 The influence of Reynolds Number on CG Number for each tested length of the SMX™ Static Mixer 134
4.30 The influence of Reynolds Number on CG Number for each tested length of the SMX™ plus Static Mixer 134
4.31 The influence of Reynolds Number on CG Number for each tested length of the CALGAVIN Static Mixer 135
4.32 Collated Chart of the effect of insert Length on Coefficient of Variance (CoV)-based Mixing for the SMX™, SMX™ plus and CALGAVIN Static Mixer 136
4.33 Collated Chart of the effect of insert Length on CG Number-based Mixing for the SMX™, SMX™ plus and CALGAVIN Static Mixer 137

4.34 Collated Chart of the Energy Penalty (Fanning friction factor) Required to Achieve Certain Mixing Levels as Assessed by Coefficient of Variance (CoV) for the SMX™, SMX™ plus and CALGAVIN Static Mixer at a Reynolds Number of 1 138
4.35 Collated Chart of the Energy Penalty (Fanning friction factor) Required to Achieve Certain Mixing Levels as Assessed by CG Number for the SMX™, SMX™ plus and CALGAVIN Static Mixer at a Reynolds Number of 1 139

5.1 Temperature Viscosity Curve for 77.8 wt.% Glycerol 144
5.2 Temperature Density Curve for 77.8 wt.% Glycerol 144
5.3 Normalised Friction Factor over Reynolds Number for SMX™ Static Mixer Insert 146
5.4 Normalised Friction Factor over Reynolds Number for SMX™ plus Static Mixer Insert 147
5.5 Normalised Friction Factor over Reynolds Number for CALGAVIN Static Mixer Insert 147
5.6 Friction Factor over Reynolds Number for the High Shear Static Mixer Designs: SMX™, SMX™ plus and the CALGAVIN Static Mixer 148
5.7 Friction Factor over Reynolds Number for the High Shear Static Mixer Designs: SMX™, SMX™ plus and the CALGAVIN Static Mixer 150
5.8 All Captured CALGAVIN Static Mixer PLIF Images for 77.8 wt .% Glycerol Solution with Each being the Average of 100 Images 154
5.9 All Captured SMX™ Static Mixer PLIF Images for 77.8 wt .% Glycerol Solution with Each being the Average of 100 images 155
5.10 All Captured SMX™ plus Static Mixer PLIF Images for 77.8 wt .% Glycerol Solution with Each being the Average of 100 images 156
5.11 Sequential Planar Laser-Induced Fluorescence (PLIF) images 0.25 seconds after each other for four units of a CALGAVIN Static Mixer at Reynolds number 110.67 157

5.12 Pixel flux heatmap for four CALGAVIN Static Mixer repeats Reynolds number 7.57 (left) and Reynolds number 110.67 (right) with proportional scaling 158
5.13 Planar Laser-Induced Fluorescence (PLIF) results for eight repeats (184 mm) for the SMX™ Static Mixer across varying temperature and Reynolds number 159
5.14 Planar Laser-Induced Fluorescence (PLIF) results for eight repeats (184 mm) for the SMX™ plus Static Mixer across varying temperature and Reynolds number 160
5.15 Planar Laser-Induced Fluorescence (PLIF) results for six repeats (192 mm) for the CALGAVIN Static Mixer across varying temperature and Reynolds number 161
5.16 Pixel flux heatmap for eight SMX™ static mixers with proportional scaling 162
5.17 Pixel flux heatmap for eight SMX™ plus static mixers with proportional scaling 163
5.18 Pixel flux heatmap for six CALGAVIN static mixers with proportional scaling 164
5.19 PLIF images of SMX™ static mixer targeting a Reynolds number of 100 for all tested lengths 165
5.20 The influence of Reynolds Number on Coefficient of Variance (CoV) for each tested length of the SMX™ Static Mixer 167
5.21 The influence of Reynolds Number on Coefficient of Variance (CoV) for each tested length of the SMX™ plus Static Mixer 167
5.22 The influence of Reynolds Number on Coefficient of Variance (CoV) for each tested length of the CALGAVIN Static Mixer 168
5.23 The influence of Reynolds Number on CG Number for each tested length of the SMX™ Static Mixer 170
5.24 The influence of Reynolds Number on CG Number for each tested length of the SMX™ plus Static Mixer 171

5.25 The influence of Reynolds Number on CG Number for each tested length of the CALGAVIN Static Mixer 171
5.26 Collated Chart of the effect of insert Length on Coefficient of Variance (CoV)-based Mixing for the SMX™, SMX™ plus and CALGAVIN Static Mixer 173
5.27 Collated Chart of the effect of insert Length on CG Number-based Mixing for the SMX™, SMX™ plus and CALGAVIN Static Mixer at Reynolds number 1 174
5.28 Collated Chart of the Energy Penalty (Fanning friction factor) Required to Achieve Certain Mixing Levels as Assessed by Coefficient of Variance (CoV) for the SMX™, SMX™ plus and CALGAVIN Static Mixer at a Reynolds Number of 50 175
5.29 Collated Chart of the Energy Penalty (Fanning friction factor) Required to Achieve Certain Mixing Levels as Assessed by CG Number for the SMX™, SMX™ plus and CALGAVIN Static Mixer at a Reynolds Number of 50 175
5.30 PLIF images at comparable Reynolds Numbers for the 99.8 wt.% and the 77.8 wt. % Tests of the SMX™ Static Mixer 178
5.31 The influence of Reynolds Number on CoV for each tested length of the CALGAVIN Static Mixer Across 99.8 wt.% and the 77.8 wt. % Tests . . 179
5.32 The influence of Reynolds Number on CoV for each tested length of the SMX™ Static Mixer Across 99.8 wt.% and the 77.8 wt. % Tests 179
5.33 The influence of Reynolds Number on CoV for each tested length of the SMX™ plus Static Mixer Across 99.8 wt.% and the 77.8 wt. % Tests . . 180
5.34 The influence of Reynolds Number on CG Number for each tested length of the CALGAVIN Static Mixer Across 99.8 wt.% and the 77.8 wt. % Tests 180
5.35 The influence of Reynolds Number on CG Number for each tested length of the SMX™ Static Mixer Across 99.8 wt.% and the 77.8 wt. % Tests . 181

5.36 The influence of Reynolds Number on CG Number for each tested length of the SMX™ plus Static Mixer Across 99.8 wt.% and the 77.8 wt. % Tests 181

6.1 Labelled Fluid Volume Model for Simulations of SMX™ Static Mixer . . 189

6.2 Mesh Independence Study of Pressure Drop Across a Nov Kenics Mixer 196

6.3 Mesh Order of Error for Pressure Drop Mesh Independence Study of Nov Kenics Static Mixer 197

6.4 Comparison of Passive Scalar CFD Mixing Simulations (Top) to the Planar Laser-Induced Fluorescence (PLIF) Experiments they were based on (Bottom) for Various Element Repeats of a Kenics Static Mixer at a Reynolds number around 0.47 198

6.5 Comparison of Passive Scalar CFD Mixing Simulations (Top) to the Planar Laser-Induced Fluorescence (PLIF) Experiments they were based on (Bottom) for Various Element Repeats of a CALGAVIN Static Mixer 200

6.6 Mesh Independence Study of Coefficient of Variance Across a Novel Kenics Mixer 201

6.7 Mesh Independence Study for Boundary Sampled and Massed Particle Tracking Mixing of a Kenics Static Mixer 204

6.8 Outlet Boundary Sample Mixing Images from a Series of Kenics Particle Tracking Simulations 205

6.9 Mixing Images of Six Kenics Elements for Particle Tracking (Left), Planar Laser-Induced Fluorescence (PLIF) (Middle) and Passive Scalar (Right) 205

6.10 Boundary Sampled Massed Particle Tracking Simulation of 8 Elements of a SMX™ plus Static Mixer at a Reynolds Number of 7.48 with 25,216,898 Particles 207

6.11 PLIF Experimental Image (Left) Compared Against Particle Tracking Simulation of 8 Elements of a SMX™ plus Static Mixer at a Reynolds Number of 7.48 208

6.12 3 Element Passive Scalar Simulation (Left) Compared Against 8 Element PLIF Experimental Image (Bottom Right) and an 8 Element Particle Tracking Simulation (Top Right) of a CALGAVIN Static plus Static Mixer at a Reynolds Number of 7.36 209

List of Tables

2.1 Summary of Journal Papers Regarding the State-of-the-art for the use of PLIF to Assess Static Mixer Performance 35

3.1 Test Parameters for Mixing Experiments 91

4.1 Test Parameters for 99.8 wt.% Glycerol Mixing Experiments 97
4.2 Flow Resistance Coefficients and Exponents for Different Static Mixers . 105
4.3 Consolidated Linear Regression Parameters for CG Mixing Number over Reynolds Number Data for All Mixer Types with 99.8 wt.% Glycerol . . 128

5.1 Test Parameters for 77.8 wt.% Glycerol Mixing Experiments 145
5.2 Flow Resistance Coefficients and Exponents for Different Static Mixers . 150
5.3 Consolidated Linear Regression Parameters for CoV over Reynolds Number Data for All Mixer Types with 77.8 wt.% Glycerol 169
5.4 Consolidated Linear Regression Parameters for CG Mixing Number over Reynolds Number Data for All Mixer Types with 77.8 wt.% Glycerol . . 172
5.5 Linear Regression Parameters and Normalised RMSE (nRMSE) for CoV and CG Mixing Number over Reynolds Number Data for All Insert Types and All Fluid Rheologies with Averages and Standard Deviations 182

6.1 Fluid Properties 189
6.2 Simulation Models, Descriptions, and Values 192

Acronyms

CAD Computer-Aided Design

CCD Charged-Coupled Device

CFD Computational Fluid Dynamics

CNC Computerised Numerical Control

CoV Coefficient of Variance

CRC Cyclic Redundancy Check

CSTR Continuous Stirred Tank Reactor

ERT Electrical Resistance Tomography

GUI Graphical User Interface

ID inner diameter

IO Input/Output

OD outer diameter

ODBC Open Database Connectivity

P&ID Process and Instrumentation Diagram

PEPT Positron Emission Particle Tracking

PID Proportional Integral Derivative

PIV Particle Image Velocimetry

PLIF Planar Laser-Induced Fluorescence

RMSE Root Mean Square Error

ROI region of interest

RTD Platinum Resistance Thermometer Device

TTL Transistor-Transistor Logic

VFD Variable Frequency Drive

Abstract

A test facility was developed to enable continuous Planar Laser-Induced Fluorescence (PLIF) for the evaluation of static mixers. By integrating an activated carbon-based filtration system, the Rhodamine 6G tracer compound was adsorbed from spent glycerol test fluid, allowing it to be recycled back into the loop. Drawing inspiration from industrial techniques, the test rig incorporated comprehensive digital data acquisition and control systems, enabling remote management of temperature (and thus viscosity) and mass flow. All operational parameters were measured automatically and recorded to a database, facilitating autonomous operation through pre-programmed state machines and control via PID algorithms. To validate the accuracy and repeatability of flow properties, static mixer pressure drop tests were conducted, confirming the reliability of the on-line pipe rheometer across different glycerol mass fractions. Comprehensive PLIF imagery was captured at the outlets of various static mixers following the injection of Rhodamine 6G dye at their inlets. Included static mixers are the SMX™, SMX™ plus, Chemineer Kenics, and a new static mixer design from CALGAVIN. The high-resolution images were quantitatively analysed using coefficient of variance (CoV) and a newly proposed CG Number to assess the consistency and effectiveness of mixing under different flow conditions Concurrently, a novel flux-based particle tracking computational fluid dynamics (CFD) methodology was developed, translating Lagrangian simulations back into Eulerian space. This approach enables CFD simulations to mirror experimental PLIF testing by producing images with a non-binary dynamic range while avoiding the numerical diffusion issues associated with passive scalar techniques. By combining this CFD method with experimental PLIF results, rapid prototyping of static mixer designs is facilitated, allowing computational testing of variations prior to fabrication and experimental validation of the most promising designs.

Acknowledgements

First and foremost, my deepest thanks go to Dr.-Ing. Peter Drögemüller and Stephen Perkins for their invaluable expertise, without which this research would be in a far sorrier state. I am equally grateful to the entire team at CALGAVIN, not only for creating the welcoming and inspiring workplace it is known for, but also funding both me and this work.

I am also deeply grateful to Dr. Richard Greenwood for his understanding and compassion for doctoral students, and to Professor Mark Simmons for his exceptional editorial insights. Special thanks to Dr. Sasha Komrakova, whose supervision - however brief - enabled the most productive and fruitful "holiday" I will likely ever experience.

Finally, to my mother, given that this is the only page she will read: you deserve at least some credit for this thesis through your relentless daily inquiries about my progress over five years. And to my father, who likely reduced those inquisitions — thank you.

This research was supported by the Engineering and Physical Sciences Research Council (EPSRC) through grant number EP/S023070/1.

CHAPTER 1

Introduction

Mixing is an ubiquitous unit operation in an array of chemical processes, especially when it comes to handling viscous substances. Components within products need to achieve a particular state of 'mixedness', or, maintain a controlled level of segregation (Kukukova et al., 2009). The implications of insufficient or uneven mixing during processing are costly and can be a potential for yield losses resulting from reaction inefficiencies where products might not achieve their intended functionality, leading to reduced efficacy and performance, a report from 1989 estimated between that in the US alone between a cost of $1-10 billion was felt by the the process industry from inadequate understanding of mixing (Nienow et al., 1992).

The challenge in chemical processing is not merely in ensuring components mix, but understanding the degree to which they have mixed. Discerning 'mixedness' presents significant issues, mirroring the complexity of understanding the mixing process itself, where often, without sampling, the determination is simply that the product is subpar on completion. The industry lacks straightforward monitoring tools comparable to those one would find in, for example, measuring thermal information. There is no thermocouple equivalent for mixing, there are limited design equations from first principles, and the measurement techniques are expensive and complicated. When is something truly mixed, or more realistically, when is it mixed enough? As it stands, to measure mixing, far more complex techniques including, but not limited to, Planar Laser-Induced Fluorescence (PLIF) (Alberini et al., 2014), Particle Image Velocimetry

(PIV) (Shen et al., 2022), Positron Emission Particle Tracking (PEPT) (Rafiee et al., 2011) and Electrical Resistance Tomography (ERT) (Forte et al., 2019) are needed. In particular, PIV can be used to analyze mixing by visualizing flow fields and identifying regions of high shear or recirculation, which are often indicative of effective mixing zones.

In attempting to reach this threshold it is not uncommon for the response to be over-mixing. Without the aforementioned robust mixing measurement techniques, it is safer to over-blend. All chemical engineering processes are designed with a margin of over-design, yet without this understanding significant time and energy (and ultimately, capital) can be wasted. It would be better then to have a comprehensive understanding of the mixing process and the tools involved in mixing.

One widely adopted solution to address these mixing challenges is the use of static mixers. Static mixers are motionless devices installed within pipelines that contain a series of baffle structures. As fluids flow through these mixers, the internal structures divide, blend, and stretch the flow, promoting efficient mixing without the need for moving parts. They are particularly utilised in handling viscous substances, where flow is often laminar and natural mixing through turbulence is minimal. In such conditions, lateral movement of fluid layers is limited, making mixing more challenging. Static mixers overcome this by repeatedly splitting and reorienting the flow through their internal structures, enhancing interfacial contact between fluid elements and thereby promoting effective mixing even in low Reynolds number regimes (Streeter & Wylie, 1975). However, despite their practical advantages and widespread use, understanding and quantifying the degree of mixing achieved within static mixers remains a complex task. This difficulty underscores the need for advanced measurement techniques to evaluate their performance accurately and optimise mixing processes.

This preamble serves as an introduction point for PLIF. PLIF is an optical technique that works by illuminating a thin plane of the fluid with a laser, causing the fluorescent molecules within a fluid to emit light at a different wavelength to the incident

laser light. When applied to static mixers, PLIF provides high-resolution insights into the mixing efficiency and distribution patterns within mixing fluids. This light emission, captured by a camera, reveals the concentration and distribution of the fluorescing element in the fluid, allowing for detailed visualisation and quantification of mixing.

The traditional methodology for PLIF involves merging multiple fluid streams; usually one fluid (doped with a fluorescent dye) is injected into a bulk flow stream before a static mixer. Once testing has completed, these fluids are directed into waste tanks. This practice, however, incurs substantial costs. The test fluids are now mixed and cannot simply be un-mixed for further testing. The research presented in this thesis looks into a process to negate this problem and postulate a methodology for continuous PLIF where fluid wastage is no longer a factor. By introducing this, further enhancements to mixing measurements are created. Temperature control becomes simpler leading to more robust and controlled data and with the limit of test fluid removed, a greater variety of tests can be completed with more opportunity for repetition. Larger static mixer diameters can be tested and a more in-depth iterative process on static mixer design can be undertaken. All of these benefits occur while also then being able to test at a greater rate of speed.

The ultimate aim of the research presented in this thesis is to develop an enhanced and novel form of continuous PLIF and validate its efficacy by using it to test and iterate upon designs for a static mixer against market available options. Beyond this, the current paradigm of static mixing understanding can be broadened. The novel PLIF will capture high-resolution mixing images and use them to quantify mixing across a broader flow range than done previously, increasing the body of knowledge in static mixers.

1.1 State-of-the-Art and Business Case

The review of the current state-of-the-art explores the current merits of PLIF and demonstrates its effectiveness for quantifying static mixer performance but also

identifies that it is very much a batch laboratory procedure in its current form. The primary limitation of this method is the destructive nature of the fluid testing process.

Firstly, test fluids at a testing grade are expensive, making destructive testing costly. If each test uses said consumable and new fluid needs to be accurately composited again, this adds a time constraint to each test. When each test has a consumable that costs money and introduces a ballooning setup time, more often than not, a reduced testing range is completed. This is either realised as a reduced number of overall static mixers being tested or, instead, each static mixer having a less comprehensive set of tests completed.

The purpose of this research is therefore to create a form of PLIF for static mixer testing that does not destructively test and can be used in an industrial setting. With this innovation, the cost, setup, and ultimately speed limitations of PLIF are heavily mitigated. To prove the viability of this rig, it will be used to evaluate market-available static mixers and benchmark them against each other and a novel design. While computational methods such as CFD can be valuable for informing design choices and exploring flow dynamics, they rely on assumptions and simplifications that must ultimately be validated. Experimental prototyping remains essential to confirm real-world performance, particularly in complex mixing scenarios where fluid behaviour is highly sensitive to geometry and material properties. If continuous PLIF proves to be an efficient and accurate method of testing static mixers, its primary business case is its ability to rapidly prototype new static mixer designs. The global static mixer industry is valued at $493 million (IndustryARC, 2019), and the ability to rapidly prototype to create and maintain the performance edge over competitors presents significant business potential.

There is also value in the exactness of knowledge of how a static mixer performs. If a manufacturer makes a static mixer that performs 5% worse than a competitor but has a greater knowledge of the performance to a more minute degree, they may be able to design for applications with more confidence and therefore less over-design,

potentially warranting a shorter or lower pressure application. This means that this updated PLIF concept allows said manufacturer to have a further edge in business in both data accuracy and perceived competence.

Further to this, if this rig can be packaged as a method with general application requiring only limited modifications for different fluid properties, the test rig can be duplicated and potentially present in multiple fluid markets across chemical, pharmaceutical, and food/beverage industries. If non-destructive PLIF is implementable, there is nothing to stop it from being utilised across other mixing fields. Without the constraint on test fluid quantities, PLIF could hypothetically be installed around different industrial mixing equipment, with one such example being Continuous Stirred Tank Reactors (CSTRs). Here it could rapidly test the mixing effects of different impellers, impeller speeds, baffle designs, and feed-rates on a fully continuous basis.

Potential risks in this avenue include that if a 'continuous' form of PLIF is developed, it may not be applicable for all testing regimes. Depending on the method, there may only be utility with certain fluid compounds or rheologies. For this reason, the method should be aimed to be as general as possible or to work with fluids that are good analogies for many industrially used compounds. PLIF is now also competing with numerical technologies. Section 2.5.2 will explore how Computational Fluid Dynamics (CFD) is becoming an increasingly used tool in mixing evaluation. Computational time is becoming ever cheaper and the models and techniques more sophisticated, but as discussed above and explored in Section 6, there are still fundamental limitations in the predictive accuracy of CFD, especially in capturing the fine-scale, three-dimensional, and transient mixing phenomena that PLIF can directly observe. CFD relies on assumptions, simplifications, and turbulence models that may not hold across all geometries and flow regimes—especially in highly viscous or non-Newtonian systems where experimental validation remains essential. While CFD may be "good enough" for certain design iterations or approximations—especially given its lower barrier to entry—it cannot fully replace physical testing when high-fidelity insight is required. For PLIF to remain

competitive, it must evolve to be cheaper, faster, and more comprehensive, offering an indispensable experimental benchmark against which numerical predictions can be validated.

Improving the PLIF technology to operate at industrial speeds offers clear benefits. These include cost savings, faster prototyping, and enhanced precision in performance data. Such advancements can provide significant competitive and operational advantages across multiple industries, solidifying the relevance and value of PLIF in the modern industrial landscape.

1.2 | Aims and Objectives

The overall aim of this research is to develop a novel, continuous, and non-destructive PLIF methodology that enables efficient evaluation and optimisation of static mixer designs without incurring fluid wastage. By implementing fluid separation techniques that allow for the reuse of test fluids, this method can be combined with automated temperature and flow control to broaden the range of flow conditions and mixer lengths that can be tested whilst also testing more quickly. Ultimately, this work aims to create a technique that can rapidly prototype static mixer designs and advance the understanding of static mixing processes; contributing more effective and sustainable mixing solutions in the chemical industry.

There is a clear business case for a form of non-destructive and 'continuous' PLIF. What follows is an outline of the proposed steps to realise this idea:

1. Research methods of fluid separation, including gravity, reaction, filtration, or other applicable techniques.
2. Test the efficacy of these methods by integrating promising candidates into a working PLIF experimental hardware setup.

3. If successful, implement control, sensors, and automation to industrialise the technology.

4. Use the setup to test market-available static mixer technologies against a novel design. This will demonstrate the potential of the novel design, allow further iterative prototyping, and serve as a means of testing the function of the test rig and its 'continuous' nature.

5. Make adjustments and improvements based on the above experiments and conduct further tests to determine the flow regime and variable fluid property limits that the rig can test.

1.3 Thesis Layout

This section provides an overview of the thesis structure, summarising each chapter's content and objectives.

- **Chapter 2: Literature Review**

  This chapter provides an overview of the relevant literature by outlining current research areas and identifies gaps that exist in the field. It provides the basic understanding through equations and explanations of the knowledge and context required to understand this research and shows what this work builds on to in order to contribute to the existing body of knowledge.

- **Chapter 3: The Development of a Novel Test Facility for Continuous PLIF**

  This chapter focuses to the development of a novel test facility designed for continuous Planar Laser-Induced Fluorescence (PLIF) testing. It explores the necessity of industrialising PLIF testing to enhance its efficiency. It outlines the design principles for creating a continuous and autonomous system, detailing the steps taken in the construction and commissioning of the test facility. This facility is then the basis for the experimental work conducted in subsequent chapters.

- **Chapter 4: Low Reynolds Laminar Static Mixer Testing**

  Using the test rig developed in the previous chapter, this one presents the experimental investigation into low Reynolds number (0.03 - 16) laminar static mixer testing. It provides a detailed account of the test parameters and methodology employed during the experiments. The various static mixer geometries tested are depicted and the energy loss data for the static mixers is presented. Alongside this captured PLIF imagery that visually represents the mixing performance is quantified into mixing numbers to assess the effectiveness of each mixer. The chapter concludes by evaluating the overall performance efficiency of the static mixers against one another.

- **Chapter 5: Boundary Separation in Laminar Static Mixing**

  Building upon the previous chapter, this section details changes in the test parameters and methodology to investigate boundary separation in laminar static mixing at a higher range of Reynolds numbers (0.5 - 126). It presents the energy loss data for the static mixers under these new conditions and combines it with the data from Chapter 4 for a comprehensive analysis. Captured PLIF imagery is shown to illustrate the effects observed and quantitative mixing numbers are calculated and compared with those from the earlier experiments. The chapter discusses the implications of these findings and suggests areas for future work.

- **Chapter 6: Computational Fluid Dynamics in Laminar Mixing**

  This chapter explores the application of Computational Fluid Dynamics (CFD) in studying laminar mixing. It details the software used for simulations and describes the setup of application models and geometries and carries out a mesh independence study to ensure the reliability of the results. Simulation are carried out to evaluate current passive scalar methodologies before introducing a novel flux-based particle tracking CFD method. This new approach is compared against passive scalar simulations and experimental PLIF results, highlighting its potential advantages.

- **Chapter 7: Conclusions and Recommendations**

  The final chapter summarises the results of the thesis as a whole, examining how the various components of research relate to each other and advance the understanding of testing laminar mixing in static mixers in order to rapidly improve them. It discusses the limitations encountered during the research, offering recommendations for future work in the area and by addressing these limitations, the chapter suggests avenues for further investigation that could build upon the findings presented in this thesis.

CHAPTER 2

Literature Review

2.1 | Introduction

Meijer et al. (2012) reports that the first use of static mixers in the process industry dates back to the 1970s, primarily as components in chemical reactors designed to improve mixing within laminar flow. The first recorded invention however is landmarked with the filing of the patent for the first form of a helical mixer by the Arthur D. Little Company in 1966 (Armeniades et al., 1966). This became the Kenics Static Mixer from Chemineer (Figure 2.1) and is now a product of National Oilwell Varco (NOV). From this point, the quantification of static mixing became a significant focus in the 1980s, coinciding with the invention and release of the still widely known Sulzer SMX™. These designs have been iterated upon - most notably with Sulzer releasing the SMX plus (Figure 2.2) - and copied by many manufacturers, and their inception marked the increasing need to quantify performance more accurately and under newly developing flow conditions. Technologies for this purpose have evolved, ranging from more rudimentary methods like two-part resin injection to sophisticated techniques such as optical fluid analysis and Computational Fluid Dynamics (CFD). This literature review explores the currently used techniques, their strengths and weaknesses, and the fundamentals of mixing itself.

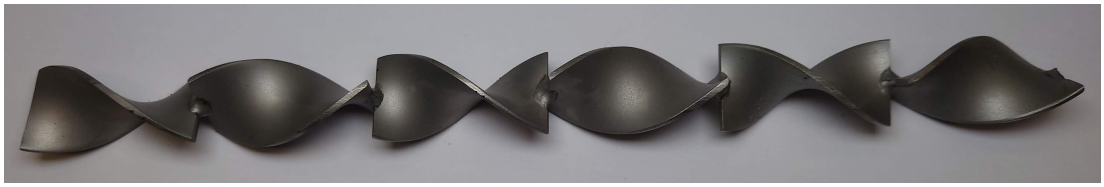


Fig. 2.1. Nov Kenics Static Mixer



Fig. 2.2. Sulzer SMX plus Static Mixer

2.2 | Fluid Fundamentals

2.2.1 General Rheology

Understanding rheology comes hand in hand with understanding mixing. "Apparent viscosity", perhaps the attribute most commonly associated with rheology, is arguably the most important factor in mixing. Viscosity is a value of a fluid's resistance to flow; the higher it is, the more difficult it is to induce internal movement and interfacial contact, both of which are necessary for mixing. Gasses have very low viscosities and will freely mix with relative ease in their volume. Liquids have orders of magnitude higher viscosities and are much slower to mix with no external input; the higher the viscosity, the slower the diffusion of molecules throughout a fluid.

A higher viscosity also means that when external energy is applied in the form of mechanical agitation or pressure-driven flow, more energy is required to induce movement in the fluid, and the more resistant it is to the onset of turbulence.

The Reynolds number is a dimensionless quantity used in fluid mechanics to characterise the flow regime of a fluid in motion. It represents the ratio of inertial forces to viscous forces within a fluid and helps determine whether the flow will be

laminar (Reynolds numbers below 2000), turbulent (Reynolds numbers above 4000), or in a transitional state between them. These ranges are specific to circular pipe flow. Reynolds number is defined as:

$$Re = \frac{\rho u L}{\mu} = \frac{u L}{\nu} \tag{2.1}$$

where ρ is the fluid density, u is the characteristic velocity, L is the characteristic length (e.g., diameter of a pipe), μ is the dynamic viscosity, and ν is the kinematic viscosity ($\nu = \frac{\mu}{\rho}$)(Reynolds, 1883).

When studying Newtonian fluids, the shear stress of a fluid is directly proportional to the shear rate by a factor of the fluid dynamic viscosity, Equation 2.2. But this response is not suitable for all fluid types. Non-Newtonian fluids do not obey Equation 2.2 and have different models where the "apparent" viscosity changes depending on a number of factors. The following section outlines a brief overview of the types of rheological behaviours and the mathematical models commonly used to fit non-Newtonian fluid responses (Barnes et al., 1989).

$$\tau = \eta \dot{\gamma} \tag{2.2}$$

where τ is the shear stress, η is the dynamic viscosity of the fluid, and $\dot{\gamma}$ is the shear rate.

For non-Newtonian fluids, the relationship between shear stress and deformation rate is non-linear. There are multiple types of non-Newtonian behaviour, each described by different models. One common model is given by the power-law equation:

$$\tau = K \dot{\gamma}^n \tag{2.3}$$

where τ is the shear stress, K is the consistency index, $\dot{\gamma}$ is the shear rate, and n is the flow behaviour index.

Shear-thinning (pseudoplastic) fluids exhibit a decrease in apparent viscosity as the shear rate increases, characterised by $0 < n < 1$. In contrast, shear-thickening (dilatant) fluids increase in apparent viscosity with increasing shear rate, which is described by the same model, but with $n > 1$.

Bingham plastic fluids have a yield stress, below which they exhibit solid-like behaviour. Once this threshold is overcome, however, they flow like Newtonian fluids.

$$\tau = \tau_y + \eta_p \dot{\gamma} \tag{2.4}$$

where τ_y is the yield stress and η_p is the plastic viscosity.

Herschel-Bulkley fluids also have a yield stress, but once overcome they exhibit shear-thinning or shear-thickening characteristics. Again, having an exponent above 1 demonstrates shear-thickening and between 0 and 1, shear-thinning.

$$\tau = \tau_y + K\dot{\gamma}^n \tag{2.5}$$

where τ_y is the yield stress, K is the consistency index, $\dot{\gamma}$ is the shear rate, and n is the flow behaviour index.

Some of the more complex non-Newtonian behaviours include thixotropic and rheopectic responses. These fluids introduce a time-dependent component, where the apparent viscosity changes over time under constant shear. Thixotropic fluids experience a decrease in viscosity with sustained shear, while rheopectic fluids exhibit an increase.

There are no comprehensive models that fully capture the behaviour of these fluids, but their behaviour can be approximated by incorporating time-dependent terms into the earlier model equations.

2.2.2 Rheological Data

With the above equations in mind, to accurately test using a specified fluid, the precise properties that constitute the constants in its relevant models are needed. This body of work extensively uses varying mass fractions of aqueous glycerol and, as such, requires the calculations of both the rheological and physical properties as the mass fraction and temperature of this fluid changes. The following empirical formulas provide these correlations based on temperature and glycerol mass fraction and are taken from Volk and Kähler (2018).

The density of pure water as a function of temperature T (in degrees Celsius) is given by:

$$\rho_W = 1000\left(1 - \left|\frac{T - 3.98}{615}\right|^{1.71}\right) \tag{2.6}$$

where ρ_W is the density of pure water [kg/m^3] and T is the temperature in degrees Celsius [°C]. The density of pure glycerol is expressed as:

$$\rho_G = 1273 - 0.612T \tag{2.7}$$

where ρ_G is the density of pure glycerol [kg/m^3]. The contraction factor accounts for the volume change upon mixing glycerol and water:

$$\begin{aligned} c = 1 &- (3.52 \cdot 10^{-6} \cdot \mathrm{WF})^3 + (1.027 \cdot 10^{-4} \cdot \mathrm{WF})^2 \\ &+ 2.5 \cdot 10^{-4} \cdot \mathrm{WF} - 1.691 \cdot 10^{-4} \end{aligned} \tag{2.8}$$

where c is the contraction factor (dimensionless) and WF is the mass fraction of glycerol in the solution (dimensionless, $0 \leq \text{WF} \leq 1$). The overall contraction of the mixture is:

$$\text{Contraction} = 1 + \frac{c}{100} \tag{2.9}$$

where Contraction is the adjusted contraction factor accounting for volume change. The density of the mixture is calculated using the densities of the pure components and the contraction factor:

$$\rho_S = \text{Contraction} \left(\rho_W + \frac{\rho_G - \rho_W}{1 + \frac{\rho_G}{\rho_W} \left(\frac{1}{\text{WF}} - 1 \right)} \right) \tag{2.10}$$

where ρ_S is the density of the glycerol-water solution [kg/m^3]. The dynamic viscosity of pure water is:

$$\mu_W = 0.001 \cdot 1.790 \cdot \exp\left(\frac{(-1230 - T)T}{36100 + 360T} \right) \tag{2.11}$$

where μ_W is the dynamic viscosity of pure water [Pa $\cdot$ s]. The dynamic viscosity of pure glycerol is:

$$\mu_G = 0.001 \cdot 12100 \cdot \exp\left(\frac{(-1233 + T)T}{9900 + 70T} \right) \tag{2.12}$$

where μ_G is the dynamic viscosity of pure glycerol [Pa $\cdot$ s]. The empirical parameters a and b, which are temperature-dependent, are used in the viscosity correlation:

$$a = 0.70 - 0.0017T \tag{2.13}$$

$$b = (4.9 + 0.036T) \cdot a^{2.5} \tag{2.14}$$

where a and b are empirical parameters (dimensionless). The mixing parameter α accounts for interactions between glycerol and water molecules:

$$\alpha = 1 - \mathrm{WF} + \frac{ab\mathrm{WF}(1 - \mathrm{WF})}{a\mathrm{WF} + b(1 - \mathrm{WF})} \tag{2.15}$$

where α is the mixing parameter. The viscosity ratio parameter A is the natural logarithm of the ratio of pure component viscosities:

$$A = \ln\left(\frac{\mu_W}{\mu_G}\right) \tag{2.16}$$

where A is the viscosity ratio parameter (dimensionless) and ln denotes the natural logarithm. The dynamic viscosity of the glycerol-water mixture is:

$$\mu = \mu_G \cdot \exp(A\alpha) \tag{2.17}$$

where μ is the dynamic viscosity of the final glycerol-water solution [$\mathrm{Pa} \cdot \mathrm{s}$] and exp denotes the exponential function.

2.2.3 Laminar Flow

Laminar flow, also referred to as streamline or viscous flow, is characterised by the smooth, orderly movement of fluid. In laminar flow: (1) layers of fluid move over one another at different speeds with negligible mixing between the layers, (2) fluid particles follow well-defined and observable paths or streamlines, and (3) the flow is typical of viscous fluids, where viscosity plays a significant role in determining the flow behaviour (*DOE Fundamentals Handbook* 1992). Viscous forces are dominant compared to inertial

forces in the fluid, and it is typically characterised by low Reynolds numbers—below 2000 in circular pipes (Batchelor, 2000). As Reynolds number tends toward zero, the flow becomes increasingly dominated by viscous effects, and inertial effects are essentially negligible.

For liquid, incompressible flows that are Newtonian, the volumetric flow rate is calculated from the Hagen-Poiseuille equation:

$$Q = \frac{\Delta P \pi R^4}{8 \mu L} \tag{2.18}$$

where ΔP is the pressure drop, R is the radius of the pipe, μ is the dynamic viscosity, and L is the length of the pipe.

Within this circular pipe, laminar flow presents with a parabolic velocity profile where the velocity $u(r)$ is a function of the radial distance r from the centre of the pipe:

$$u(r) = u_{\max} \left(1 - \frac{r^2}{R^2} \right) \tag{2.19}$$

where $u_{\max}$ is the maximum velocity at the centre of the pipe. This velocity profile integrates across the pipe's cross-section to yield the average velocity $u_{\text{avg}} = \frac{1}{2} u_{\max}$, which in turn relates to the volumetric flow rate Q via $Q = u_{\text{avg}} \cdot A = \frac{u_{\max} \pi R^2}{2}$.

The shear stress $\tau(r)$ at a radial distance r from the pipe centre is given by:

$$\tau(r) = \frac{\Delta P}{2L} r \tag{2.20}$$

where the shear stress increases linearly with radius, reaching a maximum at the pipe wall.

In this regime, enhanced mixing is often required, as the primary mode of mass transport between fluid layers is molecular diffusion. Although Taylor dispersion does

occur, on the time and length scales relevant to process engineering, such diffusion is too slow to be effective, making laminar mixing practically negligible without additional mixing mechanisms such as dynamic or static mixers.

2.2.4 Turbulent Flow

In contrast to laminar flow, turbulent flow is a far more complex flow regime. It is characterised by chaotic and irregular fluid motion. The smooth, parallel layers characteristic of laminar flow are disrupted by continuously changing fluid velocity magnitudes and directions. In a circular pipe, turbulent flow is observed at Reynolds numbers above 4000, where inertial forces dominate over viscous forces.

As originally described by Richardson and later formalised by Kolmogorov, turbulence consists of random flows that contain eddies and vortices of various sizes. Larger eddies break down into smaller ones in a process known as the energy cascade, with energy being transferred from large to small scales until it dissipates due to viscosity at the smallest scales. This energy cascade is associated with the Kolmogorov length scale, which represents the smallest eddies where viscous dissipation occurs (Richardson, 1922) (Kolmogorov, 1941). The advantage of this over laminar flow is that the chaotic motion promotes self-mixing, resulting in significantly enhanced internal heat and mass transfer. That is not to say that external mixing equipment is never required—as there are many turbulent-tuned static mixers—only that the time scale of mixing is much shorter.

The major penalty of turbulent flow is the increased energy dissipation, which manifests as higher pressure drop—sometimes 10 to 100 times more than in laminar flow depending on flow conditions. This pressure drop cannot be resolved from first principles but is instead evaluated using empirical equations. The basis of these is the Darcy-Weisbach equation, which relates pressure drop to flow velocity, pipe length, and diameter (White, 2011):

$$\Delta P = f \frac{L}{D} \frac{\rho u^2}{2}$$

where ΔP is the pressure drop, f is the Darcy-Weisbach friction factor, L is the pipe length, D is the pipe diameter, ρ is the fluid density, and u is the flow velocity. In turbulent flow, f is not constant and depends on both Reynolds number and pipe roughness. For smooth pipes and lower turbulent Reynolds numbers (below 100,000), the Blasius equation can be used:

$$f = 0.3164 \; Re^{-0.25} \tag{2.21}$$

For rough walls and higher Reynolds numbers, the more complex Colebrook-White equation is used. Since the friction factor appears on both sides, this equation must be solved iteratively:

$$\frac{1}{\sqrt{f}} = -2 \log_{10} \left(\frac{\varepsilon}{3.7D} + \frac{2.51}{Re \sqrt{f}} \right) \tag{2.22}$$

The flow profile and discrete velocities in turbulent mixing are significantly harder to evaluate due to the randomness of flow. While laminar flow is time-invariant, turbulent flow evolves continuously in both time and space. However, it has been shown that turbulence can exhibit statistical stability when averaged over time. The Navier-Stokes equations govern all fluid motion, including turbulence, but due to their non-linearity, solving them analytically for turbulent flow is currently impossible. Instead, they are averaged to produce the Reynolds-averaged Navier–Stokes (RANS) equations. Various models based on RANS will be discussed in the context of CFD in Section 2.5.2.

2.3 | Mixing Theory

The goal of a static mixer, perhaps obviously, is to mix a fluid as it flows through a pipe. Therefore, it stands to reason that a static mixer that achieves more effective mixing than others is the better mixer. There are, however, multiple factors to consider when evaluating the overall quantitative performance of a static mixer. Beyond just

how well it mixes, it is necessary to look at the penalties that including a static mixer might introduce, the most obvious of which is the energy loss of the system. Pumping through a mixer induces more pressure loss than simply pumping through an empty pipe. A mixer may mix very well, but it could do so in a very energy-inefficient manner and therefore become less suitable to the application. This factor is further explored in Section 2.4.

Another is how long the mixer needs to be to achieve the desired mixing level. In some applications, such as those on sea vessels, space is a severe limitation. In cases like these, a mixer that can be effective over a short distance may become the most appropriate, even at the cost of an increased overall energy loss. A similar effect will occur in retrofit applications. If a static mixer is to be added to a pipe already in operation due to problems noted after plant commissioning, the mixer will need to work within whatever space has already been allocated.

The final main factor is then cost; process plants have budgets. The mixer that is the best may still not be selected if it carries a significant premium over a competitor's product. For a static mixer to compete, it must strike a balance between all of these qualities. This section looks specifically into the available literature on how mixing performance is measured so that the project iterations can be objectively compared to one another and to available competition.

2.3.0.1 Coefficient of Variance

The inclusion of a static mixer in an industrial design demonstrates the need to create a homogeneous fluid, or more realistically, a fluid that has been mixed to the necessary degree for the designated application. For the static mixer to be successful, it must therefore induce a mixing action that blends the fluid mixture to this minimum required uniformity. In order to specify a static mixer for a certain process, the ability to quantify the mixing performance is a crucial part of selection and design.

One of the earliest definitions for quantifying mixing in a binary liquid mixture is the *Intensity of Segregation*, introduced by Danckwerts (1952), and shown in Equation 2.23:

$$I = \frac{\sum_{i=1}^{n} \left(C_i - \bar{C}\right)^2}{n\bar{C}(1-\bar{C})} \tag{2.23}$$

This metric measures the degree of non-uniformity or segregation in a mixture. It compares the variance of local concentrations C_i within subregions to the theoretical maximum variance of a completely segregated mixture. Here: - C_i is the local concentration at sampling location i, - $\bar{C}$ is the mean concentration across all samples, - n is the number of sampling regions.

An intensity of segregation value of $I = 0$ indicates perfect homogeneity, while $I = 1$ corresponds to complete segregation.

A related and more commonly used method is the Coefficient of Variance (CoV) (coefficient of variance), defined in Everitt and Skrondal (2010) as:

$$\text{CoV} = \frac{\sigma}{\bar{C}} \tag{2.24}$$

where σ is the standard deviation of the concentration distribution and $\bar{C}$ is the mean concentration. The standard deviation σ is calculated as:

$$\sigma = \sqrt{\frac{1}{n-1} \sum_{i=1}^{n} \left(C_i - \bar{C}\right)^2} \tag{2.25}$$

where: - n is the number of sampling points, - C_i is the concentration at each sampling point, - $\bar{C}$ is the mean concentration.

The mean concentration in normalised form (i.e., between 0 and 1) is given by:

$$\bar{C} = \frac{1}{n} \sum_{i=1}^{n} \frac{C_i - C_0}{C_\infty - C_0} \tag{2.26}$$

where: - C_0 is the background or unmixed concentration, - C_∞ is the fully mixed concentration, - C_i is the local concentration at sampling location i.

The coefficient of variance provides a measure of consistency about the mean—i.e., the more uniform the concentration field, the lower the CoV. As CoV tends toward zero, the more homogeneous the mixture becomes.

A variation of this approach is the use of log-variance, which enhances the impact of small variations in concentration and provides a more sensitive analysis of mixing performance. It is defined by Brown et al. (2003) as:

$$\log Va = \log \sigma^2 = \log \left(\frac{1}{n-1} \sum_{i=1}^{n} \left(C_i - \bar{C} \right)^2 \right) \tag{2.27}$$

While these statistical metrics are widely used, they are not universally sufficient to describe mixing quality in isolation. For example, as shown in Figure 2.3, different spatial patterns of concentration can yield identical CoV values, despite visually different levels of mixing.

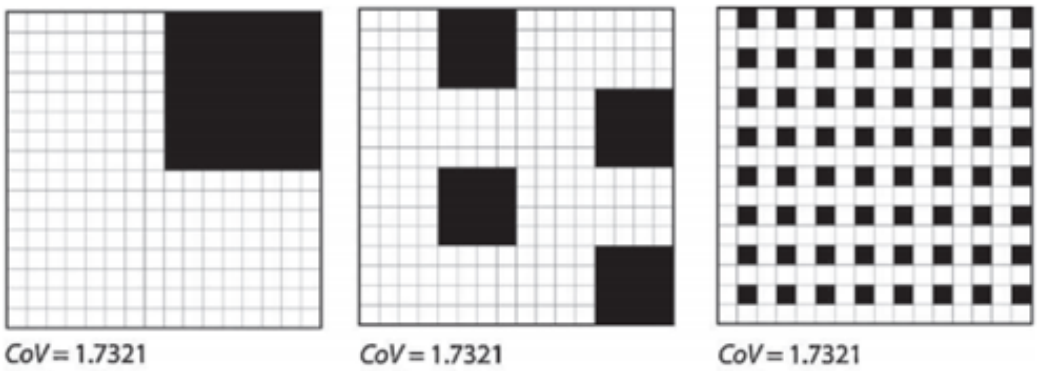


Fig. 2.3. CoV in Three Demonstrational Mixing Examples (Kukukova et al., 2009)

It can be clearly seen that the level of mixedness appears to increase from left to right, yet the calculated CoV remains the same. Kukukova et al. (2009) further

demonstrate this issue with more complex, non-binary concentration distributions. As such, CoV and related metrics are useful tools but should not be used in isolation. A broader set of metrics is often necessary to fully capture mixing behaviour (Alberini et al., 2014Kukukova et al., 2009).

2.3.1 Striation Thickness

Striation thickness is another method used in the assessment of mixing quality, but it quantifies a different aspect compared to statistical methods like CoV. As unmixed fluids are folded into each other, the number of layers of each fluid increases and the thickness of each layer decreases. Eventually, through enough folds, the layers become so thin that the fluid can be considered as fully mixed, or mixed enough—an analogy being drop dispersion in emulsions. By looking at the thickness of the layers, the level of mixing can then be assessed (Rauwendaal, 1991).

A formal definition of average striation thickness is given by Danckwerts as:

$$\delta = \frac{1}{a} \tag{2.28}$$

where δ is the average striation thickness and a is the interfacial area per unit volume (Danckwerts, 1952). This gives a geometric measure of how fine the layering has become, which is particularly relevant when mixing occurs via stretching and folding, such as in laminar systems.

In general, this is completed by computer analysis of images of the fluid due to the complexity of the fluid layers. But like the CoV method, it has inherent weaknesses. As the originally separate but miscible fluids are folded together, they do not remain as discrete layers of constant concentration. At the edges of each layer, each fluid will begin to diffuse into the other, causing regions of partial mass fractions. When measuring striation thickness, a tolerance for variation in concentration is used. This is a lossy method that largely assumes the layers are homogenous and returns the fluid to

a binary mixture. This can result in inconsistencies in mixing quantification and is also limited by needing the resolution of imaging or simulation techniques to be fine enough to resolve the layers (Alberini et al., 2014).

2.3.2 Areal Fraction Method

Alberini et al. (2014) suggested a new method, Areal Fraction, to quantify the level of mixing achieved with a static mixer and tested it with Planar Laser-Induced Fluorescence (PLIF) analysis (more information on PLIF is found in 2.5.1) to capture greyscale images of the pipe cross-section just after the static mixer. The greyscale images can then be analysed using a computer script and image analysis software. The concentration at any point is calculated when calibrated against reference runs and relating a dye concentration to pixel brightness level. Images are processed from their original, very discretised greyscale to a less discretised level. This essentially creates bins of concentrations similar to how one might find on a histogram, except that the changes are implemented on the image itself. For example on pixels at ± 60-80% of the perfect mixing level are all converted to the same value. This change makes the images easier to superficially parse and more obviously shows areas of good and poor mixing. From here, the Areal Fraction of each bin is found; this is the fractional area of the whole that corresponds to a certain mixing level. This information is used to plot bar charts of the type shown in Figure 2.4.

Figure 2.4 shows how each of the static mixers; $\#1_n$, $\#1_{nn}$ and $\#2$ have an improvement in mixing performance from 6 repeating elements in series to double the original length to 12 elements. The improvement is seen as each element having an increase in the areal fractions of high-intensity regions (areas of high dye mixedness) when static mixer length is doubled. The method also shows the improvement in mixing between each different static mixer suggesting that; $\#1_n > \#1_{nn} > \#2$.

The Areal Fraction graphing method gives a clear representation of mixedness, but often for comparison, it is desired to have a single number answer, even if this is not

the most accurate way to represent the quantification of mixing. The is a hold over from the very industrially prominent CoV and a desire to easily represent in a manner like that of heat transfer improvement. For areal fraction, this can be done by calculating the areal fraction of the total region that has the perfect mixing value to a tolerance. For example, this could be the area where the mixing is the perfect value ± 20%; this can be compared to other mixers and plotted on a graph to give a general mixing rank.

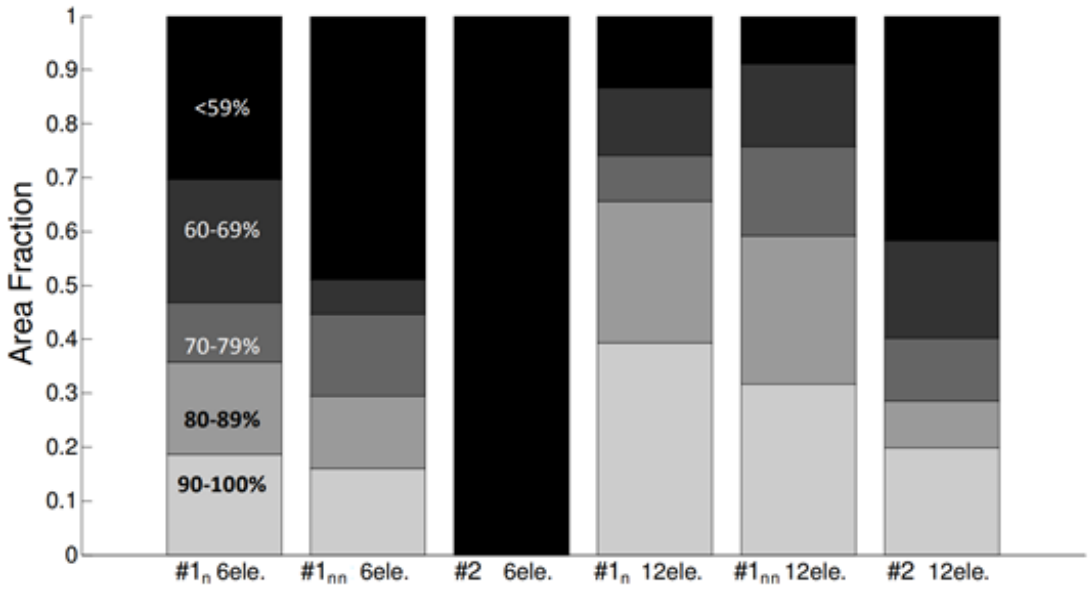


Fig. 2.4. Bar Graph Showing Discrete Areal Intensity Distributions for each Experiment (Alberini et al., 2014)

A downside here is that this number will perform poorly in representing unmixed, static regions in the flow. It is possible that a mixer could mix a portion of the flow brilliantly but at the cost of a certain area that may manage to fully bypass the blending portions of the mixer. Such a mixer may score very highly when looking at the Areal Fraction of high mixedness but still contain an area where no mixing occurs at all - which could have a serious effect on the product. It therefore remains important to look at both the captured PLIF image and the Areal Fraction histogram and not just rely on the aforementioned number.

2.3.2.1 CG Number

As part of a series of previous CFD tests done at CALGAVIN LTD, an in-house mixing evaluation technique was developed by W. Osley, S. Perkins and E. Knight (2020) with the goal of providing the advantages of all other mixing quantification techniques. When conducting a type of CFD simulation which uses a passive scalar to assess mixing level (more information on this topic can be found in section 2.5.2) the simulation outputs a significant amount of data on the proportion of tracer at the outlet of a mixer. The goal was to distil this to a single number that could fairly and quantifiably compare different static mixers. CoV is a technique that could be used here but with modern computing levels, it is still impractical to generate cell sizes that come close to the spatial resolution of experimental techniques like PLIF. There are also issues with a limitation caused by numerical diffusion, more information on this can again be found in section 2.5.2. These factors compound to have a far smaller sample size for both the total number of samples in the outlet plane and variety in each of those samples. This results in final mixing images that suggest far more mixing has occurred than reality when CoV analysis is used. Instead a more stringent method was suggested.

This 'CG Number' works by finding the total number of cells that have a range of a level of tracer in a given number of bins, as if one were presenting a histogram of the data. This total number of cells in converted to a percentage of the total area that each bin constitutes. This is much like the methodology that was suggested when assessing the Areal Fraction from Alberini et al. (2014). Each bin's percentage area is then multiplied by a weighting derived from a parabolic curve that lowers the influence of the cells that have a tracer level that is further from the perfect mixing value. This takes inspiration from the log-variance method (as seen in section 2.3.0.1) where the variance is squared; this punishes values further from the mean resulting in a high threshold requirement for mixing. Explained in another manner, the Areal Fraction of an certain tracer percentage will only have a significant impact on the CG Number if

it is close to the ideal mixing tracer amount. High Areal Fractions of a poorly mixed region have a lower weighting applied and thus affect the number less; yet crucially, all regions of the image are considered when calculating the CG Number. This is in contrast to the original Areal Fraction method that only considered the fraction of the total area that had the most mixing when collapsing the Areal Fraction histogram to a single number. These calculated weighted percentage area values are then summed to give a number up to 100 and subtracting this from 100 gives the CALGAVIN CG Number. The closer to 0 it is, the better the mixing. At 0, the entire area is within the bin that contains the perfect mixing amount.

Another factor in this method's favour is that it is very easy to alter based upon the desired mixing resolutions. This concept is explored fully in section 2.3.3, but simply, mixing level is subjective and based upon the resolution in which the resultant mixture is sampled. More, smaller samples could measure as less mixed that then same mixture measured with less, larger samples. In the case of the CG Number, the resolution can be altered by changing the bin count. Less bins reduces the threshold for an Areal Fraction to be within the ideal mixing level and will therefore lower the CG Number.

When looking at CFD, this helps to mitigate the effects of the numerical blurring of the passive scalar by being far more stringent on the threshold of mixing. The further a cell is away from the perfect mixing value, the less influence it has on the result. In essence, it requires cells to be incredibly close to the perfect mixing value to have any significant impact on the final mixedness value.

This does go some way to mitigate some of the effects of the numerical diffusion but does not remove them. At longer mixing lengths this diffusion is still a very large problem and still over predicts the mixing capability of a static mixer. The equation for this CG Number is found below:

$$CG_{\text{mix}} = 100 - \sum_{i=0}^{n} \left(\%A_i \; B\right), \quad \text{where} \quad B = \begin{cases} C_1 \; T_i^2, & \text{if } T_i < P \\ C_2 \; (T_i - 100)^2, & \text{if } T_i > P \\ 1, & \text{if } T_i = P \end{cases} \tag{2.29}$$

Where $\%A_i$ is the percentage area of the plane, T_i is the amount of Tracer, P is the perfect mixing amount, C_1 and C_2 are coefficients for the weighting curves, and n is the number of binned histogram sections.

This is similar in principle to the Areal Fraction Method developed by Alberini et al. (2014), but allows the mixing to be resolved down to a single number whilst still using all of the information from the whole area of the image, not just the area that is close to the region of perfect mixing. A practical example of the use of CG Number to quantify mixing, along with further explanation of its benefits is found in Section 4.3.4.

2.3.3 Mixing Criteria

While mixing can be broken down to fundamental principles—such as entropy generation and mass transport—it presents unique challenges compared to other unit operations in Chemical Engineering. One key difficulty is that the criteria for a "successful" mix are often dependent on the scale and resolution at which the fluid is examined. Unlike heating a fluid, where the goal and result (a target temperature) can be measured directly and absolutely, mixing performance depends on how finely the system is interrogated.

For example, imagine the fluid is analysed by splitting the sample cross-section into nine equal parts and determining the mass fraction of a particular component in each one. This could correspond to a mixing resolution of 0.333D, where D is the pipe diameter. If each of the nine segments contains the correct average fraction, the mixture might be deemed well mixed. However, if the same area were analysed at a resolution of 0.1D, resulting in 100 smaller segments, the same mixture may no longer meet the

stricter criteria of uniformity. What appeared “mixed” at low resolution now reveals heterogeneities when examined more closely.

This concept is illustrated in Figure 2.5. The left-hand image shows an original PLIF capture at a resolution of 2048x2048 pixels—equivalent to a very high analysis resolution of approximately 0.0005D. It shows significant spatial variation in intensity, corresponding to concentration gradients and a low level of diffusive mixing. Downsampling this image to 128x128 pixels (0.016D) yields the middle image, and further downsampling to 8x8 pixels (0.125D) gives the image on the right. Each image appears more homogeneous than the previous, even though they originate from the same data. The greyscale weighting (representing concentration) is preserved across all versions.

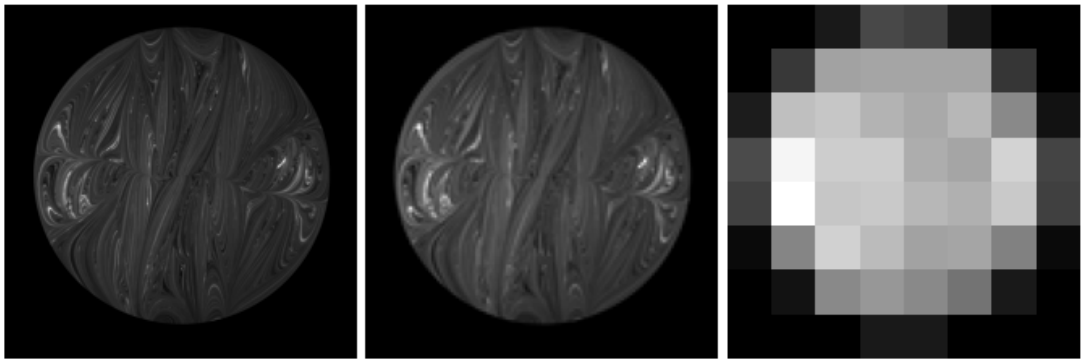


Fig. 2.5. Left – Original 2048x2048 pixel PLIF image. Middle – PLIF image downsampled to 128x128 pixels. Right – PLIF image downsampled to 8x8 pixels

As the resolution decreases, the apparent level of mixing increases. Larger sampling regions blend finer-scale gradients, making the fluid appear more uniform. The CoV associated with each image reflects this, decreasing proportionally with downsampling—a factor of 16 in each step. However, this process is not reversible: downsampling is a lossy conversion, and fine details from the original image cannot be recovered. Relying only on coarse-resolution analysis may give a false sense of uniformity, while using extremely high resolution may exceed what is necessary for the intended application.

There is no universally correct resolution for evaluating mixing; it must be chosen appropriately for the process context. A rule of thumb—based on conversations with

industry professionals—is that CoV, the most widely cited mixing metric, is typically reported at an analysis resolution of around 0.01D. At this resolution, a mixing quality of 95% (corresponding to a CoV of 0.05) is considered sufficient for a wide range of chemical processes—though, crucially, not all (Paglianti, 2008).

2.4 | Static Mixer Energy Loss

Static mixers rely on the mechanical energy of the fluid flow to promote mixing. This is achieved by inserting geometric elements into the flow path that obstruct and redirect the flow, altering local velocities, inducing shear, and generating regions of elongation and secondary motion. These mechanisms promote mixing through stretching, folding, and diffusion. However, as the fluid interacts with these internal structures, kinetic energy is dissipated due to viscous effects and turbulence, and this energy loss appears as an increased pressure drop across the mixer. Some of this energy is also converted into heat via viscous heating (Bird, 1961).

These pressure losses are measurable and are typically observed by comparing the pressure drop of a pipe fitted with a static mixer to that of the same pipe when empty (Albright, 2008). The specific geometry, length, and density of the mixing elements will all influence how much energy is lost as the fluid flows through the mixer. As discussed in Section 2.3, this energy penalty must be evaluated in parallel with mixing performance in order to assess the overall efficiency of a given static mixer. To do this, it is necessary to quantify the energy loss accurately.

Pressure drop can be measured using a differential pressure sensor across the inlet and outlet of the mixing section. A single differential pressure sensor is preferable over two absolute pressure sensors, as using two introduces compounded error—essentially the sum of the uncertainty in each sensor. Assuming the differential and absolute pressure sensors have the same rated accuracy, the differential measurement approach provides improved reliability.

To compare performance meaningfully, the measured pressure drop is expressed in dimensionless form. This allows for direct comparison with established literature values and between different static mixer designs, even under slightly different flow conditions. Dimensionless pressure drop data can also be plotted against Reynolds number (defined in Section 2.2.3) to create characteristic curves useful for design and specification.

In this work, the Fanning friction factor is used as the dimensionless pressure loss metric. This decision follows both the convention used within the collaborating industrial partner and the fact that it was the form available in their historical data.

The Fanning friction factor quantifies the wall shear stress relative to the kinetic energy of the flow. For fully developed, incompressible, and steady laminar flow in a circular pipe, the wall shear stress τ_w is calculated from:

$$\tau_w = \frac{\Delta P D}{4L} \tag{2.30}$$

where:

- ΔP is the measured pressure drop across the length L of the pipe,
- D is the pipe diameter.

The Fanning friction factor f is then given by:

$$f = \frac{\tau_w}{\frac{1}{2}\rho u^2} \tag{2.31}$$

where:

- ρ is the fluid density,
- u is the mean flow velocity.

Substituting τ_w from above gives:

$$f = \frac{\Delta P D}{4 L \rho u^2} \tag{2.32}$$

To use this formulation accurately, all other flow properties must be measured or known with sufficient precision. Pipe geometry is fixed, and modern Coriolis flow meters enable the measurement of mass flow with accuracies typically better than 0.5%. The fluid properties—viscosity and density—are the more complex variables. These require either direct measurement or modelling, as detailed in Section 2.2.1.

Additionally, because the system operates continuously and not in batch, the hygroscopic nature of glycerol must be accounted for. Glycerol will absorb moisture from the air, which can shift its mass fraction and, consequently, its density and viscosity. This means the fluid density is not only needed for pressure loss calculations but also for tracking the glycerol mass fraction in real time. Without continuous monitoring or controlled humidity conditions, fluid properties can drift over time and introduce error into performance evaluation.

Once a friction factor has been experimentally calculated, Equation 2.32 can be rearranged back into its standard form to predict pressure drop under different operating conditions. This makes the friction factor a useful tool for both mixer evaluation and system design.

2.5 | Methods of Mixing Measurement

2.5.1 Planar Laser-Induced Fluorescence (PLIF)

The most suitable experimental technology for highly detailed analysis of static mixers is PLIF, a technology originally reported by Zare (2012) in 1982. The general methodology of PLIF is to use a laser to excite a tracer dye that, after absorbing the laser light, fluoresces with light of a higher wavelength. This fluoresced light is captured by a camera and allows the imaging of a medium containing the tracer dye. If the laser

light source is left as a point source, this is known as Laser-Induced Fluorescence; if the laser light is manipulated into a thin light sheet using optics, a plane of light is created and is then referred to as PLIF. This latter version is particularly useful in the analysis of mixing since the plane of light can be shone perpendicularly across a cross-section of a pipe.

When analysing the performance of static mixers, the dyed substance is typically injected into the flow stream at the entrance to the static mixer. The mixer then blends the tracer dye into the primary flow where the flow then crosses the laser plane situated after the outlet of the static mixer. Since there is a relationship between the concentration of the fluid and the intensity of the light fluorescence, this allows the concentration of the dye to be mapped across the captured image and therefore be used to quantify how well a static mixer has performed (Alberini et al., 2014).

Advantages of PLIF include the high detail of captured images—with tests showing spatial resolution on the scale of single microns—and, with the advent of better high-speed cameras, these images can be captured multiple times per second. The optical nature does, however, necessitate the need for optically clear fluids, which can limit the choice of test fluids and is seen as one of the main downsides of PLIF. Often, to overcome this issue, model clear and colourless fluids are used that possess similar rheological properties to the desired test fluid. For Newtonian fluids, this is not a limitation in terms of validity, as the mixing behaviour should theoretically be identical if the viscosity and density profiles are matched.

With this, PLIF is a well-established process and has been used many times to evaluate the performance of a multitude of static mixers with fluids having varying rheological properties and in varying flow regimes. A comprehensive table of PLIF usage in the performance analysis of static mixers is found in Table 2.1. The limited areas of testing generally extend to fluids with complex rheological properties as well as multiphase flows. Further to this, the technique appears more frequently in the literature as a method to evaluate currently existing technologies rather than as a tool

in the design of novel models—though this does not necessarily mean such uses are absent in industry.

For testing of water-soluble fluids, a commonly used tracer dye is Rhodamine 6G. This is a deep red dye that comes in the form of a fine powder. In very small amounts, it performs as a potent fluorescence medium for PLIF. Figure 2.6 (Baj et al., 2016) depicts the range of light in which Rhodamine 6G can absorb visible light in red and the wavelengths of its re-emission curve in orange. The duplication of these lines with slight colour and wavelength variations denotes minute changes in the curves based upon the concentration of the dye. The wavelength of the 532 nm laser used for working with Rhodamine 6G is shown as a narrow vertical black line and is conveniently situated at the peak of the absorption curve. The yellow box signifies the transparency range of an optical filter that is situated on the lens of the camera. The purpose of this is to ensure that reflected laser light is blocked from entering the camera and to ensure that only light from the Rhodamine 6G fluorescence is imaged. Without it, the far brighter laser emissions would fully saturate and potentially damage the camera sensor.

Table 2.1
Summary of Journal Papers Regarding the State-of-the-art for the use of PLIF to Assess Static Mixer Performance

Paper	Flow Properties	Summary
Assessment of different methods of analysis to characterise the mixing of shear-thinning fluids in a Kenics KM static mixer using PLIF (Alberini et al., 2014)	**Velocity:** 0.1–0.6 m/s; **Pipe Diameter:** 12.7 mm and 25.4 mm; **Flow Ratios:** 10:1 and 25:1; **Reynolds Number:** 20 - 394 (laminar flow). **Fluids:** Shear-thinning Herschel-Bulkley Carbopol 940 solutions at 0.1% and 0.2% concentration	**Static Mixers Tested:** Kenics KM with six 180° twisted elements, diameters $\frac{1}{2}$-inch and 1-inch, L/D = 1.5. **PLIF Technique:** Used Rhodamine 6G dye tracer in secondary flow; 532 nm Nd-YAG laser; CCD camera; pixel-by-pixel calibration; spatial resolution of 10 μm/pixel (12.7 mm) and 20 μm/pixel (25.4 mm). **Methods of Mixing Analysis:** (1) Coefficient of Variation (CoV); (2) Maximum Striation Area; (3) Areal Distribution Method; (4) Individual Striation Method. **Findings:** High-viscosity secondary fluid hindered mixing; increasing velocity improved mixing; higher flow ratios (25:1) and center injection enhanced mixing performance. **Conclusions:** PLIF enabled quantitative analysis of mixing patterns; areal distribution and individual striation methods were effective; Kenics KM static mixers effectively promote mixing of shear-thinning fluids, especially at higher velocities and with centre injection.
Quantitative visualisation of the mixing characteristics of a multilayer static mixer by planar laser-induced fluorescence (Kim et al., 2021)	**Primary fluid:** Water; **Secondary fluid:** Rhodamine B solution (0.25 mg/L). **Main flow rate:** 0.65 L/min (Re = 383). **Secondary flow rates:** 15–65 mL/min (flow ratios 2.3%–10%).	**Mixer types:** SMX mixer with arrangement angles of 0°, 45°, and 90°. **PLIF Technique:** Used Rhodamine B fluorescence; 2-W continuous 532-nm laser producing a 1 mm-thick beam; high-speed CMOS camera capturing at 1000 fps. PLIF allowed normalised intensity images showing concentration fields. Mixing Index calculated from concentration fields. **Findings:** Mixing Index reached 90% at flow ratios ¿5% for all arrangement angles. At 2.3% flow ratio, mixing index varied with arrangement angle: 45° (74.9%), 90° (69.8%), 0° (66.4%). Pressure drop lowest at 45° arrangement angle. **Conclusions:** PLIF effectively visualised concentration fields in multilayer static mixers; 45° arrangement angle optimised mixing efficiency and minimises pressure drop.
An improvement of the Sulzer SMX static mixer significantly reducing the pressure drop (Hirschberg et al., 2009)	**Flow Conditions:** Laminar flow with Re down to 0.077; high-viscosity fluids with viscosity ratios up to 15,000; **Reynolds number:** between 430 and 1,300 for dispersions.	**Static Mixers:** SMX (8 bars per element) and SMX plus (6 bars per element, with gaps). CFD and PLIF experiments conducted. **PLIF Technique:** Laser-Induced Fluorescence illuminating cross-section of vertical acrylic tube; Rhodamine-dyed glucose solution mixed with undyed solution. **Findings:** SMX plus reduced pressure drop by ¿50% while maintaining mixing performance; SMX plus achieved similar homogeneity after 8 elements; SMX plus required one additional element compared to SMX. **Conclusions:** SMX plus offers significant pressure drop reduction without compromising mixing efficiency; PLIF effectively validated mixer performance and CFD predictions.

Continued on the next page

Paper	Flow Properties	Summary
Quantification of Laminar Mixing Performance using Laser-Induced Fluorescence (Pust et al., 2006)	**Flow Conditions:** Laminar flow in vertical pipe; **Fluids:** glucose solution with Rhodamine 6G; mixer lengths with L/D ratios of 4, 6, and 8; Reynolds number unspecified.	**Static Mixer:** Sulzer SMX. **PLIF Technique:** 532 nm Nd:YAG continuous wave (CW) laser; horizontal light sheet (400 μm thick); CCD camera with 550 nm long wave pass filter; calibration for linear fluorescence; spatial resolution limited by light sheet thickness - possible issue of CW laser **Findings:** Mixing improved with increased mixer length; CoV decreased from 0.46 at L/D = 4 to 0.073 at L/D = 8, indicating highly uniform concentration. **Conclusions:** PLIF provided non-intrusive, high-resolution analysis; longer static mixers enhance mixing quality in laminar flows; Sulzer SMX mixer effective for precise mixing applications.
LIF measurements of blending in static mixers in the turbulent and transitional flow regimes (Wadley & Dawson, 2005)	**Reynolds number:** 900 – 90,000. **Main flow rates:** 0.07×10^3 to 7.0×10^3 m^3/s. **Flow rate ratios (Q/q):** 100, 1000, 10,000. **Fluids:** Water with Rhodamine WT dye.	**Static Mixers Tested:** Chemineer-Kenics KM and HEV, Sulzer SMV; various element counts and diameters. **PLIF Technique:** Laser sheet illuminated pipe cross-section; CCD camera captured images; calibration with well-mixed solutions; CoV calculated to quantify mixing. **Findings:** Experimental data did not align with manufacturers' correlations; mixing quality insensitive to flow rate ratio; longer mixers improved mixing; Reynolds number impacted mixing in transitional regimes; feed position influenced mixing in shorter mixers. **Conclusions:** PLIF provided precise visualisation and quantification of mixing; highlighted deviations from manufacturers' data; useful for optimising mixer performance in turbulent and transitional flows.
Viscoelastic flow instabilities in static mixers: Onset and effect on the mixing efficiency (Migliozzi et al., 2021)	**Reynolds Number:** Very low (z1 to 20). **Fluids:** Boger fluid (elastic, constant viscosity); shear-thinning xanthan gum solutions (0.05% and 0.2%).	**Static Mixers Tested:** Kenics helical mixer and SMB-R mixer. **PLIF Technique:** 532 nm CW laser; high-speed camera; Rhodamine 6G dye; transparent PMMA mixer section with refractive index-matching solution. **Findings:** In Kenics mixer, fluid elasticity reduced mixing efficiency at high De; SMB-R mixer showed complex instabilities; elastic instabilities localised and did not enhance overall mixing significantly. **Conclusions:** PLIF effectively captured concentration profiles and instabilities; static mixers less efficient for highly elastic or shear-thinning fluids; PLIF provided insights into flow dynamics and limitations in mixer performance.

Continued on the next page

Paper	Flow Properties	Summary
Quantifying macro-mixing and micro-mixing in a static mixer using two-tracer laser-induced fluorescence (Lehwald et al., 2010)	**Reynolds number:** 562. **Flow Type:** Gravity-driven flow with high-viscosity fluids. **Mixer:** Seven V-shaped blades in alternating orientations. **Tracers:** Uranine (pH-sensitive) and Pyridine 2 (pH-independent).	**Experimental methods:** PIV and Two-Tracer PLIF (2T-PLIF). PIV captured velocity fields; 2T-PLIF used Uranine for micro-mixing (acid-base reactions) and Pyridine 2 for macro-mixing. Both tracers excited at 532 nm; emissions captured with separate filters. **Findings:** Macro-mixing occurred before micro-mixing; induced vortex structures needed for mixing; Fourier analysis showed coupling between velocity and mixing fields. **Conclusions:** Combined PIV and 2T-PLIF effectively quantified macro- and micro-mixing; PLIF allowed visualisation of mixing scales; method valuable for evaluating static mixers in laminar, high-viscosity flows.
Droplets formation in turbulent mixing of two immiscible fluids in a new type of static mixer (Lemenand et al., 2003)	**Reynolds Number:** 7,500 – 15,000 (turbulent flow). **Oil volume fractions:** 2.5%–15%. **Fluids:** Oil and water (immiscible).	**Static Mixer:** High-Efficiency Vortex (HEV) mixer with curved baffles. **PLIF Technique:** Visualises vortex formation; laser illuminated flow cross-sections; vortex structures captured at Re = 1,500. **Findings:** Sauter mean diameter (d_{32}) depended on flow conditions and Weber number ($d_{32} \propto We^{-0.6}$); droplet size independent of oil concentration; HEV mixer increased dissipation efficiency and reduced energy requirements. **Conclusions:** PLIF crucial for visualising vortex structures; HEV mixer efficient for emulsification with minimal energy; PLIF validated vortex-induced mixing mechanism.
Assessing Blending of Non-Newtonian Fluids in Static Mixers by Planar Laser-Induced Fluorescence and Electrical Resistance Tomography (Forte et al., 2019)	**Reynolds Number:** 25 – 220 (laminar flow). **Fluids:** Non-Newtonian fluids—CMC solution (power-law model) and Carbopol 940 solutions (Herschel-Bulkley model). **Static Mixer:** Kenics KM, diameter 25.4 mm, $L/D = 9$, six elements.	**Measurement Techniques:** PLIF and Electrical Resistance Tomography (ERT). PLIF used Rhodamine dye in secondary flow; laser illumination; high-resolution images (2048 x 2048 pixels). ERT provided conductivity maps at lower resolution (20 x 20 pixels). **Findings:** Increasing superficial velocity improved mixing; PLIF captured fine details in mixing patterns; ERT effective for general trends but limited in precision. **Conclusions:** PLIF provided detailed analysis of mixing performance; validated mixer designs; ERT suitable for inline monitoring but less precise.

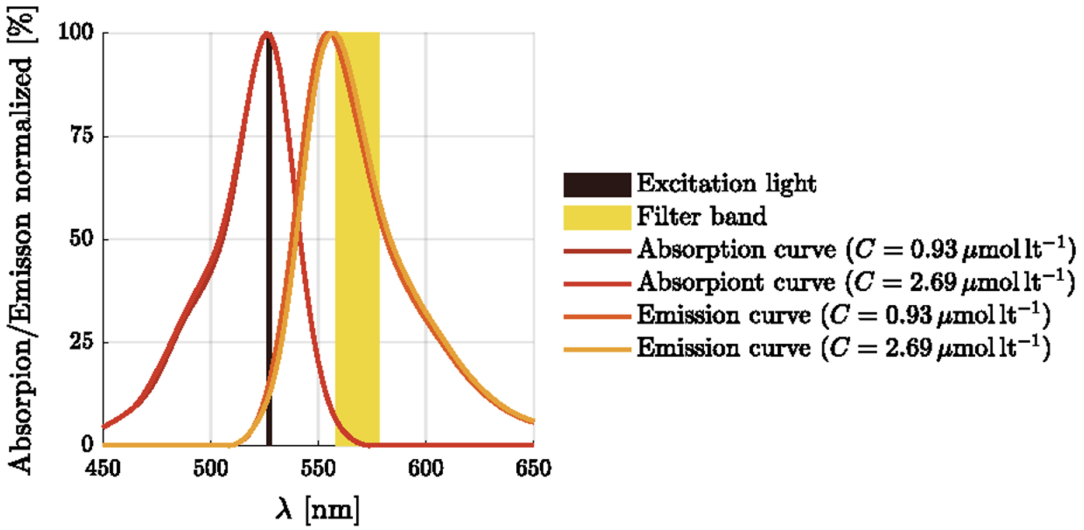


Fig. 2.6. Excitation and Re-emission Ranges for Rhodamine 6G with Respect to PLIF (Baj et al., 2016)

2.5.2 Computational Fluid Dynamics (CFD)

CFD is a simulation tool that uses numerical methods, typically the finite volume method, to approximate solutions to the Navier–Stokes equations. These equations govern the conservation of mass and momentum in fluid flow and are generally too complex to solve analytically in real-world applications. It is widely used in the analysis of static mixers and has been applied in many studies to evaluate and visualise fluid behaviour across different mixer geometries and flow regimes. It allows for detailed visualisation of flow patterns and the ability to simulate performance before moving to physical prototyping.

While CFD offers detailed insight, it is not a substitute for experimental testing. All models rely on simplifications and assumptions, especially when handling turbulence or non-Newtonian behaviour. Therefore, results still require validation against physical data. This is particularly important in static mixing, where small flow features can have a large effect on overall performance.

The physics of an incompressible, Newtonian fluid in motion is governed by two fundamental equations: the Continuity Equation and the Navier–Stokes Equation (Batchelor, 2000).

First, the Continuity Equation ensures the conservation of mass, stating that the mass entering a system equals the mass exiting it:

$$\nabla \cdot \mathbf{v} = 0 \tag{2.33}$$

Where: ∇ is the gradient operator $\left(\frac{\partial}{\partial x}, \frac{\partial}{\partial y}, \frac{\partial}{\partial z}\right)$, and $\mathbf{v}$ is the velocity vector, where $\mathbf{v} = [u, v, w]$ are the velocity components in the x, y, and z directions.

Simultaneously, the Navier–Stokes equation describes the motion of the fluid by balancing the relevant forces:

$$\frac{\partial \mathbf{u}}{\partial t} + (\mathbf{u} \cdot \nabla)\mathbf{u} = -\frac{1}{\rho}\nabla p + \nu \nabla^2 \mathbf{u} + \mathbf{f} \tag{2.34}$$

where $\mathbf{u}$ is the velocity vector, t is time, ρ is the fluid density, p is the pressure, ν is the kinematic viscosity, and $\mathbf{f}$ is the body force per unit mass (e.g., gravity).

In this equation:

- The term $\frac{\partial \mathbf{u}}{\partial t}$ represents the rate of change of velocity with respect to time (unsteady effects).
- The convective term $(\mathbf{u} \cdot \nabla)\mathbf{u}$ accounts for changes in velocity as the fluid moves through space.
- The term $-\frac{1}{\rho}\nabla p$ represents the pressure gradients that drive the fluid motion.
- The viscous term $\nu \nabla^2 \mathbf{u}$ accounts for the internal friction within the fluid due to its viscosity.

- The body force term **g** represents external forces acting on the fluid, such as gravity.

To solve these equations, the fluid volume is discretised into finite volumes, or cells, in which the fluid is assumed to be homogeneous. A centre of mass is defined within each cell, representing the start of the vector of motion. For the conservation of momentum and mass to be satisfied—and therefore for the Navier–Stokes and Continuity Equations to be solved simultaneously—the mass and momentum of the fluid entering and leaving each cell must balance.

This is done by initialising every cell with an initial guess for the flow variables. This was traditionally assumed to be zero momentum, but modern algorithms have been developed to make more educated initial guesses, thereby decreasing the solving time of the simulation. Iterative calculations are then performed to solve the Navier–Stokes and Continuity Equations, with the goal of reducing the residuals (errors) that arise from the iterative process.

To reach a solvable state, boundary conditions are also required. These are user-defined parameters based on the known physics of the simulation, such as the mass flow into and out of the system. There are various types of boundary conditions; a common example is a 'wall' boundary condition, where the velocity of fluid adjacent to the wall is set to zero (non-slip condition). These known conditions are used to attempt to solve the fluid equations. However, in practice, they are never fully solved. The discretised field is an approximation of the continuous flow. Instead, the residuals are reduced to a level where the resulting velocity, pressure, or other profiles change negligibly.

To obtain an accurate solution, the discretisation must be fine enough to capture the true flow profile. A smaller discretisation means more accurate simulation, but this introduces a trade-off. More cells result in a larger simulation with more equations

to solve, which dramatically increases computational time and hardware requirements, eventually offering diminishing returns.

This balance is critical and often limits the ability of computers to simulate laminar mixing experiments, as we will explore further.

Once the flow field is solved — and assuming the model and mesh are well-constructed — the result of the simulation is an accurate flow profile and, therefore, an accurate pressure gradient. The application of this in static mixer experiments is clear: without the need to run a physical experiment, it is technically possible to evaluate the pressure drop characteristics of a novel static mixer that exists only as a CAD model. This enables virtual iteration of designs without the need for fabrication. But can CFD also be used to evaluate mixing?

When analysing mixing, solving the flow field is only the first step in the evaluation. A common methodology for simulating mixing is the use of a passive scalar. A passive scalar is a user-defined scalar field assigned to each cell that is transported by the flow but does not affect it. In mixing analysis, it represents the concentration of one component of the fluid. It is moved through the system by advection and diffusion, following the flow field calculated in the CFD solution. Over time, this scalar spreads to neighbouring cells — both due to forced convection and passive diffusion — effectively simulating the mixing process. Evaluating its distribution then provides a quantitative measure of mixing in the simulation. This approach has been employed in numerous studies from the late 1990s through the 2020s (Bakker et al., 1998Clifford et al., 2006Joaquim Jr. et al., 2011Moghaddam, 2023Nyande et al., 2021Soman, 2016) and is considered a relatively low-cost method for simulating mixing.

However, this method has its drawbacks, particularly in laminar flows. The issue arises with the discretisation of the mesh. If a cell has a value for a passive scalar, and the momentum vector from that cell dictates any flow to an adjacent cell, the adjacent cell will inherit a value for the passive scalar as well. This behaviour is analogous to real diffusion, hence the term “passive scalar”. In practice, the scalar is moved through

the system by both convection (following the flow field) and passive diffusion (spreading into neighbouring cells).

The problem arises due to scale. True molecular diffusion occurs at the nanometre scale, whereas static mixers typically operate on the scale of tens of millimetres. Meanwhile, the smallest mesh resolutions achievable in CFD are often on the order of hundreds of microns. In laminar flow regimes, there is no turbulent mixing — all radial transport of fluid species occurs through molecular diffusion alone. However, when the discretised mesh is much larger than the true diffusive length scale, numerical diffusion dominates. This artificial spreading of the passive scalar leads to a significant overestimation of mixing quality in the simulation.

Several mitigation techniques exist, including the use of higher-order convection schemes (such as second- or third-order upwind differencing), alignment of the mesh with the flow direction to reduce cross-stream numerical diffusion, and mesh refinement to reduce the size of cells. While these techniques can reduce numerical error, they do not eliminate it, and the fundamental scale mismatch remains — at least under currently available computational power.

The papers cited demonstrate that passive scalar methods can give an indication of mixing over the length of a static mixer, but when compared to a PLIF image of actual mixing, the discrepancies become evident. For example, while passive scalar experiments often suggest that only a few static mixer elements are required for adequate mixing, the PLIF results from Hirschberg et al. (2009) show that this is not the case in practice.

An alternative approach is to use particle tracking. This method has been explored in several studies (Aubin et al., 2005Gayen et al., 2024Hobbs & Muzzio, 1998Zalc et al., 2002). Here, particles are used to simulate the concentration of the component being mixed. As with the passive scalar technique, the flow field is first solved, and then particles are 'released' at the inlet. Each particle starts in a different position and experiences different forces from the moving fluid. As the fluid flows around the static

mixer elements, the particles are advected throughout the flow. The advantage of this method is that, as point-based Lagrangian entities, the particles are immune to numerical diffusion.

However, the drawback is that the results are no longer Eulerian and do not provide the spatial resolution of real mixing experiments at the scales investigated to date. The particle tracking results are essentially collections of single points, not continuous fields like those obtained with PLIF, making quantitative comparison more difficult.

Another drawback of particle tracking is the computational expense. Superimposing a Lagrangian scheme with thousands of particles onto a flow field and tracking their progress turns a steady-state problem into a time-dependent one, as the particles "travel" through the mixer. This significantly increases computational time and hardware memory requirements. Additionally, particle tracking provides a *"soft" physics* approximation of what occurs in the static mixer. While particles can represent molecules of the component to be mixed, the number of particles that can be simulated is vastly smaller than the actual number of molecules present.

The literature on CFD reveals a rather counter-intuitive reality: despite the complexities of turbulent flow, it is actually easier to simulate accurate mixing results in these conditions than in laminar flow. This is largely due to the dominance of turbulent eddies and mixing structures, which overwhelm the effect of numerical diffusion and allow the simulation to more closely match experimental results — even if these are only time-averaged approximations. In laminar flow, however, the mixing process is slow and entirely driven by diffusion, meaning that numerical artefacts play a much larger role.

The passive scalar approach, while computationally efficient, tends to overestimate mixing performance in laminar flows, primarily due to the mismatch between the scale of real diffusion and the scale of the mesh. While improvements can be made using higher-order discretisation methods and careful mesh design, the method remains inherently limited by the available computational resolution.

The particle tracking method, while largely free from numerical diffusion, comes with its own trade-offs. Computationally, it is significantly more demanding, requiring substantial memory and processing power. And, unlike the continuous concentration fields produced by imaging techniques like PLIF, particle tracking produces a sparse set of points, limiting its ability to represent mixing gradients across a cross-section.

There is a clear need for advancements in CFD that can bridge this gap and enable more accurate, efficient simulations of mixing in laminar regimes. Improvements could mean a more robust approach to virtual prototyping, reducing reliance on costly experiments and enhancing the role of CFD in static mixer design. This would have considerable industrial benefits, supporting a shift towards more reliable virtual design and testing.

2.6 | Conclusions

Static mixer technology has developed significantly over the decades since its invention, with advancements both in mixer designs and, crucially, in the techniques used to study them. The literature highlights the ongoing challenges in achieving homogeneous mixing, often requiring a balance between mixing effectiveness and energy efficiency while addressing the complexities of quantifying mixing performance in both laminar and turbulent flows. Techniques for assessing performance range from experimental methods like PLIF, which provides high-resolution concentration mapping, to computational approaches like CFD, which enables virtual simulations of flow and mixing, albeit with notable limitations in certain areas.

PLIF has proven valuable for detailed analysis but is restricted by the requirement for optically clear fluids, limiting its applicability to certain mixing environments. Additionally, experimental testing is often constrained by the limited breadth of data collected, as shown in studies by Alberini et al. (2014), Pust et al. (2006), Kim et al. (2021), and Hirschberg et al. (2009), where only 3–6 test points are used to develop published correlations. This limited testing likely results from the high costs associated

with test fluids, which are consumed during testing, as well as the time-intensive nature of these experiments. This presents a clear opportunity to develop experimental testing methods that are both less resource-intensive and faster, or even capable of running autonomously. Furthermore, while CoV, striation thickness, and areal fraction methods provide metrics for mixing, each has limitations in accurately representing mixing: they either offer simplicity or comprehensiveness, but not both. This suggests a gap for a new technique that could combine the simplicity of CoV with the depth provided by the areal fraction method with CG number being tested as a possible option.

In CFD, challenges remain in accurately modelling laminar flow mixing due to numerical diffusion, which can exaggerate final mixing levels. Particle tracking helps mitigate this diffusion effect but is computationally demanding and does not yet provide the continuous volume data that PLIF achieves. These limitations highlight a need for a refined approach that can either overcome the numerical diffusion issues inherent in passive scalar techniques or use particle tracking in a way that allows for greater dynamic range in its output.

This research aims to address these challenges by advancing industrial-scale experimental mixing test methodologies, providing a comprehensive yet straightforward method of mixing quantification, and refining CFD techniques to achieve more accurate simulations of mixing in laminar regimes. By integrating these approaches, the goal is to establish a system that combines the strengths of both virtual simulation and experimental validation to facilitate rapid iteration and optimisation in static mixer design.

CHAPTER 3

The Development of a Novel Test Facility for Continuous PLIF

3.1 Introduction

Planar Laser-Induced Fluorescence (PLIF) is a technique that can be used for assessing the performance of static mixers in various applications. However, this method has limitations. A key drawback of PLIF is its destructive nature, meaning that once mixed, the output fluids cannot be unmixed and often result in waste. The conventional PLIF method when testing static mixers involves injecting a tracer dye-doped stream into a bulk flow. A thin plane of laser light illuminates a cross-section of the flow at the outlet of a mixer and excites the dye, causing it to fluoresce. Imaging this fluorescence captures the mixing capabilities of a static mixer by measuring the concentration and location of the tracer dye as a pixel brightness.

In this method, benchmarking a series of different static mixers under a variety of flow conditions leads to a significant amount of test fluid consumption, which then becomes a considerable capital cost and environmental factor for testing. This research chapter primarily focuses on addressing this drawback in an attempt to mitigate its impact. Specifically, this study presents a novel form of continuous PLIF, where the test fluid is regenerated and fed back to the inlet for further testing.

By closing this loop, the test fluid is no longer considered a consumable. While providing an obvious financial incentive, continuous PLIF also offers a series of further benefits. This chapter will explore these improvements and discuss the test rig development process, including its hardware, software, and achievable flow conditions.

This project has started with a completely blank slate. There was no available hardware or previous work to build upon. All of the following hardware and software design, build and implementation has been done from scratch and solely by the author for the purposes of this study.

3.2 Hardware

3.2.1 Test Rig Principle

Figure 3.1 displays the Process and Instrumentation Diagram (P&ID) developed for the continuous PLIF test rig. The process operates based on the following principle:

1. The inlet tank holds the main test fluid, which a gear pump extracts and pressurises providing the flow energy to the system. A variable speed motor, powered by a frequency inverter which is capable of adjusting the flow rate drives the pump. A float switch at the base of the inlet tank deactivates the pump if the fluid level becomes too low.

2. A 0 to 50 bar absolute pressure transducer measures the pump's discharge pressure at the outlet. If a reading above 40 bar is detected, the pump deactivates.

3. The pump outlet connects directly to a coriolis flow meter that meters the main test fluid flow.

4. A 0 to 16 bar absolute pressure transducer measures the pressure again at the flowmeter outlet. If the system pressure reaches 10 bar, the control software deactivates the pump.

5. The plate exchanger heats or cools the test fluid to the desired test temperature. The test fluid exchanges with a 40 % aqueous ethylene glycol solution work fluid, driven by the heater/chiller unit to the desired temperature. The test fluid's temperature is measured after the plate exchanger.

6. The following series of remote actuated ball valves directs the flow in one of three ways. To the test section, to the on-line rheometer or back to the inlet tank.

7. The chemical dosing pump concurrently controls the flow of a tracer-doped fluid from a secondary inlet tank. This fluid contains the fluorescent dye that enables PLIF to function.

8. The secondary flow exchanges with the main test fluid in a separate and oversized plate exchanger on the way to the mixing section when the primary fluid is routed to the main test section. Both flows have their temperature measured again.

9. An injection tube introduces the secondary fluid to the primary fluid at the inlet of an interchangeable static mixer section with pressure tap points at the inlet and outlet.

10. The subsequent part is the PLIF section located at the outlet of the static mixers. This section images the distribution of the dye.

11. The fluid temperature is measured again, and the mixed fluid flows into an outlet tank.

12. A float switch in the outlet tank activates and deactivates another gear pump that forces the waste fluid through an activated carbon filter. The filter adsorbs the tracer dye, thereby regenerating the test fluid.

13. The filtered test fluid returns to the inlet tank for reuse.

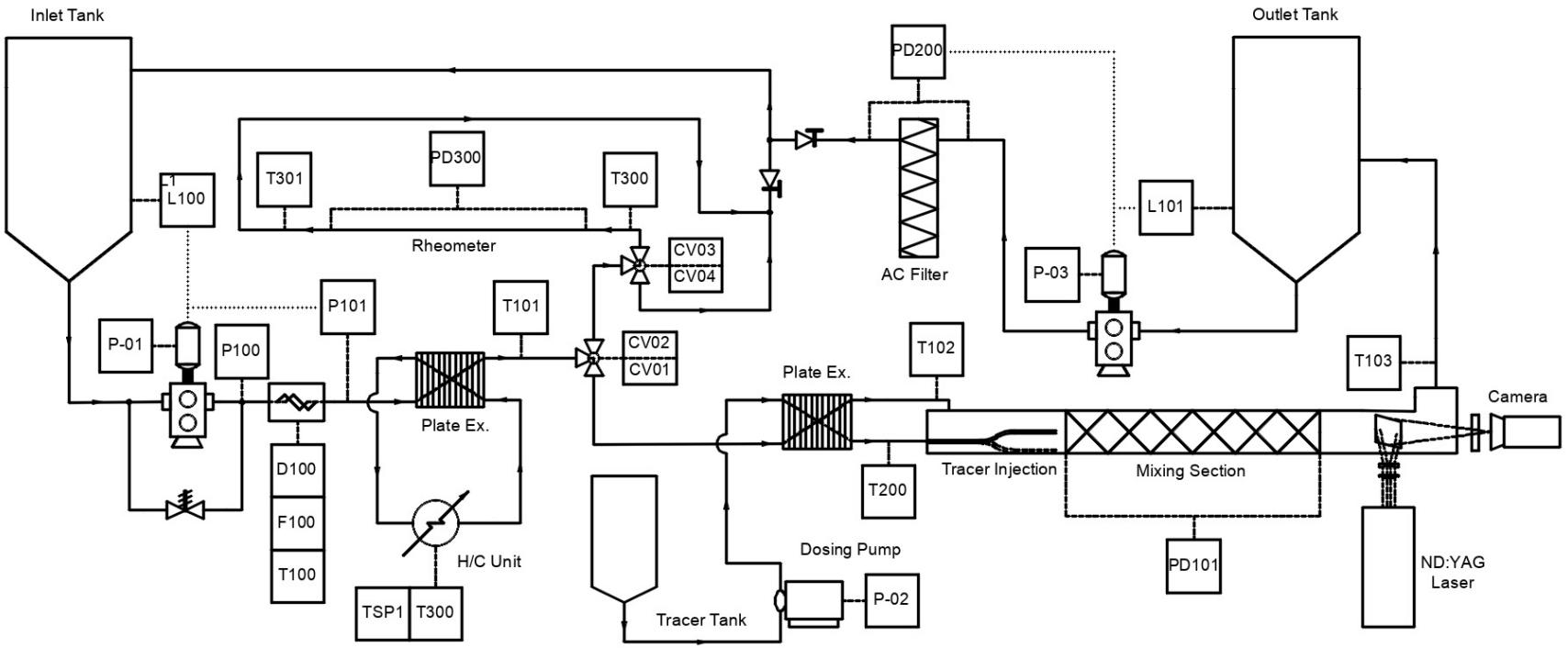


Fig. 3.1. Process and Instrumentation Diagram (P&ID) of Continuous PLIF Test Facility

3.2.2 Main Testing Rig

3.2.2.1 Principle



Fig. 3.2. Main PLIF Testing Section on Lidded Optical Table

This section presents the main testing structure for the test rig, where PLIF and pressure drop measurements take place.

This part of the test rig is made from a lidded optical test bed with evenly spaced fixing holes for attaching the test section, as illustrated in Figure 3.2. Fluids enter through fixed bulkheads at the rear, which transport the fluids from an auxiliary test rig. They then pass through a co-current and deliberately oversised plate exchanger to achieve a pinched equilibrated temperature. The prescribed testing specification required that the primary and secondary flow be within 1 °C of each other to prevent blurring in the PLIF images due to natural convection and refractive index differences between the primary and injected secondary flow. This tolerance was set to maintain an achievable

balance between practicality and accuracy of the measurements. The consistency of the temperature is verified by measurement at the outlet of both exchangers using Class 1, 100 Ω (PT100) Platinum Resistance Thermometer Devices (RTDs). To improve measurement accuracy, an array of eight copper fins was hand-soldered to the end of each RTD, providing a more representative bulk temperature measurement. In previous experiments involving laminar flow, stratification resulted in an axial temperature distribution across the piping. The copper fins can be seen in Figure 3.3.



Fig. 3.3. Custom Soldered Copper Fins on RTD

After temperature measurement, the two fluid flows reach the test section. Section 3.2.2.2 provides detailed information on the design and manufacturing process of the apparatus.

The secondary flow has the same composition as the primary flow, except for the addition of Rhodamine 6G dye. This water-soluble and deep red powder fluoresces when exposed to a specific and narrow wavelength of visible light. This light is provided by a 532 nm Nd:YAG laser. The dye is added at a concentration of 0.5 mg Rhodamine 6G per 1 L of test fluid. This concentration is chosen due to the linear response between concentration and fluorescence, which allows a direct and proportional mapping between image brightness and local dye concentration. While non-linear responses are possible at

higher concentrations, they are more difficult to model and risk reaching the saturation ceiling of the imaging sensor. Further information on this phenomenon and other PLIF theory can be found in Section 2.5.1.

The primary flow first enters a 23 mm diameter pipe, the secondary flow is introduced to it through a 6 mm internal diameter injection tube that can be positioned either at the center or wall of the main pipe, as seen in Figure 3.4. The fluid streams are velocity matched, resulting in a 1:14.7 mass flow ratio between them.



Fig. 3.4. Dye Injection Tube in Central (Left) and Wall (Right) Injection Positioning

Just after the injection, a 0.5 mm diameter pressure tap at the bottom of the pipe connects to the high-pressure side of a 0 bar to 0.3 bar Keller PD-33X differential pressure transmitter. The fluid flow then enters a removable test section that houses an insertable static mixer. The mixer blends the secondary and primary streams, distributing the dyed stream throughout the bulk flow. At the outlet of the mixer, an identical pressure tap connects to the outlet side of the differential pressure transmitter. This captures the associated pressure drop across the static mixer - one of the key characteristic parameters used to assess static mixer performance.

The next section is where a gray-scale image of dye distribution and concentration at the outlet of the mixer is obtained using PLIF. More information on the PLIF hardware and an explanation of how it works for this experiment can be found in Section 3.2.2.4.

The mixed fluid leaves the test section, and its final outlet temperature is measured again with a finned RTD. By measuring the temperature before and after the mixer, a more accurate determination of the mean temperature of the test fluid is achieved. With both measurements, operators can visually monitor on a graph when steady state is reached across the mixing section while a software differentiation module provides mathematical verification of steady-state conditions. After mixing, the waste fluid then leaves the lidded optical table through a bulkhead fitting at the rear, where it is returned to the Auxiliary rig.

The Auxiliary rig is responsible for the preparation of the testing fluid and its regeneration. It houses a wide array of components, including pumps, mass flow meters, and heater/chiller units. A detailed breakdown of its composition and design is found in Section 3.2.3.

3.2.2.2 Design

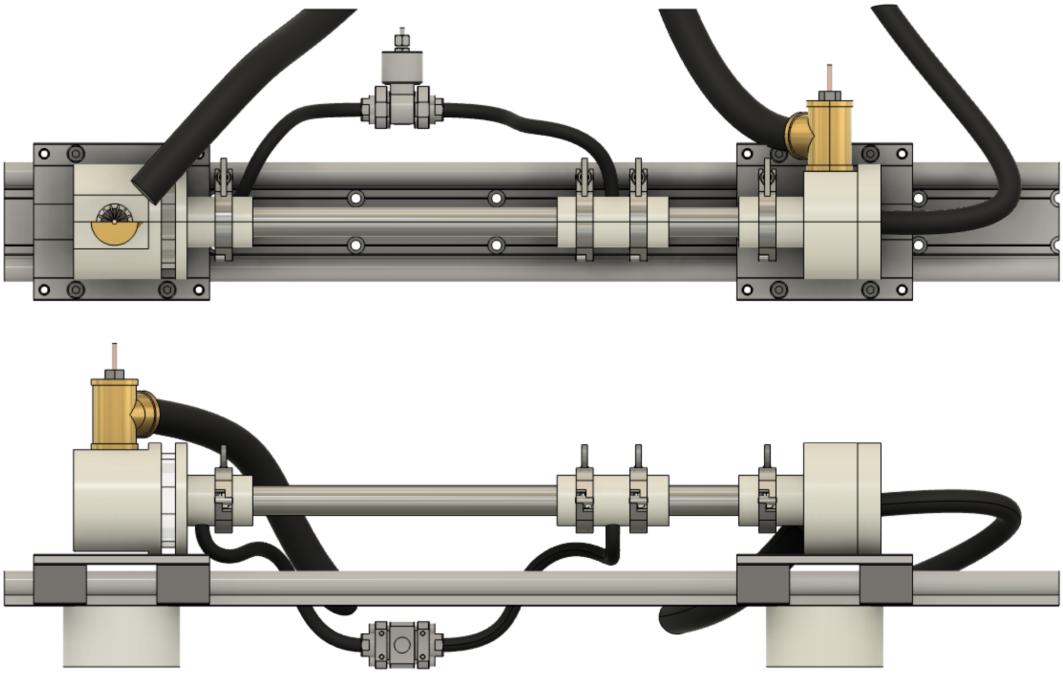


Fig. 3.5. Mixing Testing Section. Top: Top View of Test Section. Bottom: Side View of Test Section.

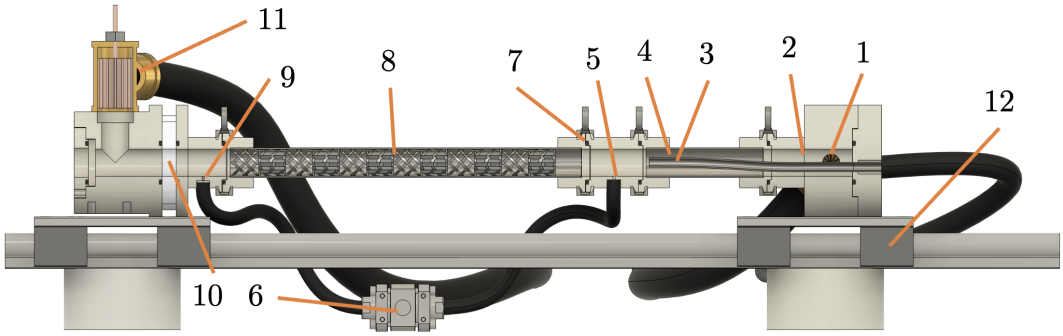


Fig. 3.6. Cross-section of the PLIF Test Section

The mixing test section, specifically designed and manufactured in-house for the PLIF testing, can be seen as a Computer-Aided Design (CAD) model in Figure 3.5 from the top and side. Figure 3.6 shows a cross-section of the side view for clarity. This next section outlines the specifications and purpose of each component with labels referring to the cross-section figure.

The primary test fluid flows in from the auxiliary supply rig through the large pipe on the right. It enters a tee fitting with a copper-finned RTD housed inside (1), where the temperature is measured. From here, it enters the test section inlet (2). This inlet and all remaining parts (excluding the injection tube) have an inner diameter (ID) of 23 mm. The secondary dyed flow reaches the test section through a smaller tube. The flow enters an 8 mm outer diameter (OD) and 6 mm ID injection tube (3) positioned off-centre in the back of the inlet section. This tube is bent such that rotating the injection tube positions it at either the centre or wall of the calming section tube, as seen in Figure 3.4, depending on its rotational position. The primary fluid enters the calming section (4), where the secondary flow is introduced through the aforementioned injection tube. The calming section, together with the inlet section, is 150 mm long. This enables a fully developed laminar flow to be created before the entrance of the mixer at Reynolds numbers up to 150 Re.

The combined fluid flow then enters a pressure tap section (5). This all these sections that make up the test section the internal walls are fully flush, maintaining an

accurate 23 mm ID down the length of the mixing section. This pressure tap section has a 0.5 mm hole at the bottom position of the pipe, which is fitted to tubing going to the high-pressure side of a differential pressure transducer (6). This and all other sections connect using a custom version of a tri-clamp fitting (7). They are designed to be 23 mm ID (a non-standard size for tri-clamp fittings) and to be self-centring with a tightly toleranced stepped design that is comprised of a male and a female coupling that seal with an o-ring - see Figure 3.7.

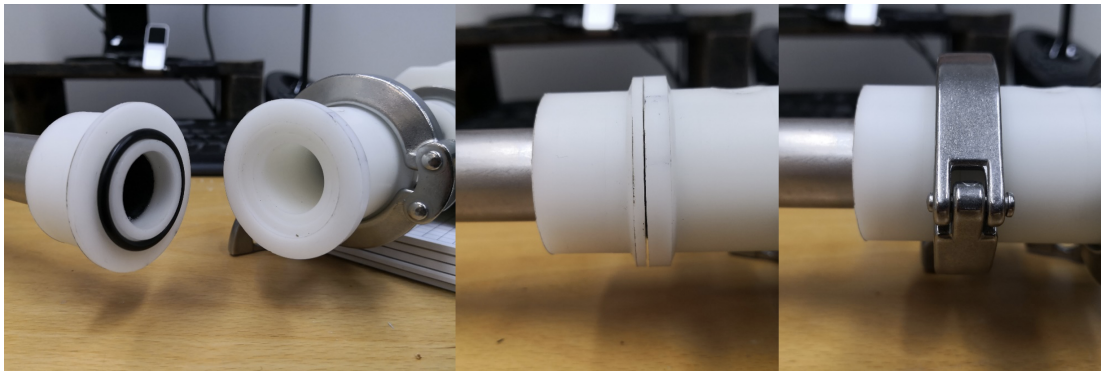


Fig. 3.7. Custom Male (Left) and Female (Right) Tri-clamp Compatible Fittings

The following section houses the static mixer (8), a 300 mm long high-tolerance, cold-rolled, seamless stainless steel pipe with an OD of 25.4 mm and an ID of 23 mm. The tube accommodates the various types and lengths of static mixers under test. Where the outlet of the steel pipe meets the coupling, there is a 0.5 mm thick, laser-cut stainless steel torus with an ID of 22 mm. This ring acts as a retaining method that prevents the static mixers from moving with the fluid flow while minimally impacting the flow profile. The stainless steel tube, retaining ring and acetal tri-clamp compatible coupling were press fit together and sealed with two-part epoxy resin.

The outlet/PLIF section follows the outlet of the mixing section. This part contains an identical pressure tap (9) connected to the low-pressure side of the differential pressure transducer (6). By measuring both the high and low-pressure sides of the static mixer, an accurate reading of the pressure drop induced by the mixer is measured. The following component is the PLIF section (10) which consists of a 12 mm thick square sheet of clear acrylic with a 23 mm hole bored in the centre. At the end of the flow path

is a 8 mm thick round glass sheet that allows a viewable path down the longitudinal length of the test section for the camera to focus on the laser plane. The PLIF section and its operation process are described in detail in Section 3.2.2.4.

The waste fluid exits through a tee fitting identical to the entry point, also housing a copper-finned RTD (11). It then leaves out of the rear bulkhead via a flexible tube that leads back to the auxiliary rig. The test section is affixed to a heavy-duty dual linear rail with a carriage at each end (12). Primarily this maintains the flat levels of the test section whilst also allowing the carriage on the inlet side to slide. This enables a change in the size of the test section and provides sufficient movement to detach the tri-clamp compatible couplings. A custom pin bracket mounts the outlet carriage to the linear rail system fixing the outlet carriage in place, ensuring that the PLIF section maintains a sturdy alignment between the acrylic sheet view window, laser light plane, and camera focal length.

The development and design of the custom parts was done in Autodesk Fusion 360, and models of these parts are located in the supplementary materials. The majority of the parts were machined on a Denford VMC 1300 Computerised Numerical Control (CNC) milling machine and Denford Turn 270 CNC lathe. The toolpaths for machining were also created in Autodesk Fusion 360. The primary material for these parts was Homo-Polymer acetal, selected for its strength, water resistance, chemical resistance, low thermal expansion, cost-effectiveness, and ease of machining.

The parts, largely manufactured from rods of varying diameters as stock material, were lathed where possible to ensure the consistency and central positioning of the 23 mm bore. In cases where lathing was not possible, the bore was precisely machined to 23 mm, and alignment was accomplished by assembling with tight-fitting dowels in the bore. More complex parts required initial lathing followed by milling from multiple axes. To install fixings such as bolts and pipe fittings, the milling machine bored tap drill holes which was followed by manual screw-thread tapping with the assistance of a manual milling machine.

The creation of the clear acrylic laser view window required significant care. Any imperfections on either the flat outer walls or the inner bore would create linear shadows across the captured PLIF image, appearing as banding. The most effective technique involved precision milling of the part from a larger acrylic sheet which ensured the correct dimensions, squareness and edge flatness. Each surface was then dry hand-sanded with 500, 1000, 1500, 2000, 2500, and 3000 grit sandpaper, then polished with three grades of polishing compound using a microfiber cloth. This created a highly polished surface that leaves almost no artifacts in the captured PLIF images. Cleaning of the perspex is done with lens cleaning solution and a clean microfibre cloth.

3.2.2.3 Optics

The optics on the laser system bend the 3.5 mm diameter circle of laser light into the thin laser light sheet, giving the "P" in PLIF its name. This conversion is achieved through the use of a cylindrical plano-convex lens with a 200 mm focal length and a plano-concave lens with a −25 mm focal length. Both lenses are square in shape, each measuring 20 mm in both height and width, and were ordered specifically for this rig from Laser2000. The plano-convex lens, positioned first in the laser's path, refracts the light to focus on a point 200 mm away from the lens by narrowing the laser horizontally. This first lens results in the thin light at the focal point in the centre of the pipe flow, as shown in the lower part of Figure 3.8. The plano-concave lens follows, stretching the light vertically. This process expands the light from 3.5 mm tall to 26 mm tall by the time it reaches the center of the cross-section. The two of these lenses in tandem therefore enable the laser to illuminate the entire cross-section vertically whilst illuminating as little of the longitudinal aspect of the flow path as possible. Keeping this latter dimension as small as possible limits any blurring caused by non-laminar aspects of the flow creating a different image just before or just after the PLIF capture point.

Custom-made acetal housings, machined in-house on a CNC Milling Machine, mount each of these lenses. The housing consists of two mirrored halves with tight slots

for the lens, which are supported on silicone rubber. The halves are aligned with 10 mm steel dowel pins and bolted together. The completed unit of two halves are bolted to a backplate. The entire mounting is then bolted to the laser aperture. The bottom half of the lens holder and the backing plate can be seen in Figure 3.8.

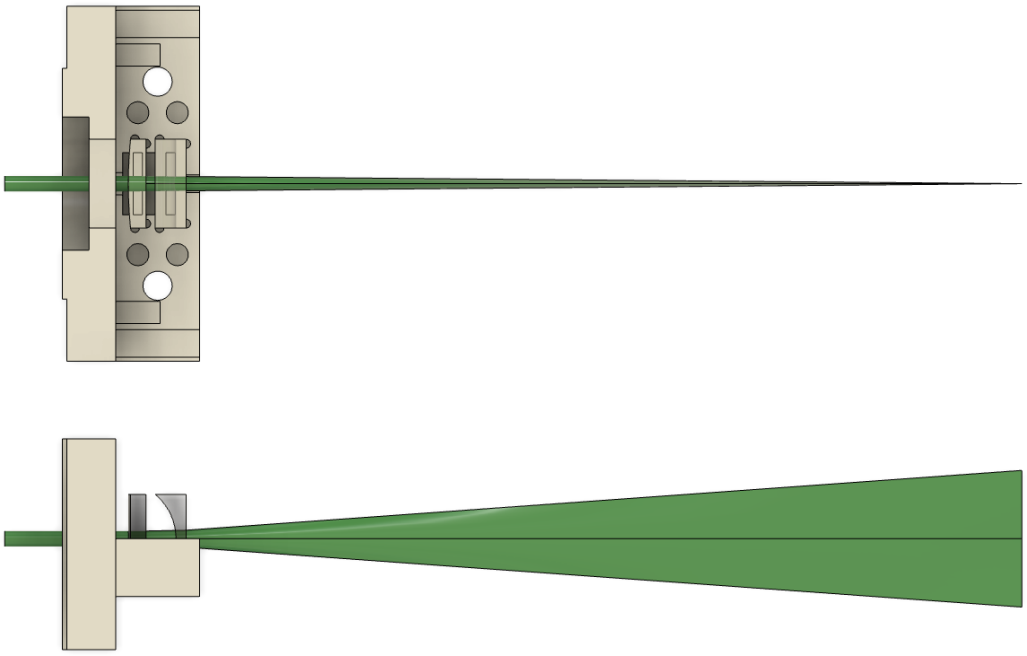


Fig. 3.8. Planar Laser Optical System. Top: Top View of Optics Depicting Laser Light Propagation from Plano-Convex Lens. Bottom: Side View of Optics Depicting Laser Light Propagation from Plano-Concave Lens

3.2.2.4 PLIF Hardware

Unabbreviated for clarity and a reminder, Planar Laser-Induced Fluorescence, or PLIF, is the key technology that enables this analysis of static mixer performance. This section features a detailed dive into how it is utilised for this research. To aid this description, please refer Figure 3.9.

A New Wave Solo III Pulsed Nd:YAG laser (1), capable of firing at up to 15 Hz, illuminates a cross-section of the flow at the outlet of the static mixer. The laser is positioned perpendicular to the test section and aimed at a highly polished, clear acrylic window (2) facing the flow. The laser emits a 3.5 mm diameter circle of light, which

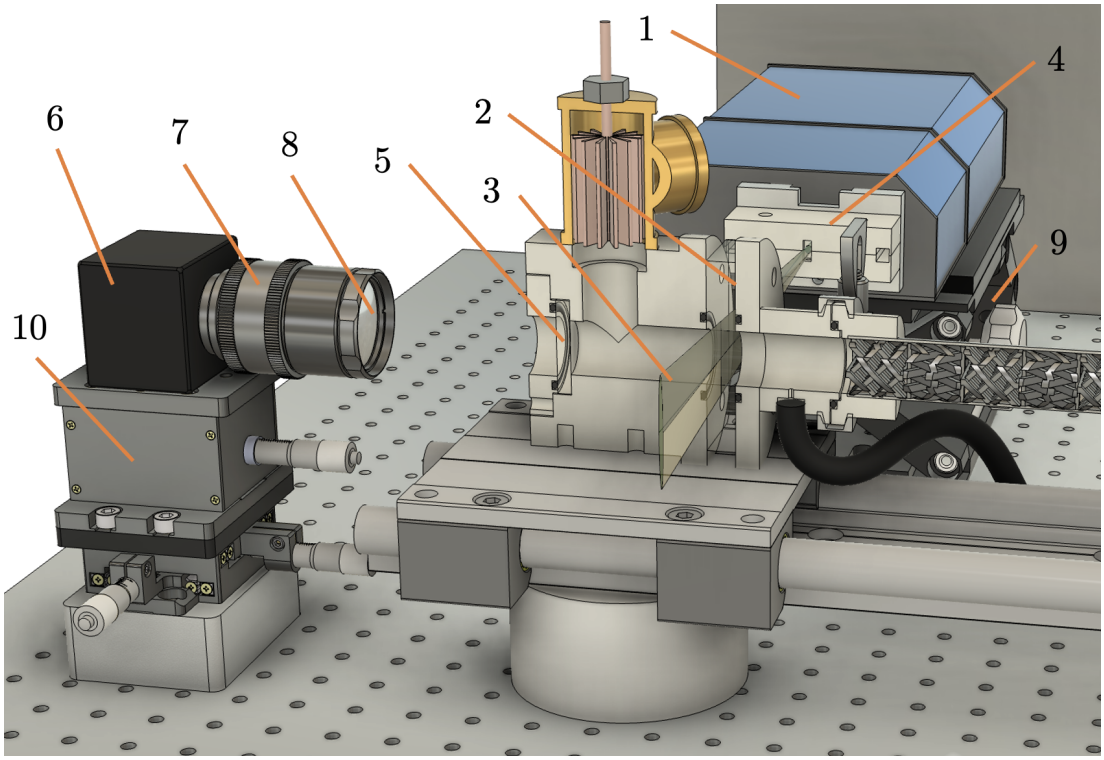


Fig. 3.9. CAD model of PLIF System Layout

is converted to a thin laser light sheet (3) wide enough to fully intersect the flow area and set to converge at the center of the pipe for maximum thinness. This plane of light illuminates the entire cross-sectional area of the pipe and is achieved through the use of glass optics (4). More information on the specification of these optics can be found in Section 3.2.2.3.

With the laser light incident on the fluid, the Rhodamine 6G dye in the flow is excited and fluoresces. At the end of the test section, a glass window (5) enables a view down the pipe against the direction of the flow through which the illuminated cross-section is visible. A PowerView 4MP 12-bit Charged-Coupled Device (CCD) camera (6), equipped with a 2:1 macro lens (7), is positioned looking down the sight glass and focused on the laser plane. With the macro lens, the pipe cross-section is set to occupy the full camera field of view. This camera is gray-scale, 15 Hz, and has a resolution of 2048 px by 2048 px across its 16 mm by 16 mm sensor. Being 12-bit, each pixel can have a value between 0 and 4095, which directly translates to allowing up to

4096 different dye concentration levels to be measured (assuming the dye concentration and therefore light emission magnitude is perfectly aligned to this range.) The lens of the camera features a 532 nm Semrock EdgeBasic™ long-pass edge filter (8). The 532 nm designation refers to the laser source in which this filter is designed to work with. The filter is transparent to light between 546.7 nm to 900 nm and is therefore designed to filter out the direct laser light being below this range and emitted at 532 nm.The filter therefore and only allows the wavelength of light from the Rhodamine 6G fluorescence and without it, the camera would only capture a fully whitened-out image from reflected laser light.

The laser head and the camera both mount on individual translation stages. The laser translation stage (9) provides movement in the X, Y, and Z axis dimensions which facilitates the laser's positional alignment with the clear acrylic viewport. The camera translation stage (10) offers movement in the X, Y, Z, and A dimensions, A being a horizontal rotational axis. These ensure that the region of interest (ROI) is central to the camera's field of view, and that the laser and camera align perfectly perpendicular to each other. The translation stages have fasteners that, when tightened, fix their position and maintain the alignment of the system.

The laser is powered, controlled and cooled by a separate controller unit that contains a safety interlock. It also contains the connectors that enable external timing control. This timing control is performed using a TSI model 10035 synchroniser unit. The synchroniser has nanosecond accurate timing control and sends pulses to the laser which control the flashlamp firing and Q-switch activation. The Q-switch operates by selectively blocking the laser beam so that the energy builds up in the gain medium. Once the energy reaches a critical level, the Q-switch is opened, allowing the laser to release the stored energy in a short burst of light. By delaying the opening of the Q-switches, the power of each laser pulse gradually dissipates by a consistent level. This dissipation is utilised in these experiments by introducing a fixed delay to manufacturer defined medium setting. This takes advantage of the dissipation to create a more

consistent light pulse brightness whilst still being bright enough to use the full bit-depth of the camera.

The synchroniser, and by extension the whole PLIF system, is controlled using TSI's Insight 4G PIV software through a Teledyne Dalsa Xcelera-CL PX4 PCIe framegrabber card with a timing expansion. The synchroniser is required to ensure that the camera exposure is precisely aligned with the laser pulse, enabling clear imaging of the fluorescence event. This software enables remote activation, timing, and parameter setting of the laser whilst also triggering and timing the camera to expose at the correct interval with the laser light pulses. The captured images can then be viewed and saved from within this software, which is explained in greater detail in Section 3.3.4.

3.2.3 Auxiliary Rig

The Auxiliary Rig primarily serves to supply fluids with specified flow rates and properties to the PLIF mixing test section, and to clean the waste fluid for reuse. Although Section 3.2.1 previously explored this during the P&ID analysis, this section will look at it in more detail, linking the Process and Instrumentation Diagram with the real hardware. The following subsections will also focus on the more complex components, explaining their purpose and how they function.

3.2.3.1 Overview

Figure 3.10 presents the fully assembled Auxiliary Rig, with numbers labeling the hardware components. The main skeleton of the rig is comprised of extruded aluminium struts to which all components are fitted.

A Witte Extru II/b 4,7 - 1 gear pump draws from the inlet tank. Rated to pump $56\,\mathrm{L\,h^{-1}}$ at 3 Hz. A geared-down variable speed motor powers the pump, and a Modbus RTU controlled 400 W Variable Frequency Drive (VFD) located in an electrical wall box powers this motor. The pump outputs directly into the inlet of an Endress + Hauser Promass 80A coriolis flowmeter with a Modbus RTU signal connection. This



Fig. 3.10. PLIF Testing Auxiliary Rig

flowmeter has a measurement capacity of up to 200 kg h^{-1} and contains a 4 mm diameter internal measurement tube, creating a significant pressure drop. The section between the pump's discharge and the flowmeter is the only part rated for a 50 bar operating pressure specifically to accommodate this flow resistance. A Gems 0 bar to 100 bar

absolute pressure transducer with 4 mA to 20 mA output is installed between the pump and the flowmeter to ensure that the pressure does not exceed 40 bar; if it does, the software that controls the rig will measure this and the pump is automatically shut down.

The primary flow enters an Alfa Laval plate exchanger configured for counter-current flow against an aqueous ethyl glycol solution. A Betta Tech CU700 heater/chiller unit temperature-controls this solution. Further information about this setup and the temperature control schema is available in Section 3.2.3.2. With the primary fluid at, or progressing towards, the desired temperature, it enters a tree of Actuation Valve electrically actuated motorised ball valves that direct the flow in one of three possible directions:

1. The simplest direction returns the test fluid to the inlet tank, a function that is used while the heater/chiller unit works to reach its set point.
2. The test fluid pumps into an on-line rheometer, which operates on the fundamentals of theoretical laminar fluid flow in a pipe. Detailed information about its setup and operation can be found in Section 3.2.3.3.
3. The test fluid moves on to the mixing test section for PLIF and pressure drop testing.

While the primary fluid undergoes pumping and temperature adjustment, the system also pumps the secondary fluid. Due to this flow stream's low flow rate (less than 100 $\mathrm{mL\,min^{-1}}$), metering the flow rate presents a challenge. Many gear pumps struggle to handle semi-viscous fluids and exhibit slip, a phenomenon where the greater the discharge pressure, the lower the flow as the fluid slips back around the tolerance between the gears and the inner housing. Incorporating a flowmeter would resolve this issue, but flowmeters for such low flow rates typically have low accuracy. A syringe pump could serve as an alternative, but its low capacities would seriously hinder the practicality of testing and conflict with the rig's purpose for continuous operation. The chosen solution

was a chemical dosing pump, specifically a form of dual-headed peristaltic pump. This type of positive displacement pump accurately dispenses fluid with far less pulsing than a typical peristaltic pump. The selected model was a Watson-Marlow Qdos 60 chemical dosing pump with a flow range of up to 1000 mL min^{-1}, controlled through a calibrated 4 mA to 20 mA signal that adjusts the output flow rate from between 0 mL min^{-1} to 125 mL min^{-1}. A dual-headed pump exhibits less pulsing than a single head peristaltic pump but was still a concern for testing. An injection experiment was done where the size of the injection was measured over time. From these tests there was no measurable change in size of the injected dye stream proving that the any pulsing had negligable effect on the flow and therefore experiments.

Although technically located on the optical test bed and not on the Auxiliary Rig, a Nordic Tec 45 kW Steel Plate Heat Exchanger also plays a role in temperature control. This component exchanges the primary and secondary test fluid co-currently in an oversised exchanger. The reason for this over-specification is to ensure that both flows achieve as much thermal equilibration as possible, for reasons previously explained in relation to PLIF in Section 3.2.2.1. Its location on the optical test bed ensures that the flows only travel a short distance before testing and therefore limits any ambient heating or cooling effects before the fluid reaches the test section.

Upon return from the test rig, the mixed primary and secondary fluids enter the Auxiliary Rig for regeneration and reuse. The returning fluid flows directly into an outlet tank. A Micropump® magnetically coupled to a Cemp S9 motor conveys the fluid from this outlet tank in a flow loop separate from the primary flow. The pump operates on an identical Modbus RTU controlled 400 W Variable Frequency Device as the one used for the primary flow pump. The fluid is directed to a filtration system that cleans the waste glycerol before it is returned to the inlet tank for re-use. This filtration system is explained in greater detail in Section 3.2.3.4.

3.2.3.2 Temperature Control

To control the temperature of the test fluids, a Betta Tech CU700 Heater/chiller unit is utilised. This hardware resembles a conventional 2.5 kW chiller unit but features an internal 3 kW heating element at the chiller flow outlet. A Modbus RTU remote-addressable hardware Proportional Integral Derivative (PID) control unit uses this heater to maintain a desired set point precise to 0.1 °C anywhere between −10 °C to 70 °C. The PID was auto tuned at a typical flow condition and both reaches and maintains a desired set point with minium overshoot and no oscillations. The heater/chiller contains a 40 vol % aqueous solution of ethylene glycol working fluid that exchanges with the glycerol test fluid through a plate exchanger.

The temperature at the outlet of the plate exchanger is measured using a high-precision 100 Ω (PT100) RTD with custom soldered copper fins. The DASYLab® software control program receives this data and interfaces with the heater/chiller through the Modbus RTU protocol, enabling the selection of a temperature set point remotely. This DASYLab® software and set up is analysed in greater detail in Section 3.3.2.

3.2.3.3 On-line Viscometer

The test fluid utilised in the test rig is glycerol, and the knowledge of its viscosity is crucial for evaluating mixer performance. The viscosity is needed to accurately calculate the values for Reynolds and friction factor that characterise a static mixer element. Glycerol, being hygroscopic, actively absorbs water from any available source including humidity in the air. As a result of this, the viscosity of the glycerol drops significantly as it absorbs more water, data regarding this in Section 2.2.1. In conventional batch testing of PLIF mixing, the glycerol always remains fresh. Therefore, the viscosity can be taken from the product's data sheet (assuming it is accurate). However, in continuous processing, there is the risk of glycerol diluting over time, making it essential to monitor this dilution.

The initial process for measuring viscosity for this rig involved off-line testing. The glycerol was sampled and its viscosity analysed using a cone and plate rheometer. This approach had major drawbacks. Firstly, it was a cumbersome process, as sampling the glycerol and transporting it to a rheometer off-site took a significant amount of time. Secondly, inaccuracies arose due to the dramatic temperature-viscosity curve of glycerol which created hysteresis in the readings over the temperature sweep. When attempting to slow the speed of the measurement to allow the glycerol more time to reach a temperature equilibrium there were two major drawbacks. It increased the measurement time even further but, more crucially, it gave more time for the glycerol to take on water from the surroundings and become less viscous over the course of the measurement. Consequently, a new methodology became necessary, resulting in the adoption, design and installation of an on-line pipe rheometer.

The theory behind this method is to direct the test fluid through a high-tolerance pipe with precisely known dimensions. Specifically, it uses a 7 mm internal diameter pipe, experimentally measured to an average of 7.074 mm by performing a total mass water test with a balance accurate to 1 mg. At a known distance of 1.2 m along the length of the pipe, two 0.5 mm pressure tap holes have been drilled through the wall, with hose tails welded to the exterior of the pipe at the hole locations. These hose tails connect to the high-pressure and low-pressure side of a 1 bar Keller PD-33X Modbus RTU differential pressure transducer.

The pipe features a 500 mm entrance length before the first pressure tap to ensure fully developed laminar flow and has a copper-finned RTD (as described in Section 3.2.2.1) at either end, accurately measuring the fluid temperature at the entrance and exit of the pipe.

The measured pressure drop, mass flow rate and density from the coriolis flow meter, and the pipe dimensions can be combined to calculate the viscosity of the fluid, provided the flow is fully developed and laminar. This calculation follows from a rearrangement of the Hagen–Poiseuille equation.

$$\mu = \frac{\pi d^4 \Delta P \rho}{128 \dot{m} L} \tag{3.1}$$

where μ is the fluid viscosity (Pa s), d is the pipe diameter (m), ΔP is the pressure drop (Pa), ρ is the fluid density (kg m^{-3}), $\dot{m}$ is the mass flow rate (kg s^{-1}), and L is the length of the pipe (m).

This can then be converted into a glycerol mass fraction using experimentally the calculated viscosity, measured temperature and literature glycerol property data. This data, in the form of polynomial equations, appears in Section 2.2.1. A custom Python script uses these polynomials to take the inputted measured variables and output a glycerol mass fraction that is stored back into the experimental data SQLlite database and from here can be recalled for further calculation.

The temperature of the glycerol is deliberately manipulated to change the viscosity of the glycerol during testing and expand the testable Reynolds range. The then means that the viscosity then becomes an unknown. By measuring the mass fraction of the glycerol each morning with aforementioned method, it can be used to actively calculate the viscosity as the experimental temperature changes by referring back to the polynomials in the Python script rearranged to have mass fraction as an input and viscosity as the result.

3.2.3.4 Filtration

A primary goal of this project is to reduce the cost and increase the speed of PLIF testing. A key strategy for achieving this is continuous operation, which necessitates the 'un-mixing' of waste, mixed glycerol that contains dye. This process involves filtering out the Rhodamine 6G and recirculating the regenerated glycerol back to the inlet. The following section details this filtration system.

As described in Section 3.2.3, the waste glycerol accumulates in an outlet tank. From here, a Micropump® gear pump drives the glycerol into the filtration system. This

system contains two Pentair CFB-PLUS20BB Fibredyne™ carbon block filters installed in parallel. These one-stage filters, consisting of activated carbon in a polyethylene matrix, remove particles up to 5 µm in size and adsorb impurities in a fluid. The glycerol's temperature strongly influences its viscosity, which in turn affects the pressure drop across the filters. Given that the filters have a maximum differential pressure of 1.5 bar, a separate flow loop is required. If the filters were installed into the primary flow loop, this would limit the variety of testable experiments, particularly when handling the highly viscous cold glycerol with high flow rates. Whilst having two filters in parallel enables a throughput that is slower that the fastest rate at which the waste can be generated, it regenerates faster than the slow flows. The 40 L of test fluid in the tank allows enough buffer for the filtration and test rate to balance out over time and enable constant testing.

A Keller PD-33X 10 bar differential pressure transducer with a 4 mA to 20 mA signal output is connected to the inlet and outlet of the filters, measuring the pressure drop across the filters. This data is then relayed to DASYLab® via the data acquisition system, as further detailed in Section 3.2.3.5. DASYLab® contains a tuned software PID control that, with the controllable output frequency of the Micropump®, targets a flow rate maximising the differential pressure across the filter to 1.4 bar thereby maintain the maximum throughput of the filters without risking any damage.

The waste glycerol from testing exhibits a light pink colour. The activated carbon in the filters adsorbs the Rhodamine 6G dye present in the waste glycerol. In testing, there was no visible fluorescence in the filtered glycerol under laser illumination, making it experimentally indistinguishable from unused, undyed glycerol.

3.2.3.5 Data Acquisition

To ensure the quantification of collected experimental PLIF images, all fluid property data must be collected. This requirement makes the data acquisition system as crucial as the PLIF laser system. The test rig includes several data sources:

- Eight RTD temperature measurements
- Two absolute pressure measurements
- Three differential pressure measurements
- One mass flow and density measurement

Some of these readings are classified as analog, such as the RTDs, one differential pressure sensor, and both absolute pressure sensors. Others are boolean digital, such as the level indicators, and some are digitally encoded through Modbus RTU, like the remaining two differential pressure sensors and mass/density flow readings.

A 16-bit Datascan 7021 data acquisition module, is used to measure the temperatures from the RTDs. This module can transmit readings at a rate of 2 Hz (one reading every 0.5 s). The RTDs are 4-wire and have an error limit of 0.25 °C when coupled with the Datascan 7021 in this configuration. To improve accuracy, each RTD is calibrated with a linear regression calibration curve between two known readings: the lower one in distilled water saturated with ice and the higher one in distilled water at a rolling boil.

The absolute pressure sensors and the differential pressure sensor across the filter output a 4 mA to 20 mA current signal. These outputs are connected to a Datascan 7032 Analogue data acquisition unit, which is essentially a highly accurate voltmeter. A high tolerance (0.05 %) 500 Ω shunt resistor is installed across the high and low terminals to convert the 4 mA to 20 mA signal to a 2 V to 10 V signal. It is then internally scaled by software in DASYLab® to convert it to the correct reading in Bar. These transducers are not calibrated further, as they are simply indicative measurements for safety, and overly high accuracy is unnecessary.

Finally, the Coriolis mass flow meter and the high-accuracy pressure transducers that measure the pressure drop across the mixing test section and the rheometry bypass communicate directly through Modbus RTU. These readings require a high degree of accuracy, and an internal direct-to-digital conversion means a controlled factory calibration is used without the need for the complication and lower accuracy of a third-party analog-to-digital conversion. The Modbus protocol is a digital encoded

communication standard that is interference-proof through the use of checksums, these factors ensure the highest possible confidence in these very crucial readings.

All Modbus RTU communication is collected through a USB Modbus "controller" device that DASYLab® addresses and sequentially polls each Modbus "worker" for data measurement.

The electrical box that was assembled to house the data acquisition and control input/output wiring and hardware is seen in Figure 3.11. This system was designed and built entirely by the author from scratch, with no pre-existing electrical setup or framework available at the outset of the project.

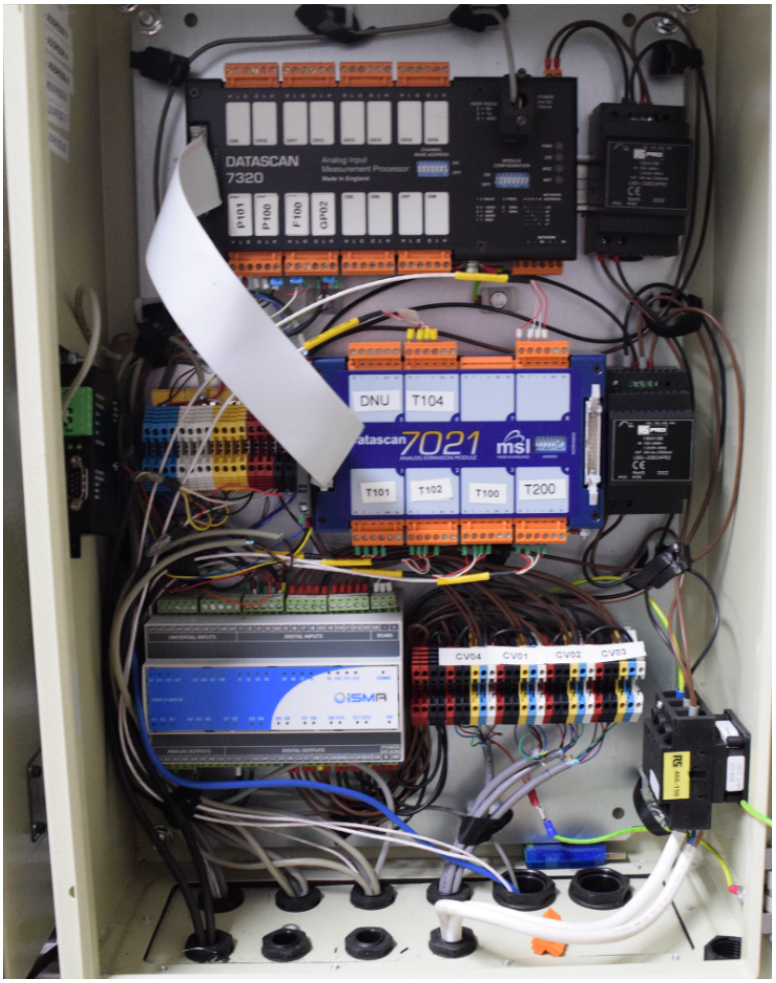


Fig. 3.11. Electrical Wall Box Housing Dat Acquisition and Input/Output Hardware and Wiring

3.2.3.6 Control Input/Output

The aforementioned Modbus RTU "controller" with a serial USB computer connection also serves as the backbone of the test rig control Input/Output (IO). It interfaces the DASYLab® software with most of the rig hardware. A detailed look into DASYLab® can be found in Section 3.3.2. Another key component, the Innon Energy iSMA-B-MiX38, is a multifunction IO module that controls a multitude of functions on the test rig. The unit sends and receives various IO controls through the Modbus RTU protocol as a "worker" of the Modbus network.

Two digital inputs read the position of glycerol vessel level switches. These are float switches, situated at the bottom of each tank. When the tank contains fluid, the bob floats. The bob contains a magnet that actuates a switch, completing a circuit and reading as "high" on the iSMA input. When the tank is depleted, the bob falls, and the circuit breaks. The iSMA unit also uses eight of its digital outputs to actuate the four remote electrical ball valves that direct the primary test flow, as described in Section 3.2.2.4. Each valve receives two outputs, one for the open and one for the closed position. The digital outputs function as relays that connect the valve motor to a 24 V supply voltage. The outputs are coupled in DASYLab® to operate in tandem, actuating one valve open while its counterpart is simultaneously closed. Eight digital inputs receive feedback signals from the eight combinations of positions so the software can ensure the valves have finished actuating correctly before allowing the flow of fluid.

An analogue output on the iSMA unit provides 0–10 V to a separate 0–10 V to 0–20 mA converter. This signal controls the chemical dosing pump that pumps and meters the dyed glycerol flow. A digital output is used to send a "run" command to the pump, which ensures that an active input has been made by the operator to activate the pump. Finally, a digital input is used to capture an "alarm" signal from the chemical dosing pump to warn the operator of a malfunction that the pump internally detects and outputs.

Two other main functions are controlled directly by the Modbus "controller" as their own "workers" in the network. The first is the control of the two VFDs that power the pump motors which, again, DASYLab® requires an active "run" command from an operator and can send the desired motor frequency. The other is the heater/chiller unit; this unit can be directly sent the desired temperature set-point whilst the current fluid temperature is also frequently polled and returned to the DASYLab® software.

3.3 | Software, Data and Industry 4.0

Up until now this chapter has focused on the hardware that makes up the test facility, what follows is the equally important software and programming that interfaces with, and controls the test rig hardware. The transition to continuous PLIF testing has both increased testing efficiency and introduced substantial complexity. There are now multiple flow loops, each with its own pressure limitation and flow requirements and the inclusion of temperature control necessitates a controlled steady state. Unlike with batch PLIF testing, this level of complexity requires more than what can be done by one or two operators without the aid of additional software.

Industry 4.0 is the trend towards automation and data exchange in manufacturing technologies. As part of this, digitisation of industry is a key component. This test rig takes some of these concepts aimed at industry and aims to take them to the lab scale. All data readings are not only digitally recorded, but they also centralised into a single control system through a data acquisition system. With the help of the Modbus protocol, every component on the rig becomes remotely controllable. This integration demonstrates a core feature of Industry 4.0 - the ability to monitor and control physical systems virtually - and allows for realistation of the improved efficiency of continuous PLIF.

Using the software, operators can control all the aspects of the test rig. This includes setting all temperature controls, adjusting all pump speeds, and modifying the flow path. Save powering the rig on and off, the PLIF testing can be conducted

fully remotely. The implemented control software, DASYLab®, along with other key software components, will be detailed in this section, exploring how they operate and integrate with the hardware, and therefore showcase the use and transition to Industry 4.0 in a lab environment.

3.3.1 Modbus

Modbus is an integral tool of this test rig and is the backbone of what allows the rig to test quickly and, in the spirit of Industry 4.0, enables the software to control the rig in such a way that it largely automates itself. This test rig communicates on a type of Modbus referred to as Modbus RTU and what follows is a brief overview on its procedure.

Modbus is a data communication protocol common in industrial automation systems. The architecture consists of a controller and workers, each with specific roles; in this case a worker could be a pressure transducer. The controller issues commands to workers, specifying tasks via function codes, and indicating where in the memory the task should be performed. Following that is the data size, register address, and, in case of a write command, the data itself. Each command features a Cyclic Redundancy Check (CRC) checksum to ensure data integrity. On receiving a command, the worker performs the CRC check, carries out the command if no corruption is detected, and sends back an acknowledgement along with any requested data.

DASYLab® supports Modbus natively and requires that each command is set up manually to the above specifications. From there however, the calling of those commands is automatic and enables DASYLab® to work as the high-level interpretor and command issuer. These commands interface with the test rig though a StarTech.com ICUSB422IS USB to RS422/RS485 Serial Adapter functioning as the controller for the network.

3.3.2 DASYLab®

DASYLab®, a Graphical User Interface (GUI)-based lab-scale control software, enables real-time data acquisition and IO control of testing hardware. While earlier sections have mentioned this software, a more in-depth exploration is written here. The program consists a series of simple, independent modules, each performing distinct functions. These modules can be 'wired' together to construct complex systems (This layout can be seen in Figure 3.12). Several types of modules exist, but the most frequently used and most important include:

- Input/output - which reads or writes data from or to data acquisition or Modbus
- Read/write - which reads or writes data to the global variables
- State machine - a logical flowchart step machine for automation
- Mathematics - used for data manipulation; actions, which performs a specified action to another module on a certain trigger
- Logic operations - which perform a variety of boolean operations on a software Transistor-Transistor Logic (TTL) signal (a binary signal either denoting a signal 'high' or 'low')
- Switches/sliders - interfaces that activate or change certain values.

A wire can carry various types of data, whether it's a number, a string, or a software TTL signal. Different modules input and output data types through these wires and use the data to carry out tasks. Though the individual wired systems actually exist in different operation 'black boxes' for neatness, Figure 3.12 shows all of the modules and wiring together for ease of demonstration. All measurement data pulls in as 'blocks' from input modules that retrieve data from the data acquisition system. By default, DASYLab® has the capacity to interface with Modbus and can communicate with

Datascan units through an installable plug-in. The software then writes the measured data to global variables that can be read in to any module anywhere in the worksheet.

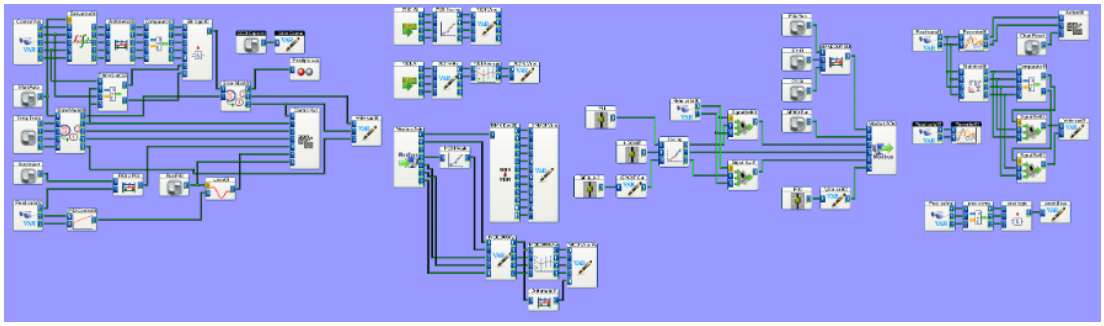


Fig. 3.12. DASYLab® Module and Wiring for the PLIF Test Rig

A primary state machine serves as the program's brain, running the test rig. Secondary state machines exist to aid the operation of the primary machine. State machines operate as a flowchart of actions, assessing available inputs and determining the subsequent operations based on this information with the goal of offering a largely automated testing experience. For example, depending on the digital switches selected by the operator, different testing parameters can be chosen, such as temperature levels at which the testing is to be conducted. Based on these switches, the state machine loads the relevant testing parameters and sends set point and run commands to various rig hardware components. For example:

- Run Pump 1 at 60 Hz.
- Set the heater/chiller set point to 15 °C.
- Recycle the main flow back to the inlet tank while waiting for the temperature steady state at the primary plate exchanger output.

DASYLab® signals the operator once the rig achieves steady state, indicating it is time to initiate the dye flow. The operator's involvement is necessary for this step as the dye is the rig's only consumable, and therefore the PLIF process requires manual input. Once the dye flow stabilises, the operator can use the PLIF software, Insight 4G™, to capture PLIF images. This process is further explained in Section 3.3.4.

After the operator is satisfied with the captured images, a button on the DASYLab® control screen can be pressed to inform the state machine. At this point, the state machine triggers the output of the averaged steady-state data from the past 60 s through Open Database Connectivity (ODBC) protocol to a SQLite Database. More detail on this is available in Section 3.3.5.

Once the data output completes, the state machine automatically advances to the next set of testing parameters. For each temperature set-point, there are five different flow velocity settings. After completing all velocity settings for a temperature set-point, the state machine progresses to the next temperature range. The test rig can perform tests across up to four different temperature ranges. The full range of potential testing parameters and resultant Reynolds numbers is available in Section 3.6.

In addition to the state machine logic that governs the rig, numerous peripheral functions play a significant role, many of which are related to safety. For instance, software limits set on every pressure transducer automatically deactivate the pump in the event of over-pressure. These safety measures function as one-shot trips, preventing automatic pump restart and requiring operator intervention to confirm the status of the rig and check why an over-pressure incident may have occurred. Each glycerol tank also features level switches. If DASYLab® detects a low level, it deactivates the pump until the level increases. DASYLab® is also where the software PID is setup though a PID module to maximise the filter throughput while limiting the differential pressure.

The framework for DASYLab®'s control of the rig relies on the module and wiring, but an interface for the operator to manage the facility is also required. DASYLab® provides a display sheet for this purpose. Its primary component is the P&ID depicted in Figure 3.1, altered to leave blank spaces for data measurements. DASYLab® dynamically displays data in these spaces, providing the operator with real-time updates on the test rig's status. A chart below this diagram depicts the inlet and outlet temperature of the main test section to confirm steady state to the operator and

alongside it is all of the buttons and sliders that control the test rig. A snapshot of the display control window as seen by an operator appears in Figure 3.13.

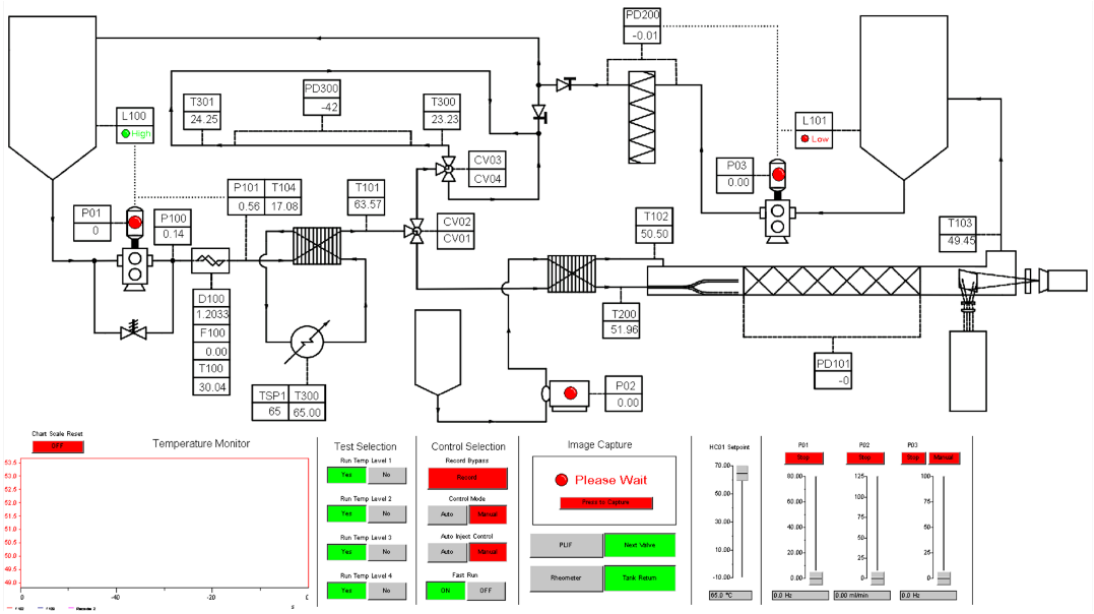


Fig. 3.13. DASYLab® Control Display for the PLIF Test Rig

DASYLab®, significantly enhances testing efficiency. It takes over most of the tasks related to maintaining the testing operating parameters, enabling the operator to concentrate on PLIF imagery and other responsibilities. Given a limited timeframe, this automation means the capturing of a larger data set, adding a great deal of value to the PLIF process. It also adds a large degree of testing consistency where there is certainty that the testing parameters are completely consistent between tests on different static mixers.

3.3.3 Control Principle

3.3.4 Insight 4G™

Insight 4G™ is a software package from TSI that is used to both control the PLIF laser and camera system and to capture and save the PLIF imagery. All of the laser parameters such as Q-switch timing, pulse spacing and pulse frequency are set up here alongside the camera capture start and exposure time. Individual tests are classified as

'runs' with each run having a unique designation and each test run containing a series of photos captured sequentially at whatever the laser/camera frequency the system is set to. These images are initially held in memory and then saved to disk if accepted by the operator.

3.3.5 SQLite Data Storage

As outlined in Section 3.3.2, DASYLab® interfaces with the data acquisition system to record and average steady-state data, which it then saves for each experimental test run. There are ten significant data measurements, excluding static mixer identifiers or run number that are recorded. Given that eventually the goal was to conduct hundreds or thousands of tests and since each test generates considerable data, it was necessary to implement a robust data storage system to ensure data safety and ease of recall. The chosen solution is an SQL database, specifically an SQLite 3 database. This is a local database on the test computer that can be interfaced via SQL command and was initially created using a Python script to generate the database table, column labels, and column data formats. This table is then linked to the built-in ODBC protocol via a third-party open-source driver available at http://www.ch-werner.de/sqliteodbc/. This connection enables DASYLab® or any standard program with database interfacing capabilities to interact with the SQLite database. The driver serves as a translation layer, converting the ODBC protocol to SQL. Now the Database has been created and communication can be established, a command from an action module in DASYLab® triggers the export of the averaged data measurements and other relevant information to the database. Python is natively compatible with SQLite and can call the data directly from the database. Since python also serves as the post-processor of the PLIF imagery, it allows the evaluation of experimental data and PLIF imagery together and exports these results back into the SQLite database. This system ensures that all data, both raw and evaluated, is stored together in a centralised, unfragmented location. Section 3.4 provides the Python script for test post-processing and a detailed breakdown of its operation.

3.4 | Image Post-Processing

PLIF generates a considerable number of images. Every static mixer tested goes through twenty different Reynolds flow conditions for each tessellating insert iteration. Approximately twelve different insert lengths are tested, each undergoing twenty tests, with each test usually producing 50 images at minimum. This process results in 12,000 images across the full range of resting for every static mixer. For redundancy of data, the testing computer backs up all data instantly to an encrypted cloud storage and nightly to a second disk on the local computer and to network attached storage in an off-site data vault Given that each image is 8.4 MB, that's approximately 100 GB of images per static mixer. A computer program is necessary to parse this volume of data and because of this, a Python script was developed for this purpose. This script needed to import, calibrate, evaluate, and export the data for each of the test sets accurately and efficiently while interfacing with the data stored in the SQLite database described in Section 3.3.5. The following described the functionality and the reasoning of the scripting created.

The image processing script begins by importing essential toolboxes required for its execution. Key among these are NumPy for mathematical functions, Pillow (PIL) for image processing, SQLite3 for database interfacing, multiprocessing for parallelising the code, and tqdm for displaying progress bars to assess processing time.

Variable inputs are then provided by the user, mostly pertaining to image size specifications. Important variables include the image pixel brightness at perfect mixing concentration, the pixel brightness of the unmixed pure tracer dye, and a previously generated weighting matrix that evens out varying brightness levels across the tube's cross-section. Due to the way laser light is shaped into a sheet using glass optics, the light intensity varies, being less bright towards the top and bottom of the cross-section. By saturating the test section with a known concentration of tracer dye, the weighting required to adjust each pixel value to the average was calculated. This was exported as

a NumPy array and is loaded here for use in the script. These pieces of information were evaluated and collected during the calibration and commissioning of the PLIF mixing section.

Next, the script compiles a list of individual folders that contain the images captured by the test rig. The PLIF software, Insight 4G™, organises each test set into a folder with a unique name—for instance, SMXV100Q02CR001A. This naming convention encodes information about the test, such as the type of static mixer, insert variation, repeat number, injection position, and run number. These folder names correspond to the test data found in the SQL database as configured in and exported by DASYLab™. Extra folders generated by Insight 4G™ are excluded from the list.

For image processing, each step is defined within the overall post-processing function applied to each test run. Initially, the script creates a list of all .TIF format images found in each test set folder. On a normal run, each test set has 50 images taken over 25 seconds to average out shot-to-shot variability in the laser and any flow variability. The Pillow toolbox is used to load each image, and they are compiled into a list. NumPy then stacks these images into a three-dimensional array, where the x and y dimensions represent the image data, and the z dimension represents each of the collected images. The data format is set to a 16-bit integer to match the 12-bit (0–4,095) pixel intensities and to reduce memory usage compared to the default 32-bit float.

A circular Boolean mask is then created to define the region of interest (ROI) within the images. This mask is generated using the x and y centre positions and a specified radius. The mask has true values for pixels within the ROI and false values outside it. This mask serves two purposes: it delineates the ROI by setting all points outside it to zero, and it ensures that statistical calculations are only carried out on the ROI, avoiding areas with zero or invalid data.

Each test run's unique data set is deconstructed into its meaningful parts for querying the database for relevant testing data. The script points to the directory where the image folders are stored.

With the functions defined, the script loads all the images for a particular test set into a three-dimensional NumPy array and applies the mask to set all points outside the ROI to zero. Using a 16-bit integer format helps reduce memory usage but does not support 'NaN' values, so the mask ensures correct calculations by including only values within the ROI.

Once the images have been loaded and trimmed to include only the ROI, the three-dimensional array is reduced to two dimensions by averaging all versions of each pixel across the collected images. This averaged image is then multiplied by the previously loaded calibration mask. This weighted matrix calibrates the image to normalize brightness levels across it, creating a calibrated image.

The calibrated image is then exported in two formats. The first is a signed integer (.png) file for lossless, accurate exporting of the matrix, suitable for further analysis. However, due to the low average brightness relative to the peak possible intensity, the image may appear black when opened in standard image viewing software. For general viewing, the image is also converted to a grayscale (.jpg) format that scales the actual maximum brightness to the peak possible brightness. This variable scaling means the images cannot be compared quantitatively but are useful for demonstration purposes and can be opened in typical image viewing software. Each image is automatically named based on the coded string that represents each test run for easier referencing to the database.

The Coefficient of Variance (CoV) is then calculated for the averaged and calibrated PLIF image as part of the mixing analysis. The CoV is a measure of variability and is given by the standard deviation of every pixel in the ROI divided by the mean of every pixel:

$$\text{Coefficient of Variance} = \frac{\sigma}{\mu} = \frac{\sqrt{\frac{\sum(x_i-\mu)^2}{N}}}{\mu} \tag{3.2}$$

In this equation, σ is the standard deviation, x_i is a pixel value, μ is the mean of all pixel values in an image, and N is the total number of pixels in the image. In Python, this calculation involves computing the standard deviation and mean of the pixel values within the ROI and dividing the standard deviation by the mean.

With the mixing results calculated, the final step is to export these results. The test flow data captured by the test rig data acquisition was exported to an SQLite database. Python's native support for SQLite enables communication with the database using standard SQL commands. The script updates pre-existing columns in the database with the calculated Coefficient of Variance, an in-house mixing number referred to as the CALGAVIN Mixing Number, and the mean pixel intensity. The unique code name for each test run is used to match variables against the information stored in the database, linking the existing flow data with the newly post-processed mixing information.

To handle the significant number of images (usually around 12,000 per static mixer tested), the script parallelises the processing by assigning each available core on the computer a test run to calculate. The core count is set at the beginning of the script; in this case, 12 cores are used. This approach requires more memory but was manageable on the computer used (12-core with 256 GB memory). The script can also run on standard computers with less memory and fewer cores by adjusting the core count, though this will affect processing speed.

The tqdm function is used to track progress, generating a progress bar in the output console that displays the percentage completed based on the total number of cases. It also shows the rate of processing and estimates the time to completion.

A benchmark of 457 test runs was established to assess the processing time of the code. Each test run contains 50 images, totaling 22,850 images (approximately 192 GB of data). Running on a single thread, the average time to process a test set was 4.32 seconds, resulting in a total processing time of 32 minutes and 52 seconds for all sets. When executed in parallel across 12 threads, the processing time reduced to 0.98 seconds per test set, or 7 minutes and 29 seconds for all test sets. This represents

roughly a fourfold speed increase. The speed increase is not linear with the number of cores due to a bottleneck in the read speed of the installed SATA III SSD, which is limited to 500 MB/s. Installing a faster PCIe or NVMe SSD would lead to more significant improvements with the added processing threads.

3.5 Rig Commissioning

The previous sections have detailed the development and construction of the test rig's hardware and software. With its completion, we now move to the commissioning phase. This phase involves the fine-tuning of the PLIF setup and calibrating its output to ensure consistency and quantifiability.

3.5.1 Image Calibration

3.5.1.1 Principle

If the pulsed laser were to fire and illuminate a cross-section of the pipe that only contained a completely mixed solution with a constant concentration of dye, the resulting fluorescence and captured image would not exhibit perfectly even brightness. Despite the laser being of high-quality scientific grade, it does not produce a perfectly circular beam with evenly distributed brightness. According to its specifications, the laser's brightness profile is fairly flat (although it was not explicitly tested here), but all lasers exhibit some degree of brightness falloff towards the edges. Additionally, the laser is being "stretched" into a light sheet. Naturally, the original laser point circle is wider at its central point. When this is flattened, it results in a higher photon concentration in the midsection of the light sheet. Consequently, a brighter midsection leads to brighter fluorescence and, in turn, a higher perceived brightness in the vertical center of the captured image. Without calibration, this would be incorrectly perceived as a higher dye concentration in the vertical centre and a lower dye concentration at the top and bottom of the image.

This function is also intertwined with the relationship between dye concentration and light intensity measured at the CCDs pixel. To quantify the PLIF images, it is necessary to model this relationship. Fortunately, the following experiment can be used to find both the image brightness unevenness and the concentration/brightness relationship.

3.5.1.2 Method

As previously mentioned, the tracer dye used in the experimentation is Rhodamine 6G, dissolved in the glycerol test fluid to a concentration of $0.5\,\mathrm{mg\,L^{-1}}$. To conduct the calibration experiments, the test section was flooded with flows of $0.0\,\mathrm{mg\,L^{-1}}$, $0.1\,\mathrm{mg\,L^{-1}}$, $0.3\,\mathrm{mg\,L^{-1}}$, and $0.5\,\mathrm{mg\,L^{-1}}$, and a series of PLIF images were collected for each flow.

With the laser brightness and camera exposure set up to ensure a suitable intensity level range across the applicable dye concentrations, this procedure generated sets of images of grey circles with varying brightness. The $0.0\,\mathrm{mg\,L^{-1}}$ flow essentially produced purely dark images, the $0.5\,\mathrm{mg\,L^{-1}}$ flow produced bright white circles, and the middling concentration flows produced shades of grey.

The different dye concentration tests can be used to map the dye concentration to the perceived pixel brightness. Each test captured at least 50 images, all of which were first averaged into one image using a simple Python program to even out laser shot-to-shot variability. The mean brightness of the ROI was computed for the average image from each concentration, and this mean was plotted against the concentration to display the relationship. If this relationship can be modelled with an equation, the concentration of the dye can be quantifiably mapped to the image brightness, and PLIF will successfully operate as a dye concentration measurement tool.

To calibrate for the uneven light distribution across the image, a modified version of the python program was used to process the 100 images from the $0.5\,\mathrm{mg\,L^{-1}}$ test. These images were then averaged to create a single image. This composite image clearly

showed the higher brightness in the midsection, with dimming towards the top and bottom. Additionally, artifacts in the form of horizontal linear banding were observed. These were caused by minute imperfections on the surface of the acrylic block through which the laser passes, despite meticulous polishing. These imperfections result in minor brightness variation as the laser propagates through the acrylic and into the cross-section.

A weighting map was generated by dividing every pixel value in the composite image by the mean value of the entire ROI. This map contained the necessary multiplier to adjust all the values in the image to the mean value. This is saved as the matrix and is used to calibrate and normalize the captured PLIF images, by multiplying it with them. Since the top-to-bottom light variation and the banding are always in the same position, this correction matrix effectively neutralises them, resulting in a cleaned and evenly distributed image. A key stipulation here is that for this weighting to apply at any brightness level, the relationship between concentration and brightness must be linear. Otherwise, the proportional weighting coefficient will be dependent on the dye concentration. This linear relationship is examined in the following results section that looks into the tests described in this method section and illustrates the mapping of dye concentration to image brightness.

3.5.1.3 Results

Figure 3.14 depicts the results of the mean brightness from the flows of $0.0\,\mathrm{mg\,L^{-1}}$, $0.1\,\mathrm{mg\,L^{-1}}$, $0.3\,\mathrm{mg\,L^{-1}}$, and $0.5\,\mathrm{mg\,L^{-1}}$ as measured by PLIF. Conducting a linear regression across these points gives an r-squared value of 0.9988. This proves that this concentration range of Rhodamine 6G can be linearly mapped to the PLIF brightness and therefore follows the Beer-Lambert law and allows an easy conversion between the two. This concentration range is also suitable for the optical range of the camera sensor. With $0.5\,\mathrm{mg\,L^{-1}}$ the measured mean brightness is roughly 3000 and the max of around 3500. The camera sensor saturates at 4095. At 1% of full range, a concentration of $0.005\,\mathrm{mg\,L^{-1}}$, the image brightness is therefore at around 30. A value that is still image-

able given a camera background mean value of 4. The images of the four concentrations tested in the empty pipe that correspond to the points in Figure 3.14 can be seen in Figure 3.15.

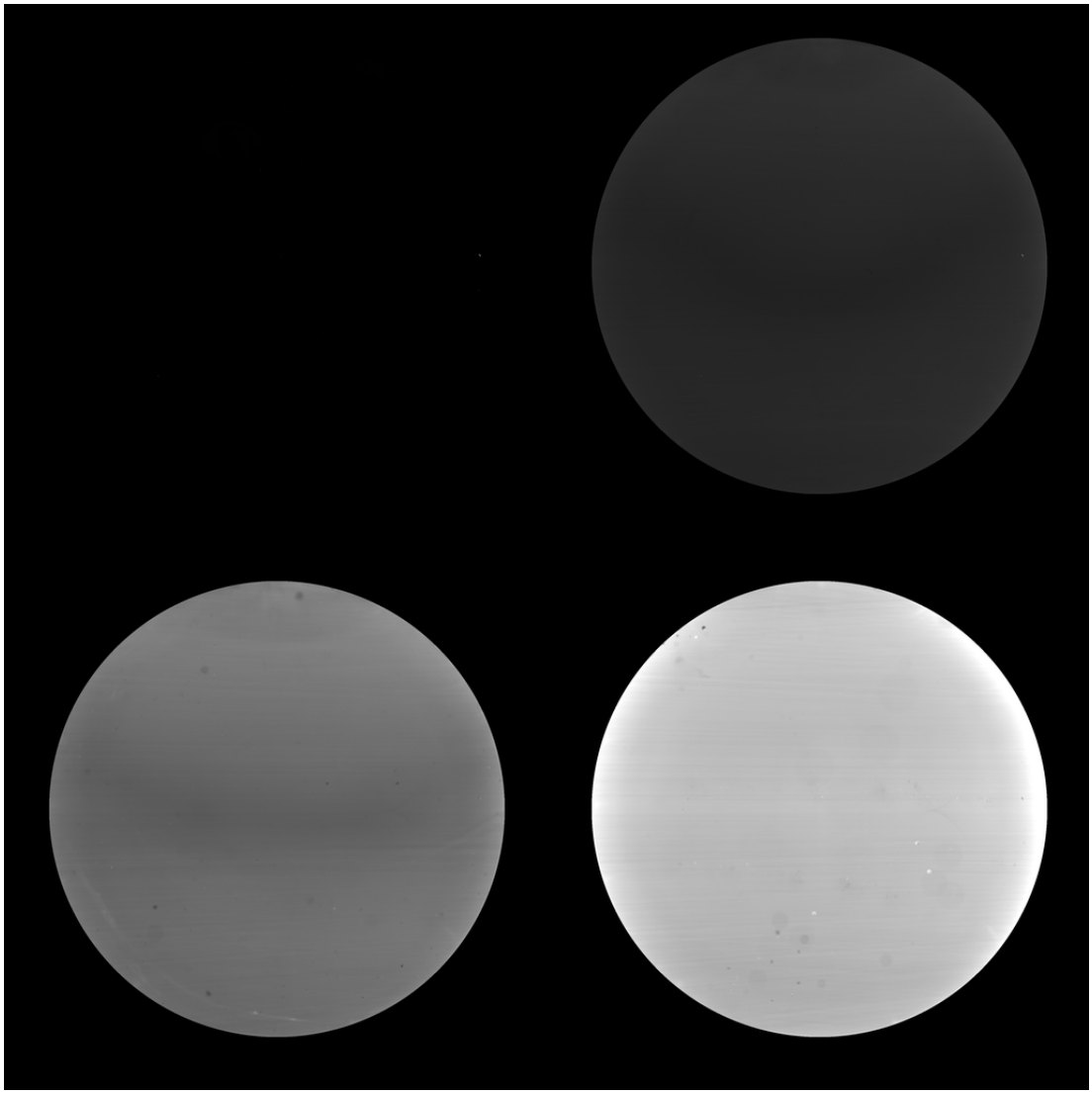


Fig. 3.14. PLIF Images of Test Section Flooded with Rhodamine 6G Concentrations of $0.0\,\mathrm{mg\,L^{-1}}$ (Top Left), $0.1\,\mathrm{mg\,L^{-1}}$ (Top Right), $0.3\,\mathrm{mg\,L^{-1}}$ (Bottom Left) and $0.5\,\mathrm{mg\,L^{-1}}$ (Bottom Right)

Another aspect required is to categorise whether a temperature change affects the luminance of the fluorescing Rhodamine. If there is, this would need to be modelled in order to introduce a calibration that accounts for this to prevent this being a factor alters the quantitate mixing analysis. Figure 3.16 shows the results of this testing and

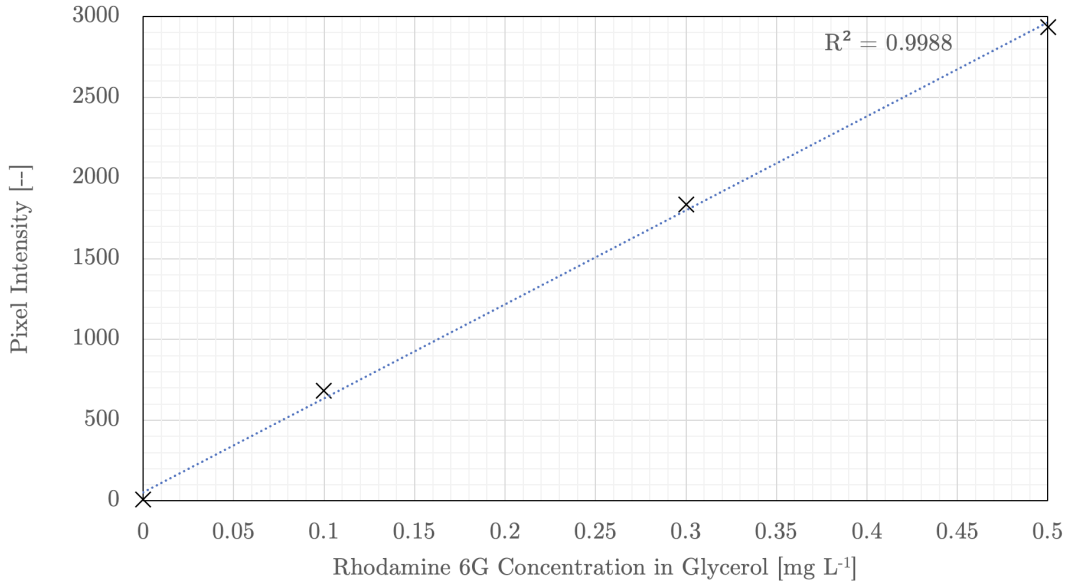


Fig. 3.15. Rhodamine 6G Concentration to Mean PLIF Image Intensity

proves that temperature has no measurable effect with all results within 3% of each other across the full testing temperature range.

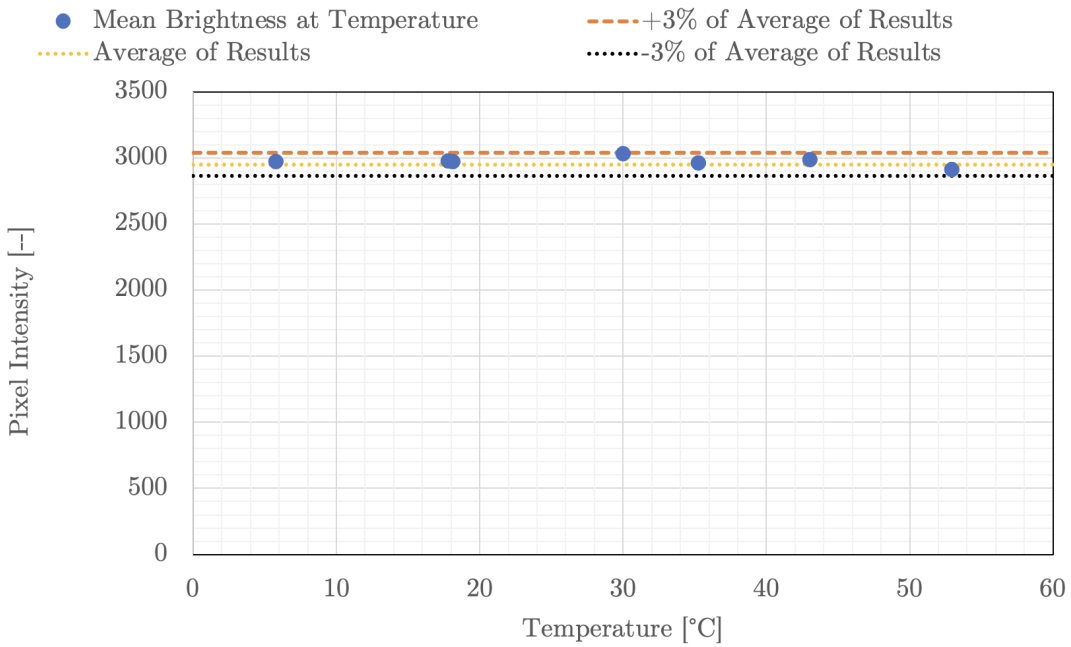


Fig. 3.16. Temperature Dependence on Rhodamine 6G Fluorescence Luminance

3.6 | Test Rig Fluid Parameter Capabilities

3.6.1 Viscosity Control

As discussed in the previous literature section (Section 2.5.1), much PLIF research is conducted at a single temperature and often without any control, resulting in a limited Reynolds number data range unless multiple test fluids are used. Controlling the temperature has two advantages: firstly, it ensures consistency between tests; secondly, by leveraging the viscosity-temperature curve of glycerol, this test rig can fix this issue. The viscosity of pure glycerol changes dramatically across a reasonably small range of temperatures: from 12 Pa s at 0 °C to 0.05 Pa s at 70 °C (please refer to Section 2.2.1 for the plotted data). Since viscosity is inversely proportional to Reynolds number, this manipulation allows a dramatic extension of the Reynolds number range in a way that is not possible with just a variable flow rate.

Additionally, diluting glycerol with water also has a dramatic effect on its viscosity. To broaden the testing range further, static mixer tests were conducted using both pure glycerol (measured with the on-line rheometer to be 99.92 % by weight glycerol) and glycerol diluted to around 80 % by weight. Note that all actual concentrations were measured before each experiment to ensure the hygroscopicity of glycerol had not diluted the test fluid.

This dilution changes the viscosity of glycerol to approximately around 0.25 Pa s at 0 °C and 0.007 Pa s at 70 °C. This adds an order of magnitude to the top end of the Reynolds range whilst still having an overlap which can be used to ensure this variables independence on testing by plotting all experiments together.

As a reminder, the temperature is controlled using the Betta Tech CU700 described in Section 3.2.3.2.

3.6.2 Velocity Control

The primary flow is pressurised using the Witte Extru II/b 4,7 - 1 gear pump, which is rated to pump $56\,\mathrm{L\,h^{-1}}$ at 3 Hz. The pump itself is powered by a geared-down variable speed motor and a Modbus RTU controlled 400 W Variable Frequency Drive (VFD). The VFD is configured with an output frequency of between 0 Hz to 60 Hz. The variable speed motor this VFD feeds to has 4 poles, resulting in 1800 RPM with a 60 Hz source. This speed, through a 10:1 gearbox, gives a pump output of 180 RPM, or 6 Hz. The pump has helical gears as opposed to straight-cut gears, resulting in a lower pulsing flow effect and therefore allowing a more even flow rate even at the low end of pump duty. The VFD is run as low as 4 Hz, giving a pump output of 0.2 Hz with no noted pulsing effect—this would potentially be seen as image brightness flickering in the PLIF imagery. At this lowest pump speed, the measured flow rate was $2.85\,\mathrm{kg\,s^{-1}}$.

The pump used is designed for ultra-high viscous flows of molten polymers, with a design viscosity range from 50 Pa s to 40 000 Pa s. All tests conducted with glycerol are far below this range. This necessitated the design and fabrication of a stuffing box that sealed the rotating pump shaft at both ends to prevent pump leakages. The upside of this is that the pump is heavily over-specified for maximum torque and allowed the pump to be run over-speed. The limit of the VFD was set to 80 Hz, resulting in a 33.33 % over-speed. From this, the highest pump speed is beyond the rated 3 Hz at the pump, and is instead increased to 4 Hz. This resulted in a maximum measured mass flow rate of $63.77\,\mathrm{kg\,s^{-1}}$.

Up until now, only the primary flow control methodology has been discussed. The subsequent focus is on the secondary dye flow. A Watson-Marlow Qdos 60 chemical dosing pump is used for this purpose. It is capable of outputting up to $1000\,\mathrm{mL\,min^{-1}}$, but in this experiment, it is calibrated to output between $0\,\mathrm{mL\,min^{-1}}$ to $125\,\mathrm{mL\,min^{-1}}$. The pump is controlled with a 4 mA to 20 mA signal. By reducing the flow range to output $125\,\mathrm{mL\,min^{-1}}$ at 20 mA instead of $1000\,\mathrm{mL\,min^{-1}}$, the resolution of the desired flow rate increases eightfold.

As a reminder, the main test section has a diameter of 23 mm and contains an injection tube with an OD of 8 mm and an ID of 6 mm. The secondary pump is not manually controlled, but instead, it reacts to the primary flow. DASYLab® reads the primary mass flow rate using the coriolis mass flow meter and computes the required secondary flow to match the capillary's flow velocity. This information is then used to send the corresponding 4 mA to 20 mA signal to the chemical dosing pump. To match the velocities, the area of the primary test section minus the ID area of the capillary is divided by the primary system's volumetric flow rate. This calculated velocity is then multiplied by the ID area of the capillary to provide the desired volumetric flow rate of the secondary flow stream. It is crucial to match these velocities to maintain the developed laminar flow. Mis-matched velocities could introduce radial flows, potentially leading to premature mixing of the dye into the bulk stream before the mixer. This would result in an overestimation of the static mixer's mixing ability.

3.6.3 Resultant Reynolds Range and Testing Parameters

In practical terms, this test rig is capable of operating over three orders of magnitude of Reynolds numbers by controlling the flow parameters while using one test fluid. With pure glycerol (measured at 99.81% using the on-line pipe rheometer), at temperature range between 5 °C to 60 °C, a mass flow between 4 kg h^{-1} to 64 kg h^{-1} and a fixed diameter of 23 mm, the flow rig is capable of operating at Reynolds numbers between 0.02 - 20. When the glycerol is diluted with water to lower its viscosity (measured at 78.8%), the test rig then gives a Reynolds number range from 1 - 100. Overlapping these plots then means the test rig can generate data across five orders of magnitude and give comprehensive mixing results. The rig itself has a current practical limit of a Reynolds number of 200 due to the length of the calming section before the mixer. Any higher and there would not be a guarantee of fully developed laminar flow before the mixer.

A table containing the test parameters that each insert is tested with is seen in Table 3.1, these points are all with the diameter of 23 mm and density is evaluated in

data processing but not included in this table for brevity considering its minor change to Reynolds across temperature and mass fraction:

Table 3.1: Test Parameters for Mixing Experiments

Glycerol Mass Fxn. [–]	Temperature [°C]	Viscosity [Pa s]	Velocity [m s-1]	Reynolds Number [–]
0.998	10	3.69	0.002	0.02
			0.005	0.04
			0.010	0.08
			0.020	0.16
			0.040	0.31
	20	1.36	0.002	0.04
			0.005	0.11
			0.010	0.21
			0.020	0.42
			0.040	0.85
	35	0.39	0.002	0.15
			0.005	0.37
			0.010	0.73
			0.020	1.47
			0.040	2.94
	50	0.14	0.002	0.42
			0.005	1.04
			0.010	2.08
			0.020	4.17
			0.040	8.33
0.778	10	0.08	0.002	0.72
			0.005	1.80
			0.010	3.61
			0.020	7.22
			0.040	14.44
	20	0.04	0.002	1.34
			0.005	3.34
			0.010	6.68

Continued on next page

Table 3.1: Test Parameters for Mixing Experiments (Continued)

			0.020	13.37
			0.040	26.73
	35	0.02	0.002	2.94
			0.005	7.34
			0.010	14.68
			0.020	29.36
			0.040	58.72
	50	0.01	0.002	5.30
			0.005	13.25
			0.010	26.50
			0.020	53.00
			0.040	106.01

3.6.4 Conclusions

A test facility was designed, fabricated, assembled, and commissioned, capable of reliably capturing PLIF (Planar Laser-Induced Fluorescence) images to assess the mixing performance of a given static mixer. This data can be combined with concurrently measured pressure drop data to develop insights into mixing efficiency. By developing a testing program in DASYLab®, largely autonomous test parameter settings have enabled rapid and consistent testing of these inserts. The software is integrated with the hardware through a digital I/O and data acquisition system, allowing for remote operation and measurement. The temperature and flow control apparatus, along with the capacity to run tests with multiple fluids, has facilitated the ability to test across more than five orders of magnitude in Reynolds number. Additionally, the integrated pipe rheometer provides confidence in the accuracy of real fluid viscosity measurements.

The inclusion of an activated carbon filter system has introduced the novel concept of continuous PLIF, effectively eliminating the otherwise recurring cost associated with test fluid waste. This setup not only ensures sustainable operation but also contributes to the overall efficiency and cost-effectiveness of the testing process. Notably, for the

entire duration of testing, there was no need to replace the activated carbon filters. The filtered glycerol was periodically tested for fluorescence and showed no signs of filter degradation. Each filter is rated to process 100,000 litres of water, and with two in place and the system operating with recycled glycerol—where the only addition is milligrams of Rhodamine—the expected filter lifetime is substantial.

The total cost of constructing the test facility was approximately £25,000. However, this figure is heavily reliant on the use of second-hand equipment and auction-sourced components. If all parts were purchased new, the cost is estimated to rise to around £40,000. The facility's design and capability to accommodate a wide range of test conditions make it a robust platform for advancing the understanding of static mixer performance.

CHAPTER 4

Low Reynolds Laminar Static Mixer Testing

4.1 Introduction

This chapter describes the results for pure glycerol, characterised by highly laminar fluid flow, and contrasts the performance of market-available static mixers with a first-generation design from CALGAVIN LTD. Chapter 3 discusses the development of a mixing test facility designed to evaluate the performance of static mixers using Planar Laser-Induced Fluorescence (PLIF). The rig allows for the assessment of mixing level and comparison of pressure drop data in the Reynolds number range using pure glycerol (measured at 99.81 wt.% with the on-line pipe rheometer). Additionally, it can be used to measure Reynolds Numbers ranging from 1 to 100 by diluting the glycerol with water to reduce its viscosity (experimentally measured at 78.8 wt.%).

4.2 Materials and Methods

Chapter 3 serves as the detailed Methods and Materials section for this, and the following, experimental chapters. This brief section lists specific set up that only applies to the body of work within this Chapter.

A series of auxiliary components deliver a temperature and flow-controlled stream of test fluid to the inlet of a mixing section. Simultaneously, a stream doped with Rhodamine 6G dye is injected into the primary stream at the inlet of the mixing section. The mixing section contains any of a variety of static mixers that blend the primary and dye streams. Pressure drop is measured across the mixing section and at the outlet of the mixer. The blended fluids then enter the PLIF section, where a plane of laser light excites the Rhodamine 6G, causing it to fluoresce. A camera captures this fluorescence, imaging the location and concentration of the dye. These images can be processed to determine a mixing value. When evaluated with the pressure drop data, this offers a means to compare the quantifiable performance of different static mixers. The remaining components in the auxiliary rig regenerate the test fluid using an activated carbon filter, enabling continuous PLIF operation.

4.2.1 Test Fluids

The test fluid chosen for this low laminar flow test set is 99.8 wt.% glycerol. The temperature/viscosity graph, shown in Figure 4.1, and the temperature/density curve, shown in Figure 4.2, are calculated using the correlations in Section 2.2.1.

The secondary dyed flow consists of the same fluid as the primary flow, but with an addition of Rhodamine 6G to achieve a concentration of $0.5\,\mathrm{mg\,L^{-1}}$.

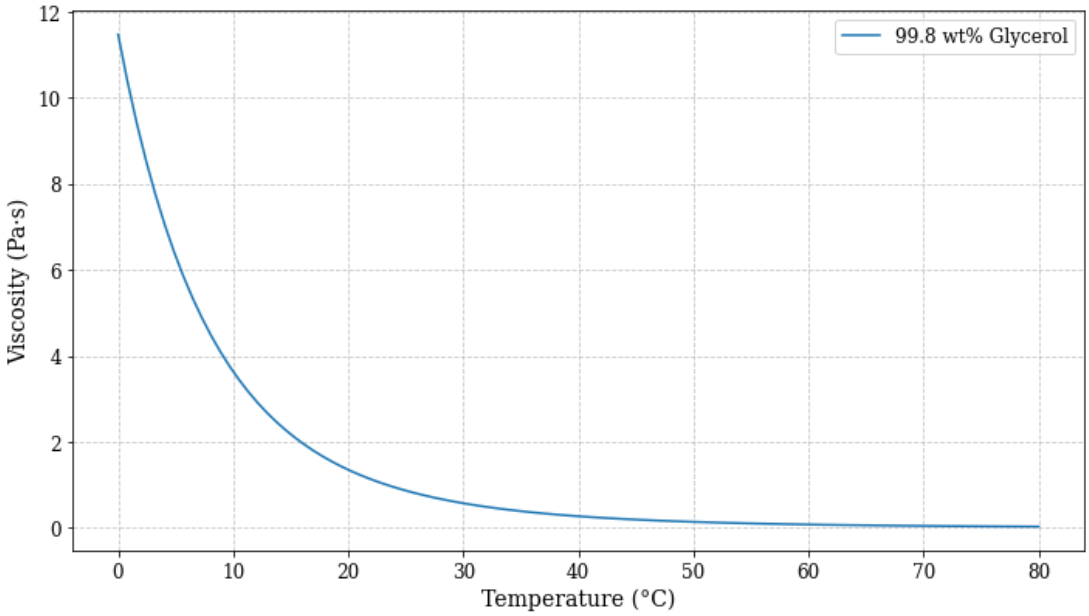


Fig. 4.1. Temperature Viscosity Curve for 99.8 wt.% Glycerol

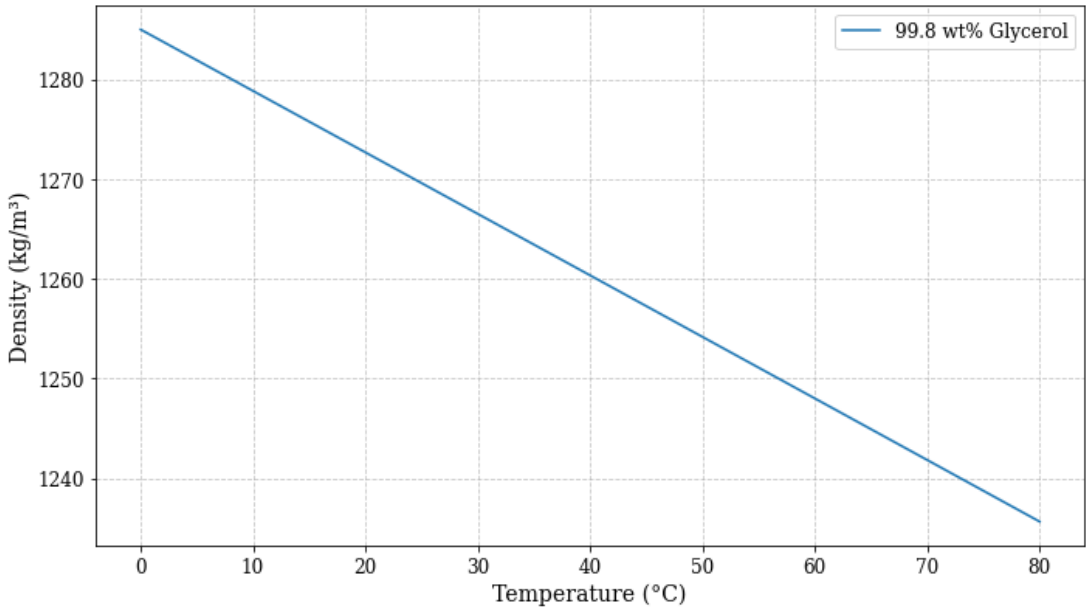


Fig. 4.2. Temperature Density Curve for 99.8 wt.% Glycerol

4.2.2 Test Parameters

Table 4.1
Test Parameters for 99.8 wt.% Glycerol Mixing Experiments

Glycerol Mass Fxn. [–]	**Temperature** [°C]	**Viscosity** [Pa s]	**Velocity** [$m\,s^{-1}$]	**Reynolds Number** [–]
0.998	10	3.69	0.002	0.02
			0.005	0.04
			0.010	0.08
			0.020	0.16
			0.040	0.31
	20	1.36	0.002	0.04
			0.005	0.11
			0.010	0.21
			0.020	0.42
			0.040	0.85
	35	0.39	0.002	0.15
			0.005	0.37
			0.010	0.73
			0.020	1.47
			0.040	2.94
	50	0.14	0.002	0.42
			0.005	1.04
			0.010	2.08
			0.020	4.17
			0.040	8.33

The high viscosity of the glycerol serves to enable the very low Reynolds number seen in these experiments. A series of repeated test steps were set up to maintain a level of consistency between tests conducted on static mixer inserts - these testing parameters are in Table 4.1. Temperature were conducted at four different intervals dictated by the thermal capacity of the heater chiller unit; as discussed prior, changing the temperature of the glycerol has a dramatic effect on the fluid viscosity. The data tables and plots for these changes can be found in Section 2.2.1. For each temperature range a series of flow rates were repeated by setting pump motor frequencies. All of these parameters are programmed in to the DASYLab™ software control program and are automatically stepped through in the program logic and remote controlled.

4.2.3 Tested Static Mixer Geometries

4.2.3.1 SMX™

The SMX™ mixer is one of the earliest example of static mixers and has stayed in operation for the decades since its release. It is manufactured by many parties with subtly different parameters but largely has a similar structure. The insert consist of a series of a total of eight baffles situated at 45°to the flow and 90° to each other effectively segmenting alternating parallel lines of the flow in opposite directions. Each repeat consists of three rows of these baffles with a 11.5 mm spacing but each baffle is cut at the extents of the 23 mm long insert. The insert is a tessellating square (is also 23 mm) with each subsequent insert being installed at 90° to the one before it. This results in the baffles of the next insert instead dissecting the flow first vertically then horizontally and so on with each repeating insert.

The tested static mixer was specified for the 23 mm inner diameter (ID) tube and had an external diameter of 22.8 mm to allow enough clearance to fit in the tube whilst limiting any gap to the wall that could allow any significant fluid bypass. A technical figure of the insert from the side, top and orthogonally can be seen in Figure 4.3.

For the tests conducted in this research the SMX™ is tested every two inserts. As these inserts are installed at 90° to one another, the third insert is then installed in the same orientation as the first. This makes it sensible for one 'repeat' for testing to consist of two SMX™ inserts. This results in tested lengths for this insert being steps of 46 mm up to the maximum tube size of 300 mm - this makes the maximum length tested 276 mm.

4.2.3.2 SMX™ plus

The SMX™ plus is a generation improvement of the SMX™ that is identical save for thinning the width of the baffles. Instead of the baffles being wide enough to reach the neighbouring baffle, they are 66% of their original width from the SMX™ and there

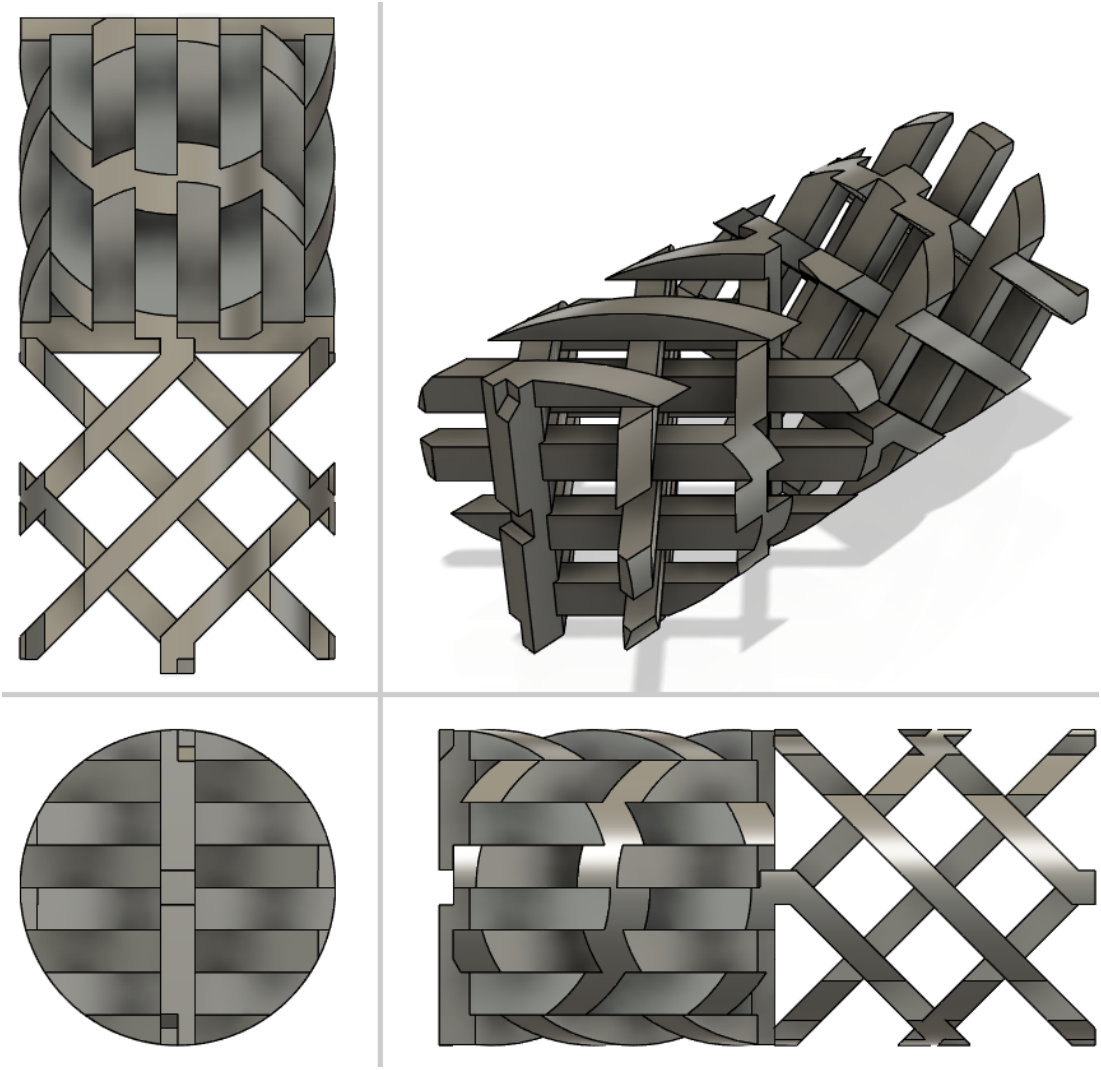


Fig. 4.3. Technical Drawing of SMX™ Static Mixer Insert

are only 6 total baffles per width as opposed to the 8 in the original SMX™. This change leaves a free flowing path for the fluid between baffles without deflection. The goal of this change is to have an insert with lower pressure drop characteristics. A technical figure of the insert from the side, top and orthogonally can be seen in Figure 4.4.

In an identical manner to the SMX™ insert, the SMX™ plus is also tested in 46 mm intervals up to the maximum length of 276 mm.

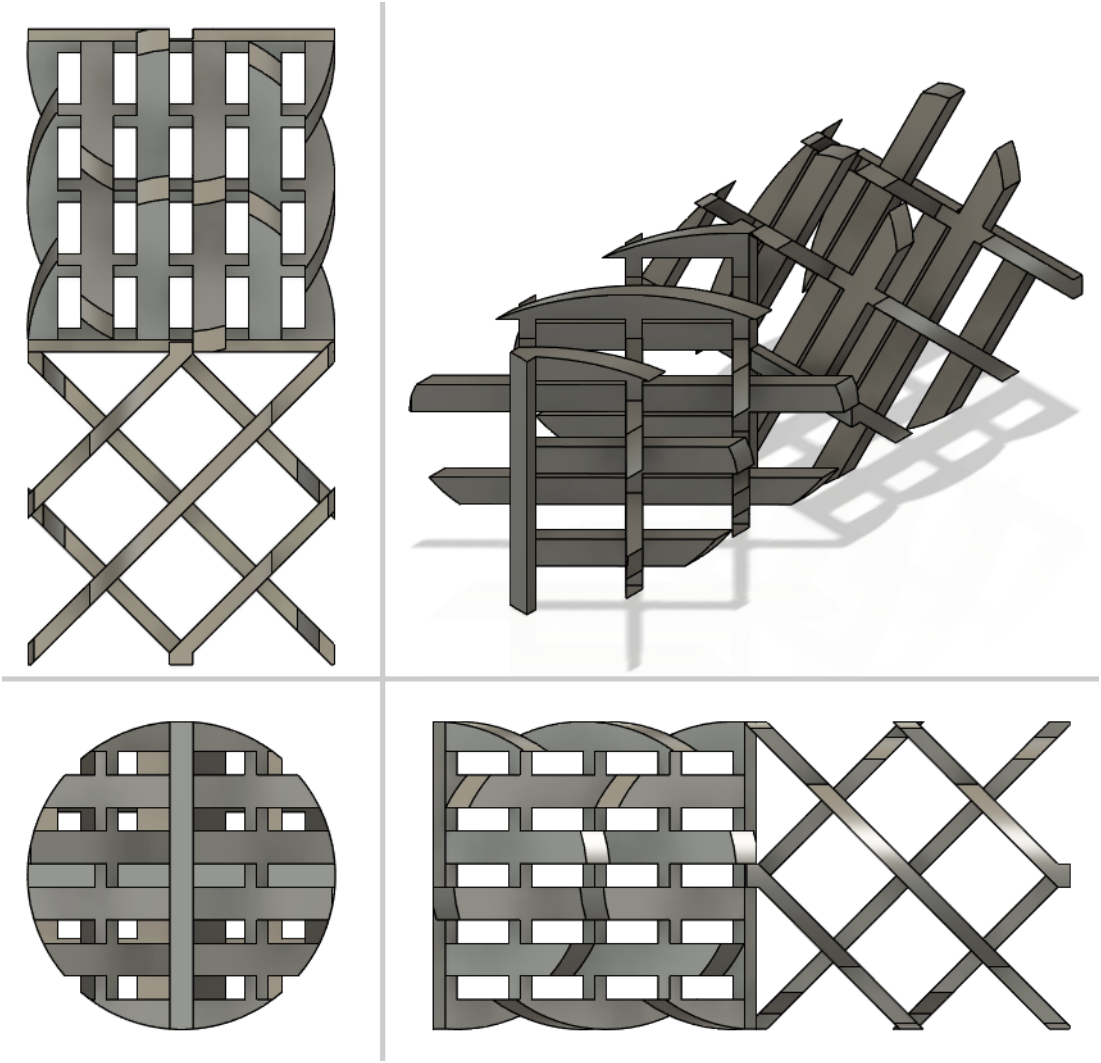


Fig. 4.4. Technical Drawing of SMX™ plus Static Mixer Insert

4.2.3.3 CALGAVIN Static Mixer

This mixer is a first-generation design proposed by CALGAVIN LTD. The premise of the currently undisclosed insert design is to funnel the flow into holes sitting on opposite edges of the leading face of the insert that are internally channelled to shift each incoming flow segment to a position 90° around the pipe looking in the direction of the flow. The next insert does the same but each new leading face hole captures half of the flow from two different holes on the trailing face of the preceding insert. The premise of this design was to prevent remixing of already mixed parts of the flow and

instead continually stretch and blend segments of the flow that have not come into contact yet, thereby providing optimal mixing without wasted energy.

The inserts longitudinal extents overlap meaning that though each insert is 48 mm long they tessellate at 32 mm intervals without any rotation between connecting inserts. The CALGAVIN Static Mixer is tested at each 32 mm repeating interval up to a maximum of 320 mm.

Due to commercial sensitivity, a visual of the insert geometry is not shown here. The design remains confidential and under development by CALGAVIN LTD.

4.3 | Results and Discussion

4.3.1 Pressure Drop

Pressure drop is one of the crucial factors in the static mixer design. The mixer redirects the flow and, in doing so, dissipates energy which is seen as an increased pressure loss compared to having a bare empty tube. The rest of this section contains the experimentally measured pressure drops for each of the tested static mixer inserts for all of its tested lengths and for each Reynolds number flow condition tested. From there each pressure drop was converted to a Fanning friction factor for use in the comparison between inserts. Fanning friction factor is calculated from Equation 2.31.

In the following figures, the friction factor is normalised by multiplying it by the insert length and dividing by the maximum tested length of 300 mm. Friction factor is typically a dimensionless unit, but this normalised form separates the data points and allows a proportional comparison of how the pressure drop changes with increasing static mixer length.

Figures 4.5, 4.6 and 4.7 display the Fanning friction factor for the SMX™, SMX™ plus and the CALGAVIN static mixer inserts for each tested length up to 300 mm, respectively.

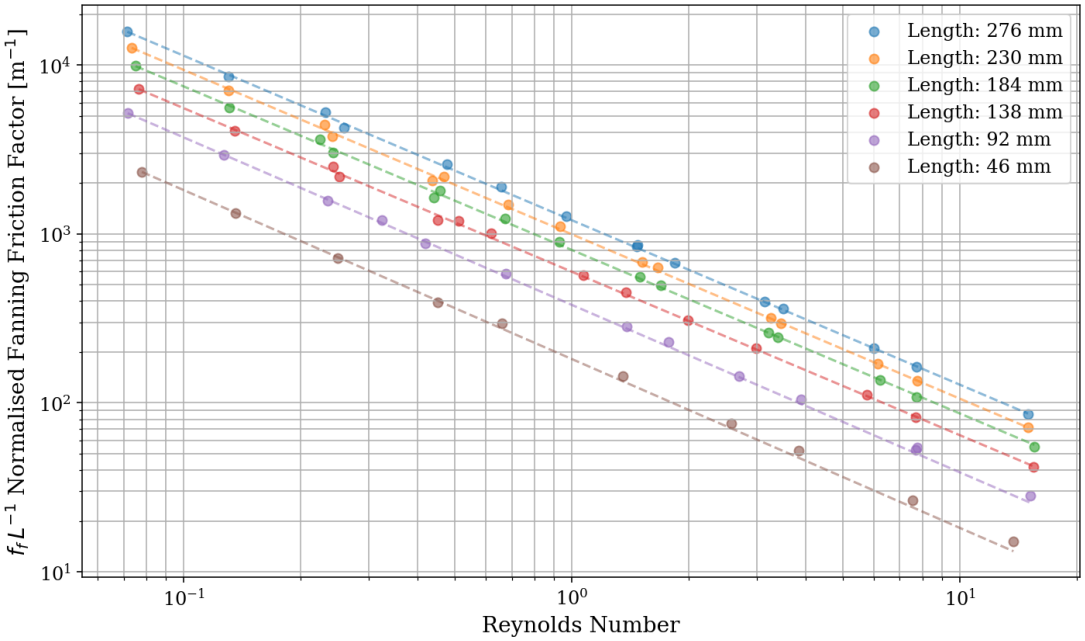


Fig. 4.5. Normalised Friction Factor over Reynolds Number for SMX™ Static Mixer Insert

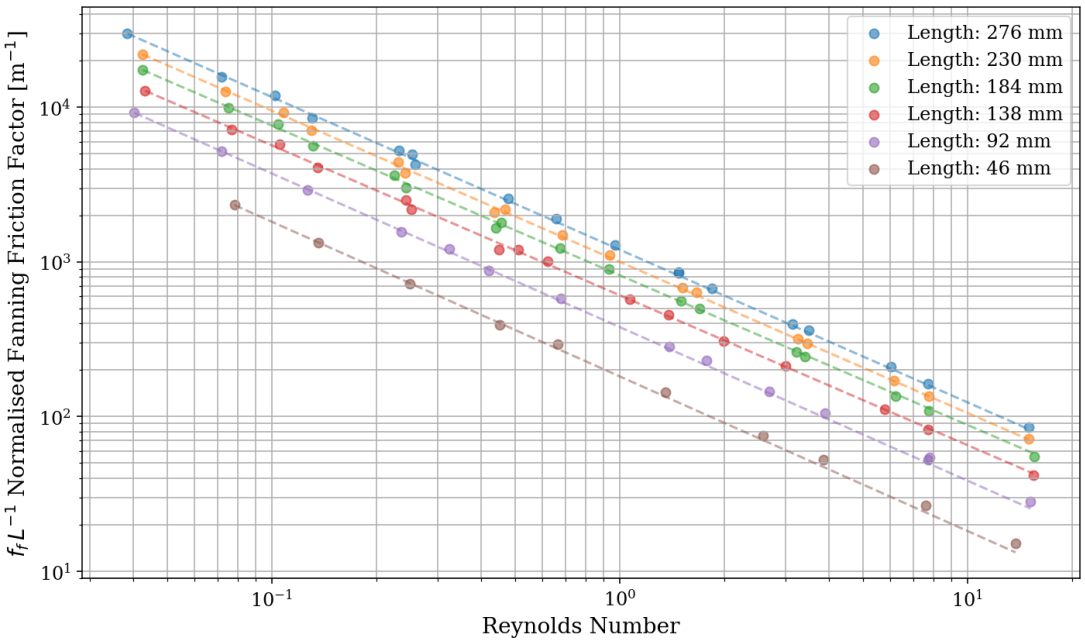


Fig. 4.6. Normalised Friction Factor over Reynolds Number for SMX™ plus Static Mixer Insert

Each dashed line is a power law regression of the individual experimental data points. These trend lines demonstrate that as Reynolds number increases, the friction

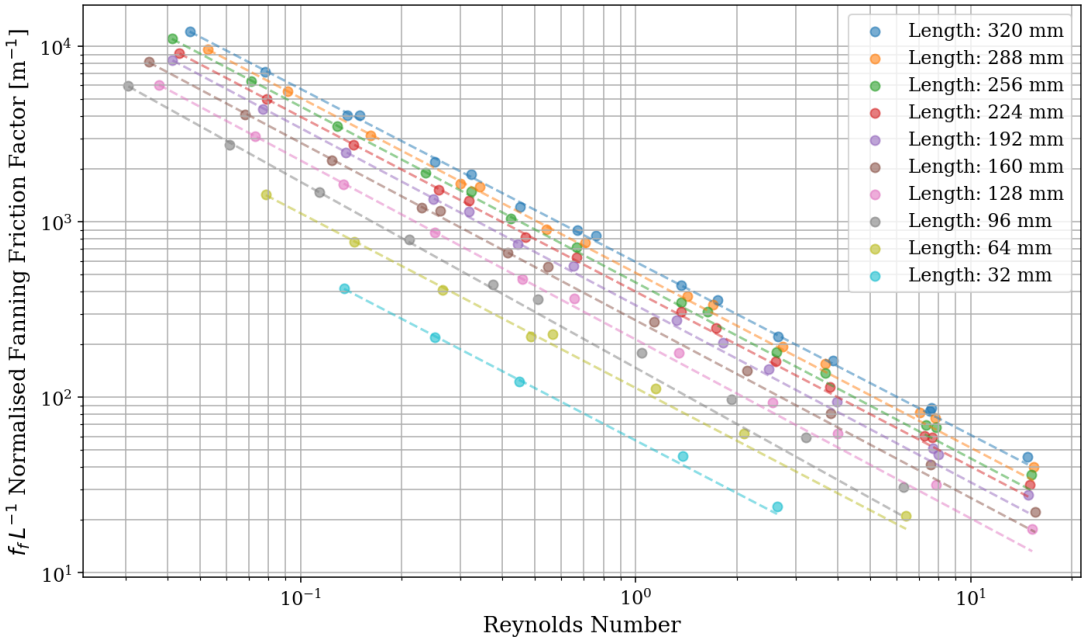


Fig. 4.7. Normalised Friction Factor over Reynolds Number for CALGAVIN Static Mixer Insert

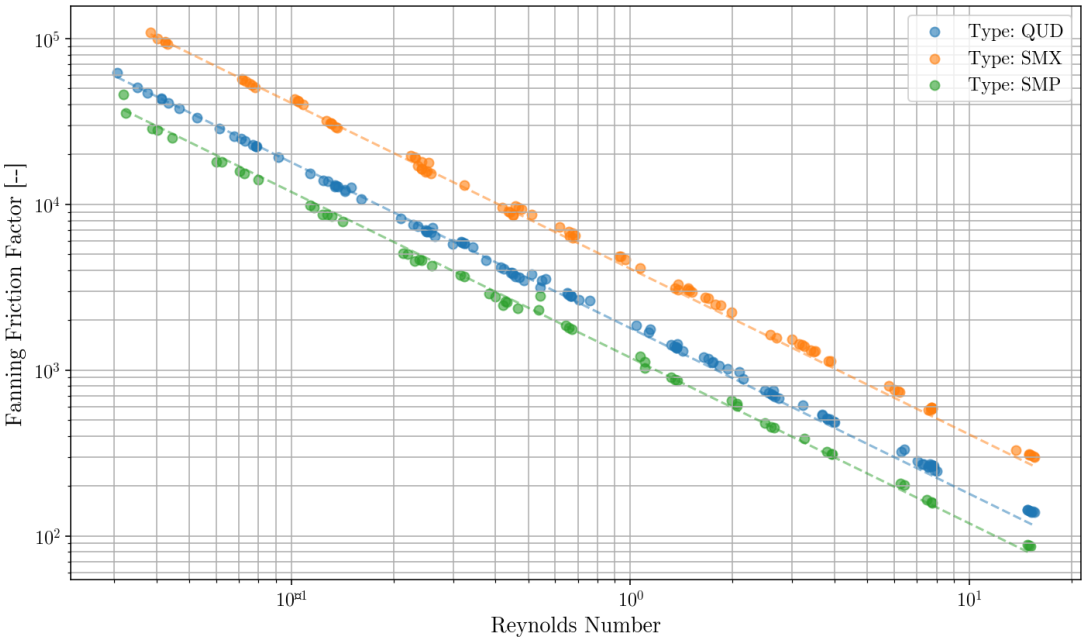


Fig. 4.8. Friction Factor over Reynolds Number for the High Shear Static Mixer Designs: SMX™, SMX™ plus and the CALGAVIN Static Mixer

factor decreases in a clearly defined manner that is strongly correlated across all experiments. It is important to note that a decreasing friction factor does not imply

a decreasing pressure drop with increasing Reynolds number; instead, it shows that the pressure drop becomes proportionally less severe with respect to the square of the velocity.

The staggering of the trendlines also demonstrates that with increasing static mixer length, the friction factor increases at a given Reynolds number, corresponding to an increased resistance to flow and therefore greater energy dissipation. However, when the friction factor is no longer normalised and instead calculated as the true Fanning friction factor, all of the data points collapse onto a single curve for each insert. This is shown in Figure 4.8, confirming the consistency of the measurements across velocity and, more critically, across the temperature range—thus demonstrating the accuracy of the pipe rheometer and fluid property model discussed in Section 2.2.1.

Additionally, the pressure drop of the empty pipe before the static mixer was analytically calculated and subtracted from the measured pressure drop to ensure that only the pressure loss induced by the static mixer itself is considered in the results presented.

The use of Fanning friction factor instead of the more also used K_p loss coefficient is justified firstly, due to the the internal convention adopted by CALGAVIN LTD, the sponsor company. It is also more suitable for inclusion in conventional pipe system design equations, making it more industrially relevant for modelling pressure drop over multiple static mixer elements or scaled-up processes. In this context, friction factor offers a more physically representative and transferable dimensionless model of the impact of static mixer design on system pressure loss.

Although it is well known that laminar friction factor follows an inverse relationship with Reynolds number ($f = \frac{16}{Re}$), the trendlines presented here were intensionally not forced to this slope. A central aim of this work is to validate the capability and accuracy of the novel test rig. If the experimental results naturally produce a power law exponent close to -1, in line with the analytical model, it supports the rig's performance and demonstrates the accuracy of the measurement systems.

Table 4.2
Flow Resistance Coefficients and Exponents for Different Static Mixers

Static Mixer	Flow Resistance Coefficient (A)	Exponent (B)
CALGAVIN Static Mixer	1800.5	-0.9903
SMX™	4263.4	-0.9777
SMX™ plus	1145.5	-0.9873

With reference to Table 4.2, the relationship between the Fanning friction factor (f_f) and the Reynolds number (Re) for each type of static mixer is given by:

$$f_f = A \cdot Re^B$$

Where A is the Flow Resistance Coefficient, a constant representing the magnitude of the pressure drop induced by the mixer, and B is the exponent describing how the friction factor changes with Reynolds number.

The exponent is very close to -1 for all tested inserts, which is likely its true value. For laminar flow in circular tubes, the theoretical relationship is:

$$f_f = \frac{16}{Re} \tag{4.1}$$

This suggests that the experimental data closely match the analytical model, again validating the rig's ability to accurately measure pressure drop across a wide range of Reynolds numbers.

For each mixer the power law model fit when holding the exponent to -1 is as follows:

- CALGAVIN Static Mixer:

$$f_f = 112.5\frac{16}{Re}$$

- SMX™:

$$f_f = 266.5\frac{16}{Re}$$

- SMX™ plus:

$$f_f = 71.6\frac{16}{Re}$$

As expected, the ratios of the multipliers between each static mixer quantify the proportional increase in energy loss compared to an empty pipe.

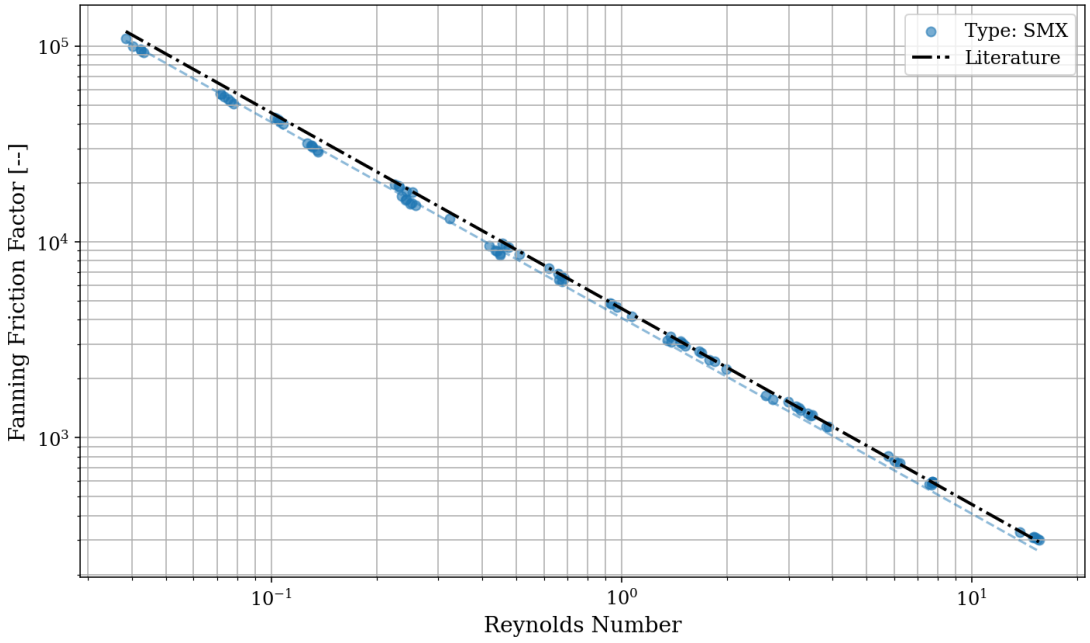


Fig. 4.9. Experimental Fanning friction factor for the SMX™ insert compared to literature. (Thakur et al., 2003)

Figure 4.9 shows the experimental Fanning friction factor data for the SMX™, plotted against the prediction based on a literature value of $Z = 1140$ (Thakur et al., 2003). The parameter Z is a dimensionless geometry-dependent friction factor ratio defined as:

$$Z = \frac{f_{\text{Darcy, SM}}}{f_{\text{Darcy, EM}}}$$

where $f_{\text{Darcy, SM}}$ is the Darcy friction factor for the insert configuration, and $f_{\text{Darcy, EM}} = 16/Re$ is the corresponding value for an empty (smooth) tube in laminar flow. For laminar conditions, the Darcy friction factor for the insert may therefore be written as:

$$f_{\text{Darcy}} = \frac{16Z}{Re}$$

Converting this to the Fanning friction factor using the relationship $f_{\text{Fanning}} = f_{\text{Darcy}}/4$ gives:

$$f = \frac{4Z}{Re}$$

Substituting the literature value of $Z = 1140$ results in the expression:

$$f = \frac{4560}{Re} = 285.0\left(\frac{16}{Re}\right)$$

The experimental data gathered for the SMX™ as depicted above gives the following mirrored expression:

$$f = \frac{4264}{Re} = 266.5\left(\frac{16}{Re}\right)$$

This fitted curve lies approximately 6.49% below the prediction, indicating excellent agreement with literature data. The small discrepancy may be attributed to manufacturing tolerances/differences, installation differences, or measurement uncertainty but overall, the result validates the experimental method and supports the suitability of the literature-based Z value in representing the SMX™ geometry under laminar flow.

4.3.2 PLIF Results

Concurrent to the pressure drop measurements, mixing experiments were conducted as outlined in Section 3.2.2.1. Each static mixer listed in Section 4.2.3 was tested at the lengths specified. This generated a large series of PLIF images: 100 images per Reynolds number for the 20 different Reynolds numbers at length of each tested insert. Figures 4.10, 4.11 and 4.12 contain all the images taken for the testing in this Chapter, each of which is an average of 100 images. The images at this scale are too small to see in detail but are included to show the extensiveness of the testing capable with the test rig given minimal test fluid wastage. As the Chapter progresses, relevant images will be scaled up to show greater detail where needed. A key note from these images is despite each of them being averages of 100 images over 3 seconds, each image is sharp and contains no blurring. This proves that the images, and therefore outlet flow of each static mixer was very stable - a factor expected in this very laminar flow. To also demonstrate this clarity, Figure 4.13 shows a selection of twelve images from a representative test of four units of the CALGAVIN static mixer at a Reynolds number of 7.57. Each images was captured 0.25 seconds after the last over a total of 3 seconds and show no discernable discrepancies between each other.

Please note that for viewability, all the PLIF images here and throughout this work have been brightened. To do this, the pixel brightness value for true white (4096) is divided by the 99th percentile brightness value from each image. Then the whole field is multiplied by the this weighting; this brightens the image but leaves the proportional nature of the brightness to dye concentration. These means that the images are still representative of the dye concentrations within themselves but not comparable to one another. Any calculations completed on the image were done in their raw form.

For Figures 4.14, 4.15,4.16 and 4.17 the Reynolds number is an emergent property of input temperature of a mass flow rate conditions. This condition set point is identical across all images but subtle differences in measured glycerol mass fraction, ambient temperature and flow back pressure result in different calculated Reynolds numbers.

The average Reynolds number and the absolute ± range is listed in the caption for each Figure. Figure 4.14 shows the resultant PLIF mixing image for each tested length for the SMX™ static mixer up to the maximum that would fit in the mixing test section. Figure 4.15 does the same for the SMX™ plus static mixer and Figures 4.16 and 4.17 for the CALGAVIN static mixer.

As a reminder, white on the PLIF image signifies the Rhodamine 6G dye that fluoresces as light from the laser excites the dye molecules. A brighter white signifies an area of higher high concentration. Pure black is a pure area of the bulk main flow containing no dye concentration with the middling greys signifying areas where the bulk and injection flows have been mixed.

Following all the Figures 4.14, 4.15, 4.16 and 4.17 it is clear that increasing the length of the mixer directly translates to a more mixed outlet flow. The initial short mixer lengths have stark areas of black and white with limited middling greys and large, thick striations. As the mixer length increases, the striations become thinner and the image becomes more clearly even.

The comparative performance between static mixers can be subjectively gathered by viewing the similar lengths of the different static mixers against each other. It appears that the SMX™ and the SMX™ plus have a very similar mixing process and develop outlet mixing patterns with a lot of similarity, they also appear to mix to a very similar level at equivalent lengths. The CALGAVIN static mixer has a very different outlet mixing pattern and subjectively appears to achieve a marginally less mixed state for each mixer length. To gather a quantitative measure of this however, a numerical analysis of the PLIF images needs to be completed and is done using two different methods seen in Sections 4.3.4 and 4.3.3.

An observation of note during these experiments was the effect of ambient cooling or heating on the fluid during experiments. The test section itself was insulated but at the temperature extremes and very low minimum flow rates show clear natural convection in the flow field - shown in Figure 4.18. This data is included due to the fact

that this phenomenon would also be present in an industrial example with similar flow conditions.

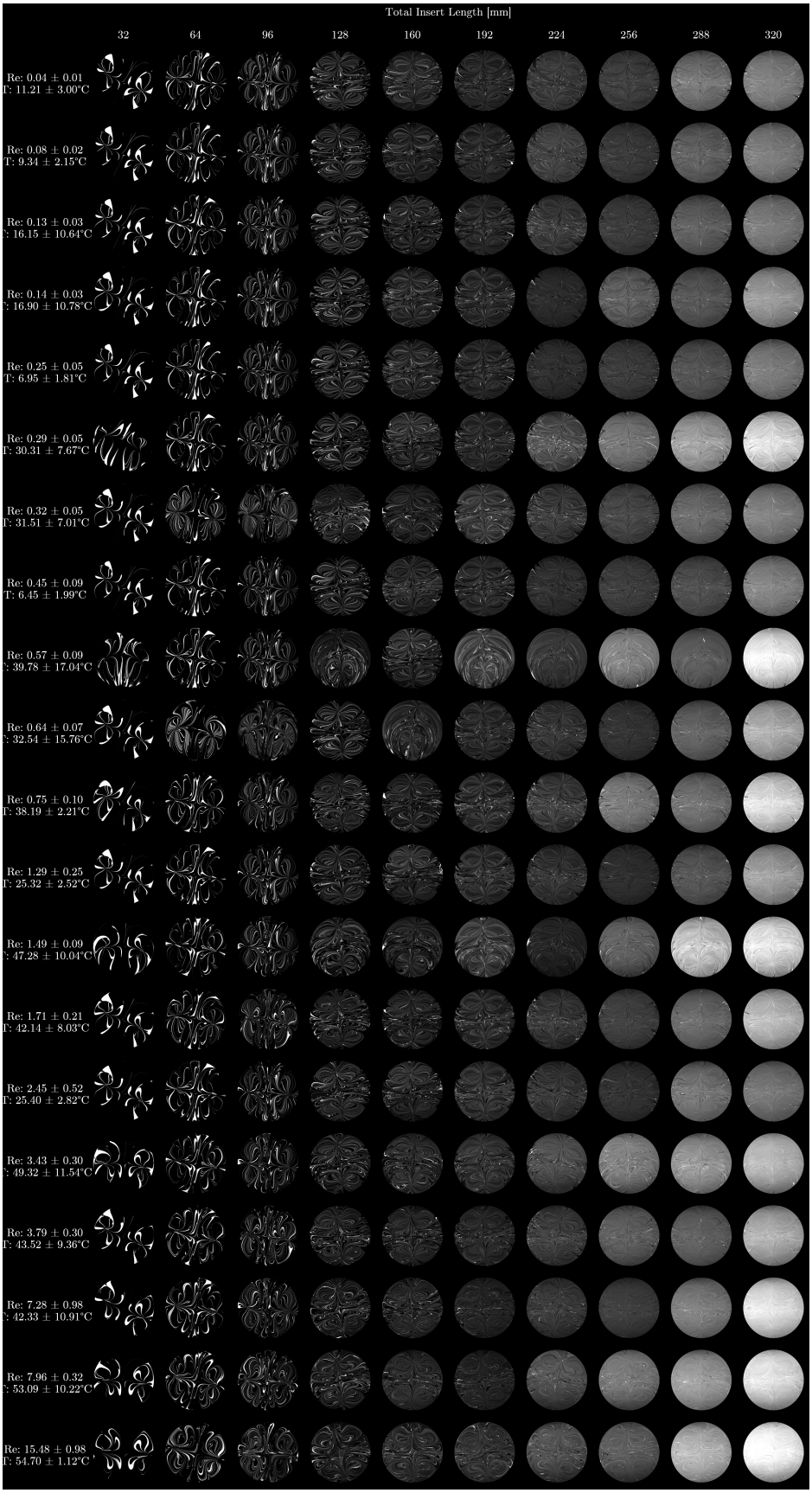


Fig. 4.10. All Captured CALGAVIN Static Mixer PLIF Images for 99.8 wt .% Glycerol Solution with Each being the Average of 100 Images

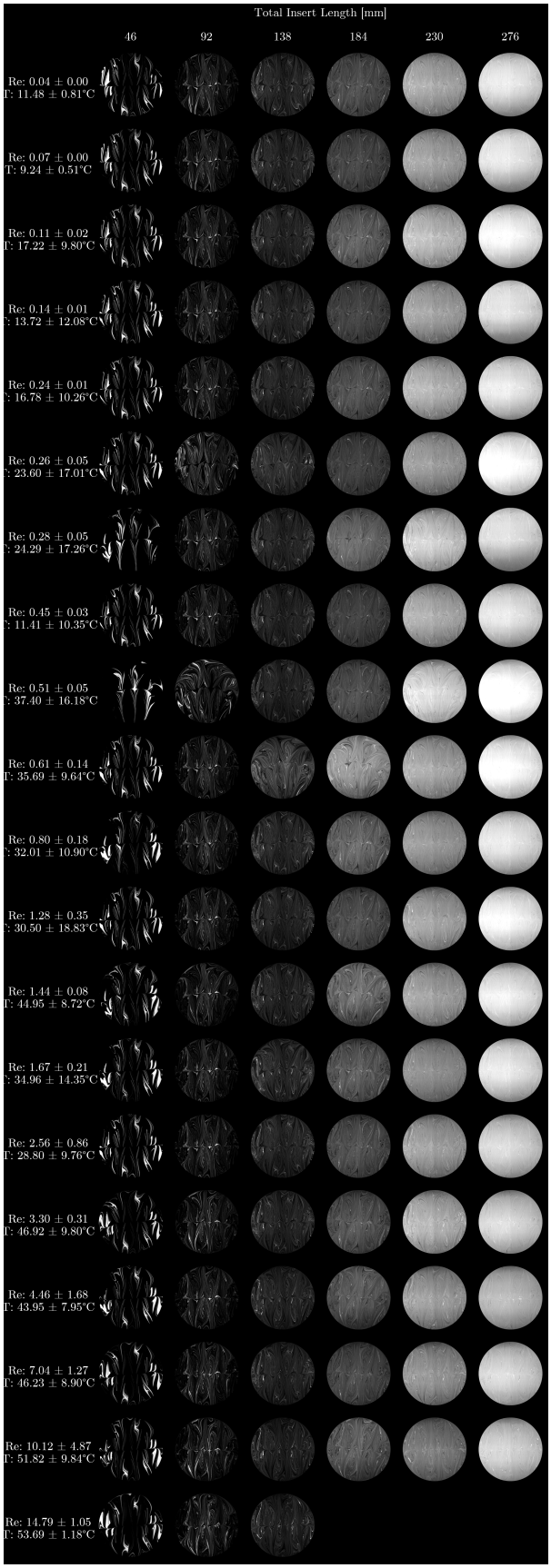


Fig. 4.11. All Captured Sulzer ™ Static Mixer PLIF Images for 99.8 wt .% Glycerol Solution with Each being the Average of 100 images

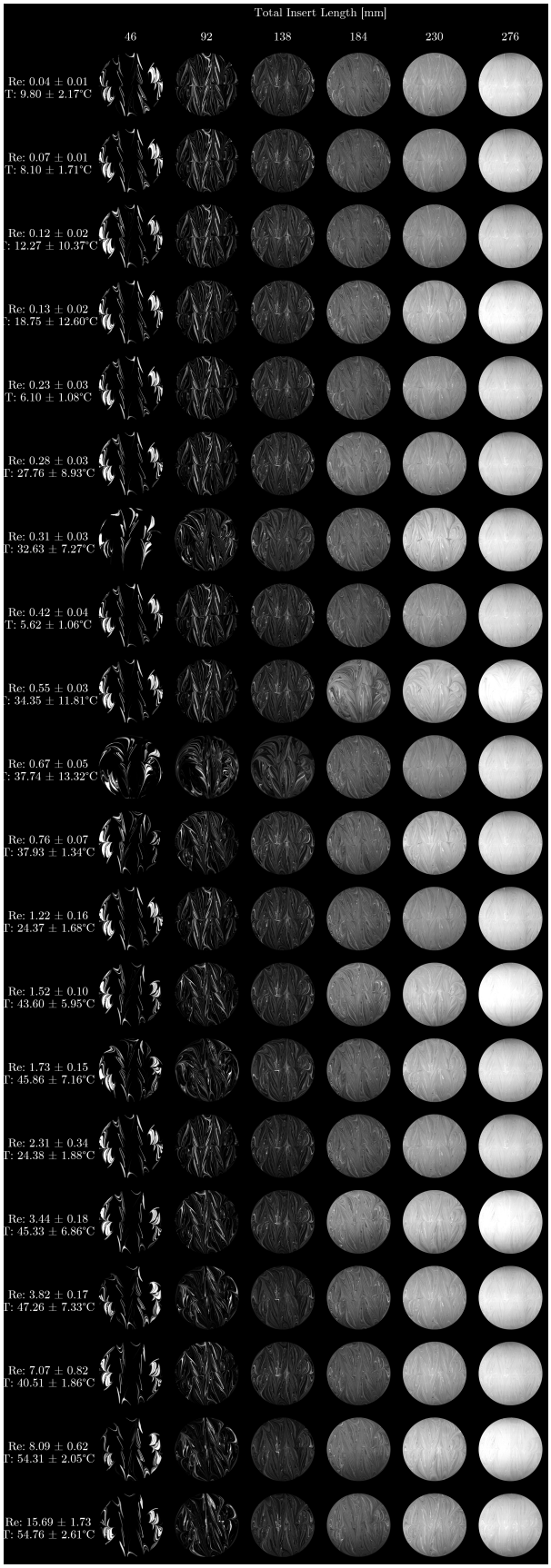


Fig. 4.12. All Captured Sulzer ™ plus Static Mixer PLIF Images for 99.8 wt .% Glycerol Solution with Each being the Average of 100 images

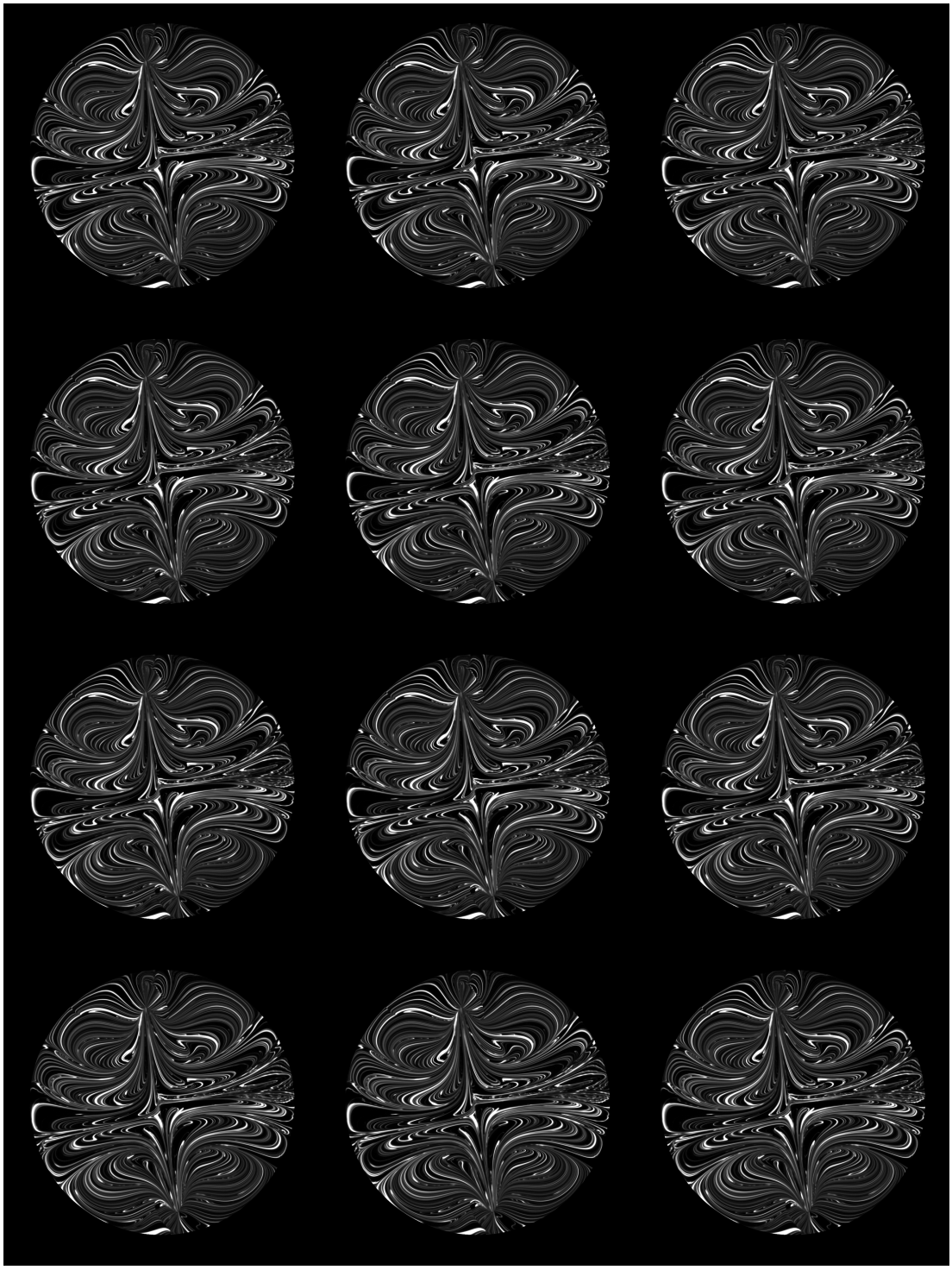


Fig. 4.13. Sequential PLIF images 0.25 seconds after each other for four units of a CALGAVIN Static Mixer at a Reynolds number of 7.57

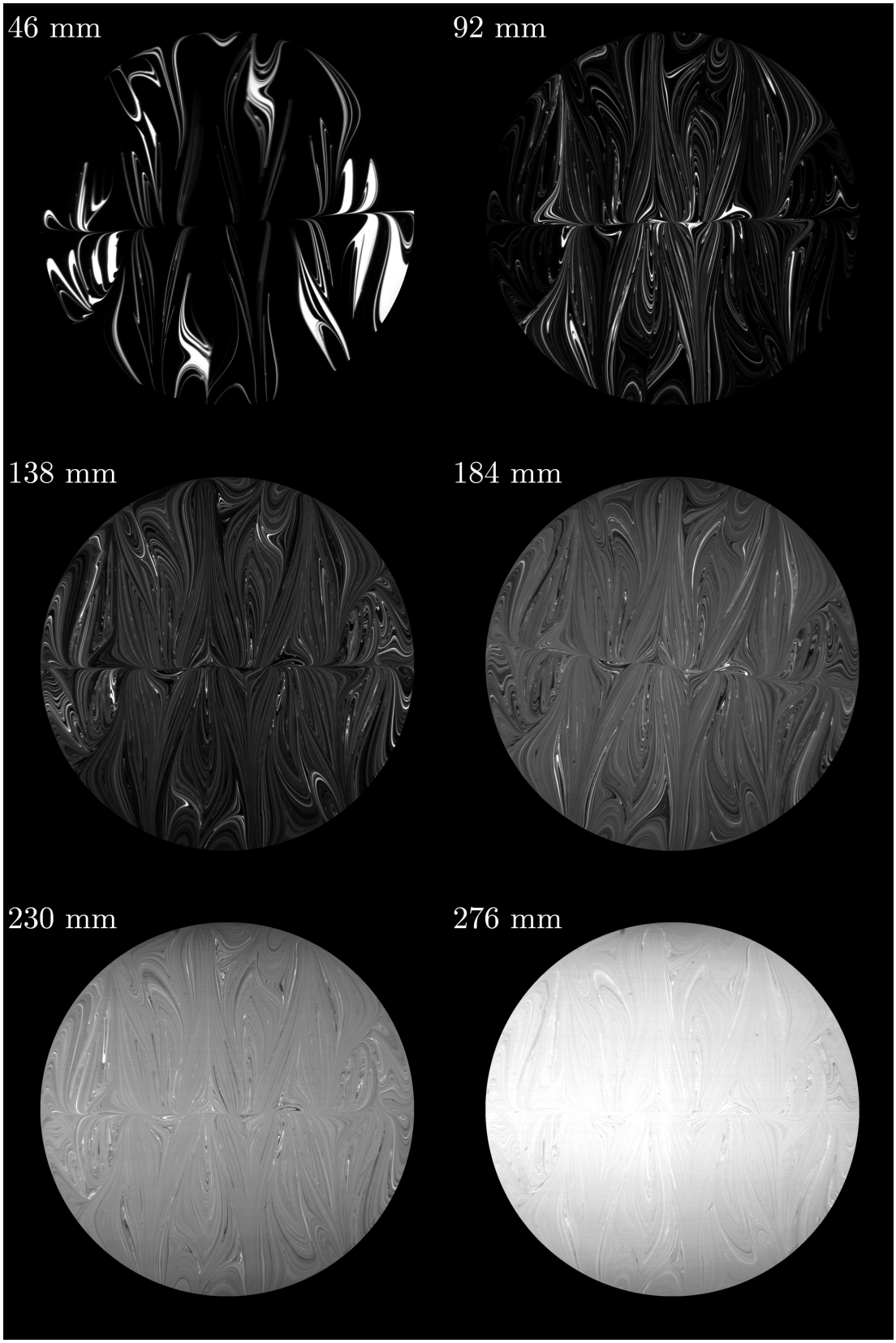


Fig. 4.14. PLIF Mixing images for the tested lengths of the SMX™ Static Mixer at a Reynolds number of 3.74 ± 3.95

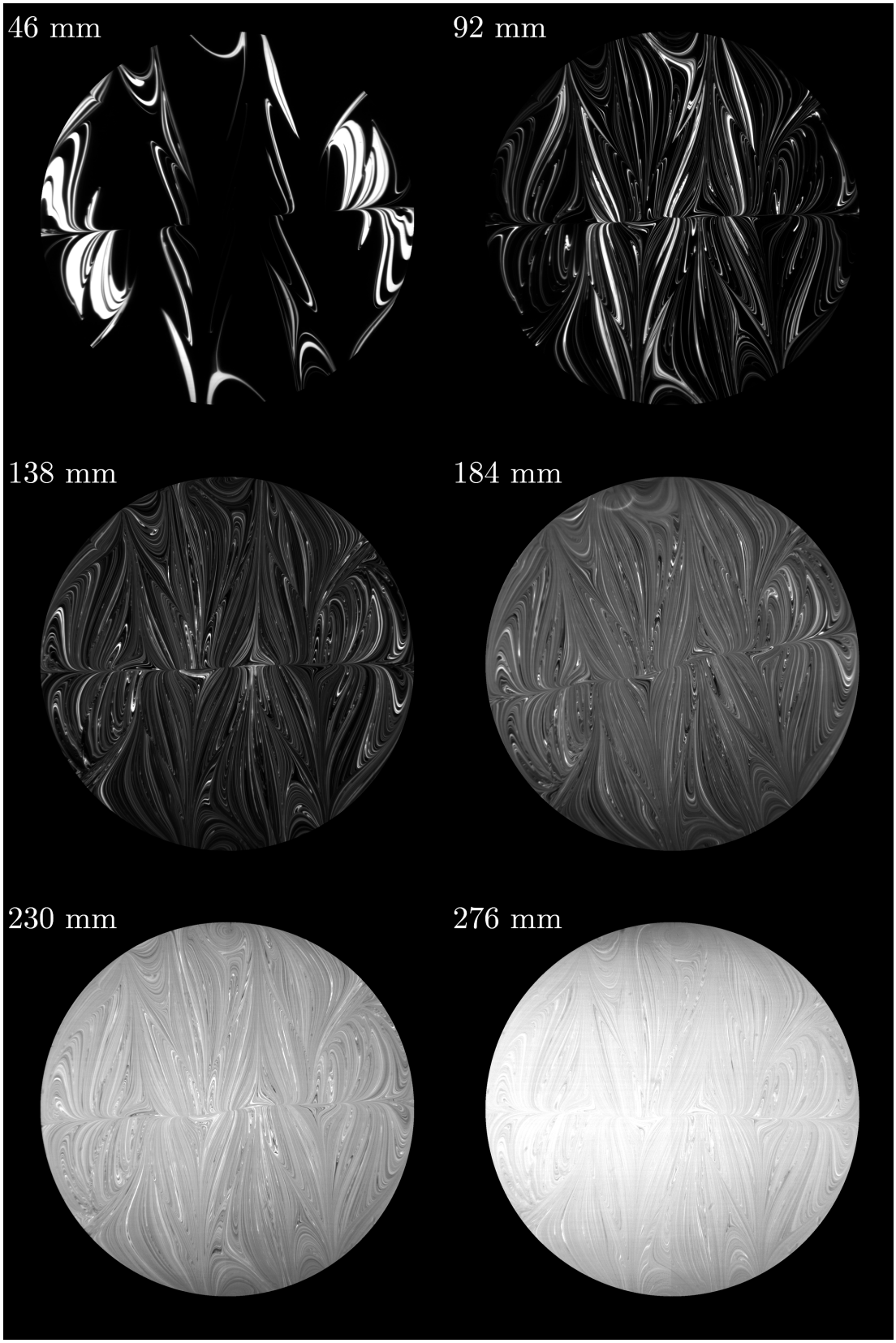


Fig. 4.15. PLIF Mixing images for the tested lengths of the SMX™ plus Static Mixer at a Reynolds number of 4.85 ± 2.92

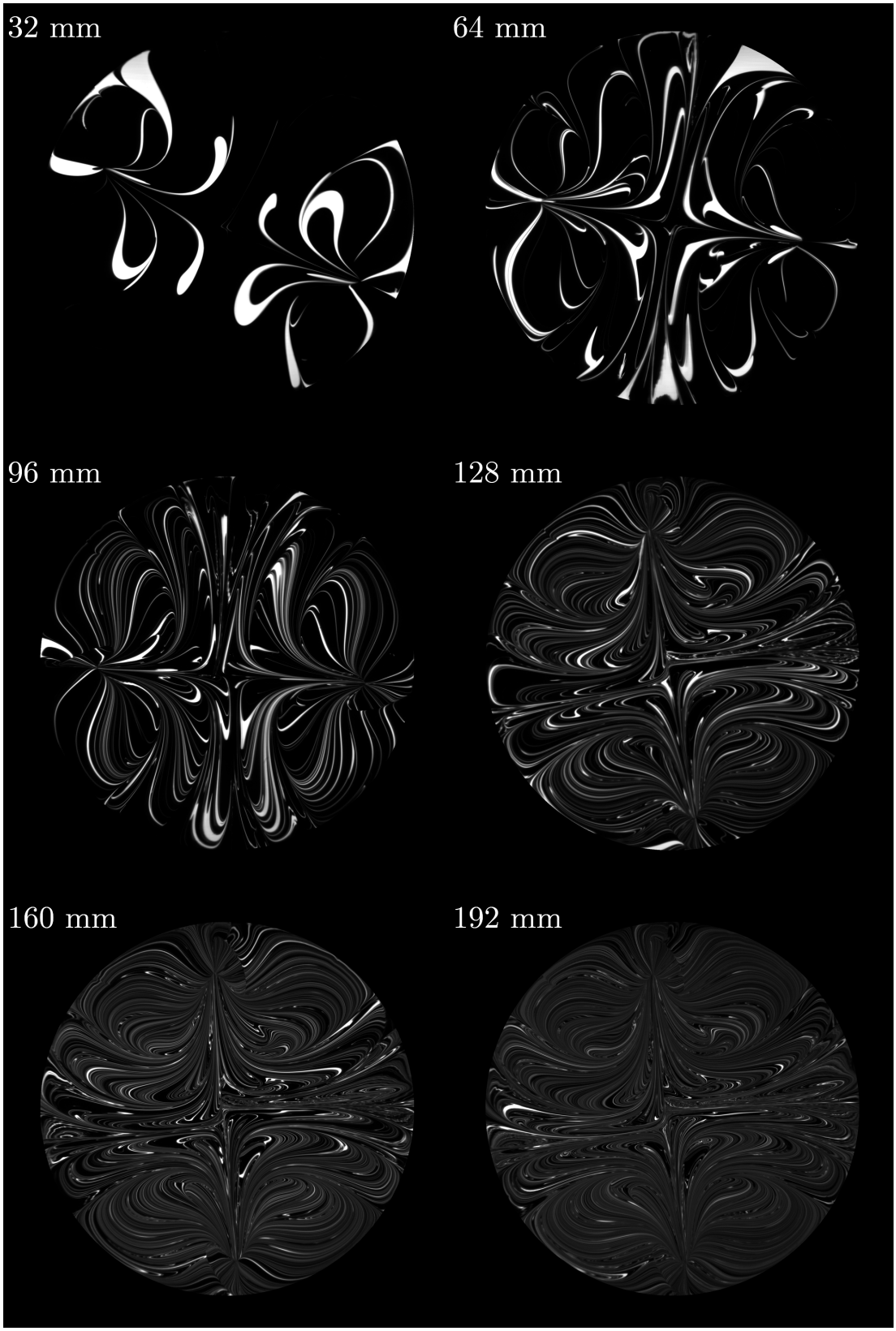


Fig. 4.16. PLIF Mixing images for the tested lengths of the CALGAVIN Static Mixer at a Reynolds number of 6.44 ± 4.51 - Part A

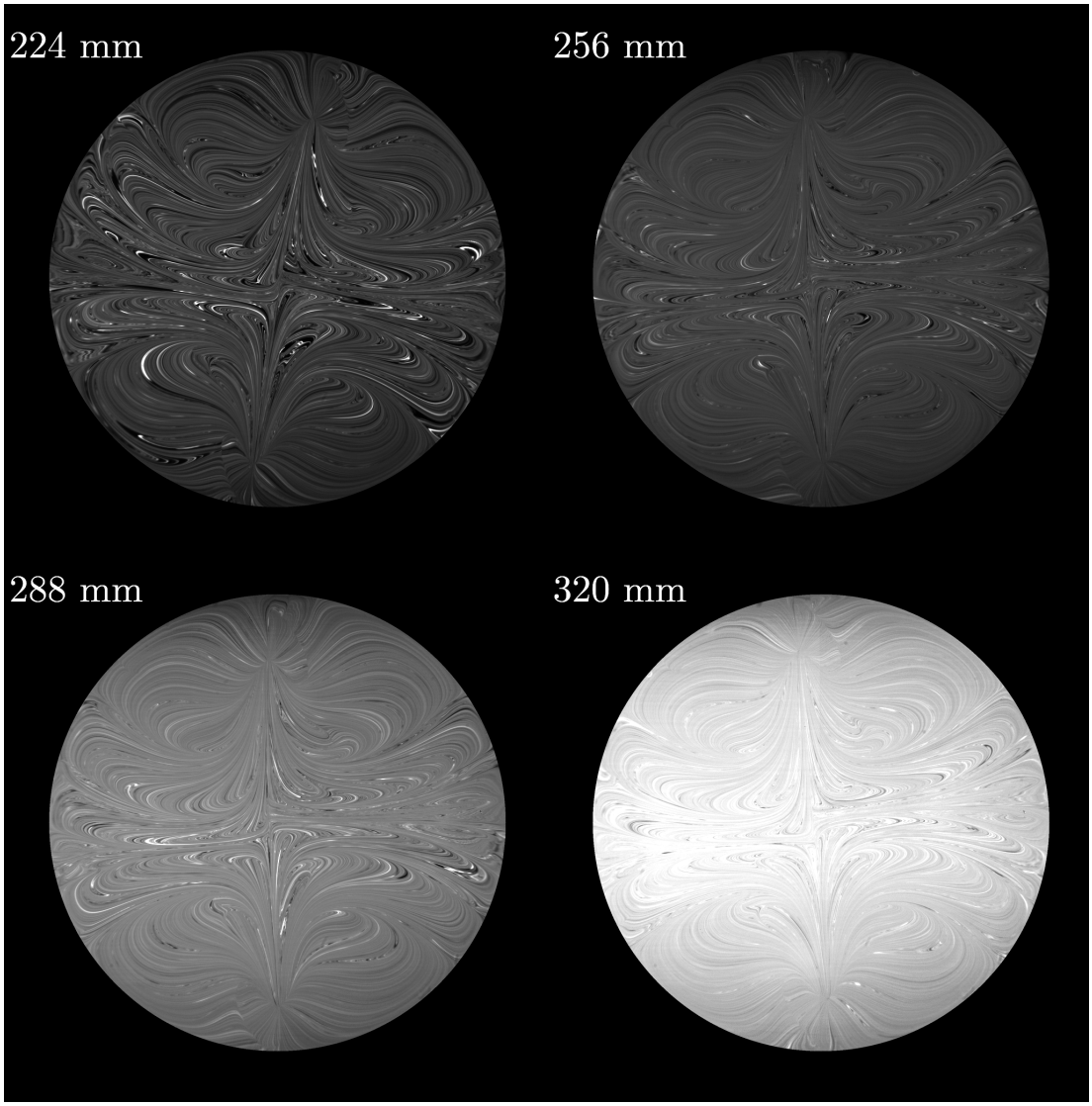


Fig. 4.17. PLIF Mixing images for the tested lengths of the CALGAVIN Static Mixer at a Reynolds number of 6.44 ± 4.51 - Part B

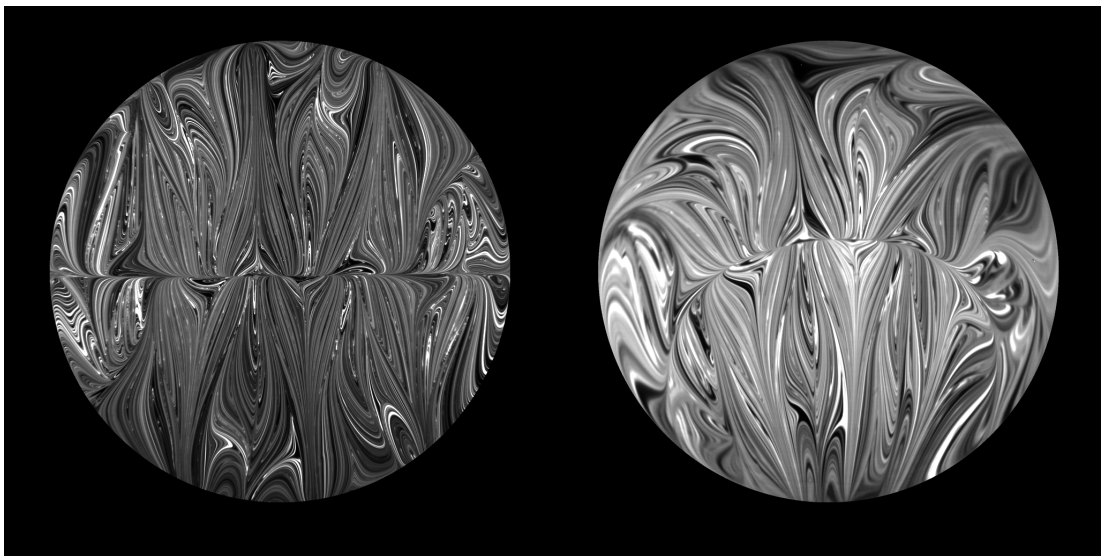


Fig. 4.18. PLIF Imagery at the outlet of a SMX™ at $0.002\,\mathrm{m\,s^{-1}}$ with Fluid Temperature 20 °C (Left) and 50 50 °C (Right)

4.3.3 Coefficient of Variance

Coefficient of Variance (CoV) is the classic form of mixing analysis that described fully in Section 3.2. It works by taking the statistical standard deviation of every pixel value from a captured mixing PLIF image that is within the region of interest and divides this number by the mean of the same pixels. This essentially describes how much variance there is across the image; a value of 0.5 would mathematically denote that 68% of the pixel values are within ±50% of the mean. The equations used in the calculation of CoV are as follows:

$$CoV = \frac{\sigma}{\bar{C}} = \frac{\text{Standard Deviation}}{\text{Mean Concentration}} \tag{4.2}$$

Where the standard deviation is equal to the square root of the variance:

$$\sigma = \sqrt{s^2} = \sqrt{\frac{1}{n-1}\sum_{i=1}^{n}\left(C_i - \bar{C}\right)^2} \tag{4.3}$$

And where the mean concentration is found using the following equation:

$$\bar{C} = \frac{1}{n}\sum_{i=1}^{n} C_i \tag{4.4}$$

To do this analysis on the PLIF images, each of the pixels within the region of interest (ROI) and therefore part of the pipe cross-section are evaluated together.

Figures 4.19, 4.20 and 4.21 show the CoV calculated from the PLIF mixing images for each Reynolds number for each tested length of the SMX™, SMX™ plus and CALGAVIN static mixer up to 300 mm long. Each total insert length has had a linear regression applied to form a trend line through the experimental data.

The relationship between CoV in this flow regime can be gathered from looking at Figures 4.19, 4.20 and 4.21. For each insert tested it is clear that a change in Reynolds

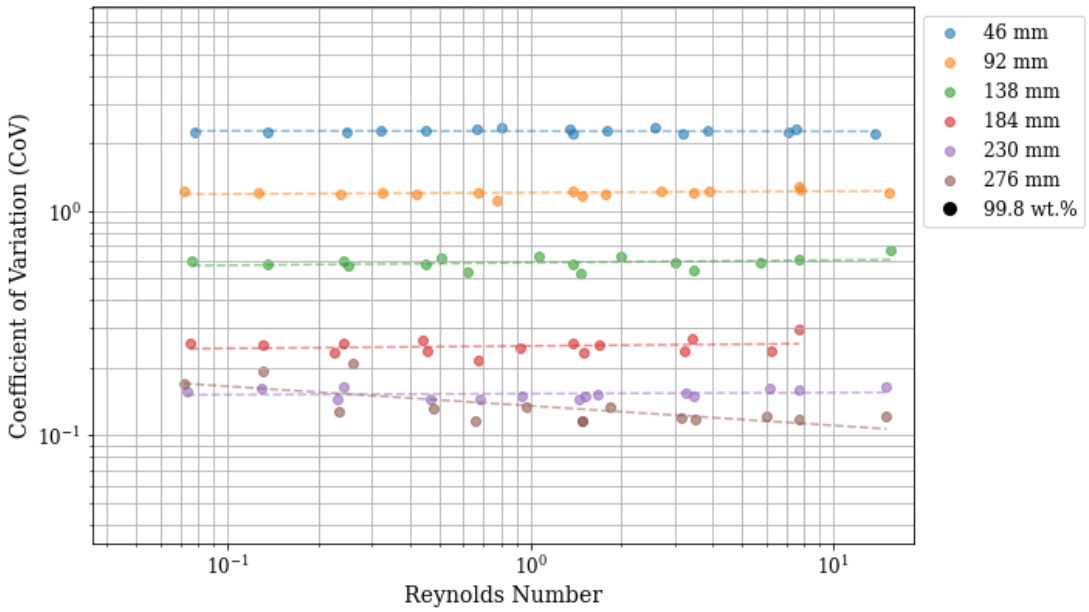


Fig. 4.19. The influence of Reynolds Number on CoV for each tested length of the SMX™ Static Mixer

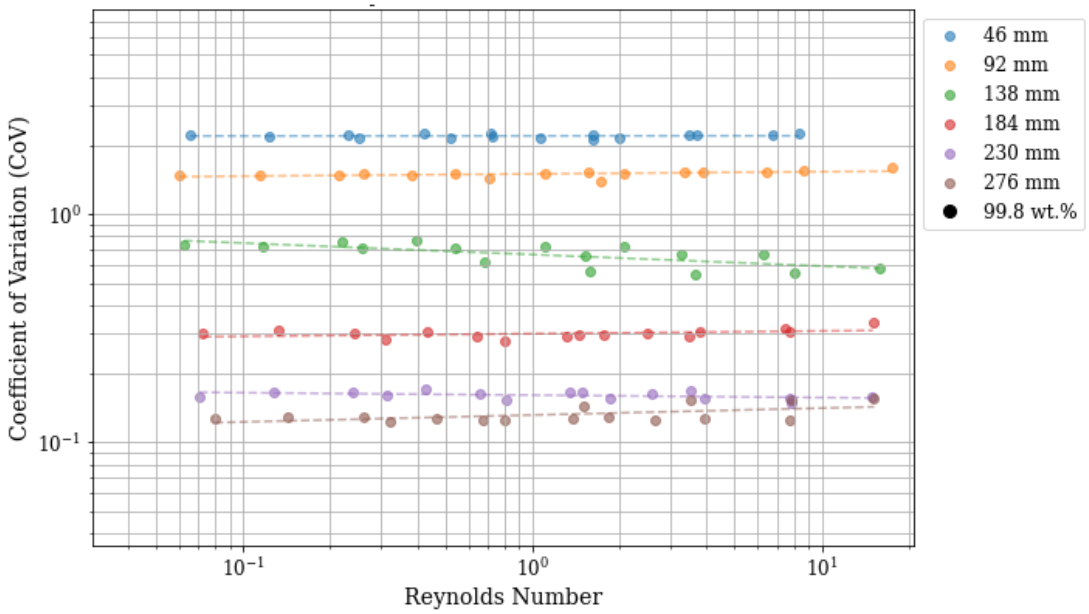


Fig. 4.20. The influence of Reynolds Number on CoV for each tested length of the SMX™ plus Static Mixer

number (achieved by dramatically changing velocity, viscosity and temperature) has no significant effect on the mixing level as assessed by the CoV. This is shown by the

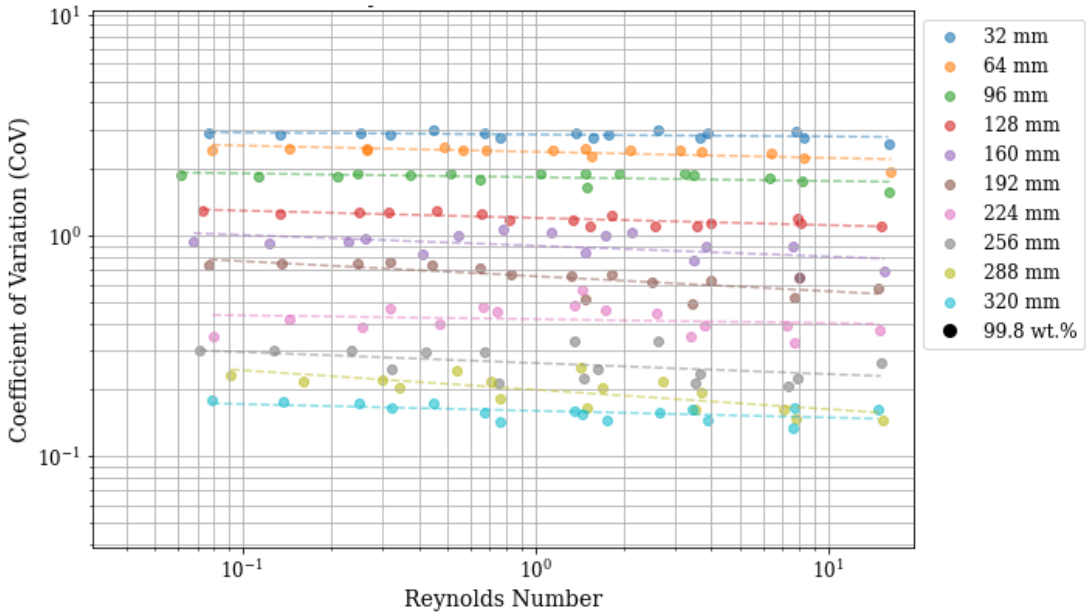


Fig. 4.21. The influence of Reynolds Number on CoV for each tested length of the CALGAVIN Static Mixer

nearly level trend lines created by completing a linear regression on the experimental data viewed on the log-log scale. As with the pressure drop data in Section 4.3.1, the gradients of these trend lines are not forced to any known theoretical value. The expected gradient in this regime is zero, but here the gradient is calculated directly from the experimental results to demonstrate the accuracy of the rig. The fact that the values are so close to zero offers confidence in both the measurement method and the rig's ability to maintain consistency across changes in Reynolds number.

The gradients across all the linear regressions have an absolute maximum of -0.083, 0.098 and -0.0208 for the SMX™, SMX™ plus and CALGAVIN mixer respectively — but as Table **??** shows, have an average of -0.086, 0.012 and 0.0017 and standard deviations of 0.006, 0.0051 and 0.0054. This indicates that if there is an effect on mixing with Reynolds, it is negligible. The Table also contains the constants of the linear regressions for all of the trend lines in Figures 4.19, 4.20 and 4.21 respectively.

These charts also show that upon lengthening the static mixer, the calculated CoV also decreases for all of the static mixers tested. Also of note is the relatively even

spacing of the trend lines for each increase of the insert. This suggests that increasing the length of the insert demonstrates an exponential increase to the mixing. The longest inserts then reach an area of diminishing returns where increasing the length no longer has this effect. This suggests that at this point, the insert is at the highest level of mixing the static mixer can achieve or the highest level of mixing this PLIF system can differentiate.

Although the performance of the CALGAVIN static mixer differs from the other tested designs, a discussion on how its geometry might explain the observed differences in CoV is not included due to the confidential nature of its design.

4.3.4 CG Number

The CG Number is comprehensively discussed in Section 2.3.2.1 but to remind the reader is briefly explained here. Similar to the Areal Fraction Method proposed by Alberini et al. (2014), this method works by binning the frequency of the number of pixels with a range of brightnesses. Since these brightnesses correspond directly to different concentrations within the imaged mixture, calculating the area which has a brightness range closes to the perfectly mixed brightness value can give you an indication of how mixed a fluid is. The CG Number takes it a step further by adding a weighing function to the bin based on a parabolic curve where bins closer to the perfect mixing value have more weight. Normalising these numbers against area, applying the weighting then subtracting them from the total normalised area then gives you the CG Number - the closer to 0, the more of the area of the mixing outlet is equivalent to the perfect mixing value and the more mixed the fluid is. The equation that this number is based up on is as follows:

$$CG_{\text{mix}} = 100 - \sum_{i=0}^{n} \left(\%A_i \cdot B\right), \quad \text{where} \quad B = \begin{cases} C_1 \cdot T_i^2, & \text{if } T_i < P \\ C_2 \cdot (T_i - 100)^2, & \text{if } T_i > P \\ 1, & \text{if } T_i = P \end{cases} \tag{4.5}$$

This equation is best presented in a chart for clarity. Figure 4.22 displays a representative histogram of an image. The X-axis represents bins of the intensity of a pixel in the image as a percentage of the maximum intensity. The Y-axis represents the percentage of pixels that fall into each of these bins. The red dotted line indicates the pixel intensity that corresponds to the perfect mixing value—this represents the perfectly mixed concentration of dye. The green and yellow curves are parabolic functions that provide weightings to the bins. The closer the intensity is to the perfect level, the more impact it has on the mixing number. The weighting curve is split across the perfect mixing line to accommodate cases where the perfect mixing point is not central, such as when unequal quantities of fluid are to be mixed. These functions aim to penalise mixers that achieve good mixing in limited areas of the cross-section while leaving other areas poorly mixed. Points far from the perfect mixing level have negligible impact on the mixing number, while areas closer to the perfect level have increasingly higher importance. The frequency of each bin is multiplied by the corresponding weighting from the curve, and this product is subtracted from 100 to give the CG Number. The closer this number is to zero, the better the mixing. The only way to achieve a perfect mixing number is to have all intensities fall within the perfect mixing bin. The amount subtracted for each bin is shown by the blue line.

The weighted function has advantages over CoV in several key areas. The first and most important is in the case of experimental or industrial error. For example, if compound A of an intended 50:50 mixture of compounds A and B is over-dispensed by 25%, the resultant mixture could still be well mixed, but the mean concentration will have shifted. In the case of the CG Number, the desired mean is fixed, so any change in the distribution of the fluid will cause it to shift across the weighted curve and increase the mixing number. However, with CoV, the change will be minimal and may even cause a decrease if the overall concentration increases, as the ratio of variance to the mean decreases. This example is depicted in Figure 4.23. While monitoring both CoV and the mean could counteract this, doing so introduces two numbers, eliminating the simplicity of the single-number mixing calculation that CoV promotes.

This weighting also improves upon the areal fraction it is based on, as it distinguishes between cases of poorer mixing. The areal fraction could be reduced to a single number by calculating the fraction of mixing values within 10% of perfectly mixed. However, this is a lossy solution. One mixing result could have a significant fraction just beyond this threshold, while another could have the bulk of the area fully unmixed, yet both would yield the same value. The weighted function accounts for these differences, providing a better score for the first example.

Another major advantage is the human interpretability of the number. CoV is vague in its meaning—0.05 is better than 0.5, but there is no clear indication of what these values represent beyond the fact that the larger number implies greater variance. By introducing a weighting and an area-based method for deriving a single mixing number (the CG Number), a value of 0.20 indicates that around 80% of the area is approaching perfect mixing, since only that portion significantly reduces the number. While this advantage is not strictly scientific, the human accessibility of understanding a scientific concept is important.

The same PLIF images analyses that were previously conducted on the CoV data in Section 4.3.3 is also conducted here, but calculated instead using the CG Number. Figures 4.24, 4.25 and 4.27 show histograms and CG Number calculation curves for the SMX™, SMX™ plus and CALGAVIN static mixer. For viewability, the X-axes are limited to 800 for all three mixers, there are only a very small number of frequencies counted above this point due to the injection stream constituting such a small fraction of the total cross-sectional area compared with the un-dyed bulk stream.

The shorter mixer lengths show data very skewed to the low pixel intensities with very limited areas of perfect mixing. At these points, despite the high frequency, the low weighting from the parabolic function means they have very limited impact on the CG Number - this therefore results in a mixing number close to 100. As the mixer lengths get longer the histograms shift right to where they begin to build charts approaching normal distributions around the perfect mixing intensity. The longer the mixer, the

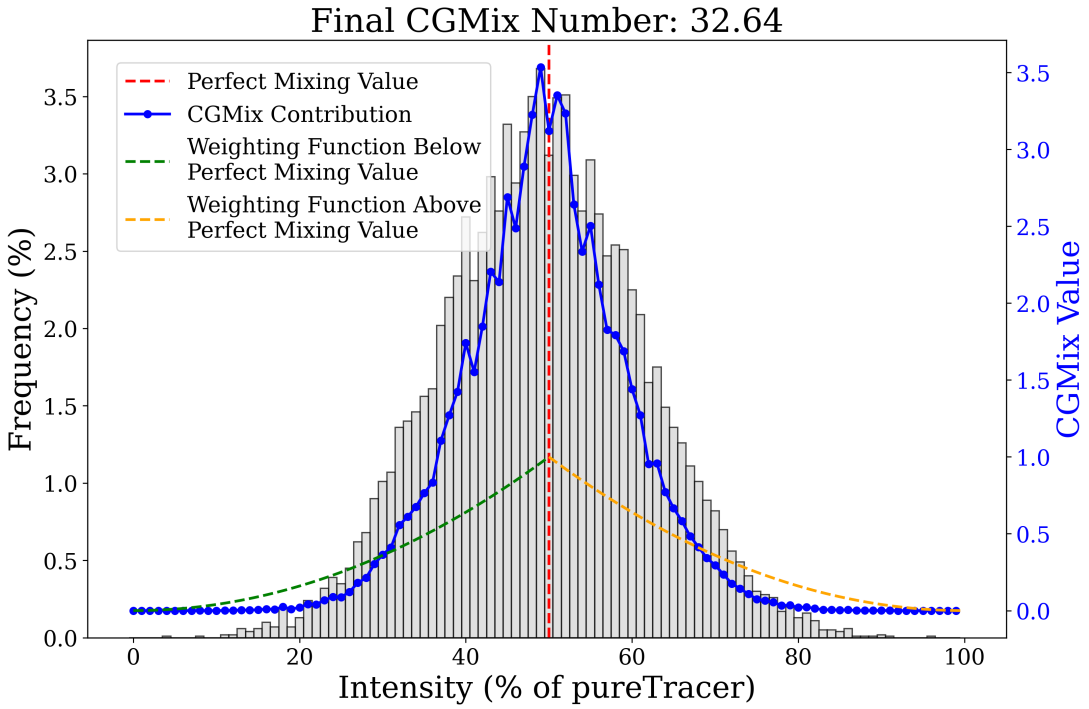


Fig. 4.22. Reference Chart for Understanding CG Number

narrower the distribution. Around the perfect mixing number, the high weighting from the parabolic function means these bins have a high impact on the CG Number and the number is closer to zero.

One plot is depicted (Figure 4.28) that plots the full X-axis range for the SMX™ plus static mixer, but with the Y-axis with a logarithmic scale. This shows the frequencies that are too low to be seen in the linear chart. With the shorter mixer lengths, the highest frequencies are with the bins of low pixel intensity, but there are also moderate amounts at the high pixel intensities. These are the small areas of the pure injected dye. This region gets lower over time as the highest frequency tends towards the perfect mixing intensity. With the longest mixer lengths, banding appears where there the distribution is no longer continuous. These are constituted of un-mixed striations in the fluid that remain at the micro-scale at the point where the mixed begins to become less effective.

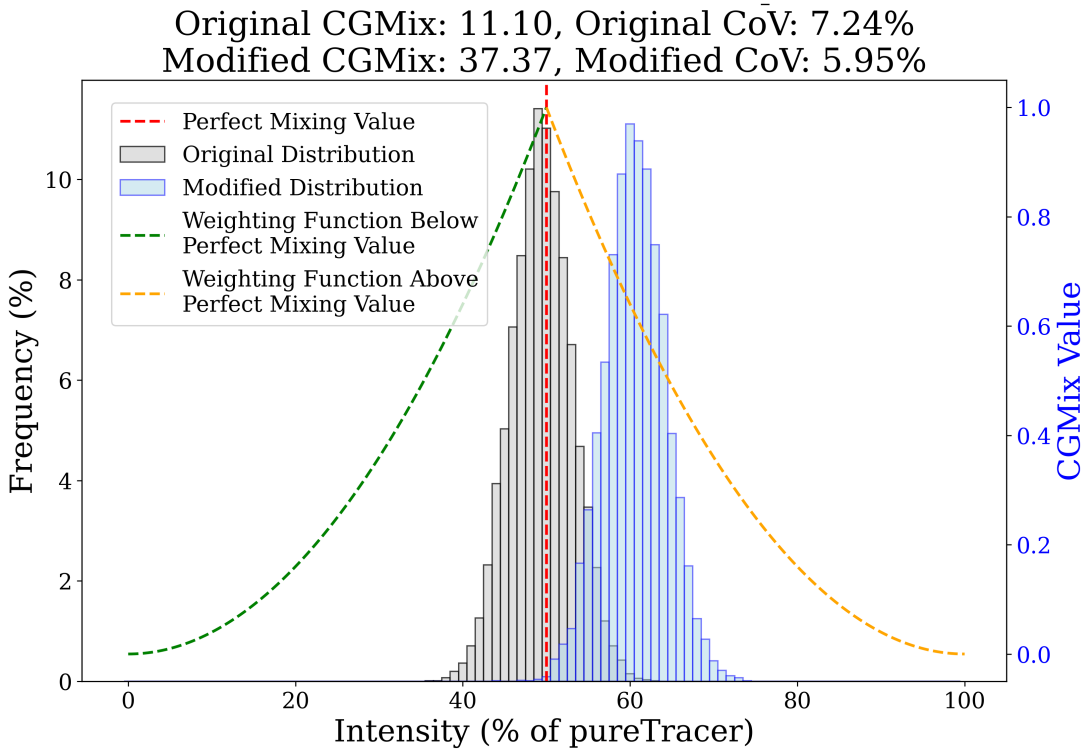


Fig. 4.23. Example of the Affect on CG Number and CoV when Incorrect Ratios of Mixture Components are Introduced

These figures effectively show how the mixing quantification occurs but it less effective at showing how the fluid flow impacts mixing. The plotted data of how CG Number changes with Reynolds number is seen in Figures 4.29, 4.30 and 4.31.

As with the CoV data, the trend across all three mixers is that, over this range of Reynolds number, Reynolds number has very little effect. This is shown with the largely flat trendlines and subsequently static CG Number as Reynolds number increases. Table 4.3 shows the calculated constants of linear regression for the three static mixers with the slope being around zero. It also contains the calculations for standard deviation and shows that the absolute difference from the average is well within one standard deviation for all the mixers tested. Like the CoV data, these calculations shows that increasing the length of the mixers decreases the CG Number and therefore represents increased mixing.

Mixer Type	Size (mm)	Slope	Intercept	nRMSE (%)
CALGAVIN Static Mixer	32	-0.0038	4.5581	1.02
	64	-0.0110	4.4859	1.87
	96	-0.0147	4.3251	3.21
	128	-0.0263	4.0631	2.76
	160	-0.0371	3.8498	7.41
	192	-0.0356	3.6125	5.50
	224	0.0150	3.3107	7.69
	256	0.0034	3.0285	4.75
	288	-0.0217	2.8948	3.39
	320	0.0042	2.8239	1.89
	Average	**-0.0125**	**3.7052**	**3.95**
	Std Dev	**0.0204**	**0.6202**	**2.12**
SMX™	46	-0.0041	4.4772	0.74
	92	0.0011	4.0781	1.50
	138	0.0022	3.6084	3.54
	184	0.0204	3.0631	6.87
	230	-0.0003	2.8431	2.20
	276	-0.0373	2.8052	8.18
	Average	**-0.0030**	**3.8125**	**3.84**
	Std Dev	**0.0218**	**0.6629**	**2.61**
SMX™ plus	46	-0.0019	4.5013	0.91
	92	0.0037	4.2423	1.34
	138	-0.0333	3.7283	5.10
	184	0.0214	3.2261	3.04
	230	-0.0077	2.8670	2.28
	276	0.0148	2.7655	1.87
	Average	**-0.0005**	**3.8884**	**2.76**
	Std Dev	**0.0182**	**0.6814**	**1.40**

Table 4.3
Consolidated Linear Regression Parameters for CG Mixing Number over Reynolds Number Data for All Mixer Types with 99.8 wt.% Glycerol

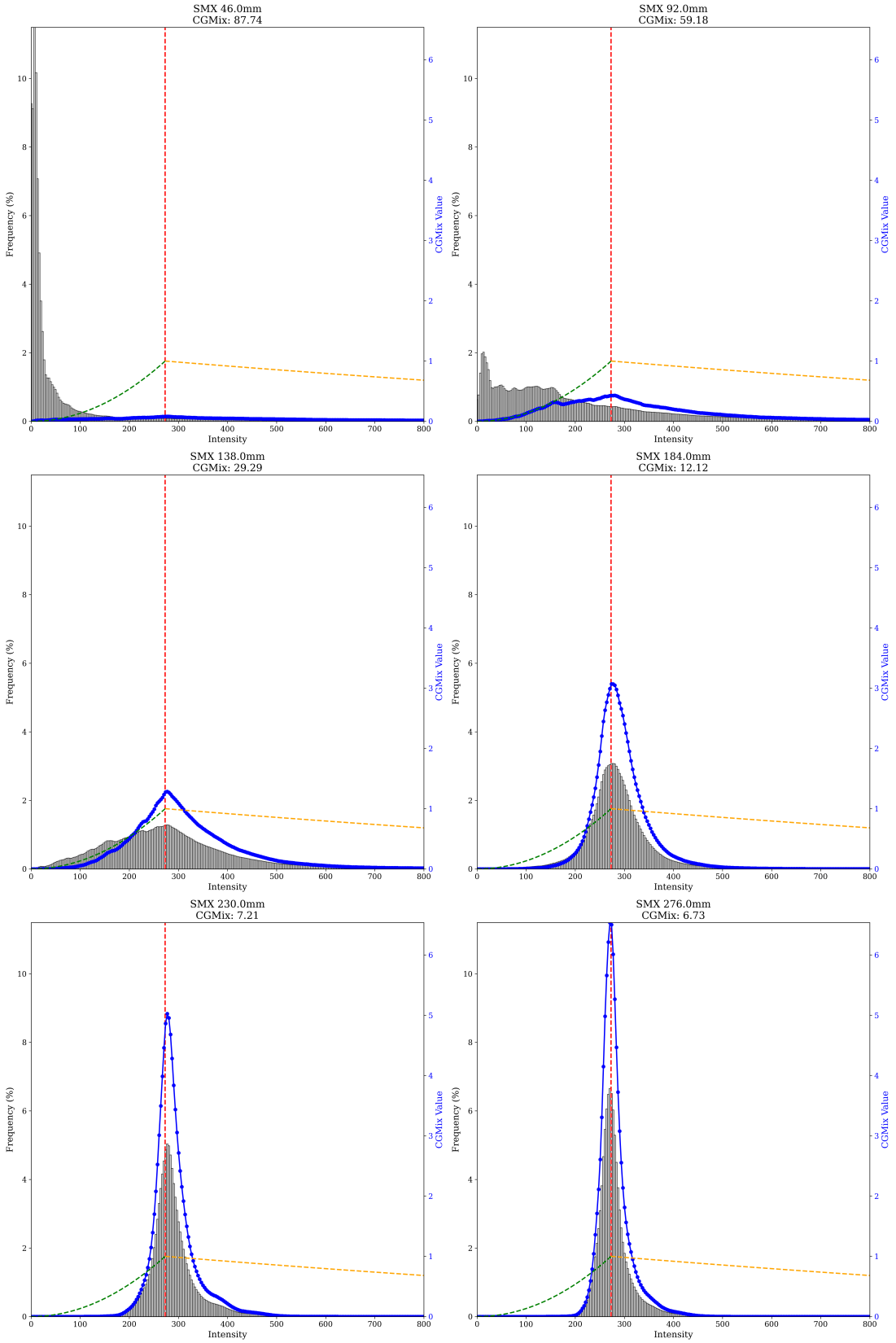


Fig. 4.24. Histogram of PLIF images for the SMX™ Static Mixer with Calculation Curves for CG Number

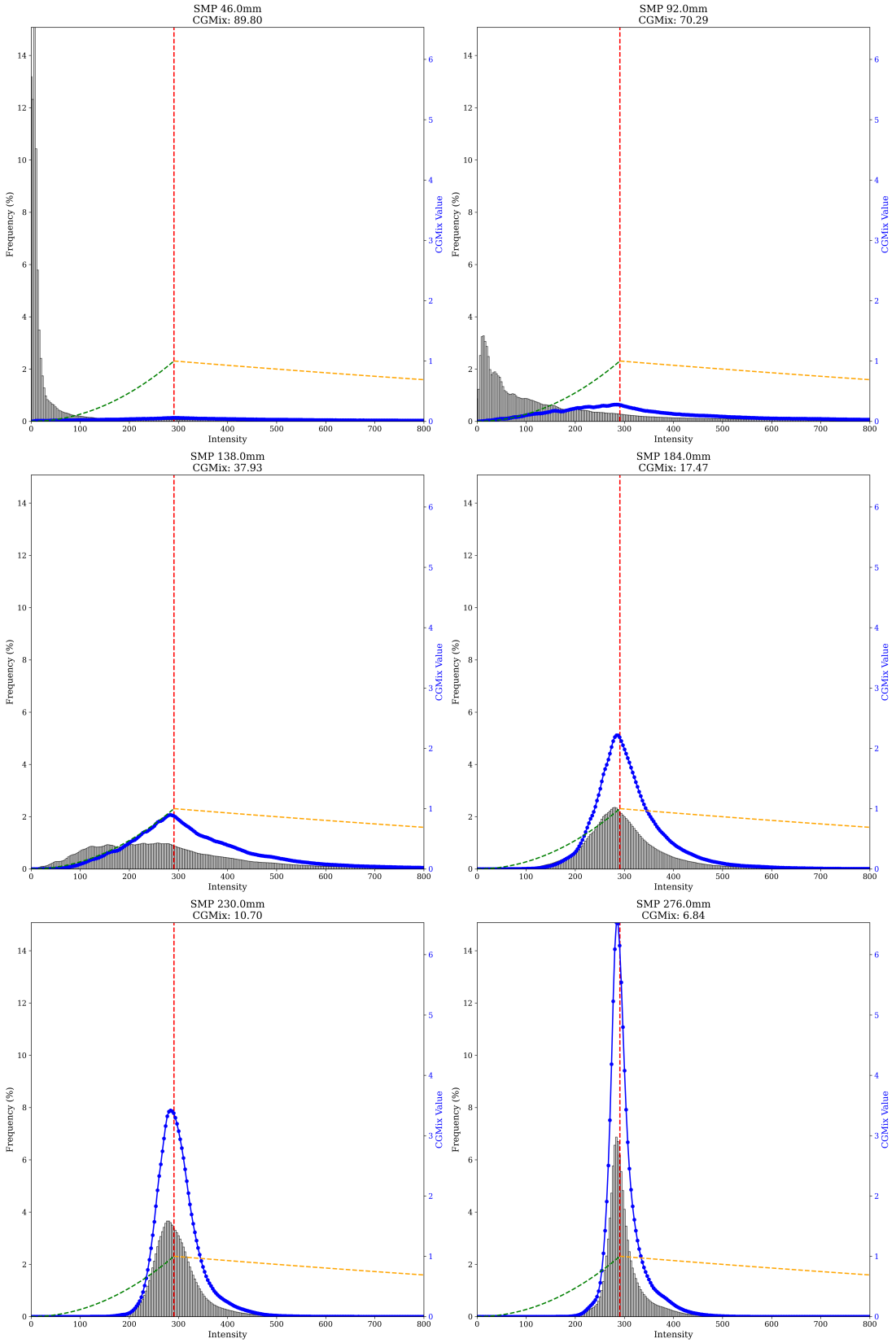


Fig. 4.25. Histogram of PLIF images for the SMX™ plus Static Mixer with Calculation Curves for CG Number

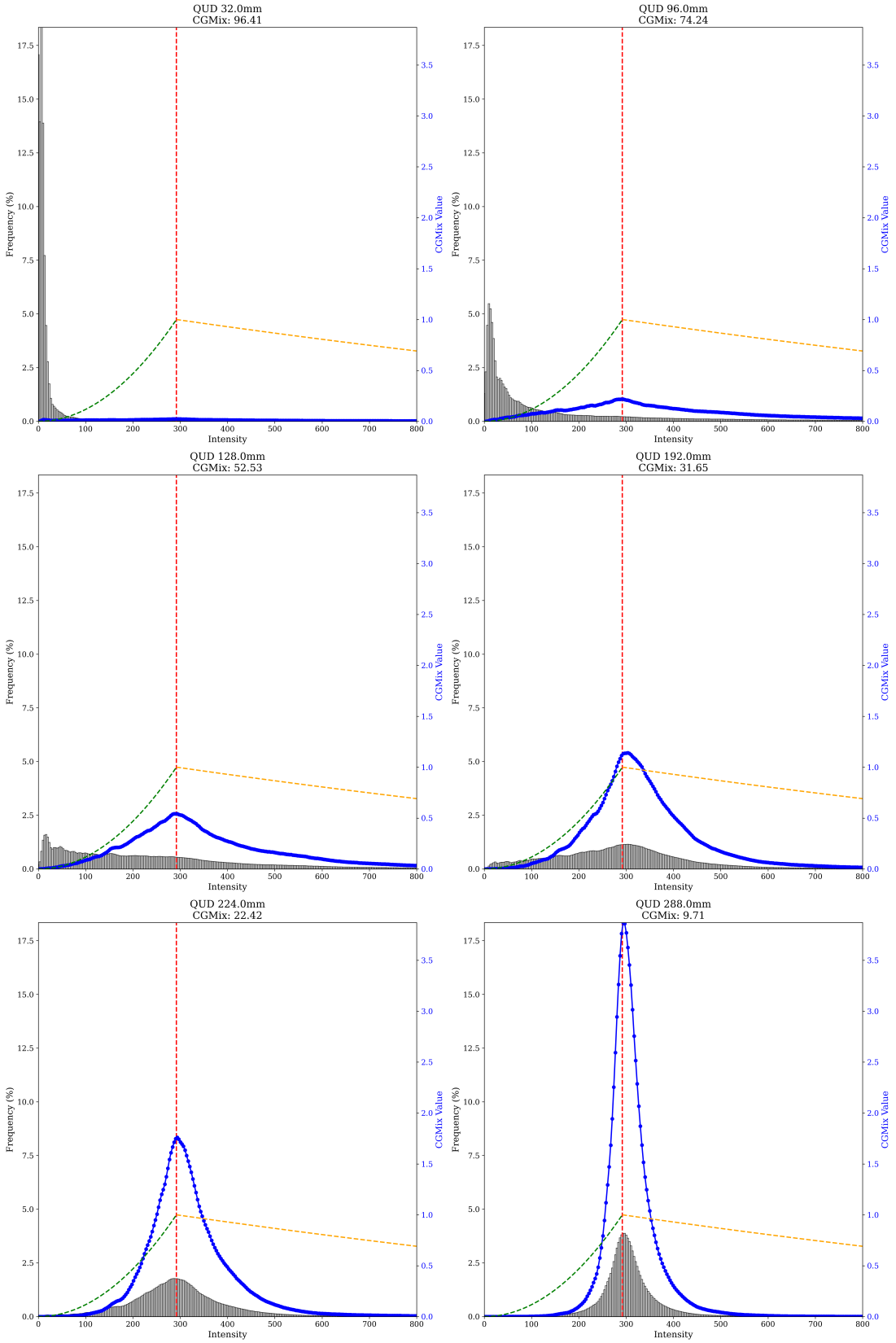


Fig. 4.26. Histogram of PLIF images for the CALGAVIN Static Mixer with Calculation Curves for CG Number

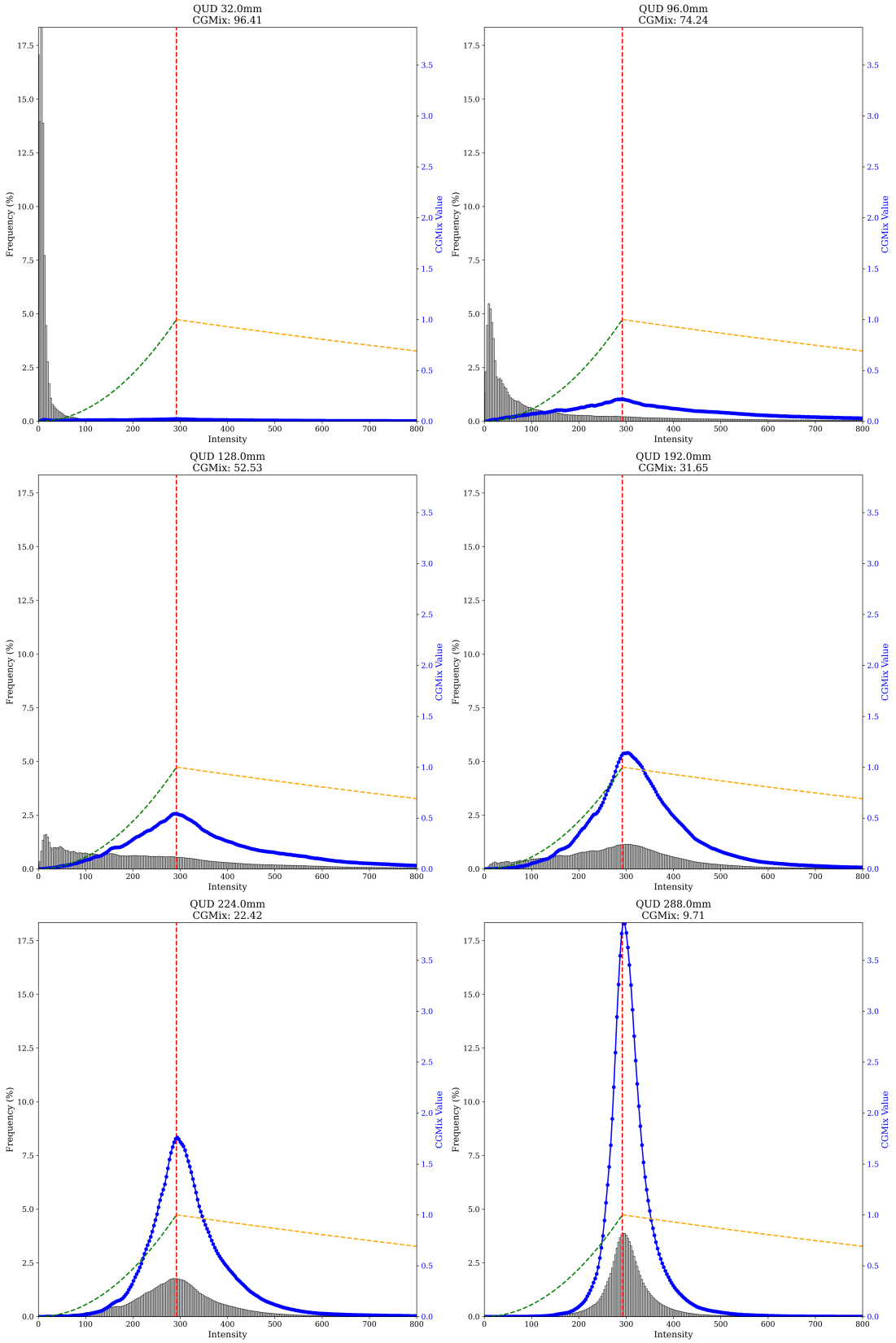


Fig. 4.27. Histogram of PLIF images for the CALGAVIN Static Mixer with Calculation Curves for CG Number in Log Scale

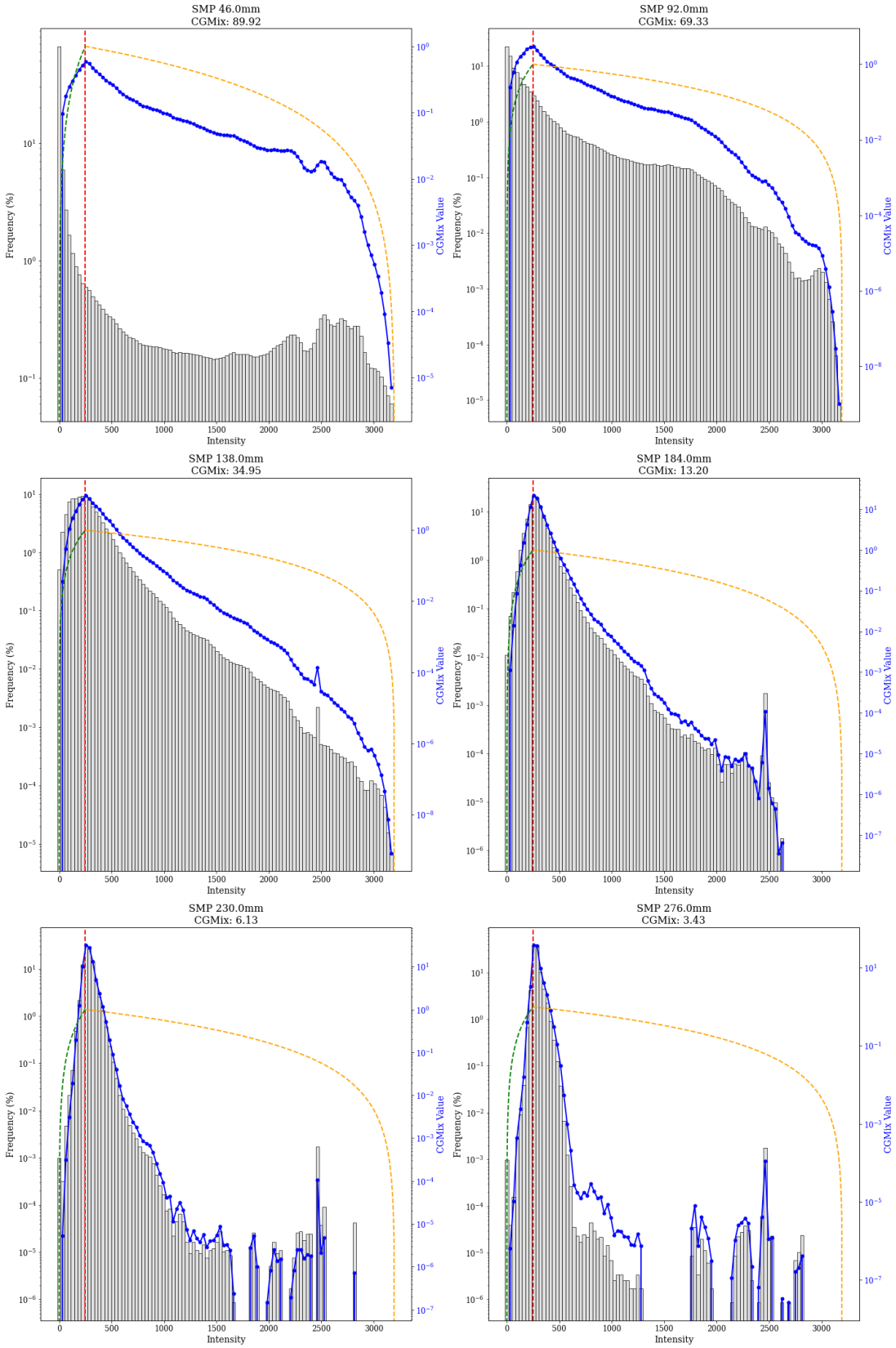


Fig. 4.28. Histogram of PLIF images for the CALGAVIN Static Mixer with Calculation Curves for CG Number in Log Scale

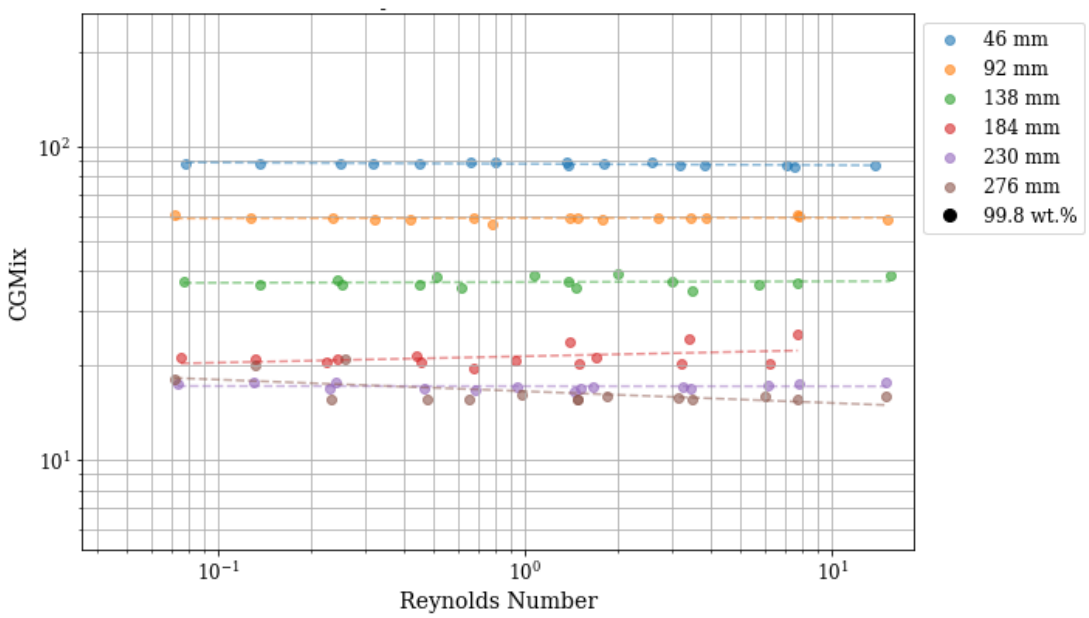


Fig. 4.29. The influence of Reynolds Number on CG Number for each tested length of the SMX™ Static Mixer

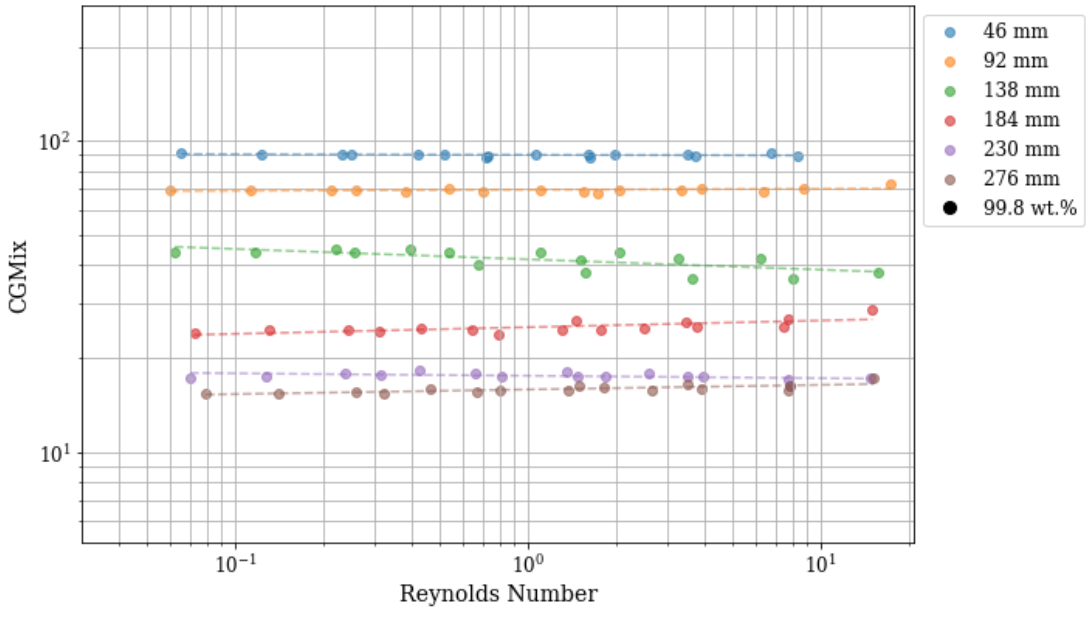


Fig. 4.30. The influence of Reynolds Number on CG Number for each tested length of the SMX™ plus Static Mixer

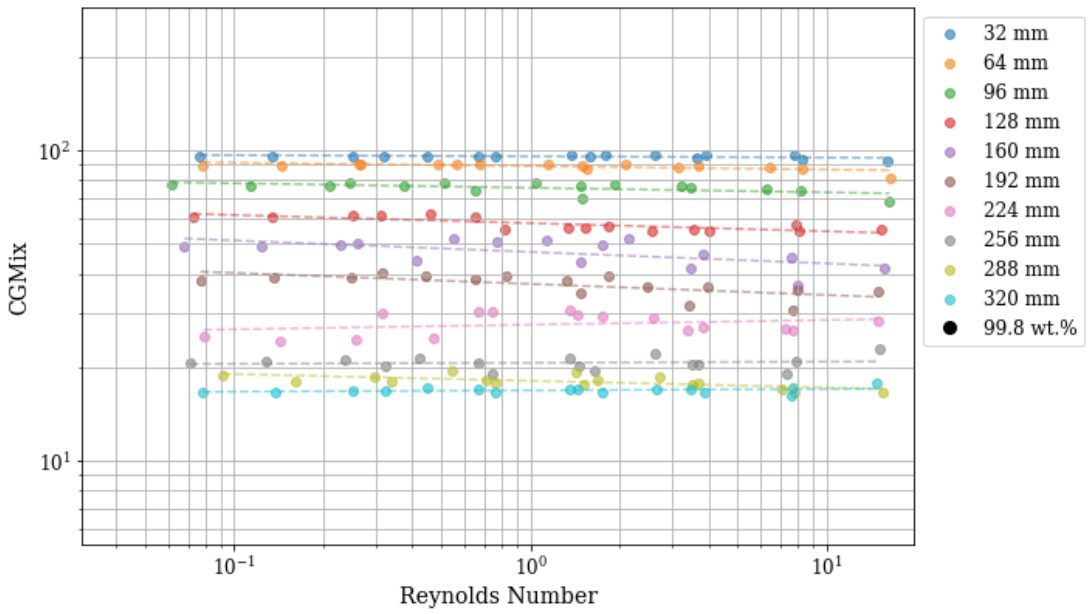


Fig. 4.31. The influence of Reynolds Number on CG Number for each tested length of the CALGAVIN Static Mixer

4.3.5 Mixing Efficiency

Mixing efficiency can be assessed in multiple ways depending on a designers properties. The main two are pressure penalty and the total length required for mixing, but factors such as maximum shear for biological processes or capital cost are also valid criteria. This Section will look at the mixing these first two and use that to rank the performances of the static mixers.

4.3.5.1 Length efficiency

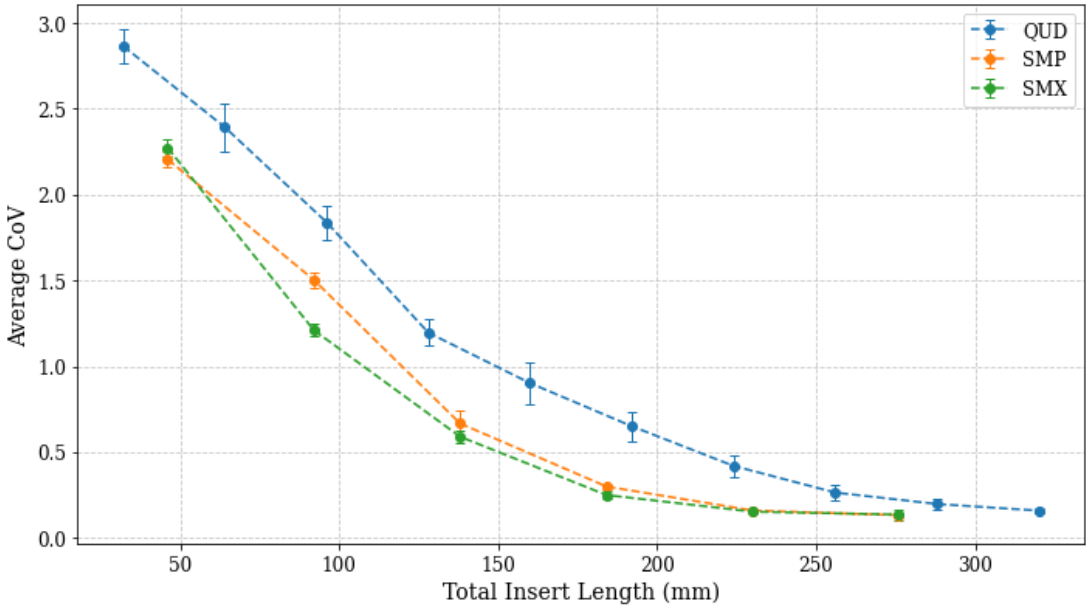


Fig. 4.32. Collated Chart of the effect of insert Length on CoV-based Mixing for the SMX™, SMX™ plus and CALGAVIN Static Mixer

With the earlier confirmation that, over this range of Reynolds Number, mixing level is unaffected by Reynolds number, new plots, Figures 4.32 and 4.33 were developed. In these plots, the calculated mixing numbers were averaged for all the different Reynolds numbers for each insert length for each static mixer. This instead allowed a plot of how these values changed over the length of a static mixer. It can be seen in these plots, that increasing insert length decreases the CoV and the CG Number and therefore increases mixing. The plots have a shape most similar to a sigmoid function where the rate

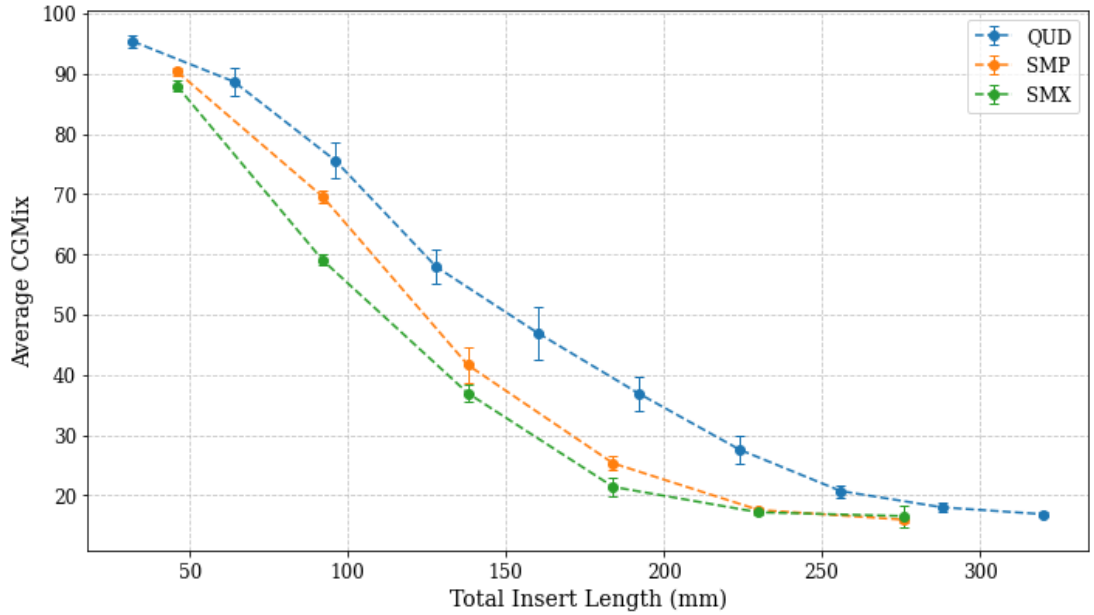


Fig. 4.33. Collated Chart of the effect of insert Length on CG Number-based Mixing for the SMX™, SMX™ plus and CALGAVIN Static Mixer

of mixing increases slowly with length before accelerating and eventually plateauing. This plot also allows the easy comparison of mixing length efficiency between the static mixers. It shows that with the highest CoV per length, that the CALGAVIN mixer has the lowest performance with the SMX™ and SMX™ plus having better and roughly equal mixing performance. All the mixers plateau at the same CoV and CG Number again suggesting that this style of mixing can only mix to a certain level or that the PLIF system can no longer distinguish a difference. Also of note is the similarity between the two types of mixing criteria, there is no significant difference with how they characterise the mixing of the tested static mixers

4.3.5.2 Energy Loss Efficiency

This will use the Fanning friction factor as a dimensionless assessment this pressure penalty. This plot is generated by taking the power law curves generated in Section 4.3.1 and calculating the friction factor at a specified Reynolds number for each insert length and plotting the friction factor against the CoV and CG Number. Though Reynolds number has negligible effect on CoV, it has a dramatic affect on the pressure drop and

therefore friction factor of the test. This means that changing the Reynolds number used for the assessment of friction factor in this plot would change the scale of the friction factor x-axis, but not the CoV on the y-axis. For this reason only one plot is shown here to give the indicative relationship between the energy penalty and mixing performance of a static mixer that will be representative of any Reynolds number tested in this data set. These plot is seen in Figures 4.34 and 4.35.

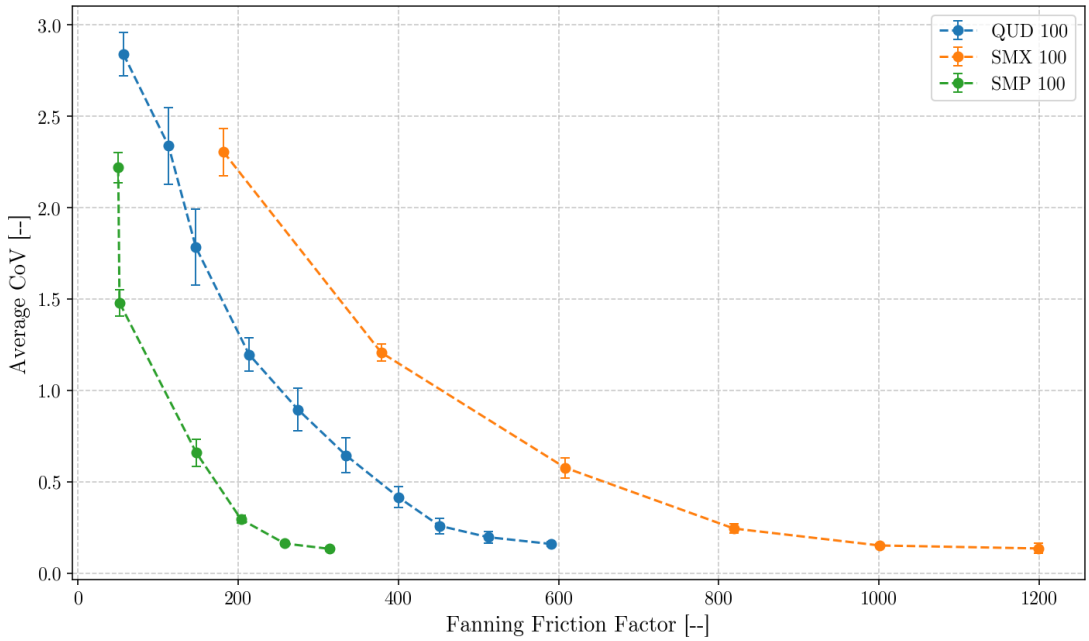


Fig. 4.34. Collated Chart of the Energy Penalty (Fanning friction factor) Required to Achieve Certain Mixing Levels as Assessed by CoV for the SMX™, SMX™ plus and CALGAVIN Static Mixer at a Reynolds Number of 1

Both plot of CoV and CG Number are very similar. The higher the friction factor required to achieve a level of mixing, the less energy efficient a static mixer is. By noting the level of friction factor at a specific mixing number where the higher it is shown that the the SMX™ is the least efficient mixer for its induced pressure drop, followed by the CALGAVIN static mixer and finally the SMX™ plus, which is the most efficient by the criteria.

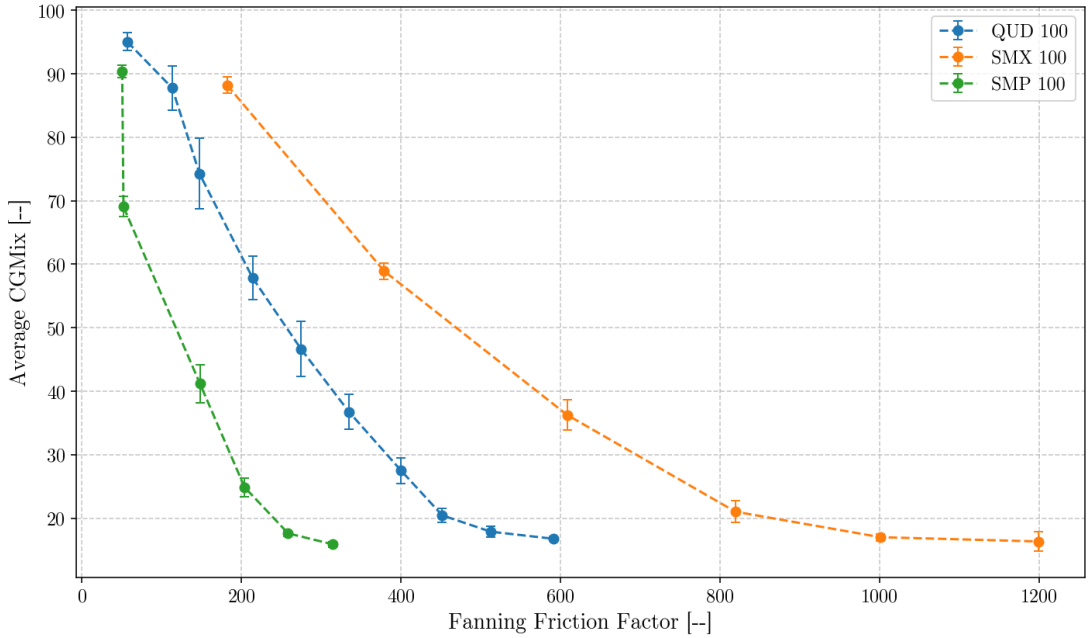


Fig. 4.35. Collated Chart of the Energy Penalty (Fanning friction factor) Required to Achieve Certain Mixing Levels as Assessed by CG Number for the SMX™, SMX™ plus and CALGAVIN Static Mixer at a Reynolds Number of 1

4.4 | Conclusion and Next Steps

This testing in laminar flow at Reynolds numbers between 0.02–16 has shown that Reynolds number has a negligible effect on mixing. What does increase mixing is increasing the length of a static mixer, but not all tested mixers are as length-efficient. The most efficient mixer tested by length is the SMX™, followed by the SMX™ plus, with the CALGAVIN static mixer as the least efficient. The SMX™ and the SMX™ plus perform at a very similar level with this criterion.

When instead looking at mixing versus energy loss, the order of efficiency changes. The SMX™ plus is the most efficient, followed then by the CALGAVIN static mixer. An equal step down from this is then the SMX™ mixer, which has the highest energy penalty for its mixing level.

This data also functions to prove the effectiveness of the developed test facility. The data taken has low scatter and consistent data points, forming the most comprehensive

level of static mixing data taken on a single rig to date. This analysis consists of 440 tests across the three mixers. Although the result that Reynolds number does not affect mixing in this range is known in literature, the purpose of this testing is to demonstrate that the developed rig is capable of detecting such a lack of variation and doing so repeatably and accurately. The fact that all results conform to this expectation validates the measurement system and supports its use in future, more complex tests.

The clearest avenue for further work is examined in the following Chapter, which explores whether the trends seen here between mixing level and Reynolds number are maintained as the Reynolds number range is expanded upon. Given that the current PLIF images show there is almost no shot-to-shot variability and demonstrate a complete steady state of the laminar flow field, it was deemed unlikely that lowering the Reynolds number further would elicit any change in the mixing. However, this may not be the case as the Reynolds number is increased. In empty tube flow, it is expected that turbulence to some degree begins around 2000 Reynolds, yet this does not necessarily hold when an insert is in the tube. Previous research conducted in heat transfer experiments at CALGAVIN LTD demonstrates that there is an uptick in both heat transfer and pressure drop at around a Reynolds number of 50–100. The hypothesis is that chaos is introduced by the tube insert, where eddies form at the tail ends of the mixer structure. If this were the case, PLIF would be the perfect technology to examine these eddies by showing the altered and altering flow field at the outlet of the mixer.

CHAPTER 5

Boundary Separation in Laminar Static Mixing

5.1 Introduction

Chapter 4 demonstrated that at a Reynolds numbers below 20, Reynolds number has no effect on mixing. The conclusion was drawn by graphing the Coefficient of Variance (CoV) from Planar Laser-Induced Fluorescence (PLIF) experiments of static mixers against Reynolds number and demonstrating that there is a flat correlation between the two. This was hinted at during the experiments while taking the PLIF images and before the CoV of each test was even analysed. During the experiment, the conditions were so stable that significantly changing the velocity would have no effect on the resultant mixing image - this was over three orders of magnitude of Reynolds number. The next stage is then to examine how far this flat trend continued up the range of Reynolds number and if, at a certain point, the stable structure breaks down.

The glycerol test fluid was diluted with deionised water to around 80 wt.% aqueous glycerol. The purpose of this was to lower the viscosity to a level that maintained a test range crossover with the 100 wt.% glycerol used previously but to also take the Reynolds number range up to around 100. The motivation for this is from previous heat transfer experiments conducted at CALGAVIN LTD. These experiments demonstrated

a dramatic step change in the heat transfer capabilities with their hiTRAN™ turbulator elements between values of Reynolds number between 60 - 80. The proposed theory from those results was that boundary separation starts to occur in these conditions as the flow begins to form eddy's as it flows around the internal structure. This would add a chaotic element to the flow stream that would then result in different patterns as the velocity is changed. If this also occurred in mixing experiments, it would mean there would not be a flat trend of CoV for Reynolds as they approach and exceed this 60-80 Reynolds range.

The goal of this Chapter, is then to test the mixing characteristics of the same static mixers as in Chapter 4. Reynolds number at which we might expect to begin to see boundary separation. Then, evaluate if there is a change in the mixing performance of these static mixers at these levels and if there is a relative ability change between the tested mixers; potentially making some inserts better suited for different flow regimes than others.

5.2 | Materials and Methods

As with the previous Chapter, the methodology is largely detailed in Section 3.2.2.1 Exactly as before the mixing system involves a dyed stream of the now targeted 80 wt.% aqueous glycerol (measured at 78.8 wt.% with the on-line rheometer) injected into a rheologically equivalent un-dyed primary flow at the inlet of the static mixer. PLIF is used to quantify the mixing levels induced by a static mixer. Simultaneously, the pressure drop induced by said static mixer is also measured and used to quantifiably assess the energy penality associated with it.

There is however a significant data processing change. As predicted from the previously run heat transfer experiments on turbulators at CALGAVIN LTD, there is a degree of chaos added to the flow stream. The implication of this is that the PLIF images are no longer in a steady state. Over time vortices and randomness are seen in the images as they are taken over time. This fact means that the Python data processing

needed to be edited since previously every image was averaged into one image; this was only possible when the images did not change with time. Averaging the images now, when there is a shot-to-shot discrepancy, would result in a wholly inaccurate mixing image which would be a blurred amalgamation of the differing images over time. Instead the program was edited to find the CoV for each captured image after calibration, and then determine the average for all the images taken. This way a representative mixing level was found over time. From here, as before, the CoV for each static mixer and static mixer length was compared to the Reynolds number and induced dimensionless pressure drop to compare their effectiveness against each other. This will then show if there is indeed a change in mixing with Reynolds number once a certain critical threshold is reached.

An additional aspect however is that even though a level of chaos was seen in the captured images, it does not necessarily mean that there is any higher or lower level of mixing. It is possible that the induced eddys may enhance heat transfer without noticeably improving the level of mixing. It is therefore necessary to not only quantify the change in CoV with Reynolds number but also how much, if at all, the CoV changes shot-to-shot within one flow experiment. This can be evaluated by calculating the standard deviation of the CoVs for each image within one test. A higher standard deviation could suggested that there is more variation from chaos within the flow which may or may not translate to more quantified mixing from the As before all the data for the flow characteristics are collected by data acquisition hardware, collated by the custom DASYLab™ software and stored in an SQLite3 database. The Python script calls this information when calculating the quantified properties and stores the results back in the database with the relevant experiments.

5.2.1 Test Fluids

The now diluted glycerol test fluid chosen for this test came out to 77.8 wt.% glycerol. The equations used to generate the temperature/viscosity graph, shown in

Figure 5.1, is detailed in Section 2.2.1. Similarly, equations for Figure 5.2, which displays the temperature/density curve for this fluid, is also provided in that section.

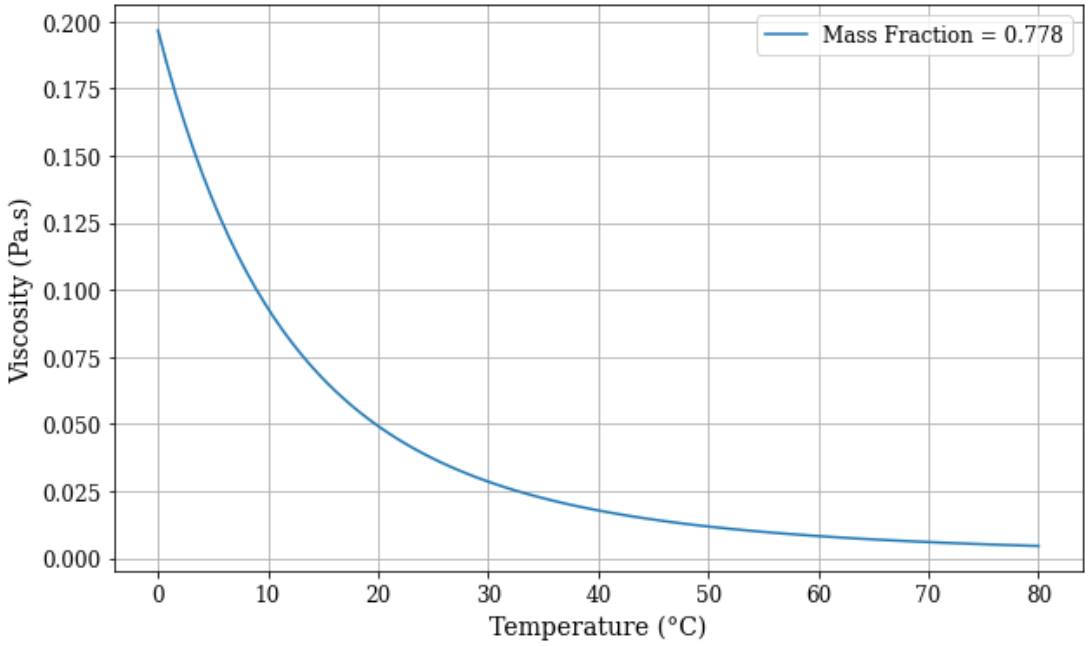


Fig. 5.1. Temperature Viscosity Curve for 77.8 wt.% Glycerol

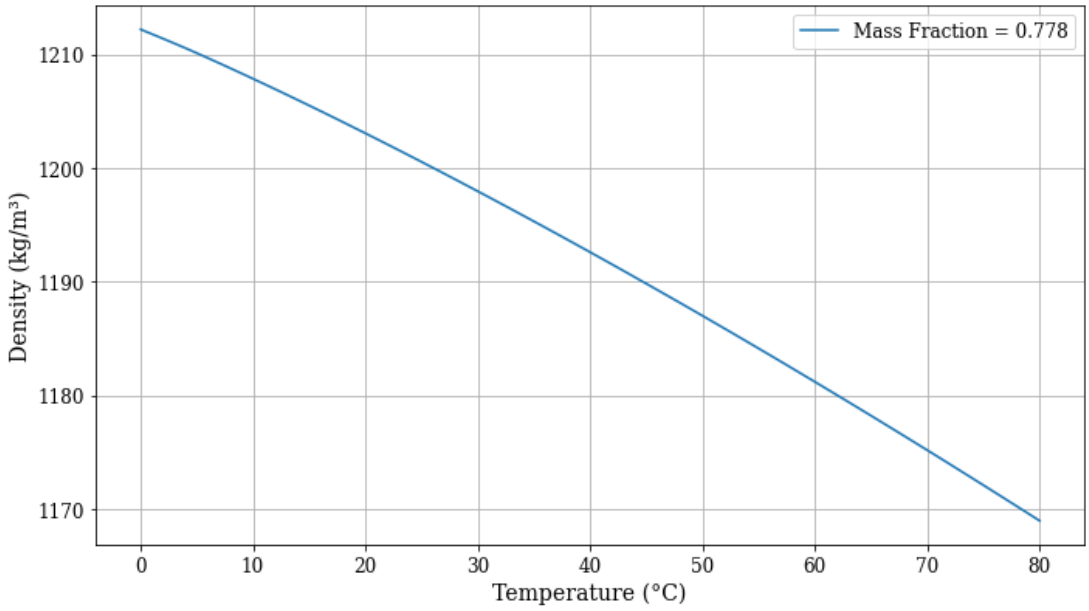


Fig. 5.2. Temperature Density Curve for 77.8 wt.% Glycerol

The secondary dyed flow consists of the same fluid as the primary flow, but with an addition of Rhodamine 6G to achieve a concentration of $0.5\,\mathrm{mg\,L^{-1}}$.

Table 5.1
Test Parameters for 77.8 wt.% Glycerol Mixing Experiments

Glycerol Mass Fraction	Temperature (C)	Viscosity (Pa s)	Velocity (m/s)	Reynolds
0.778	10	0.08	0.002	0.72
			0.005	1.80
			0.010	3.61
			0.020	7.22
			0.040	14.44
	20	0.04	0.002	1.34
			0.005	3.34
			0.010	6.68
			0.020	13.37
			0.040	26.73
	35	0.02	0.002	2.94
			0.005	7.34
			0.010	14.68
			0.020	29.36
			0.040	58.72
	50	0.01	0.002	5.30
			0.005	13.25
			0.010	26.50
			0.020	53.00
			0.040	106.01

A series of repeated test steps were set up to maintain a level of consistency between tests conducted on static mixer inserts - these testing parameters are in Table 5.1. Temperature were conducted at four different intervals dictated by the thermal capacity of the heater chiller unit; as discussed prior, changing the temperature of the glycerol has a dramatic effect on the fluid viscosity. The data tables and plots for these changes can be found in Section 2.2.1. For each temperature range a series of flow rates were repeated by setting pump motor frequencies. All of these parameters are programmed in to the DASYLab™ software control program and are automatically stepped through in the program logic and remote controlled.

As before in Chapter 4 the testing will be conducted on the SMX™, SMX™ plus and the CALGAVIN static mixers insert which can be seen pictured and described in Section 4.2.3.

5.3 | Results and Discussion

5.3.1 Pressure Drop

In the following figures, the Fanning friction factor is normalised by calculating the friction factor divided by the maximum tested length of 300mm. Friction factor is typically a dimensionless unit, but this normalised form separates the data points and allows the proportional comparison of each static mixer length to one another.

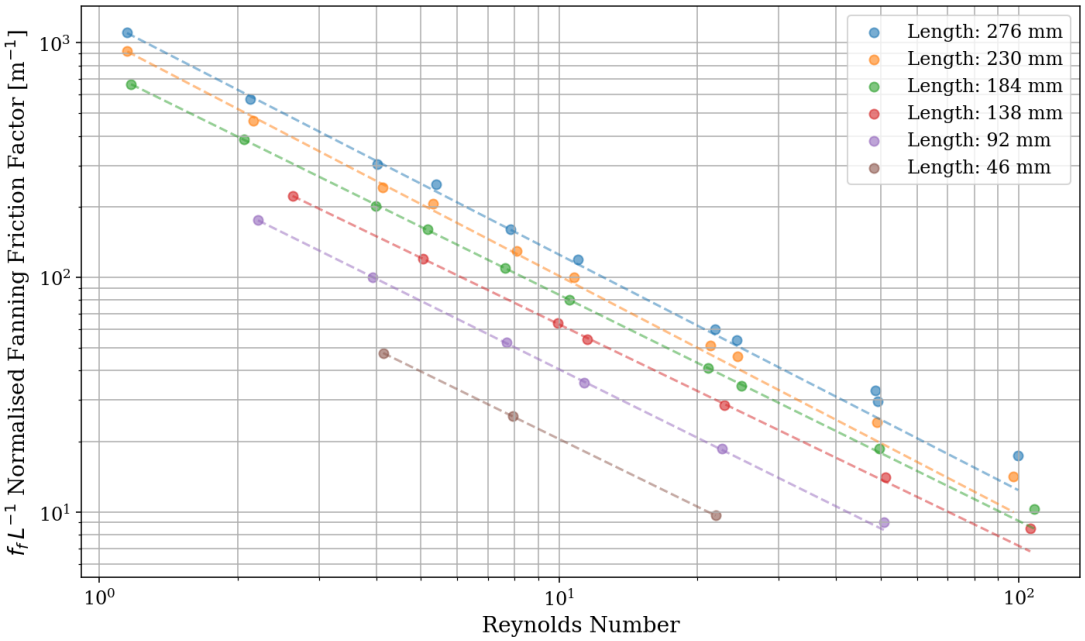


Fig. 5.3. Normalised Friction Factor over Reynolds Number for SMX™ Static Mixer Insert

Figures 5.3, 5.4 and 5.5, displays the Fanning friction factor for the SMX™, SMX™ plus and the CALGAVIN static mixers insert for each tested length up to 300 mm respectively.

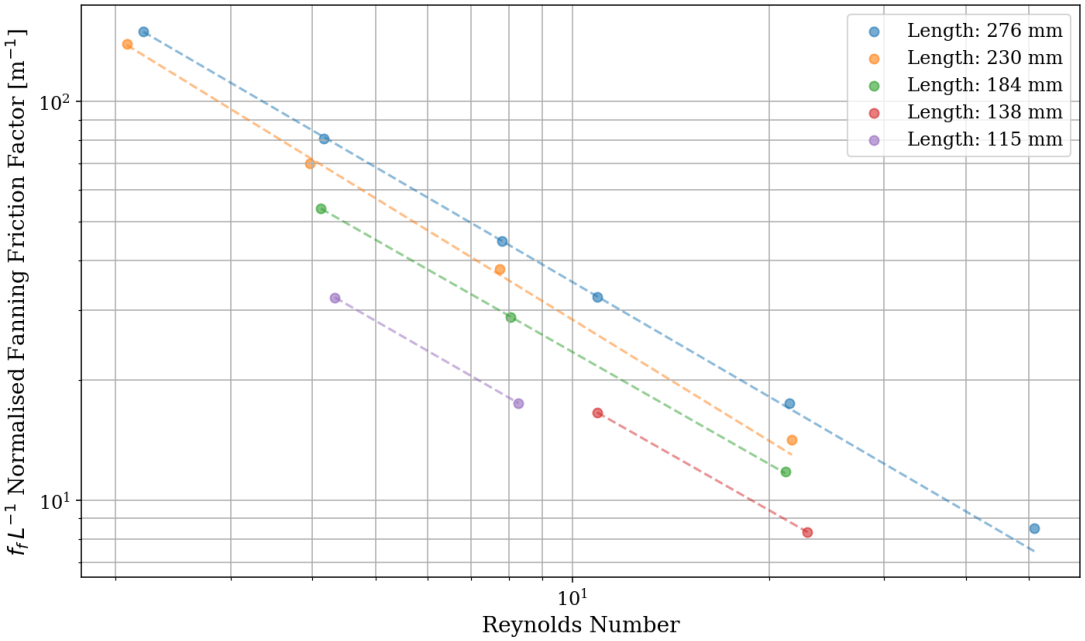


Fig. 5.4. Normalised Friction Factor over Reynolds Number for SMX™ plus Static Mixer Insert

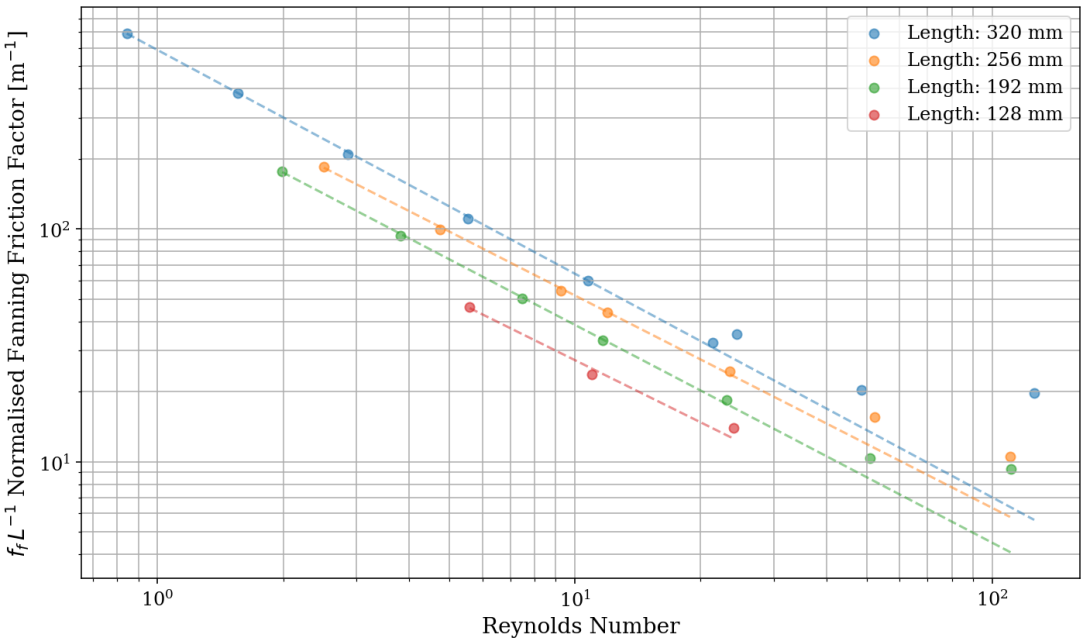


Fig. 5.5. Normalised Friction Factor over Reynolds Number for CALGAVIN Static Mixer Insert

Unfortunately this data is less complete than that of the very low Reynolds number data. The lowest available range of a wet/wet connection differential pressure

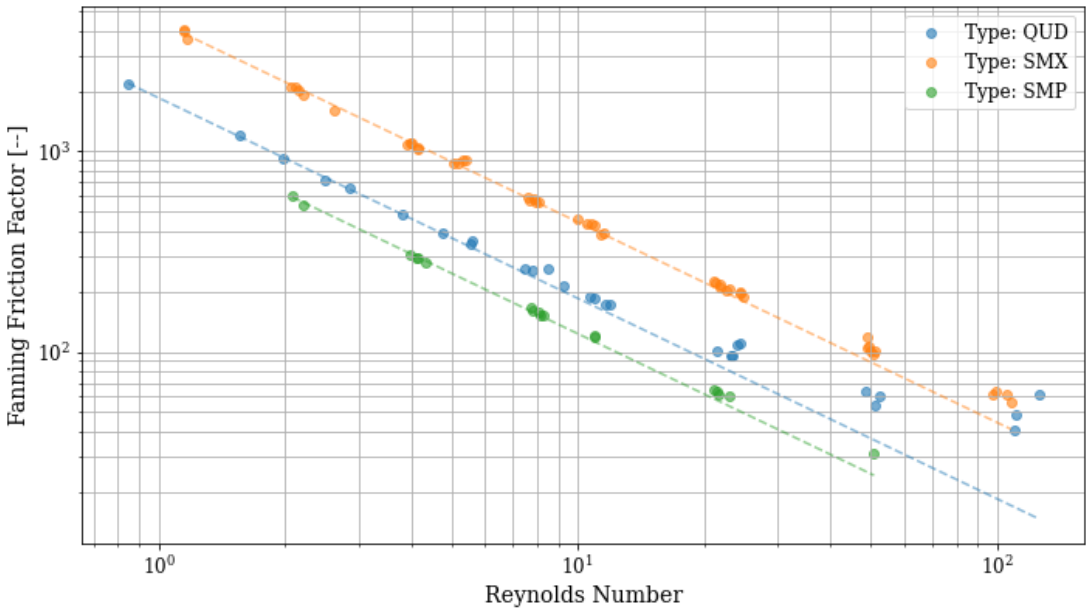


Fig. 5.6. Friction Factor over Reynolds Number for the High Shear Static Mixer Designs: SMX™, SMX™ plus and the CALGAVIN Static Mixer

transducer of 300 mbar was not sensitive enough to reliably capture the data with the lower viscosity test fluid coupled with a test length of only 300 mm. The transducer was rated to a minimum reading of 1% of full range, or 3 mbar mBar (300 Pa), any pressure readings below this value were disregarded and thus created the incomplete dataset seen.

With the data remaining, the trends of increasing static mixer length leading to higher Friction factor can still be seen. Unlike with the lower Reynolds number data, there is an diversion from the trend as the Reynolds number reaches the top end of these tests. This matches the literature which also describes this flattening of the trend between Reynolds numbers 10 - 100. This is attributed to the beginning of the separation of the boundary layer causing vortices to form off the trailing edges of the static mixers. This induces a forced turbulence that causes increased energy to be dissipated in the added chaos when compared to true laminar flow.

By removing the normalisation that separates the different insert lengths and plotting making the dimensionless friction factor, the separate trends collapse to a single

line for each static mixers as shown in Figure 5.6. Again as with the lower Reynolds number data, the SMX™ mixer exhibits the highest pressure penalty, followed by the CALGAVIN static mixer with the SMX™ plus having the least.

Joining this data with the data from the previous chapter generates the contiguous trends seen in Figure 5.7 where the data from the 99.8 wt.% glycerol experiments connects smoothly with the data from the 77.8 wt.% experiments. This continuation demonstrates the accuracy of pressure drop-based mass fraction evaluation, the pressure drop measurement equipment and the glycerol property data. Table 5.2 contains the evaluated Flow Resistance Coefficient , A and the Exponent, B for the data up until a Reynolds number of 30 where there is evidence of boundary separation. Like in the previous chapter the exponent is very close to negative 1 and, again, is likely its true value - matching the analytical solution for Fanning friction factor being equal to a Reynolds number of 16. Combining power-law model of the 99.8 wt.% and the 77.8 wt.% experiments for each static mixer and fixing the model with an exponent of minus 1 generates the Flow Resistance Coefficients seen at the bottom of Table 5.2. This would generate these intuitive models for pressure drop penalty in static mixers for the flow regime at Reynolds numbers between 0.02 to 50:

- For CALGAVIN Static Mixer:

$$f_f = 109.9\frac{16}{Re}$$

- For SMX™:

$$f_f = 253.4\frac{16}{Re}$$

- For SMX™ plus:

$$f_f = 69.5\frac{16}{Re}$$

Static Mixer	Flow Resistance Coefficient (A)	Exponent (B)	Glycerol Conc.
CALGAVIN Static Mixer	1800	-0.990	99.8 wt.%
SMX™	4263	-0.978	99.8 wt.%
SMX™ plus	1145	-0.987	99.8 wt.%
CALGAVIN Static Mixer	1825	-0.965	77.8 wt.%
SMX™	4456	-1.006	77.8 wt.%
SMX™ plus	1207	-0.983	77.8 wt.%
CALGAVIN Static Mixer	1759	-1.000	Combined
SMX™	4054	-1.000	Combined
SMX™ plus	1111	-1.000	Combined

Table 5.2
Flow Resistance Coefficients and Exponents for Different Static Mixers

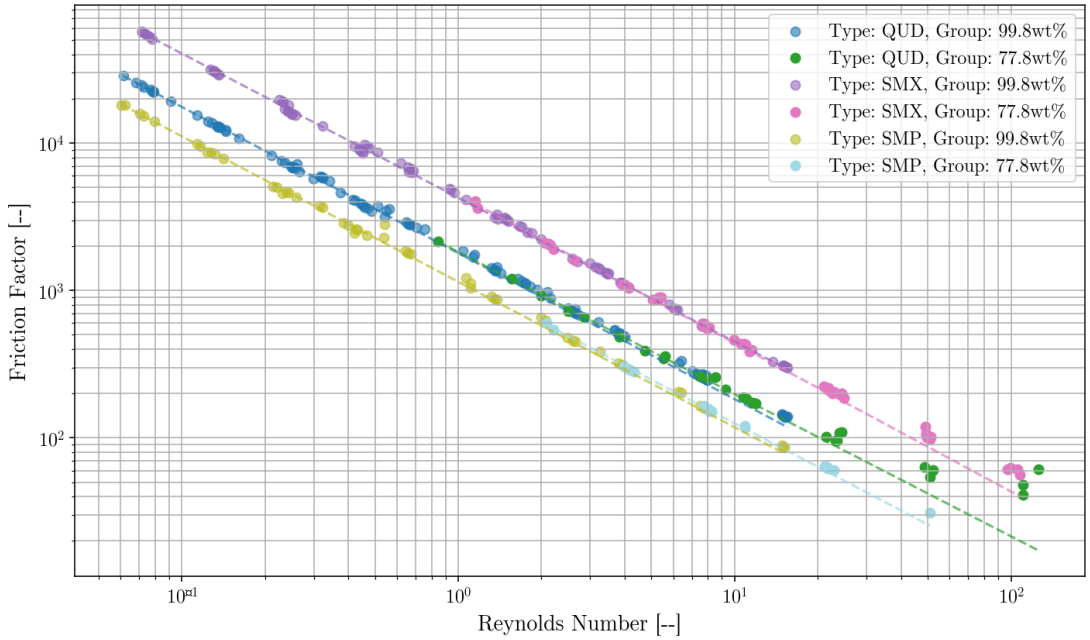


Fig. 5.7. Friction Factor over Reynolds Number for the High Shear Static Mixer Designs: SMX™, SMX™ plus and the CALGAVIN Static Mixer

5.3.2 PLIF Results

Figures 5.8, 5.9 and 5.10 present all the images captured for the lower viscosity and therefore higher Reynolds number testing described in this chapter, with each image representing an average of 100 individual captures. While the images at this scale are again too small to display fine details, they are included to demonstrate the

comprehensive testing achieved with the test rig. Throughout the chapter, relevant images will be enlarged to reveal more detail where necessary.

The two key differences between these images and those captured in the previous chapter are that, at higher Reynolds numbers, the flow dynamics are no longer static within a single run and neither are they unchanged by Reynolds number. The boundary layer separation leads to the formation of vortices off the trailing edges of the mixer structures, in contrast to the previous laminar regime where the flows converged smoothly. In the previous chapter, PLIF images from a test with five units of the CALGAVIN static mixer at a Reynolds number of 7.57 were shown. In this collage, the images were taken 0.25 seconds apart over 3 seconds. Figure 5.11 has the same static mixer arrangement and image collage but at a higher Reynolds number of 110.67. Unfortunately, this phenomenon does not translate well to frame-by-frame images as the flux in the images is slight. Here is a hosted video of the experiment that more clearly shows the added chaos as well as another video which is the previous 7.57 Reynolds number test for comparison.

To visualise the change, a heatmap of pixel change was created. Pixels that change the most frequently appear as pure white, and pixels that are static appear as black. For both tests, Reynolds number 7.57 (left) and Reynolds number 110.67 (right), the brightness scale was fixed. This means that the greater the image flux, the brighter the image. This analysis is shown in Figure 5.12. The higher Reynolds number test shows markedly higher pixel change than the low Reynolds number test, as indicated by the brighter image. In comparison, the lower Reynolds number image is too dim to see with the fixed brightness scale. Though the linked videos are the clearest way to see how vortices begin to form, this heatmap helps to visualise the added variation and mixing chaos when everything is equal except Reynolds number.

This trend continues across all static mixers tested irrespective of the length of static mixer - as the Reynolds number increases over the range tested from around one to one-hundred, there is shift from a steady state image to an image in flux. There

is also a change in the mixing pattern at the outlet, no longer the fixed result that was seen for all Reynolds numbers below approximately 20. The added variable of changing mixing outlet over Reynolds number means that this higher Reynolds number testing has generated 360 unique test sets of images - which too bulk to display here. The following figures show a small selection of the PLIF images captured that are representative of the results from the whole. However all tests will be analysed in the quantitate mixing analysis in the following section. The full array of images that were captured as part of this testing set are displayed in the Appendices.

Figures 5.13, 5.14 and 5.15 contain a selection of the PLIF mixing results for the three high shear mixers, the SMX™, SMX™ plus and CALGAVIN static mixer - all at a similar total length of around 190 mm. Please again note that the images have been individually enhanced to display greater contrast for improved viewability in this text. Therefore they are not quantifiable against each other as displayed here.

In these tests, the flow velocity and temperature, and consequently viscosity, were altered to manipulate the Reynolds number. For Reynolds numbers below approximately 20, the image remains in a steady state and fixed regardless of flow conditions, and therefore unique to each length of each static mixer. However, around a Reynolds number of 20, a transition starts to occur. At this point, the mixing outlet begins to vary and continues to do so as the Reynolds number increases. Additionally, the image variation from shot to shot within a test becomes noticeable. Figures 5.16, 5.17, and 5.18 depict the heatmap methodology described earlier on the tests forming the images in Figures 5.13, 5.14, and 5.15 again normalised to the same scale of pixel variation across the whole image. It is observed that below a Reynolds number of 20, there is limited variation on a shot-to-shot basis within a test, i.e., the mixing outlet remains steady. However, as the Reynolds number increases, the image not only varies, but the fluctuation from shot to shot within a test also becomes more pronounced, with higher Reynolds numbers showing greater image flux, as evidenced by a brighter image. What is not obvious from these images alone is whether the increase Reynolds number causes

a quantitate increase in mixing despite the added chaos - this will be further explored in the following section.

This final representative Figure, Figure 5.19, demonstrates that as static mixer length increases the apparent mixing that is seen in the PLIF images also increases at this higher Reynolds number.

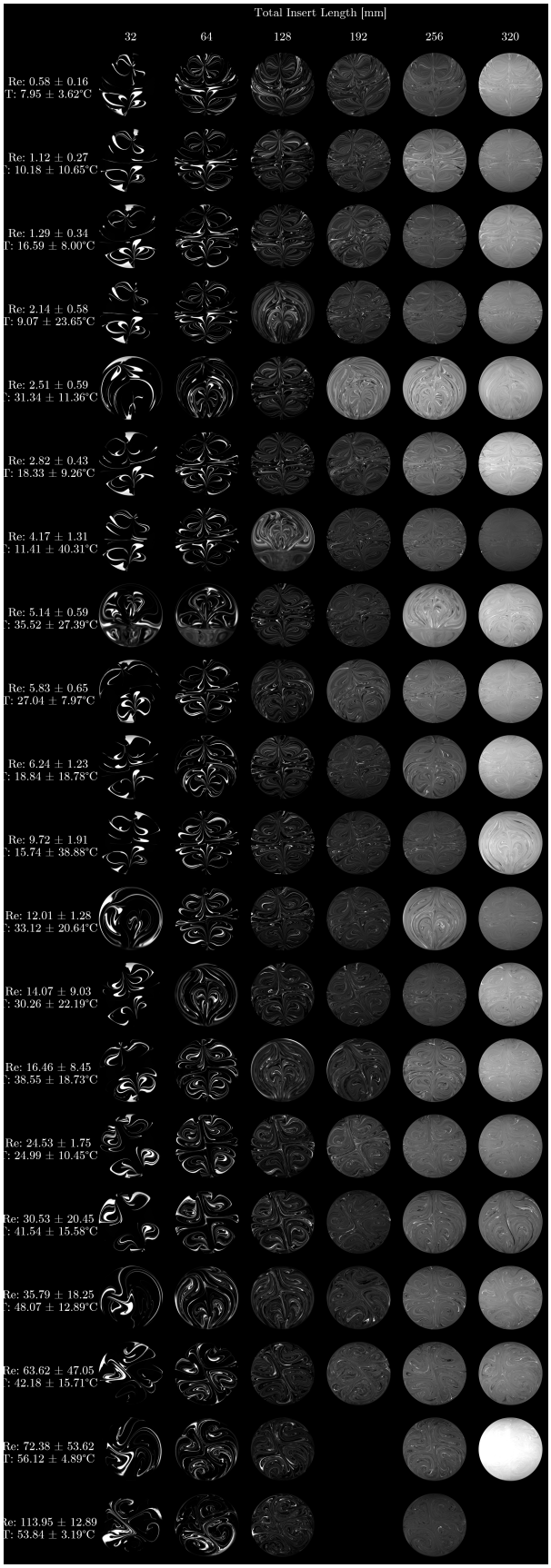


Fig. 5.8. All Captured CALGAVIN Static Mixer PLIF Images for 77.8 wt .% Glycerol Solution with Each being the Average of 100 Images

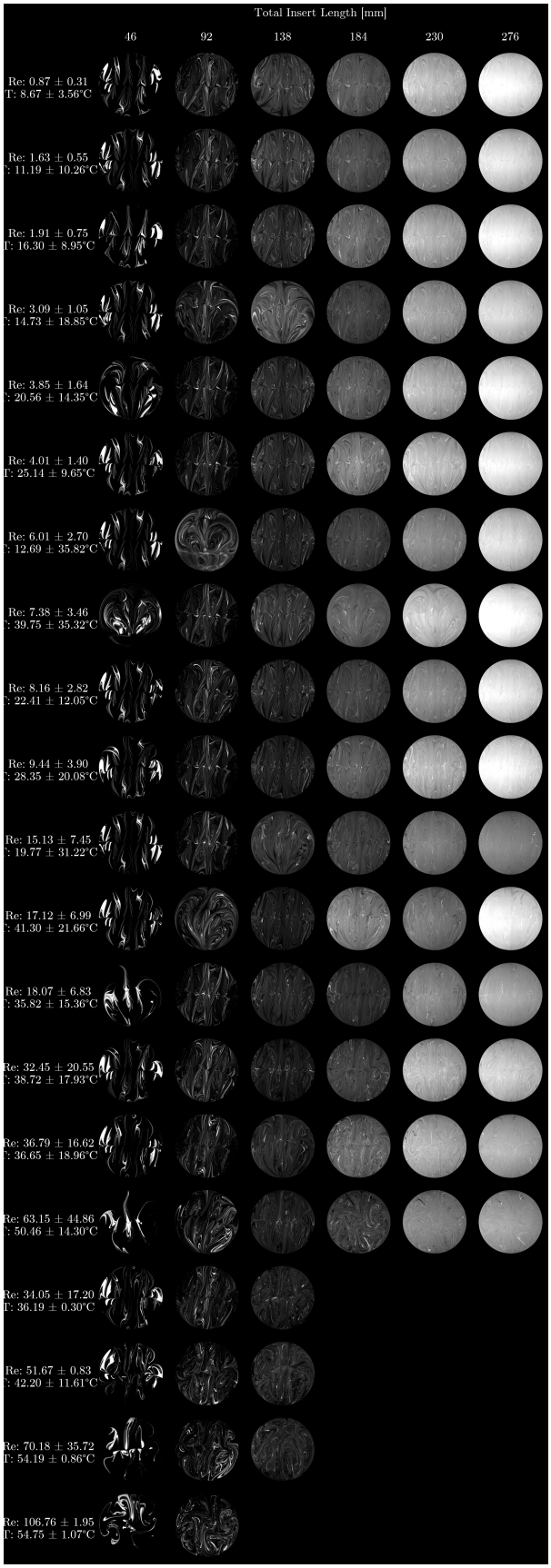


Fig. 5.9. All Captured SMX™ Static Mixer PLIF Images for 77.8 wt .% Glycerol Solution with Each being the Average of 100 images

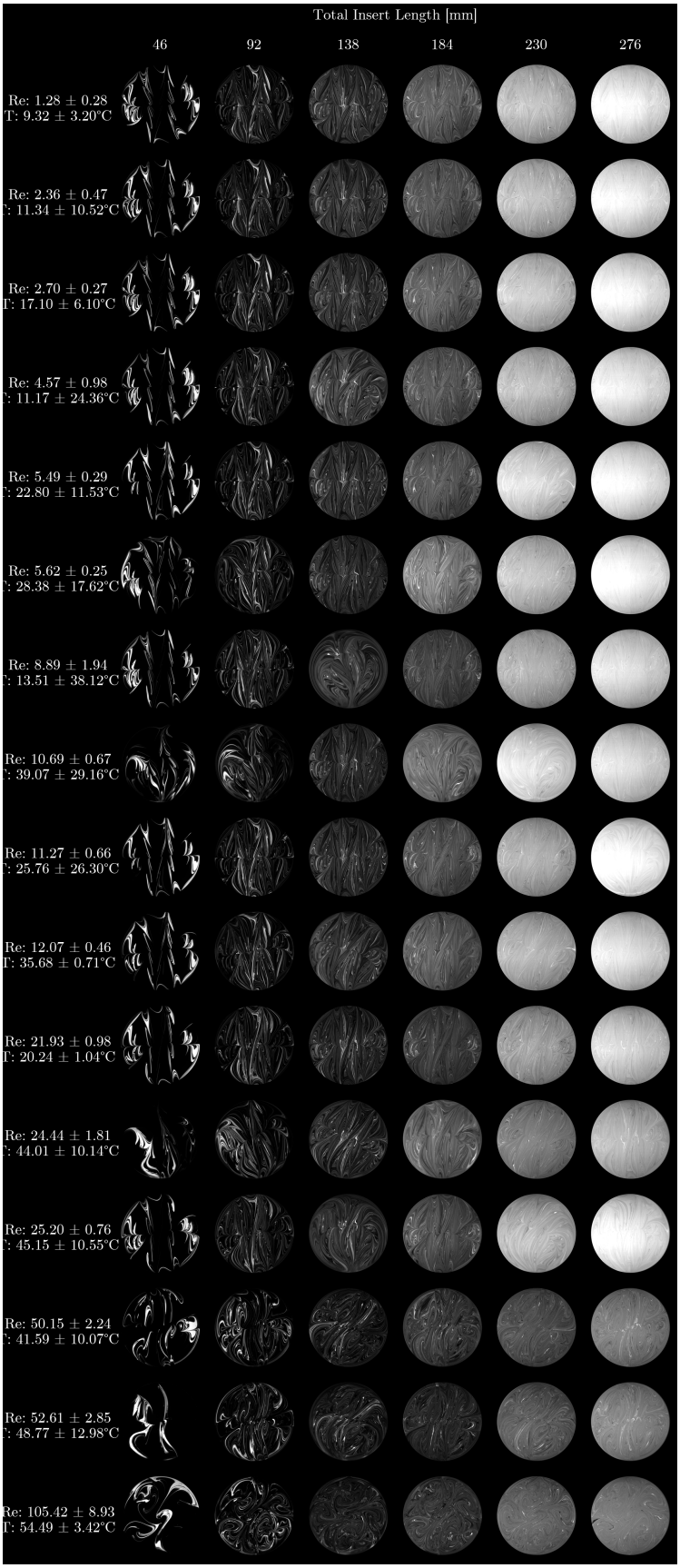


Fig. 5.10. All Captured SMX™ plus Static Mixer PLIF Images for 77.8 wt .% Glycerol Solution with Each being the Average of 100 images

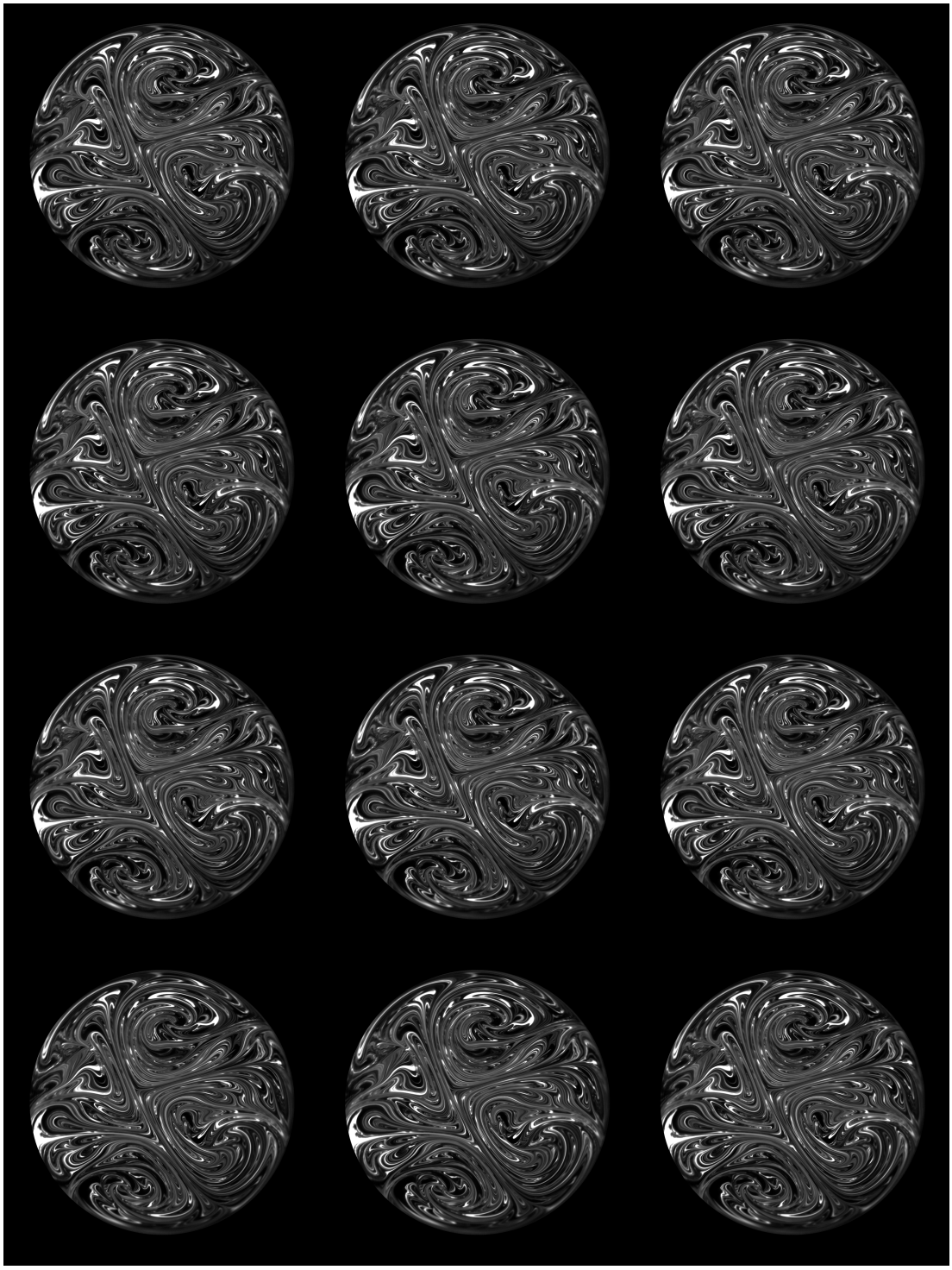


Fig. 5.11. Sequential PLIF images 0.25 seconds after each other for four units of a CALGAVIN Static Mixer at Reynolds number 110.67



Fig. 5.12. Pixel flux heatmap for four CALGAVIN Static Mixer repeats Reynolds number 7.57 (left) and Reynolds number 110.67 (right) with proportional scaling

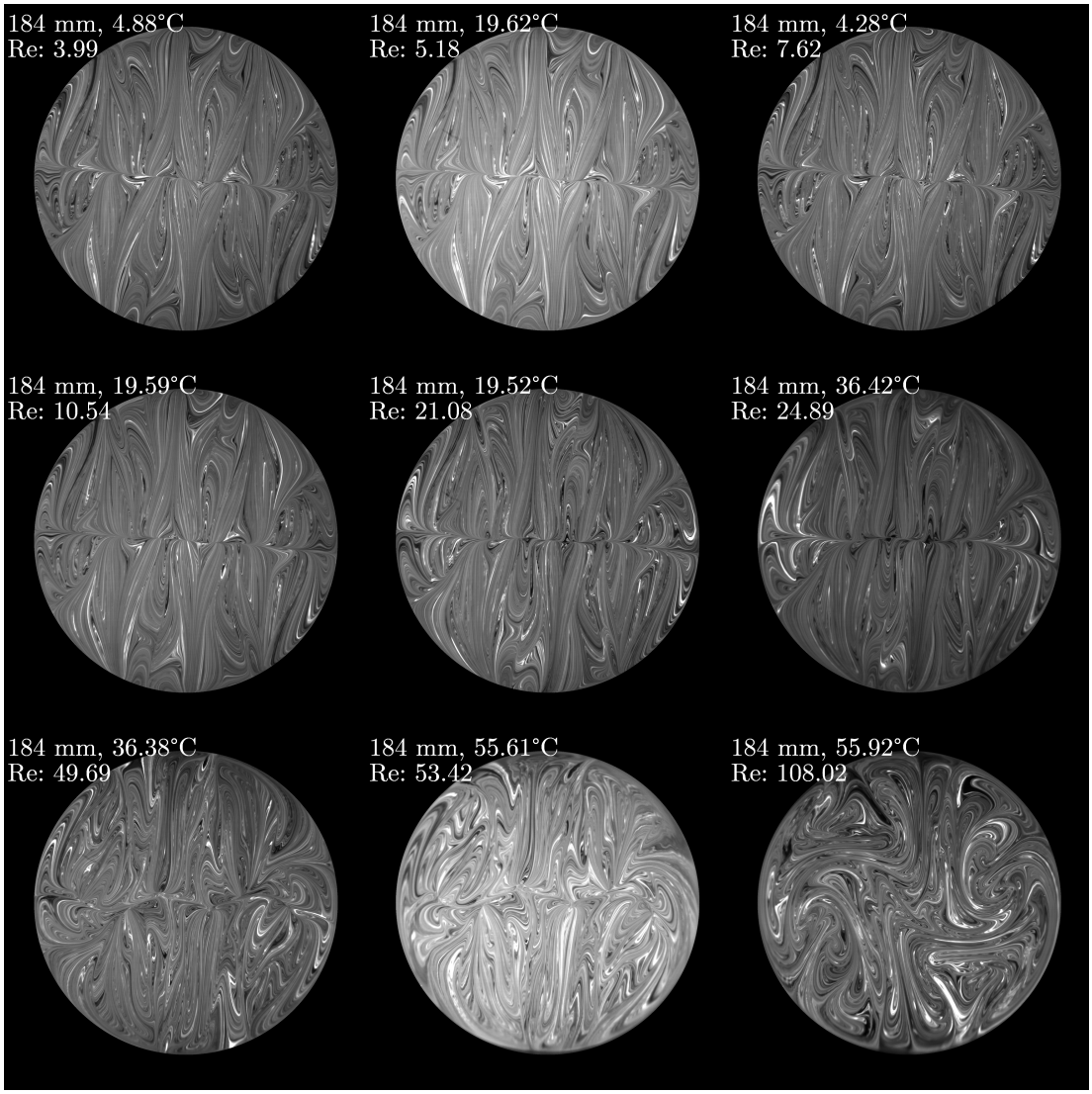


Fig. 5.13. PLIF results for eight repeats (184 mm) for the SMX™ Static Mixer across varying temperature and Reynolds number

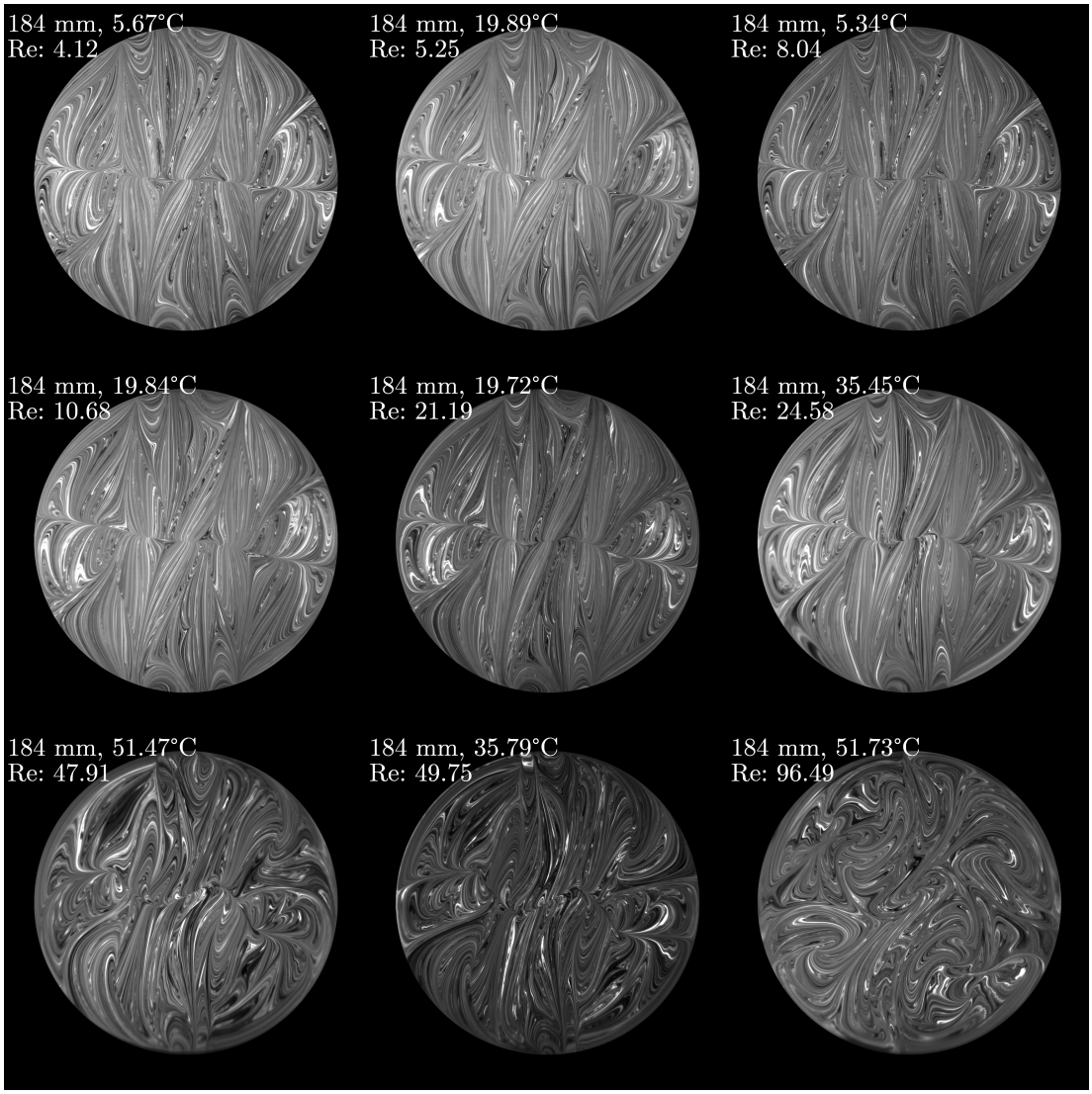


Fig. 5.14. PLIF results for eight repeats (184 mm) for the SMX™ plus Static Mixer across varying temperature and Reynolds number

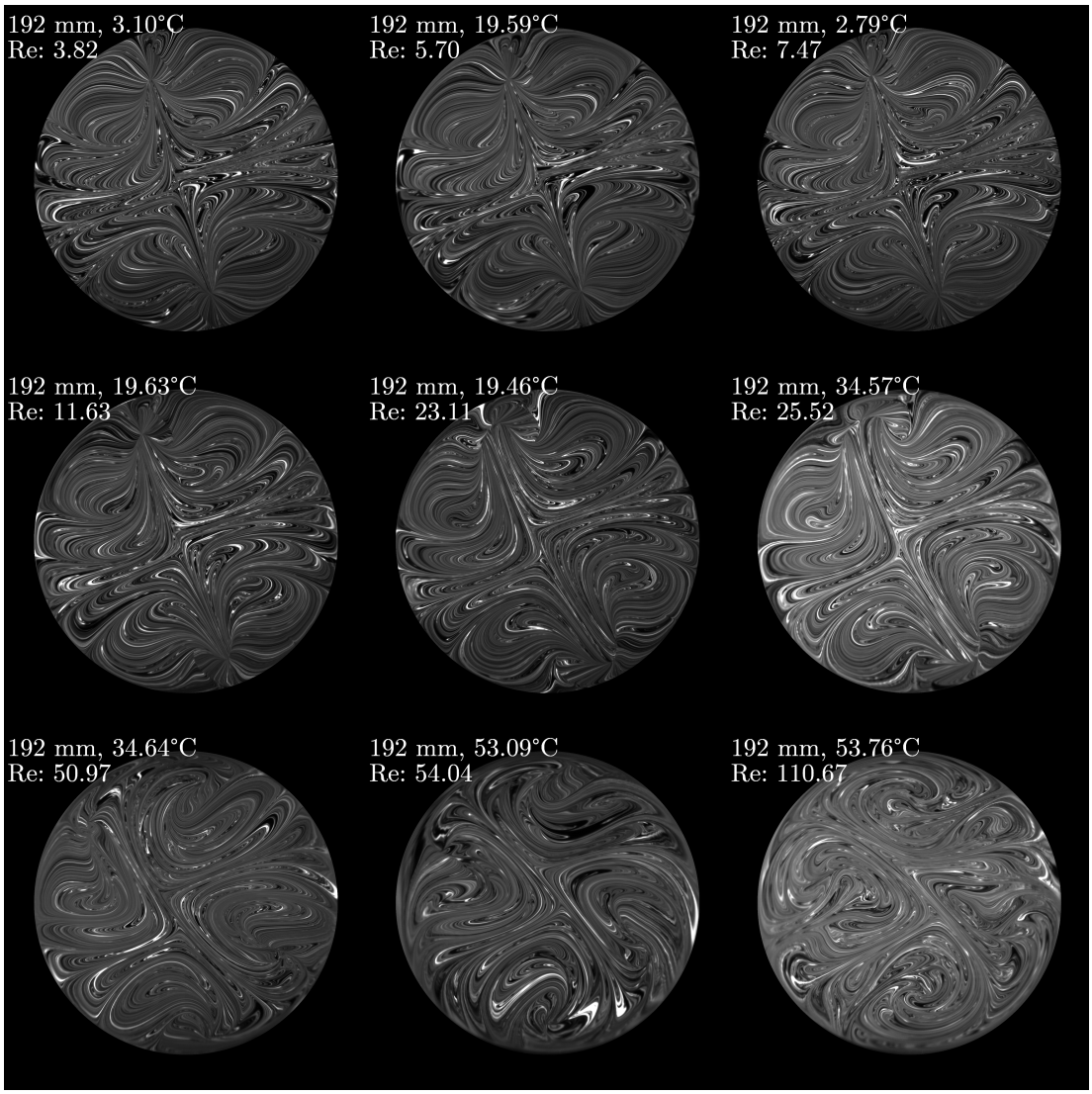


Fig. 5.15. PLIF results for six repeats (192 mm) for the CALGAVIN Static Mixer across varying temperature and Reynolds number

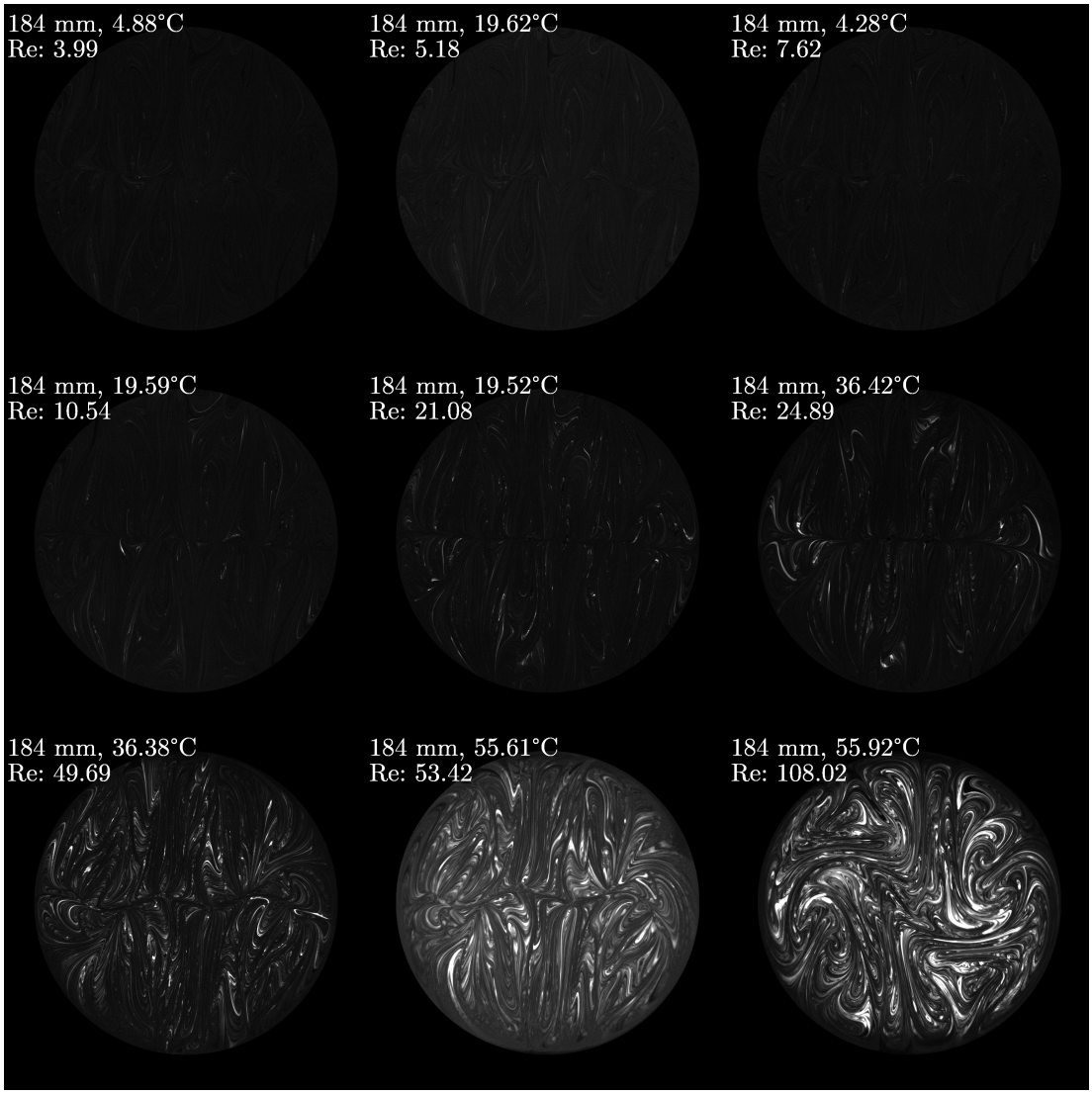


Fig. 5.16. Pixel flux heatmap for eight SMX™ static mixers with proportional scaling

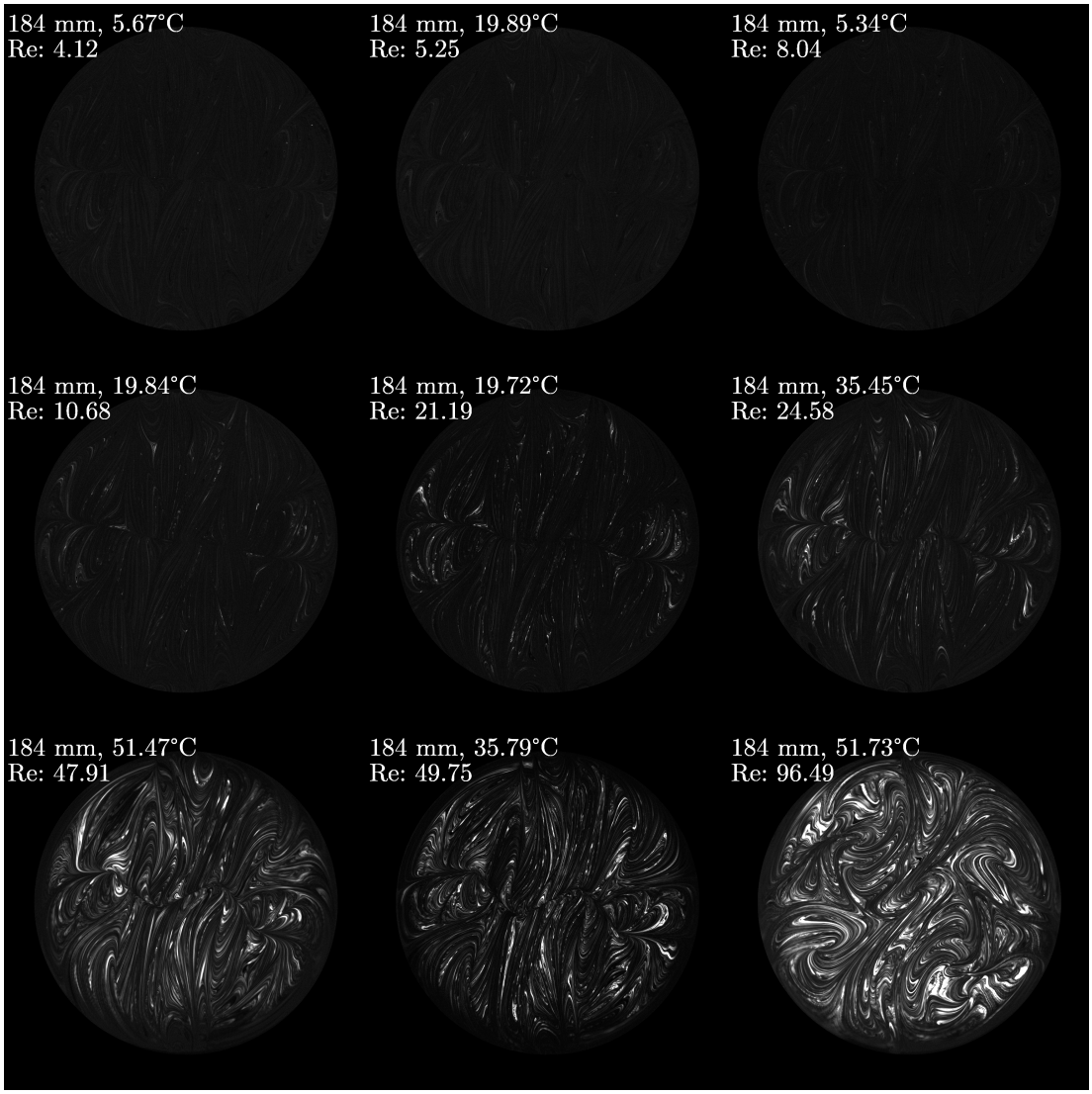


Fig. 5.17. Pixel flux heatmap for eight SMX™ plus static mixers with proportional scaling

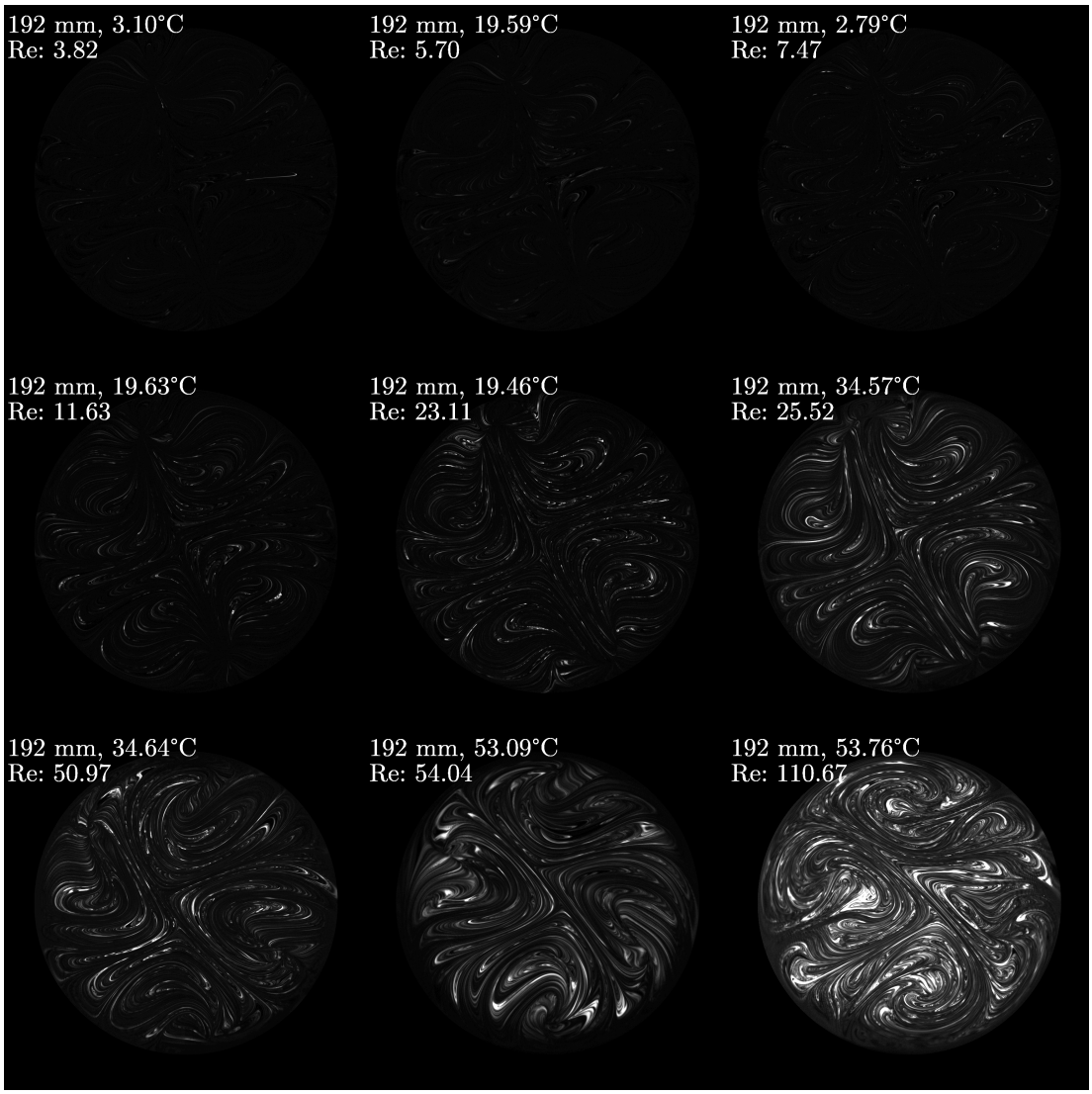


Fig. 5.18. Pixel flux heatmap for six CALGAVIN static mixers with proportional scaling

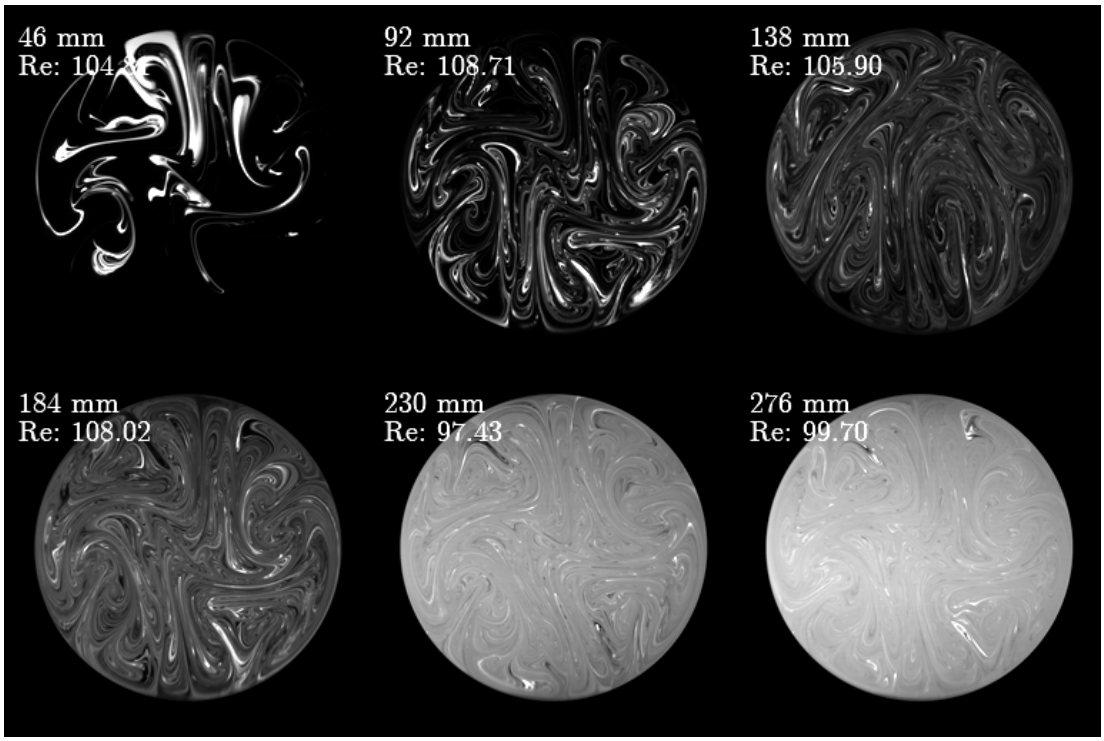


Fig. 5.19. PLIF images of SMX™ static mixer targeting a Reynolds number of 100 for all tested lengths

5.3.3 Coefficient of Variance

In the previous Chapter it was proven that increasing insert length improved mixing by a quantitatively measurable amount, but that changing Reynolds number tested in the 0.01-10 range had no effect on mixing. The PLIF images in the previous section showed that at around the Reynolds number 20 point, the mixing outlet image began to change. This section will explore what, if any, impact this has on the CoV.

Another result from the PLIF images is the observation that there was no longer shot-to-shot stability within a test run. Each test run consisted of 100 images taken in sequence every 0.25 seconds and the added chaos meant this was no longer a steady state. The consequence of this is that the images could no longer be averaged before a statistical analysis. The pixel variability would have skewed the results making the averaged images appear more mixed than they were in reality. To compensate for this, the statistical analysis was conducted on each image in the test run and then these analyses were averaged to create a final CoV. Figures 5.20, 5.21 and 5.22 show the relationship between Reynolds number and mixing assessed by CoV.

As with the lower Reynolds number testing, increasing the static mixer length decreases across the CoV and therefore represents an increase in mixing. However, when fitting a linear regression to the points, the trend is no longer largely flat. For the CALGAVIN static mixer there is a very slight downward trend suggesting that the increases Reynolds number has a minor positive influence on mixing. Yet for the SMX™ and SMX™ plus, there is still slight, but more pronounced trend indicating that an increased Reynolds number makes the final mixing level slightly worse. These trends are verified in Table 5.3 and show the coefficients of the slopes from Figures 5.20, 5.21 and 5.22. As seen visually, the mean slope shows that mixing for the SMX™ and SMX™ plus static mixers gets worse as Reynolds number increases and decreases slightly for the CALGAVIN static mixer. These means are very slight with a mean value of zero being very nearly within one standard deviation away from the calculated value.

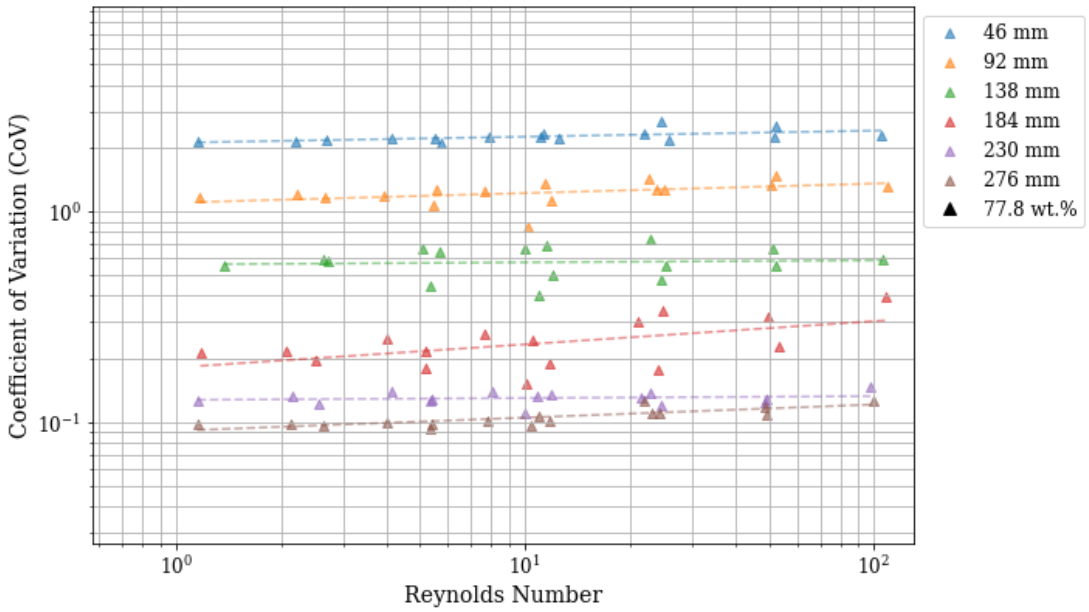


Fig. 5.20. The influence of Reynolds Number on CoV for each tested length of the SMX™ Static Mixer

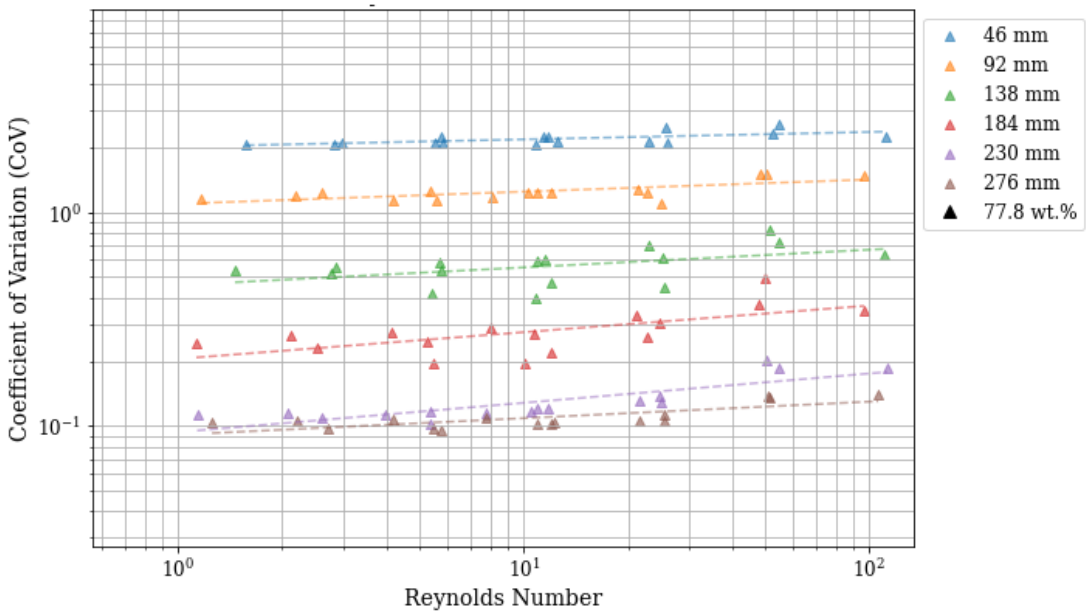


Fig. 5.21. The influence of Reynolds Number on CoV for each tested length of the SMX™ plus Static Mixer

This is an interesting result. The PLIF images clearly show an increase in chaos and the two dimensional slices of vortices yet this does not increase mixing level and may in fact decrease it slightly for some static mixers when CoV is used as the metric.

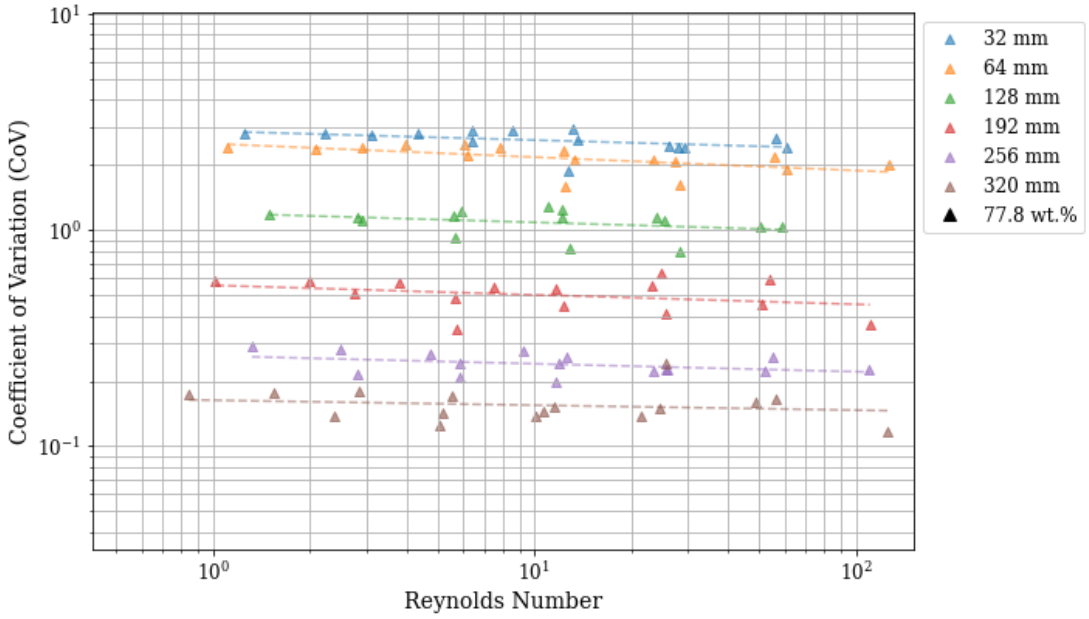


Fig. 5.22. The influence of Reynolds Number on CoV for each tested length of the CALGAVIN Static Mixer

Mixer Type	Size (mm)	Slope	Intercept	nRMSE (%)
CALGAVIN Static Mixer	32	-0.0411	1.0528	8.87
	64	-0.0620	0.9196	9.65
	128	-0.0430	0.1811	11.93
	192	-0.0439	-0.5887	15.65
	256	-0.0367	-1.3396	9.82
	320	-0.0229	-1.8128	17.92
	Average	**-0.0416**	**-0.2646**	**12.31**
	Std Dev	**0.0126**	**1.1836**	**3.68**
SMX™	46	0.0287	0.7541	5.47
	92	0.0452	0.0993	10.33
	138	0.0097	-0.5758	15.78
	184	0.1099	-1.7023	21.03
	230	0.0089	-2.0568	6.69
	276	0.0623	-2.3935	5.88
	Average	**0.0441**	**-0.9792**	**10.86**
	Std Dev	**0.0382**	**1.2653**	**5.96**
SMX™ plus	46	0.0345	0.7101	4.96
	92	0.0569	0.0943	7.11
	115	0.0015	-0.2135	21.91
	138	0.0830	-0.7840	16.60
	184	0.1249	-1.5792	19.26
	230	0.1375	-2.3704	12.07
	276	0.0775	-2.3981	8.09
	Average	**0.0736**	**-0.9344**	**12.57**
	Std Dev	**0.0454**	**1.0964**	**6.18**

Table 5.3
Consolidated Linear Regression Parameters for CoV over Reynolds Number Data for All Mixer Types with 77.8 wt.% Glycerol

5.3.4 CALGAVIN Mixing Number

Moving to the CG Number, largely the same evaluation is seen as shown in Figures 5.23, 5.24 and 5.25 as with CoV. The increase in static mixer length improves mixing as seen by a decreasing CG Number, but Reynolds number in this range has a negligible effect. There is less effect seen with CG Number than with CoV with straighter trendlines and less scatter. Unlike with CoV, there is no overriding correlation of increased or decreased mixing at the high end of Reynolds number. This again indicates that despite the beginning of boundary separation and increased chaos, there is no resultant increase in mixing that accompanies it.

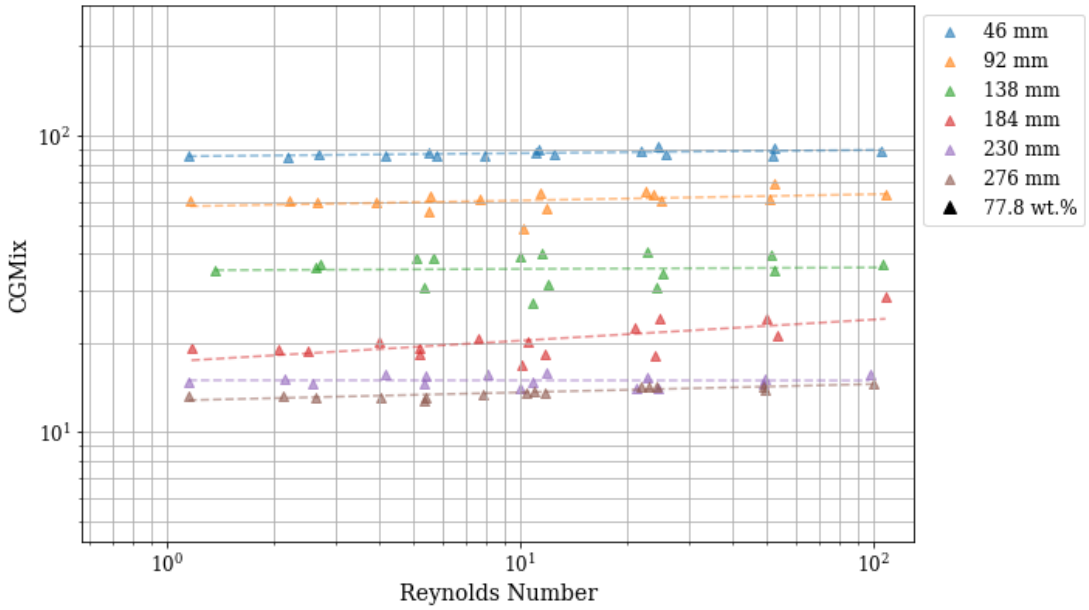


Fig. 5.23. The influence of Reynolds Number on CG Number for each tested length of the SMX™ Static Mixer

The trendlines from these Figures have the coefficients and average statistics seen in Table 5.4. As with the CoV data, the SMX™ and SMX™ plus data show a very slight trend of mixing getting marginally worse as Reynolds number increases with the CALGAVIN static mixer getting slightly better. The coefficients are small and are consistent between CoV and CG Number.

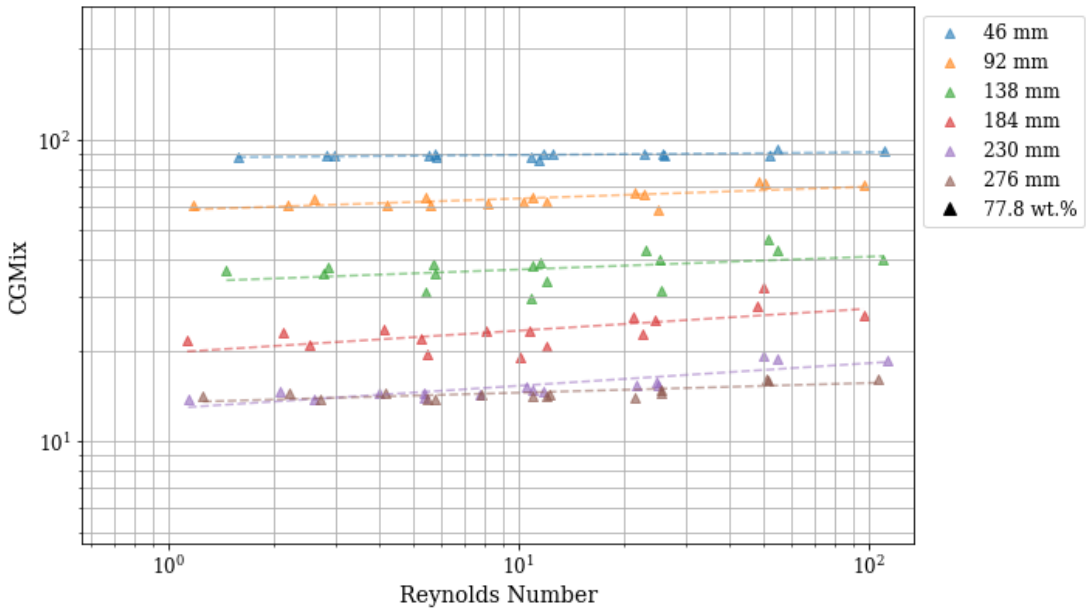


Fig. 5.24. The influence of Reynolds Number on CG Number for each tested length of the SMX™ plus Static Mixer

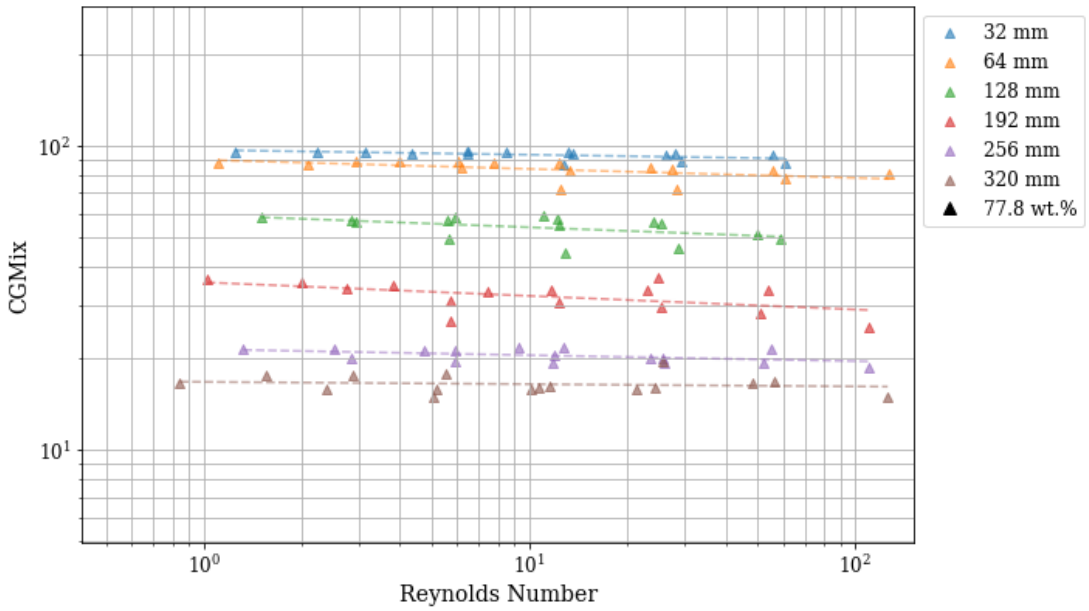


Fig. 5.25. The influence of Reynolds Number on CG Number for each tested length of the CALGAVIN Static Mixer

The conclusion here is that despite the dramatic differences in the PLIF images in this higher Reynolds range compared to that in Chapter 4, the result on mixing is

Mixer Type	Size (mm)	Slope	Intercept	nRMSE (%)
CALGAVIN Static Mixer	32	-0.0157	4.5731	2.61
	64	-0.0296	4.4979	5.20
	128	-0.0398	4.0799	7.35
	192	-0.0446	3.5719	9.04
	256	-0.0196	3.0658	4.32
	320	-0.0074	2.8187	6.88
	Average	**-0.0261**	**3.7677**	**5.90**
	Std Dev	**0.0137**	**0.7379**	**2.21**
SMX™	46	0.0108	4.4435	1.87
	92	0.0209	4.0539	6.70
	138	0.0048	3.5592	10.60
	184	0.0711	2.8503	10.23
	230	-0.0004	2.7064	3.93
	276	0.0280	2.5478	1.95
	Average	**0.0225**	**3.1935**	**5.88**
	Std Dev	**0.0218**	**0.6928**	**3.59**
SMX™ plus	46	0.0089	4.4663	1.48
	92	0.0390	4.0648	4.45
	115	-0.0171	3.9074	14.59
	138	0.0425	3.5145	10.54
	184	0.0728	2.9781	10.35
	230	0.0749	2.5523	5.59
	276	0.0323	2.5974	3.63
	Average	**0.0362**	**3.4401**	**7.52**
	Std Dev	**0.0312**	**0.6874**	**4.59**

Table 5.4
Consolidated Linear Regression Parameters for CG Mixing Number over Reynolds Number Data for All Mixer Types with 77.8 wt.% Glycerol

slight if there is any real difference at all. The suggestion is that although an increased macro level of mixing does clearly occur at this level, it simply results in the changing of the direction of laminar flow streams. There is not yet enough energy in the vortex dissipation to shear through the flow layers and they are instead just redirected. This would be expressed as having a Kolmogorov scale above the micron level. With this happening the outlet mixing cross-section is altered but the mixing at micron-scale evaluated in PLIF is not actually improved at all. What is not necessarily clear here

however is if this change in mixing is not captured by either CoV or CG Number or whether this is a real physical phenomenon.

5.3.5 Mixing Efficiency

As previously done in Chapter 4, mixing efficiency is evaluated by plotting how the CoV and CG Number change with the insert length and with the Fanning Friction Factor. This allows the evaluation of efficiency both in terms of mixing in the shortest length and with the smallest energy penalty. The first set of Figures (5.26 and 5.27) contain the insert length efficiency curves for CoV and CG Number respectively.

Using either CoV or CG Number as the mixing criteria, the CALGAVIN static mixer requires a longer mixer to achieve the same level of mixing as an SMX™ or SMX™, the latter two performing almost identically.

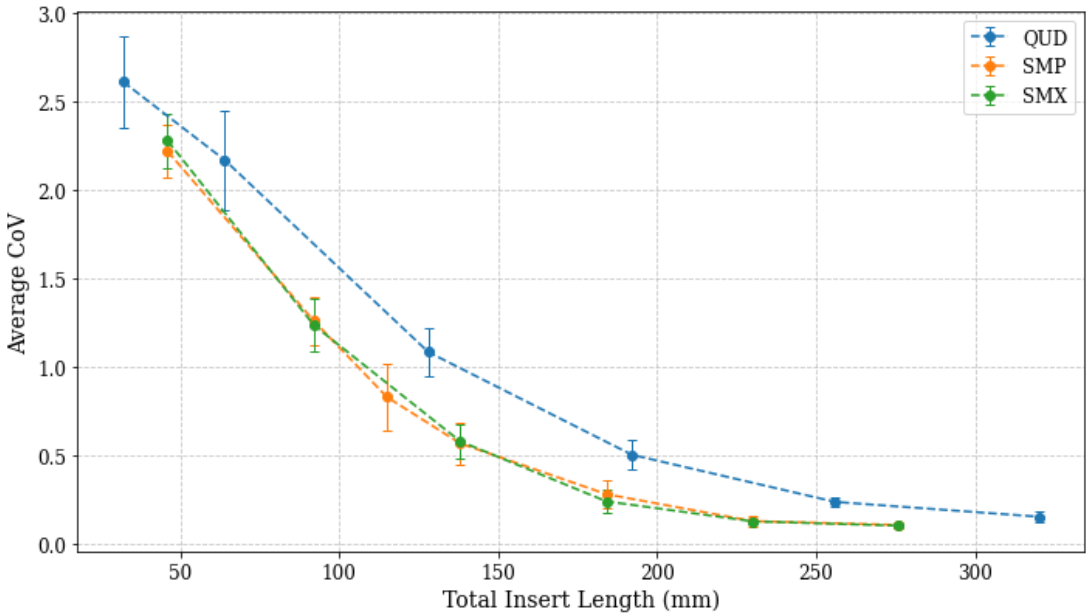


Fig. 5.26. Collated Chart of the effect of insert Length on CoV-based Mixing for the SMX™, SMX™ plus and CALGAVIN Static Mixer

Plotting energy efficiency for CoV and CG Number in Figures 5.28 and 5.29 respectively shows that the SMX™ is the least efficient. The SMX™ plus is the most efficient and the CALGAVIN Static Mixer sits evenly (on a logarithmic scale) between

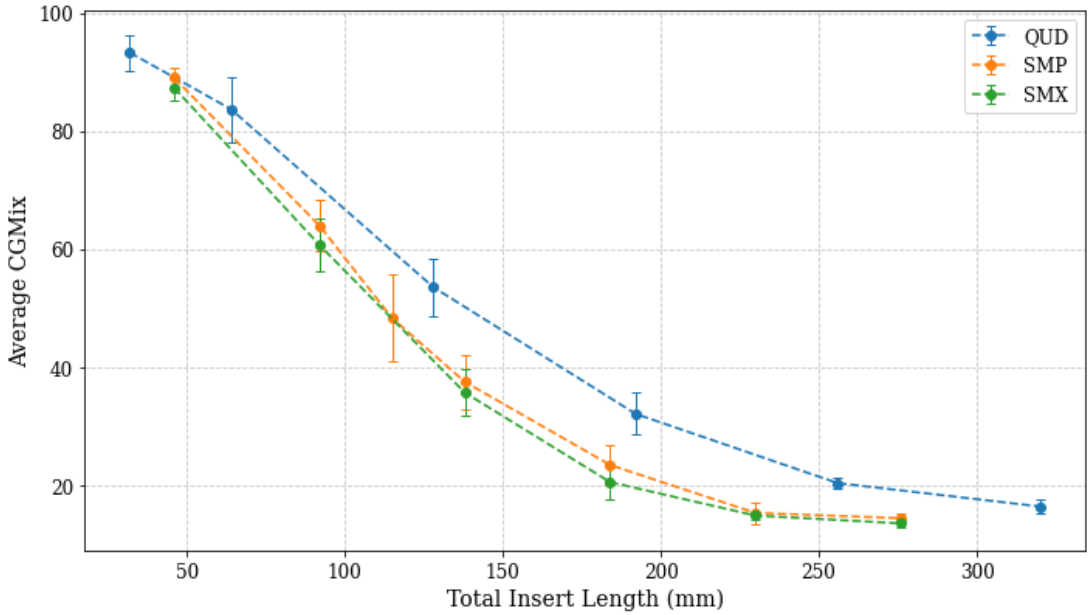


Fig. 5.27. Collated Chart of the effect of insert Length on CG Number-based Mixing for the SMX™, SMX™ plus and CALGAVIN Static Mixer at Reynolds number 1

the two. The data is more sparse and shows unusual jumps with the SMX™ plus data. This is experimental error caused by the very low pressure drop that this lower viscosity fluid caused.

5.4 | Mixing Results Across Glycerol Mass Fractions

An important aspect of having a mixing test rig that is built to test varied rheologies is that the data should remain consistent went tested across these different rheologies. Excellent pressure drop consistency (and therefore on-line viscosity measurement) was proven in Section 5.3.1. This section will explore this concept for mixing results.

The 99.8 wt.% and 77.8 wt.% glycerol mass fractions were chosen, in part, to ensure an overlap between the two test regimes. This allows the comparison of PLIF tests at the same Reynolds number emergent from different flow properties. Figure 5.30 contains PLIF images for both these mass fractions where the tests have similar

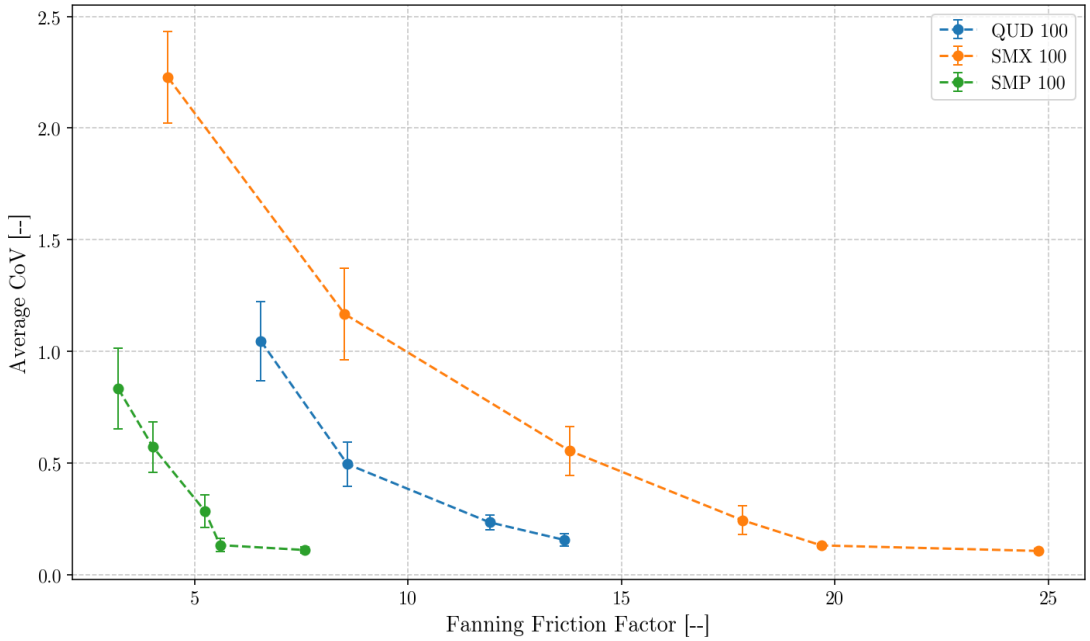


Fig. 5.28. Collated Chart of the Energy Penalty (Fanning friction factor) Required to Achieve Certain Mixing Levels as Assessed by CoV for the SMX™, SMX™ plus and CALGAVIN Static Mixer at a Reynolds Number of 50

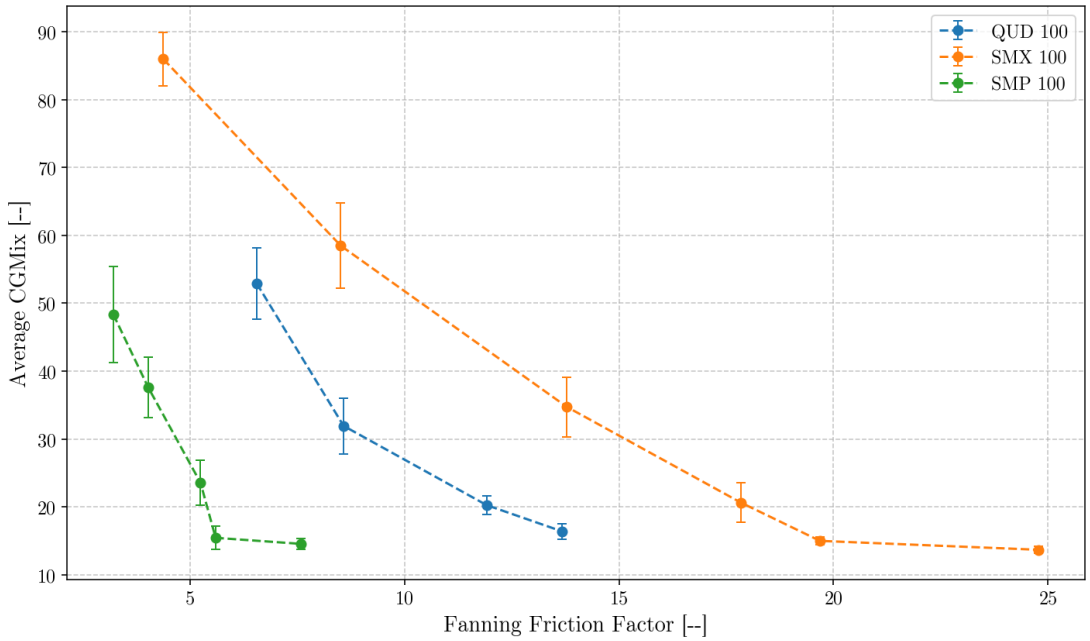


Fig. 5.29. Collated Chart of the Energy Penalty (Fanning friction factor) Required to Achieve Certain Mixing Levels as Assessed by CG Number for the SMX™, SMX™ plus and CALGAVIN Static Mixer at a Reynolds Number of 50

Reynolds numbers but different flow velocities, viscosities and temperatures for six units of the SMX™ static mixer. Subjectively the images appear to be very similar despite the different flow velocities, temperatures and mass fractions used to take them which demonstrates the consistency of testing on the test rig in a rough extent but to prove this the images need comparing numerically.

To quantitatively test the crossover of the two different mass fractions, the calculated mixing number data for both sets of mass fractions can be combined onto one graph. For CoV based calculation, this generates Figures 5.31, 5.32 and 5.33 for the CALGAVIN static mixer, the SMX™ and the SMX™ plus, respectively. For CG Number based calculation, see Figures 5.34, 5.35 and 5.36.

Table 5.5 is a comprehensive table containing the linear regression constants and Root Mean Square Error (RMSE) value of the data that is used to calculate the regressions for each length of each mixer for both the 99.8 wt.% and the 77.8 wt. % glycerol tests using both the CoV and CG Number mixing quantification method. The table also contains the average and standard deviation when combining all the different lengths for each static mixer. As with the separate tests, the data shows that there is very little impact of mixing from Reynolds number in the Reynolds number range of 0.05 to 120. With all data combined there is a minor negative correlation between the two giving the indication that increasing Reynolds number has a marginal effect on increasing mixing. However, by computing the change in CoV caused by increasing the Reynolds number from 0.05 to 120 for the SMX™ gives a change of -0.009 and demonstrates the lack of any practical affect.

Normally a metric such as the Root Mean Square Error (RMSE) can be used to assess the validity of a fitted model, however, since CoV and CG Mixing Number utilise different scales (0 to 1 and 0 to 100 respectively), the evaluated numbers are not comparable. To correct this, the RMSE values are normalised creating a normalised RMSE (nRMSE) by dividing them by the mean of observed values. The equation for this analysis is seen in Equation 5.1. Using nRMSE allows an expression of the error as

a percentage of the data range, making it dimensionless and comparable across these different metrics.

$$\text{nRMSE} = \frac{\sqrt{\frac{1}{n}\sum_{i=1}^{n}(y_i - \hat{y}_i)^2}}{\bar{y}} \times 100\% \tag{5.1}$$

Where y_i are the experimentally measured values, $\hat{y}_i$ are the model predicted values, n is the number of data points, and $\bar{y}$ is the mean of the measured values.

The nRMSE values in Table 5.5 indicate that the CG Mixing Number models have lower normalised errors compared to the CoV models across all insert types and insert lengths. This suggests that the CG Mixing Number provides a more consistent measure of the mixing performance of each static mixer tested with nRMSE averaging at 6.39% for CG Number and 11.46% for CoV (80% higher) for the static mixers tested.

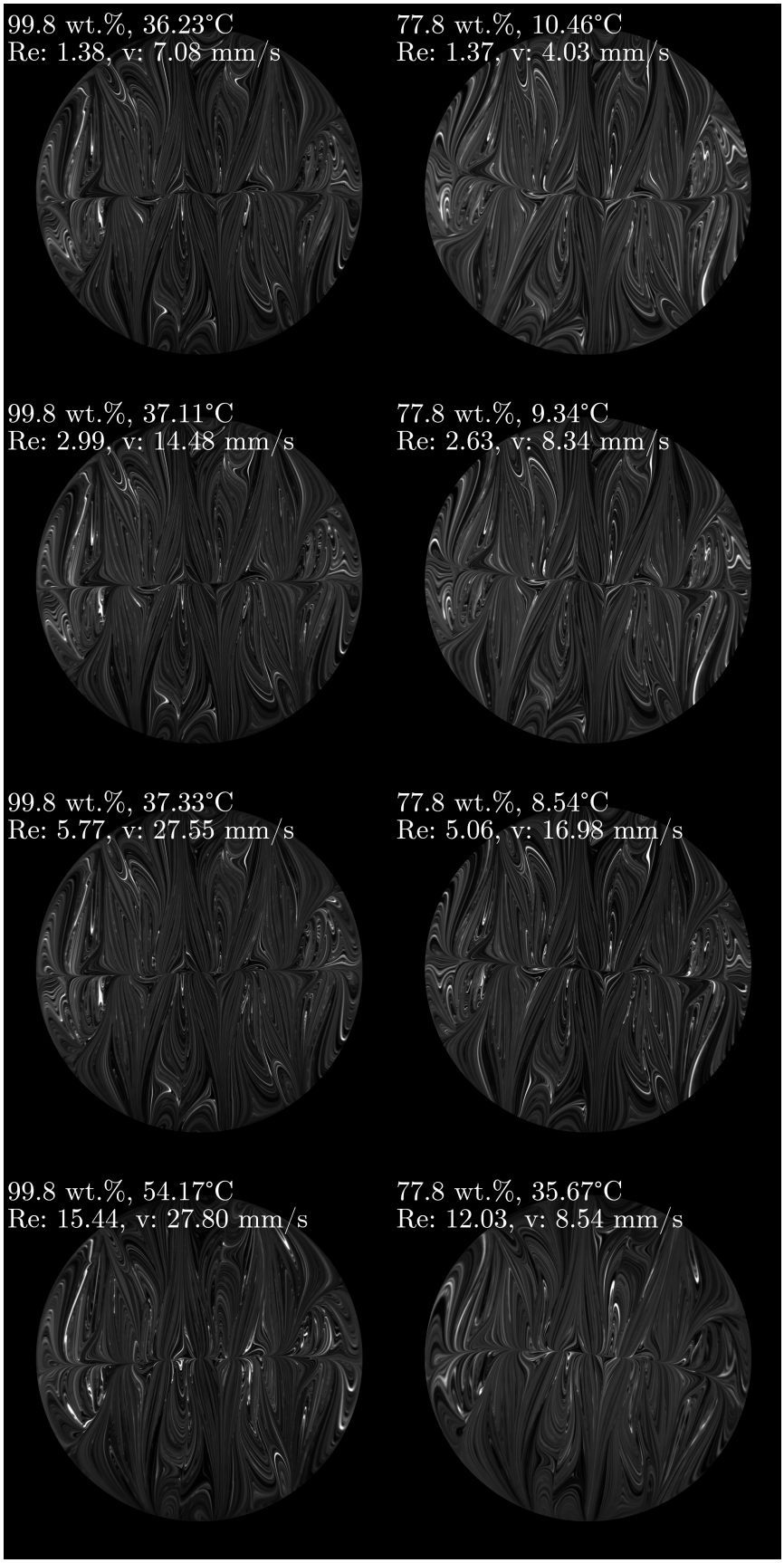


Fig. 5.30. PLIF images at comparable Reynolds Numbers for the 99.8 wt.% and the 77.8 wt. % Tests of the SMX™ Static Mixer

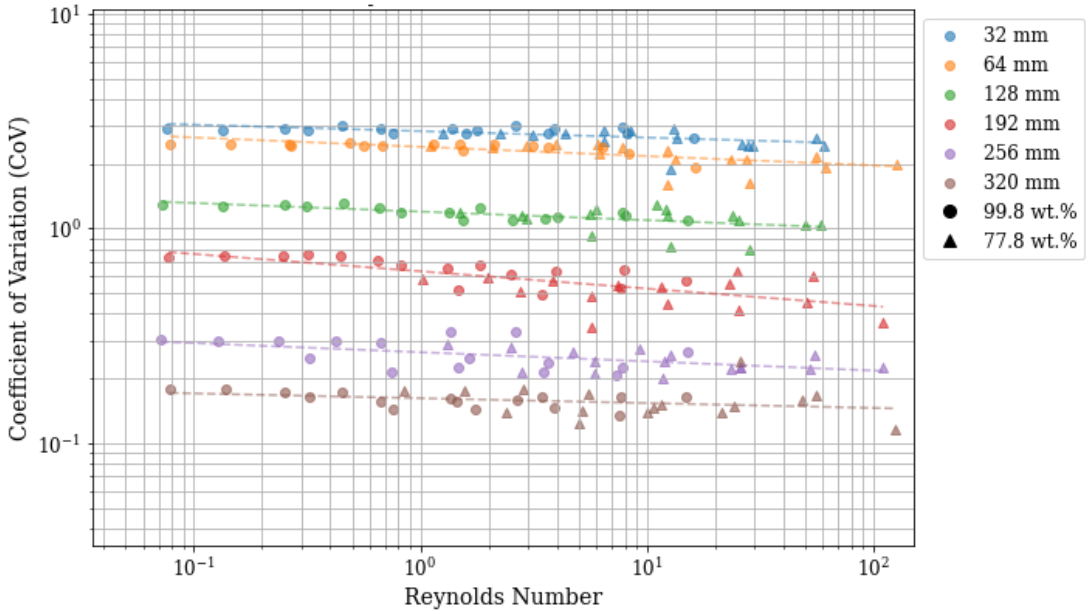


Fig. 5.31. The influence of Reynolds Number on CoV for each tested length of the CALGAVIN Static Mixer Across 99.8 wt.% and the 77.8 wt. % Tests

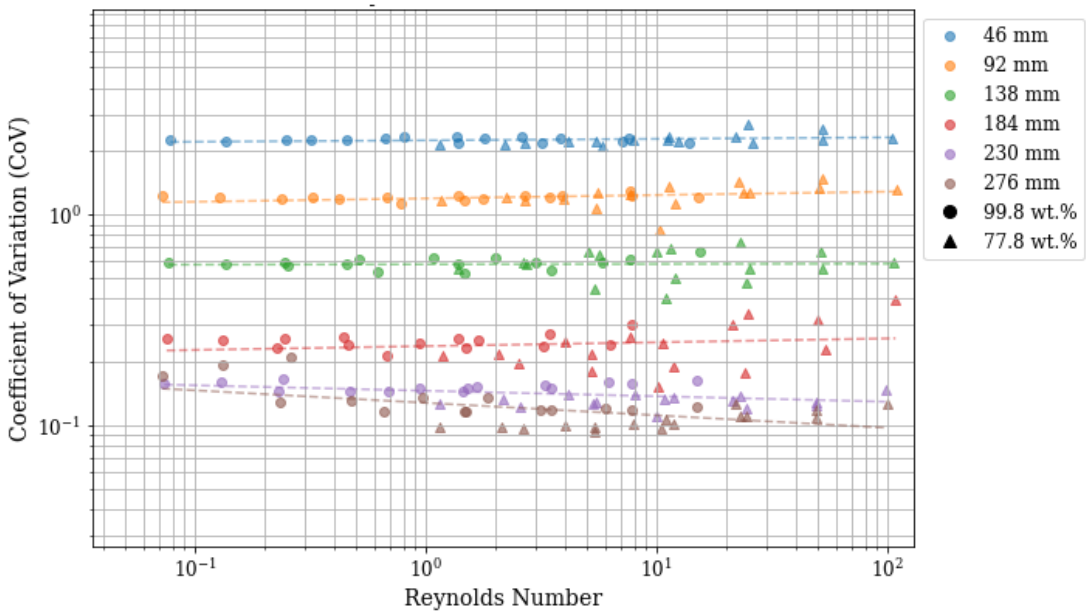


Fig. 5.32. The influence of Reynolds Number on CoV for each tested length of the SMX™ Static Mixer Across 99.8 wt.% and the 77.8 wt. % Tests

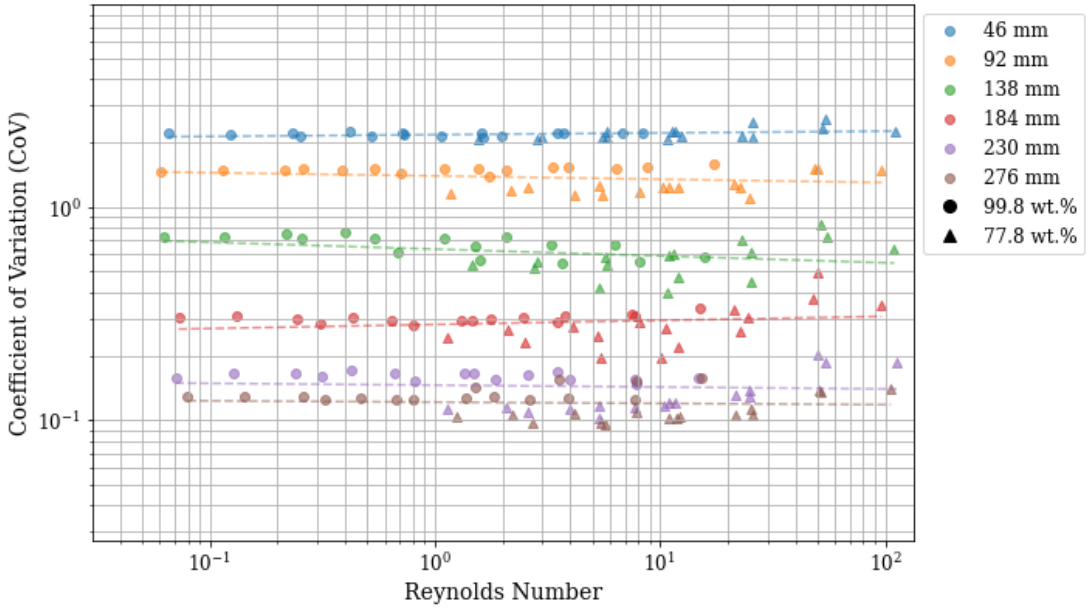


Fig. 5.33. The influence of Reynolds Number on CoV for each tested length of the SMX™ plus Static Mixer Across 99.8 wt.% and the 77.8 wt. % Tests

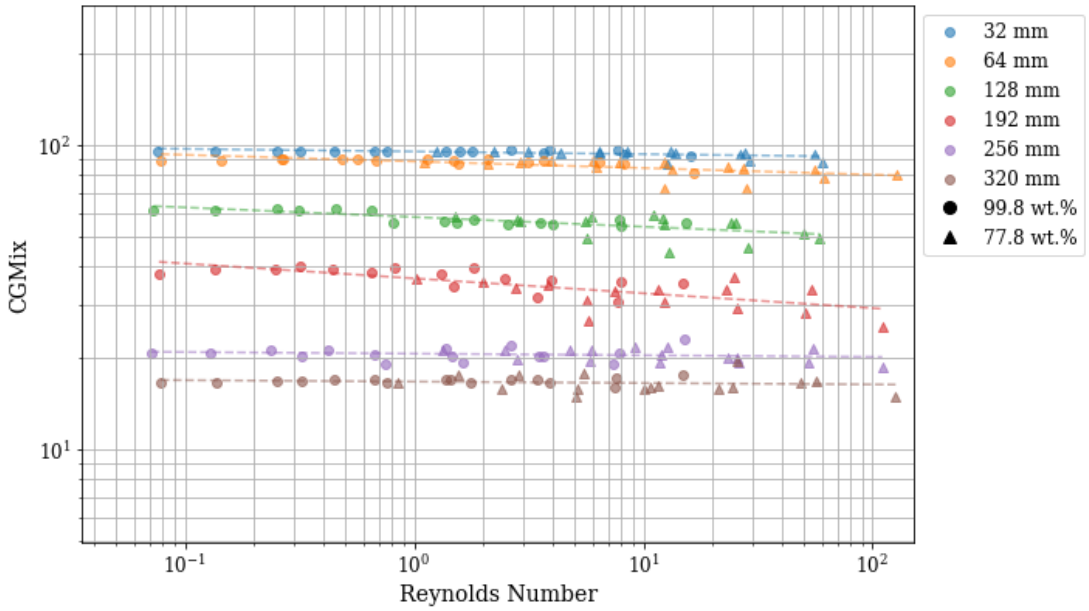


Fig. 5.34. The influence of Reynolds Number on CG Number for each tested length of the CALGAVIN Static Mixer Across 99.8 wt.% and the 77.8 wt. % Tests

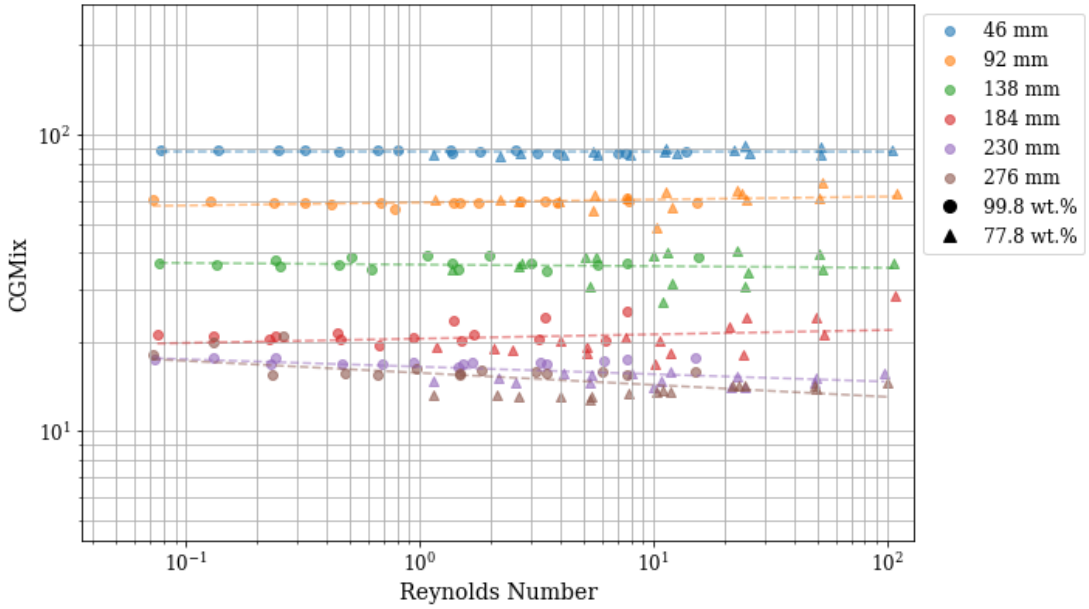


Fig. 5.35. The influence of Reynolds Number on CG Number for each tested length of the SMX™ Static Mixer Across 99.8 wt.% and the 77.8 wt. % Tests

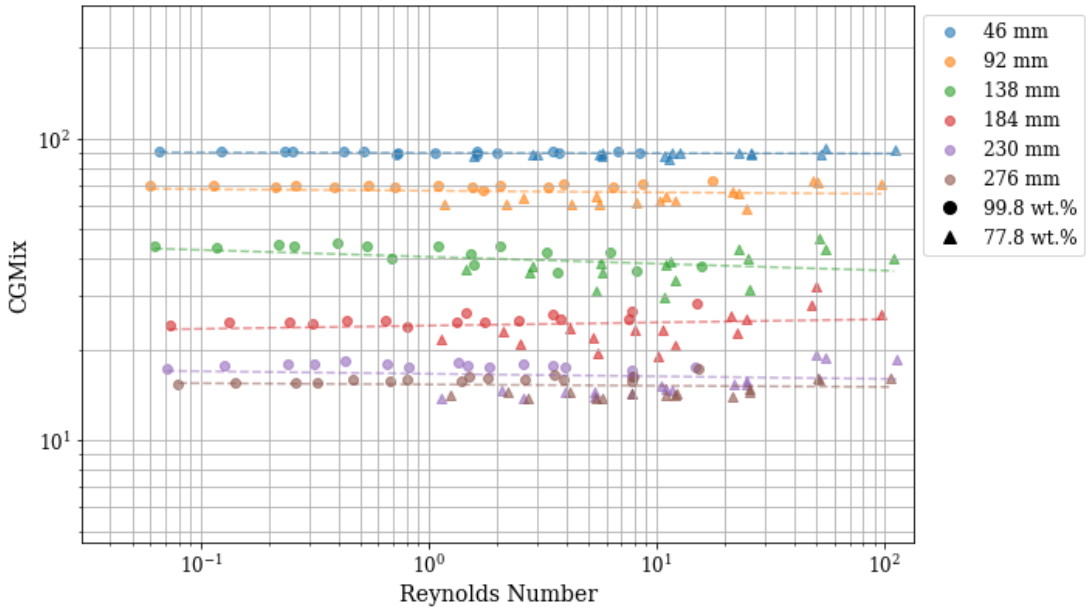


Fig. 5.36. The influence of Reynolds Number on CG Number for each tested length of the SMX™ plus Static Mixer Across 99.8 wt.% and the 77.8 wt. % Tests

Insert Type	Size (mm)	Coefficient of Variation (CoV)			CG Mixing Number		
		Slope	Intercept	nRMSE (%)	Slope	Intercept	nRMSE (%)
CALGAVIN Static Mixer	32	-0.0299	1.0431	6.95	-0.0086	4.5579	2.08
	64	-0.0433	0.8751	7.68	-0.0217	4.4829	4.07
	128	-0.0399	0.1799	8.42	-0.0317	4.0625	5.39
	192	-0.0806	-0.4602	12.70	-0.0488	3.5990	7.55
	256	-0.0427	-1.3283	12.13	-0.0053	3.0303	4.79
	320	-0.0226	-1.8219	13.40	-0.0046	2.8190	5.12
	Average	**-0.0432**	**-0.2521**	**10.21**	**-0.0201**	**3.7586**	**4.83**
	Std Dev	**0.0200**	**1.1670**	**2.46**	**0.0168**	**0.6652**	**1.80**
SMX™	46	0.0069	0.8130	4.66	-0.0001	4.4731	1.78
	92	0.0159	0.1785	8.17	0.0100	4.0782	5.12
	138	0.0015	-0.5421	11.94	-0.0053	3.5964	7.94
	184	0.0182	-1.4360	18.90	0.0145	3.0217	11.01
	230	-0.0260	-1.9240	8.82	-0.0252	2.8038	6.09
	276	-0.0593	-2.0560	17.62	-0.0404	2.7557	9.80
	Average	**-0.0071**	**-0.8111**	**11.02**	**-0.0077**	**3.4548**	**6.96**
	Std Dev	**0.0301**	**1.2498**	**5.54**	**0.0191**	**0.6829**	**3.37**
SMX™ plus	46	0.0082	0.7834	4.44	-0.0014	4.4966	1.56
	92	-0.0154	0.3371	10.84	-0.0052	4.2061	6.14
	138	-0.0320	-0.4537	16.09	-0.0227	3.7017	9.98
	184	0.0190	-1.2683	17.61	0.0106	3.1761	10.48
	230	-0.0087	-1.9244	17.74	-0.0085	2.8085	9.99
	276	-0.0059	-2.1076	14.19	-0.0041	2.7271	6.25
	Average	**-0.0058**	**-0.7723**	**13.15**	**-0.0052**	**3.5194**	**7.40**
	Std Dev	**0.0163**	**1.0884**	**5.15**	**0.0117**	**0.6725**	**3.29**

Table 5.5
Linear Regression Parameters and Normalised RMSE (nRMSE) for CoV and CG Mixing Number over Reynolds Number Data for All Insert Types and All Fluid Rheologies with Averages and Standard Deviations

5.5 | Conclusion and Next Steps

5.6 | Conclusion and Next Steps

This chapter has expanded the Reynolds number range from the previously tested 0.05 to 12 up to 120 by increasing the water content in the glycerol test fluid, creating a 77.8 wt.% glycerol solution from the original 99.8 wt.%. The data was combined considering both Fanning friction factor and two forms of mixing quantification, CoV and CG Number. In all of these cases, the excellent continuation of data demonstrated that the constructed test rig facility has accurate online viscosity measurement and can produce repeatable results. It was proven that the friction factor strongly followed the power law until around a Reynolds number of 20, where an expected increase in forced turbulence caused higher Fanning friction factors per Reynolds number for all mixers tested. This turbulence was clearly visible in the PLIF images that exhibited visual changes as the Reynolds number increased beyond 20 and showed shot-to-shot variability in previously static images; the variability was likely the result of slicing vortices that formed off the tail of the structures of the static mixer.

Despite the obvious visual change, this increased turbulence did not impact the evaluated mixing quantification numbers, with CoV and CG Number regressions fitting linear models with good accuracy and negligible slope. This result is likely showing that the increased turbulence is causing spatial movement of fluid components, but that it lacks sufficient energy to blend at the 12 μm resolution of the PLIF imaging system and therefore has no quantifiable impact on mixing. Combining the data sets did not change the ranking of the tested static mixers, with the SMX™ being the best performing mixer, followed by the SMX™ plus, and then the CALGAVIN Static Mixer. In energy loss, however, the order was reversed, with the CALGAVIN mixer incurring the least pressure drop. By combining these factors and looking at mixing per unit energy loss, the SMX™ plus becomes the most efficient, followed by the CALGAVIN mixer, with the SMX™ last.

Comparing the performance of the CoV and CG Number models for assessing the mixing level using normalised RMSE showed that CG Number could map the experimental data with an average of 80% less spread than the CoV data. The conclusions of the mixer performance were the same for both methods, with no static mixers changing ranked positions, showing that CoV is still a reliable indicator of performance. CG Number is more computationally expensive to calculate—though negligibly so for modern computational hardware—but is recommended when benchmarking more closely matched static mixer inserts—for example, with design iterations of a similar model. CG Number also has the benefit of indicating setup errors, such as decreased flow rate of a component, as it will react to the deviation from the mean where CoV will not. It also considers the whole mixing area in its final number, unlike the areal fraction method, and finally is the most human-readable number with the final value indicating roughly the percentage area that is not fully mixed.

The novelty of this thesis lies primarily in the design, construction, and validation of the test rig itself. The facility created here is the fastest, most accurate, and most capable of its kind, generating the highest quality PLIF mixing images to date. This rig allows for rapid prototyping and evaluation of static mixer designs at a level of consistency and fidelity previously not achieved. The data it has produced is extensive, rigorous, and repeatable, forming a solid experimental foundation for future analysis of static mixer performance.

Further novelty lies in the generation of multiple static mixer geometries created and iteratively refined using this test rig. These inserts were developed specifically through testing within this system, allowing for unique optimisation of performance. However, due to confidentiality agreements, neither the exact designs nor the reasons behind their performance can be disclosed in this thesis.

While this work does not set out to exhaustively explore the theoretical models of static mixing or conduct statistical comparisons between studies, the facility created here

enables others to do so with confidence. The focus was to build the best experimental system possible, and the results clearly show that goal has been achieved.

As always with experimental testing, there is a desire to expand the parameter range. Further increasing the Reynolds number range of the system is the most interesting direction—particularly in search of the point at which increasing Reynolds number does have an effect on mixing. The test facility has been proven to be consistent across fluid rheologies, and this further testing could be easily conducted by further increasing the water content of the aqueous glycerol. A worthwhile alteration to the facility would be to find a method to accurately measure differential pressure below 3 mbar to facilitate measuring the pressure drop with a lower viscosity fluid. Yet given that the pressure drop has so far been proven to be exactly proportional to the length of the mixer, the lower insert length tests that are difficult to measure could be calculated from the full insert length tests. Further to this, mixing is nearly complete at the end of the 300 mm test section, but increasing the length would enable finding the limits of this PLIF system in addition to making tests on low shear static mixers more comprehensive.

CHAPTER 6

Computational Fluid Dynamics in Laminar Mixing

6.1 Introduction

Being able to conduct accurate numerical simulations of static mixer flows is hugely beneficial to static mixer design. For every design iteration to be tested experimentally, each design needs to be fabricated, resulting in substantial time and capital penalties—though this has been made easier with the modern advent of 3D printing to some degree. If the numerical simulation was accurate enough, the static mixer could be 3D modelled and tested fully in computer space; then the best-performing design could be fabricated and tested. One step further is the very recent innovations in generative design that could allow an algorithm or neural network to subtly change static mixer designs or innovate new ones entirely. These could be automatically simulated and enable static mixer innovation with limited human input. The stipulation with this though is that the laminar mixing simulations must be representative. This chapter will generate mixing results from typical passive scalar plots and compare them to a novel form of particle tracking and then to real experimental Planar Laser-Induced Fluorescence (PLIF) results.

6.2 | Materials and Methods

6.2.1 Numerical Theory

The literature review in Section 2.5.2 discussed the governing equations for incompressible Newtonian flow, including the Navier–Stokes equations and their role in modelling fluid dynamics in laminar flow. Here, these principles are applied specifically to the simulation of static mixers, with particular focus on the passive scalar method and particle tracking to evaluate mixing efficiency.

6.2.2 Modelling and Simulation Environment

The mixing geometries were modelled to scale in Autodesk Fusion, a parametric Computer-Aided Design (CAD) design software that can accurately represent static mixers in computer space. Once modelled, these were exported as STEP files for use in Siemens STAR-CCM+.

STAR-CCM+ is a comprehensive pipeline-based CFD software developed by Siemens, widely used in both academic and industrial fluid dynamics. It supports a wide range of built-in physics and solver models, including laminar, turbulent, and multiphase flows. Its strength lies in the seamless integration of the complete CFD workflow—from CAD import and meshing to solver setup, execution, and post-processing—within a single environment. This minimises errors during data transfers and enables efficient optimisation of the simulation process.

With the STEP files imported, the inbuilt CAD modeller was used to compute the fluid volume and to label all the boundaries. Like all Computational Fluid Dynamics (CFD) software, the boundary conditions were established alongside the relevant physics and solver parameters before running the simulation and resolving the flow field. STAR-CCM+ also includes post-processing tools used to visualise the flow field and eventually to image the mixing.

Further analysis of exported results was conducted in Python and Microsoft Excel.

6.2.3 Application Model

The same static mixer geometries tested in the PLIF experimentation were modelled and tested here, the CALGAVIN static mixer, the SMX™ and SMX™ plus. These are described in detail in Section 4. In addition to these, the NOV Kenics mixer was also tested as part of these simulations. The NOV static mixer is a helical design static mixer with alternative clockwise and anticlockwise baffles that span the diameter of the tube diameter. Each element starts as a thin metal rectangle that is twisted 180 degrees and attached to the following counter-rotating element at 90 degrees to the prior. The result is alternating splits and folds of the fluids in a manor considered low shear when compared with mixers tested so far. This was included because of its comparatively low level of mixing which would allow easy 1:1 visual comparison of mixing between it and any PLIF images.

To develop the fluid volume required for CFD, these geometries where imported in STAR-CCM+ where the rest of the model was created. To do this, the design of the experimental PLIF set up was copied by surrounding the static mixer in a cylinder of the tube inner diameter (ID) at 23 mm. The injection tube was modelled at the inlet (6mm ID and 8mm ID) and was given sufficient length for a fully developed laminar flow profile to develop given by (Bergman, 2011).

$$L_e = 0.0575\,\mathrm{Re} \cdot D \tag{6.1}$$

Given that there is a case for psuedo-turbulence beyond 20 Reynolds as shown in Chapter 5, this limit was selected at the highest possible Reynolds test case. This gave a minimum hydrodynamic entrance length of 26.45 mm which was increased to 50 mm for both a safety margin and to allow for higher Reynolds tests if needed. This mesh was then used for all Reynolds tested for efficiency due to the extensive computational

time required to generate meshes and the limited computational penalty from this being a minor length compared with the full length of the tested model.

The fluid volume is then the boolean subtraction of the static mixer geometry and the solid injection tube structure from the internal diameter volume of the modelled tube. This fluid volume is given properties modelling the glycerol used in the PLIF experiments. The flow parameters were as follows, with specific flow properties matching an experimentally tested case:

Property	Value(s) Used
Density (ρ)	1249.768428 kg/m^3
Viscosity (μ)	1.783114 Pa·s
Flow Rate (Q)	0.0009677 m^3/s
Velocity (u)	0.02899 m/s
Pressure Drop (ΔP)	4174.07 Pa
Characteristic Length (L)	0.276 m
Reynolds Number (Re)	0.4673

Table 6.1
Fluid Properties

An example of the model fluid volume and surface boundaries is shown with labels in Figure 6.1. This labels the named surfaces as they are referred to in the following text.

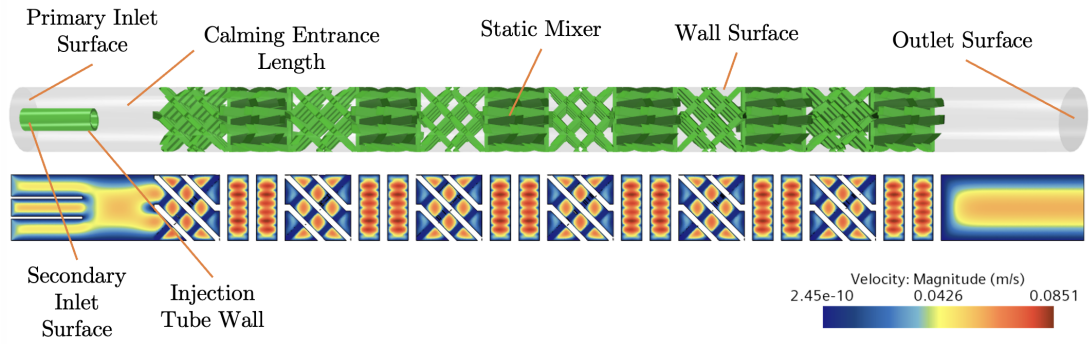


Fig. 6.1. Labelled Fluid Volume Model for Simulations of SMX™ Static Mixer

6.2.4 Numerical Model

To run the simulation, the physics of the model also needs defining. This lists all the models used across all simulations done (though not necessarily all of them in every simulation simultaneously), their function and their set values are seen in Table 6.2.

With the appropriate solver models chosen the remaining parameters are the boundary conditions that copy the experimental test:

- Primary Inlet
  - Boundary Type: Mass Flow Inlet
  - Mass Flow Rate: 0.01408 kg/s
- Secondary Inlet
  - Boundary Type: Mass Flow Inlet
  - Mass Flow Rate: 9.7346e-4 kg/s
- Outlet
  - Boundary Type: Pressure Outlet
  - Backflow Pressure: 0 Pa

These boundary conditions are set to closely replicate the physical test conditions of the mixing rig. A mass flow inlet was used for both the primary and secondary inlets, as this allows precise control over the flow rate entering the domain—critical when attempting to mimic the experimental setup. By defining the mass flow rather than velocity, the simulation automatically adjusts the inlet velocity based on the local fluid density and area, which is more robust for simulations involving changing conditions or non-uniform geometries.

The primary inlet introduces the bulk of the fluid and is set to a mass flow rate of $0.014\,08\,\mathrm{kg\,s^{-1}}$, matching the experimentally measured flow of the undyed glycerol

solution. The secondary inlet represents the dyed fluid stream and is introduced at a significantly lower mass flow rate of $9.7346 \times 10^{-4}\,\mathrm{kg\,s^{-1}}$, again matching the experimental conditions. This mass ratio mimics the experimental dye injection system used in the PLIF tests.

The outlet is set as a pressure outlet with zero backflow pressure (i.e., atmospheric pressure). This allows the fluid to leave the domain freely, simulating an open-ended outlet pipe where the flow is driven purely by the upstream pressure gradient and momentum. Setting the outlet pressure to zero ensures numerical stability while still allowing reverse flow if necessary during transient startup or under complex flow conditions.

Together, these boundary conditions create a controlled and realistic flow scenario that mirrors the actual test rig, ensuring that the simulation results can be directly compared to the experimental data.

Table 6.2
Simulation Models, Descriptions, and Values

Category	Model	Description	Value(s) Used
Flow Continuum	Laminar Flow	Solves the Navier-Stokes equations for low Reynolds number flows where viscous forces dominate over inertial forces.	N/A
	Segregated Flow	Solves mass and momentum equations separately for steady-state incompressible flows. Additional settings include convection, positivity rate limit, and flow boundary diffusion.	Convection: 2nd-order Positivity Rate Limit: 0.2 Flow Boundary Diffusion: true Secondary Gradients: On
	Constant Density	Assumes the liquid phase (glycerol) has a constant density, valid for incompressible flow conditions where density variations are negligible.	1249.768428 kg/m^3
	Constant Viscosity	Assumes that the dynamic viscosity of glycerol is constant, appropriate for isothermal conditions.	1.783114 Pa·s
Initial Conditions	Pressure	Specifies the initial pressure throughout the domain.	0.0 Pa
	Velocity	Specifies the initial velocity throughout the domain.	0.0 m/s, 0.0 m/s, 0.0 m/s
Particle Models	Lagrangian Multiphase	Tracks the trajectories of individual particles within the flow by solving Newton's second law for each particle.	N/A
	Material Particles	Models the solid phase using aluminum particles with constant density. Particles are assumed to be spherical for simplified calculations.	2700 kg/m^3
Particle Forces	Drag	Computes the drag force acting on particles based on their Reynolds number. Suitable for spherical particles in laminar flow.	Schiller-Naumann Model

Continued on next page

Category	Model	Description	Value(s) Used
	Pressure Gradient	Accounts for the effect of pressure variations on particle acceleration and direction, particularly important in non-uniform pressure fields.	N/A
Wall Interaction	Normal Restitution Coefficient	Defines the particle rebound behaviour after collisions with walls, controlling the energy lost or retained.	1.0
	Tangential Restitution Coefficient	Controls the tangential behaviour of particles after wall collisions, influencing their post-collision trajectories.	1.0
Boundary Sampling	Boundary Sampling	Tracks and counts particles crossing specific boundaries, allowing for the collection of particle data such as residence time, mass, and count.	Outlet Boundary Sampling
Solver and Methods	Steady-State, 3D Simulation	Assumes the flow is steady and three-dimensional, focusing on fully developed flow without time-dependent calculations.	N/A
	Solution Interpolation	Enhances the accuracy of the velocity and pressure fields within the flow domain by interpolating the solution between nodes.	Nearest Neighbour Method
Reference Values	Reference Pressure	Ensures that the pressure field remains physically realistic by setting maximum and minimum allowable pressure values to prevent negative pressures.	Maximum: 1.0E8 Pa Minimum: 1000.0 Pa Reference: 101325.0 Pa

Continued on next page

Category	Model	Description	Value(s) Used
Passive Scalar	Passive Scalar Transport	Solves the transport equation for a passive scalar (e.g., concentration) without affecting the momentum field. Used to track scalar quantities within the flow domain.	Diffusion Coefficient: Smallest possible (near zero) Initial Scalar Value (Injection): 100 Initial Scalar Value (Main Flow): 0 Scalar Boundary Conditions: Dirichlet (inlet), Neumann (outlet) Numerical Scheme: 3rd-order accuracy

6.2.5 Meshing and Mesh Independence

The meshing of a model is the discretisation of the fluid volume into finite volumes where the fluid parameters and conditions are homogenous in each cell. It is obvious then that a suitable and high quality mesh is essential for an accurate model. The complex shapes of static mixers do not lend themselves to the use of hexahedral cells. This leaves tetrahedral and polyhedral. Polyhedral have been shown to be more memory efficient and with having more faces, are more likely to have a face normal to the flow direction (the reason why hexahedrals are also not desirable) which will have a positive affect on limiting numerical diffusion - a key characteristic of passive scalar experiments.

The next step is a mesh independence study to assay the cell size requirement. These map the change of a chosen simulated characteristic with the target cell size of a mesh. A finer mesh is more readily accurate representation of the real flow, but is more hardware and time intensive. There is a point of diminishing returns at which making the mesh finer is no longer worth the increased computational penalty. At least one range of this type of experiment is necessary at the start of a study to know what the desired mesh size would be.

The mixer was 6 units of a Nov Kenics with an aspect ratio of 2. The total cell counts ranging between 200,000 and 200,000,000 cells across a series of different mesh types. After running these steady state laminar simulations, the pressure drop across that static mixer was evaluated both as a function of cell total and in comparison to each other and the experimental result. Pressure drop is a good candidate for a mesh independence study due to its coupling with velocity, pressure and fluid properties. The interconnected nature means it requires good corroboration of simulation results to be accurate. This data generates the graph seen in Figure 6.2.

This figure shows that for all the mesh types, there is a good consistency of pressure drop results. There is also a clear plateau for pressure drop as the total cell number increases revealing that mesh independence has been reached with the

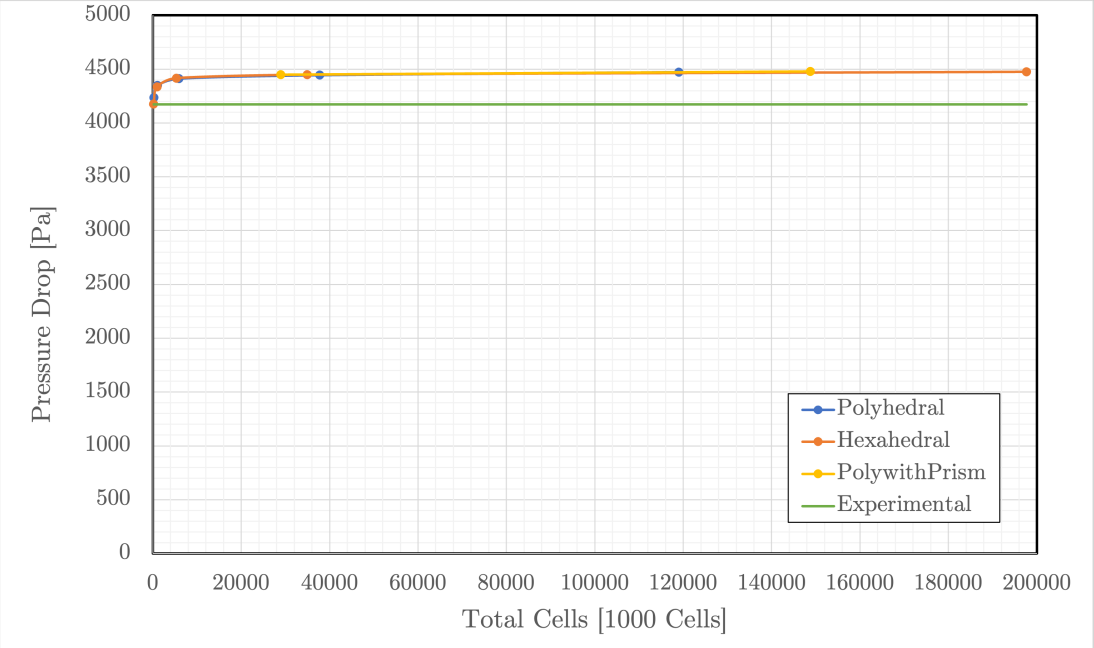


Fig. 6.2. Mesh Independence Study of Pressure Drop Across a Nov Kenics Mixer

final pressure drop value only changing by 0.59% when increasing the cell count 5x for hexahedral cells. The offset for the experimental data from the highest cell count simulation is also only 7.18% suggesting a high degree of simulation accuracy. A minor difference is expected due to the simplification of the model that resulted in the removal of the gap between the static mixer and the tube wall in the simulation that would in reality allow for a level of bypass and therefore lower pressure drop in the experimental test. Another proof of this criterion of mesh independence being met is to look at the mesh order of error. This plot is shown in Figure 6.3

The final point at the finest mesh size shows the progression of relative error from 1st to 2nd order. Having 2nd order error means that the relative error is now decreasing at squared relationship to the grid space as opposed to the linear decrease seen in 1st order. 2nd order is a good balance of accuracy vs the computational cost of higher orders.

From this experiment then, a target mesh size as fine as at least 0.1 mm is needed to be over the plateau of changing pressure drop and to push the schema into 2nd order

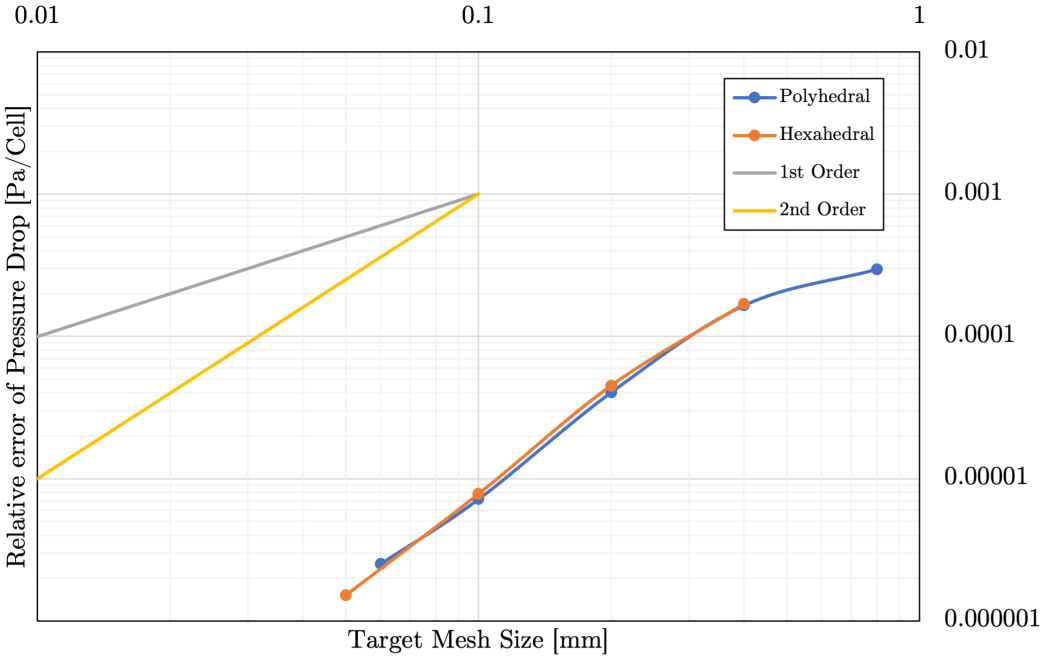


Fig. 6.3. Mesh Order of Error for Pressure Drop Mesh Independence Study of Nov Kenics Static Mixer

relative error. It is worth noting at this point that this proves that the simulation is now mesh independent for velocity and pressure gradients only. Whether it is fine enough for mixing is not guaranteed and a point that will be explored. With a level of sub 1 mm being mesh independent for at least the flow profile, a value of 0.06 mm was selected as the target mesh size, this was the top end value tested in the mesh independent study. Though this is computationally unnecessary for the flow profile, literature on numerical diffusion suggested that as fine a mesh as possible would be advantageous for passive scalar experimentation. 0.06 mm cells was the hardware limit of the available computer resources for simulations at 256 GB of random access memory.

6.3 | Passive Scalar Mixing

The first step of this solve was to resolve the steady-state velocity field to convergence and subsequently activate the passive scalar model with the settings in

Table 6.2, leaving any particle models deactivated. The initial scalar value of 100 in the injection tube is propagated throughout the model following the velocity profiles as the fluid is forced around the static mixer. Fluid that enters the fluid volume from the bulk inlet at the annulus around the injection tube has a scalar value of 0. Note that these values are completely arbitrary—100 was chosen simply as a high contrast upper limit for visualisation. The simulation was run in single precision mode, meaning all values are held as IEEE 754 32-bit floating point numbers, giving approximately 58.7 million independent values between 0 and 100—far more than the 4095 possible in PLIF.

The proximity of a cell with the scalar to one without causes it to both diffuse and mass transport, with the magnitude of the latter set by the fluid velocity vector field. By the time the fluid reaches the outlet of the fluid volume, the scalar has been mixed into the flow and, in theory, should analogise the PLIF experiment. By mapping the outlet plane to render the highest values of passive scalar as pure white and the lowest values as pure black, this should generate an image that is directly comparable to PLIF. The result of this is seen in Figure 6.4; the flow regime targets for these experiments are seen in Table 6.1.

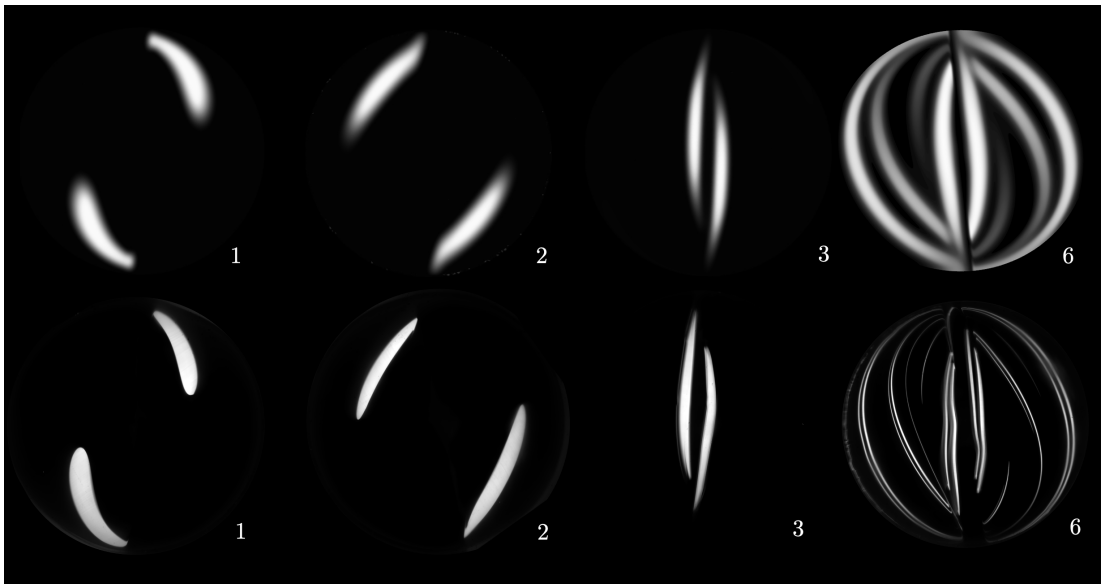


Fig. 6.4. Comparison of Passive Scalar CFD Mixing Simulations (Top) to the PLIF Experiments they were based on (Bottom) for Various Element Repeats of a Kenics Static Mixer at a Reynolds number around 0.47

With one repeat of the Kenics there is very clear qualitative visual comparison between the simulation and real results. The images are essentially identical, showing how the Kenics splits the centrally injected flow in half and sweeps it to opposite sides with the rotating helix. The same is true for two and three repeats of the mixer, yet the breakdown begins at six mixers. Here, the effects of numerical diffusion begin to show. The thin striations seen in the PLIF experiments have begun to blur to the point that the number of striations has been lost, the lines are thicker, and the simulation begins to give the hint of more diffusion than reality.

To reduce numerical diffusion, a third-order MUSCL convection scheme was used for the scalar transport. This scheme offers a higher accuracy approximation of the scalar field by using multiple cell neighbours to reduce artificial smearing. While this approach increases computational cost significantly—especially when combined with the fine polyhedral meshing used here—it remains one of the best strategies to resolve scalar transport in laminar flows without implementing impractical mesh alignment or unstructured refinement for each specific case. This work was conducted at the limits of a 36-core, 256GB RAM machine.

This problem is only exacerbated by modelling high shear mixers. The following example in Figure 6.5 is the same experiment conducted with a CALGAVIN Static Mixer. In this case, a loss of detail is seen after only the first element repeat. The quality drops off further with the second, and by the third, the diffusion has introduced so much blurring that there are regions of mixed grey, as opposed to the very binary levels seen in the PLIF experiment. It takes twice the length of static mixer in a PLIF test to get to a barely subjectively similar level of mixing to the CFD image, with the former showing considerably more detail. Again, this could lead a tester to conclude a high level of effectiveness of a short length of static mixer when only considering CFD.

The slope direction of testing is correct—a greater length and a higher shear mixer will produce a more mixed result—but the gradient of these effects is drastically wrong with passive scalars. The root of this problem is effectively expressed in a mesh

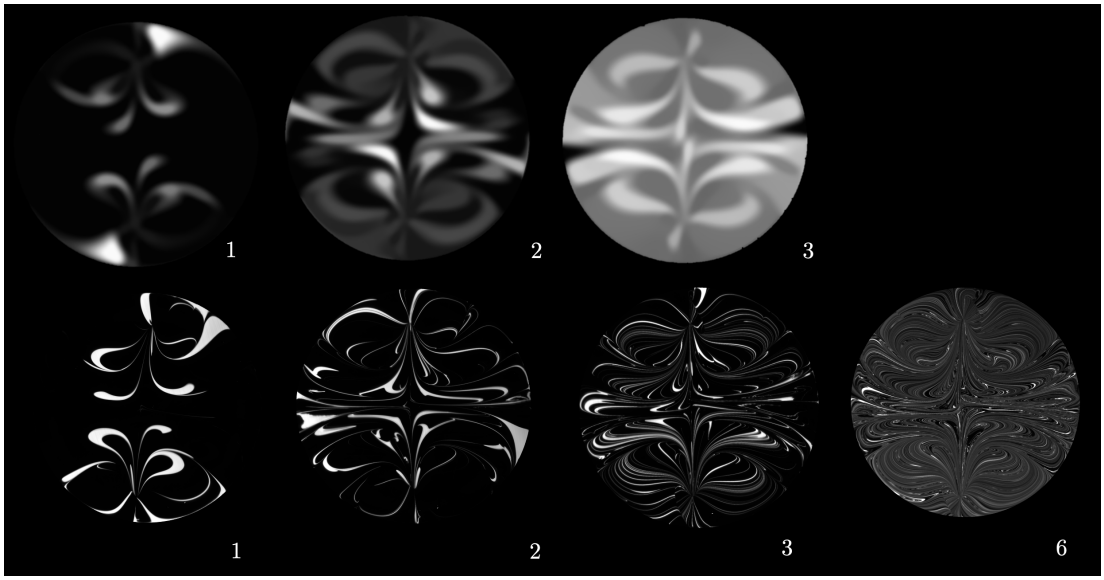


Fig. 6.5. Comparison of Passive Scalar CFD Mixing Simulations (Top) to the PLIF Experiments they were based on (Bottom) for Various Element Repeats of a CALGAVIN Static Mixer

independence study of the Kenics mixer that complements the early one evaluating the independence of pressure drop but tracks the change in Coefficient of Variance (CoV) with mesh size. When previous literature looks to mesh independence for laminar static mixing, the proof of this being established is almost always the pressure drop change with mesh size—despite this not representing the mixing level. The reason being that it is disadvantageous to plot mixing level against grid size when it is unfavourable. This relationship is charted in Figure 6.6. Unlike with the pressure drop study, independence is not reached and the result is not consistent with different mesh types. Numerical diffusion is the reason for both—for the former it produces premature diffusion and therefore apparent mixing, and for the latter because it is dependent on the cell face normality to the flow direction, meaning mesh type is hugely influential.

This work shows that although passive scalar could be used for an indication of mixing, it should not be done alone or used as conclusive evidence. Instead, a different method is needed.

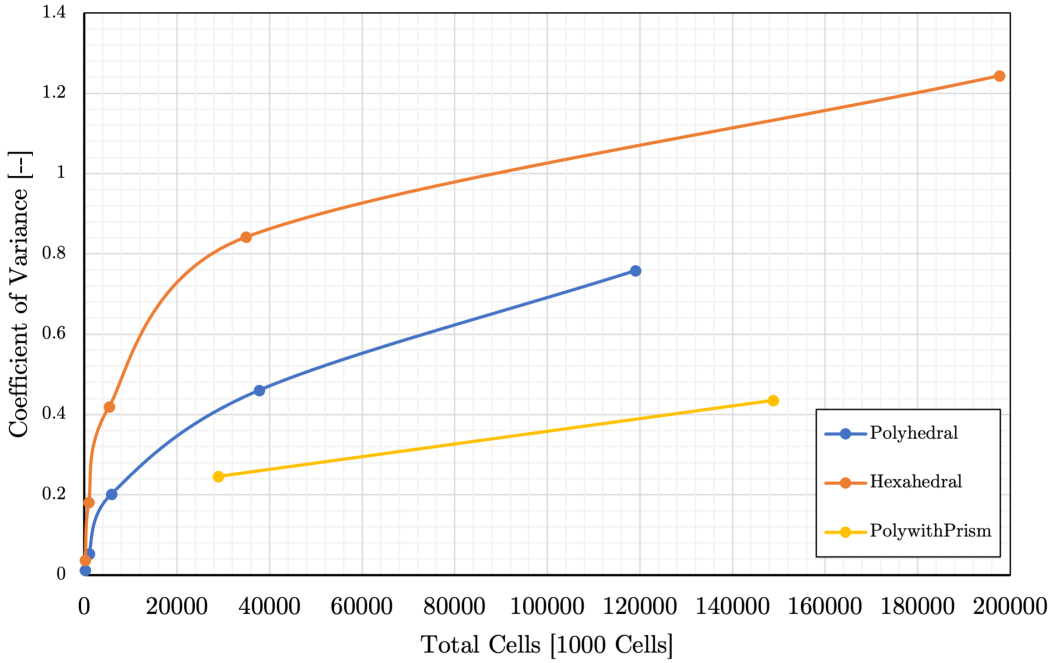


Fig. 6.6. Mesh Independence Study of Coefficient of Variance Across a Novel Kenics Mixer

6.4 | Particle Tracking Mixing Evaluation

Particle tracking has been conducted to assess static mixing before as discussed in the literature review. The premise is to inject inert particulates into the already computed flow profile tracking their progress as they propagate through the medium until they exit the simulation. Being point entities, they are immune to numerical diffusion giving a clear advantage over passive scalar simulation. The downside is that the schema is now Lagrangian and therefore more difficult to compare to PLIF images which are Eulerian being concentrations of dye at a spatial location.

A few methods were tested to set up the model. The first kept the mesh used for passive scaling and super imposed a circular array of particles even distributed across the injection inlet face. This worked in a limited capacity but reached a point where adding more particles no longer caused a difference in output. This is expected

to be a limitation in STAR-CCM+ where these particles where moved and allocated to the nearest cell from their initial position. This meant that adding more particles than number of cells at the inlet had no effect other than increasing computational time. This meant that for now, the number of particles was increased by decreasing the target mesh size of the simulation. To solve this, alternate meshes were made with local mesh rules that applied a smaller mesh size to the injection inlet surface, thus allowing more unique injection positions. This worked to a limited degree but again reached a new plateau where adding more inlet cells and therefore inlet particles stop resulting in changing particle output positions. Additionally added particles would exit the simulation exactly stacked upon other particles and therefore be of no benefit in building a more detailed outlet image.

The key addition was to step away from the established convention and no longer consider the particles as massless point entities. The hypothesis was that when the particles do not have mass, all particles that enter a fluid volume end up following the same path. However, when a particle has mass it has an inertia that factors into its vector calculation in the next pseudo-time step. The downside of this type of analysis is that penalty to computational time is very significant, in the order of four times the massless simulation. But in return this reintroduces differentiation between the particles and enables them to remain separate from one another. To limit any adverse effects giving the particles inertia might have - namely them having enough momentum to skip through flow streams - their diameter was set to 0.1 μm. Their density was set to the same as the surrounding fluid to negate any buoyancy effects.

Another issue with particle tracking is that the result have in the past viewed the results as a large series of point sources superimposed on the outlet. This can give a representation of mixing, but not is not directly comparable to the concentration of a substance in a fluid volume. To solve this the final mixing image is instead developed using the boundary sampling model. This model is applied to the outlet surface of the fluid volume and functions to count the particles as they travel through the outlet.

First by running the steady state fluid simulations to convergence, then running the lagrangian flow on the fully solved flow profile, these particles track the fluid volume until the escape through the outlet surface. The lagrangian model is a transient model that tracks the particles over time. These were run with a maximum Courant number of 0.35 and a minimum of 0.05. Having a Courant number below one means that a particle never skips a cell and ensures a highly precise passage through the fluid volume. The simulation ends when 99.5% of the particles have left the simulation - this was needed as a small fraction of the particles can become trapped within the geometry. Upon completion, opening a scalar results view of the outlet surface and plotting the incident mass flux of the particle phase over the outlet mesh creates a heatmap of the location and frequency particles left the domain. Changing the colour scale to greyscale copies the rendering of the PLIF images where white represents cells with the most particles and black the least, through any given outlet cell. The flow rate through each outlet cell is also considered to weigh the particles accordingly.

Admittedly very limited runs were conducted on this type of simulation due to the size and time requirements to run them. Yet the few that were done allow the first direct image to image comparison between PLIF and CFD mixing imagery.

The first set of experiments was a mesh independence study conducted on the Kenics set up described previously. Each test had progressively more particles added starting at around 1,500 up to nearly 2,000,000 with each test adding detail to the final image. The outlet boundary sample images can be seen in Figure 6.8. The first image with 1,478 particles still has the obvious signs that it was built from point sources and lacks the detail that the subsequent images contain. Including and above 125,931 particles, the images become nearly indistinguishable save for the thin tails at the radial periphery of the images with the final image at 1,996,425 particles looking superficially no different from what one might expect of a PLIF image. In fact comparing it directly with the corresponding PLIF experiment, as seen in Figure 6.9, shows the marked similarity between the two with essentially all details captured in the simulations. This

is in stark contrast to the passive scalar experiment that is diffused to the point of an unacceptable detail loss.

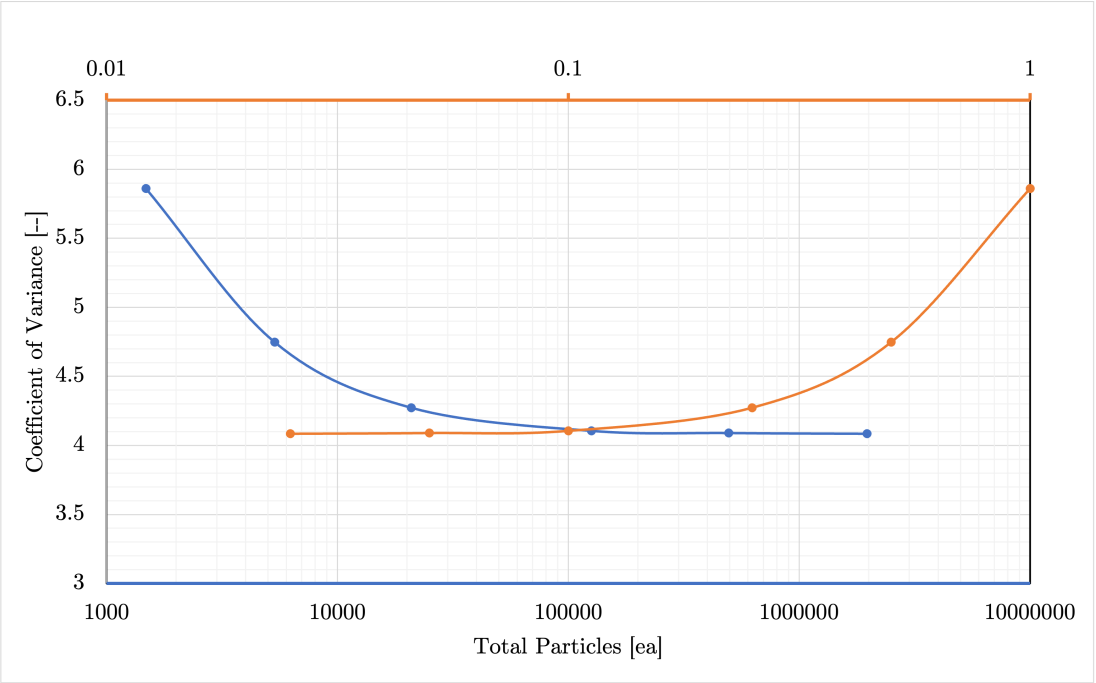


Fig. 6.7. Mesh Independence Study for Boundary Sampled and Massed Particle Tracking Mixing of a Kenics Static Mixer

As shown in Figure 6.7, plotting this mesh independence study with how the CoV changes with both the target mesh size and the total number of injected particles shows the desired plateau. With how this simulation is set up, the mesh size and particle count are inversely linked and dependent upon one another. At a mesh size of 0.1 mm or a particle count of 125,931 there is diminishing returns on changing CoV which proves that mixing is no longer mesh dependent.

The Kenics experiment shows this new version of particle tracking works for low shear allowing direct image to to image comparison between simulation and reality. The conventional method of particle tracking that builds images from point sources can produce images that approximate the images generated here and would allow a subjective comparison, but are still clearly made of individual point sources (Hobbs & Muzzio, 1998) (Gayen et al., 2024) and crucially are binary. Low shear at this mixer length is inherently simpler with it still containing clear striations and therefore

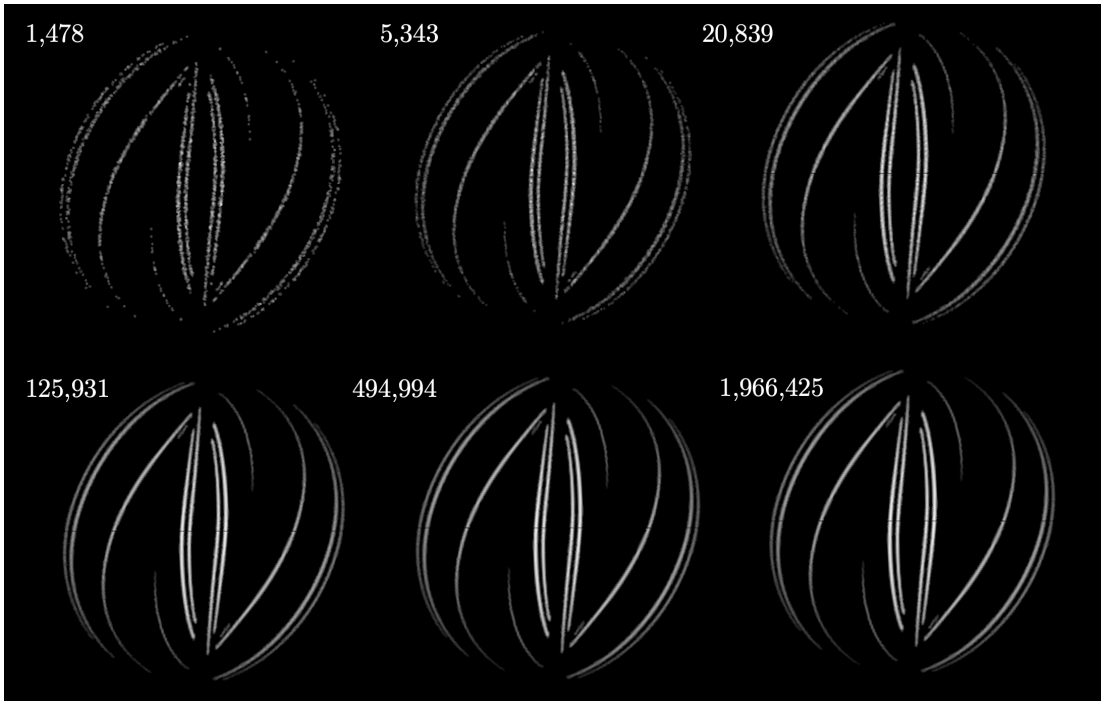


Fig. 6.8. Outlet Boundary Sample Mixing Images from a Series of Kenics Particle Tracking Simulations



Fig. 6.9. Mixing Images of Six Kenics Elements for Particle Tracking (Left), PLIF (Middle) and Passive Scalar (Right)

binary component separation. With particles, binary solutions are easier because they inherently require less particles - as long as there are enough particles to cover the total area that the component reaches - it is only required that one particle reaches that reason for it to be represented in the outlet boundary sampling. With a graded system, seen on the route to total mixing, the resolution of image contrast is only as deep as the dynamic range of the number of particles counted at the outlet. 125,000 was enough for

this particular Kenics test but it likely that multiple orders of magnitude more particles will be needed to create a one-to-one representation of being near mixed.

The original models used for the high shear mixer passive scalar experiments were modified to have the new smaller local surface mesh sizes at the dye injection inlet. The maximum total for the particles approached 20 million constrained by the available memory - i.e. the inlet injection surface alone had 20 million cells. With this set up, the complexity of tracking the massed particles resulted in a simulation run time of 8 days, but allowed the development of high shear mixing images, the first of which is seen in Figure 6.10.

This is new level of detail for a laminar mixing study of a high shear static mixer which shows excellent comparison to the PLIF testing. This shown in Figure 6.11 which depicts the particle tracking output next to the experimental test from which its flow conditions are drawn from. The images show a good similarity in striation position and crucially, for the first time, show comparable contrast - especially considering that no contrast beyond binary mixtures have been shown in particle tracking static mixer modelling before. There is however still difficulty in directly comparing mixing numbers for this data versus PLIF. All mixing quantification techniques are sample resolution dependent. A courser sample grid results in more averaged data as striations are combined within one 'pixel' thereby giving the impression of better mixing. With PLIF still being much finer than this flux-based particle tracking simulation, the quantitate mixing numbers will not match between them, with the CFD simulation results reading as more mixed than the experimental. To combat this, the PLIF would need to be downsampled, reducing its precision. However the intended scenario for this simulation technique is comparative testing of iterative designs and would therefore still be applicable when comparing CFD simulations against each other.

Figure 6.12 contains the results for 8 elements of a CALGAVIN Static Mixer for the new particle tracking technique against an experimental PLIF result and a passive scalar result. The passive scalar result was conducted on only 3 elements due to the

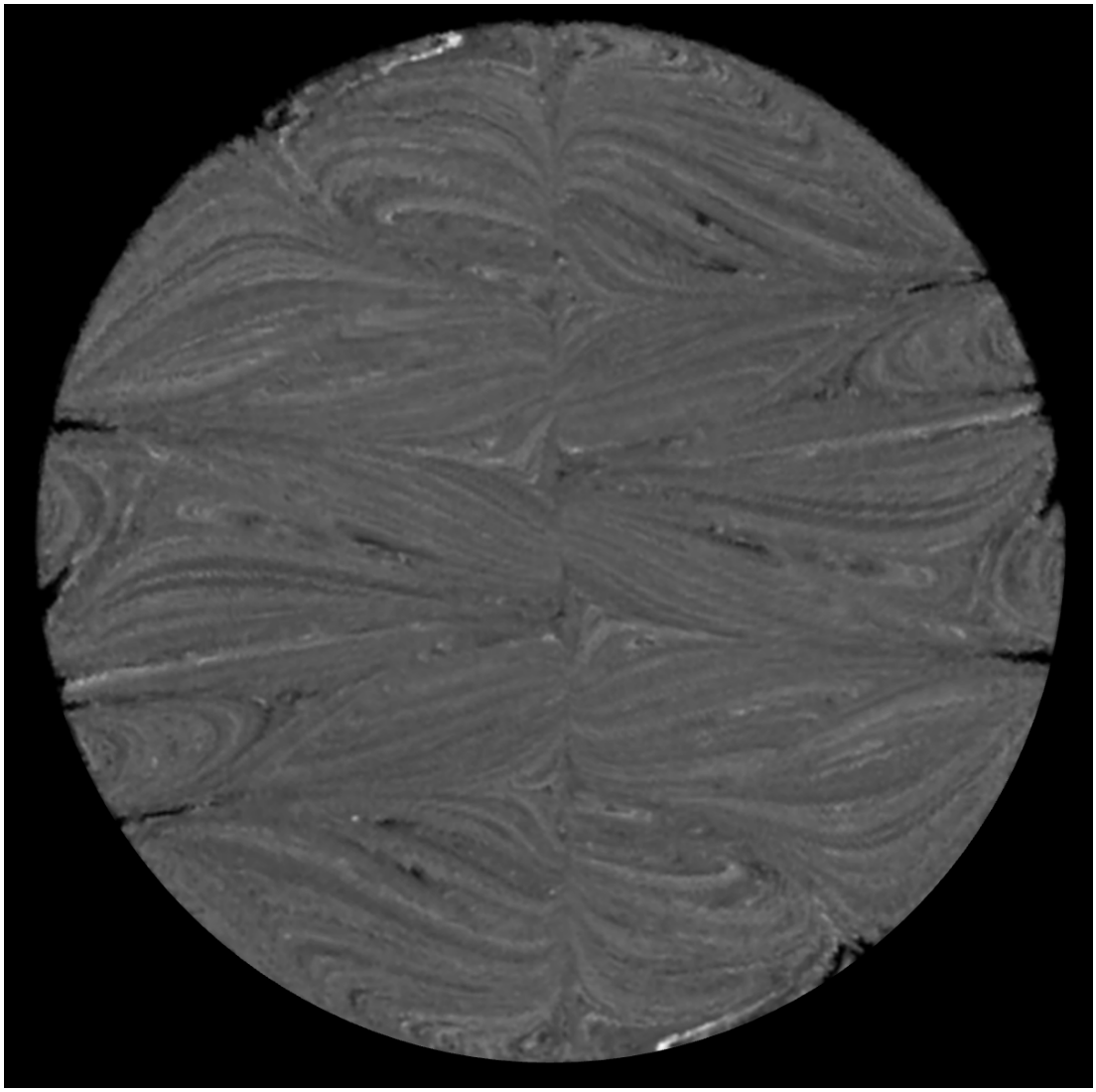


Fig. 6.10. Boundary Sampled Massed Particle Tracking Simulation of 8 Elements of a SMX™ plus Static Mixer at a Reynolds Number of 7.48 with 25,216,898 Particles

memory constraints from having an even finer mesh in an attempt to limit numerical diffusion. This figure shows that the passive scalar model fails to capture any of the fine detail and is not suitable to gauge the level of mixing that occurs in reality. The particle tracking image contains the same striation patterns as the PLIF image, again with comparable contrast.

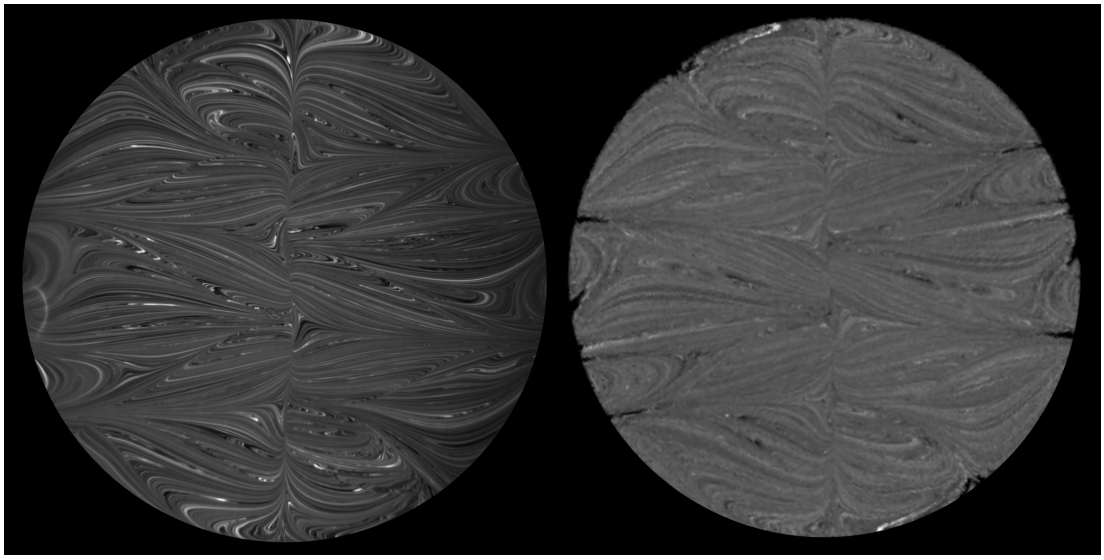


Fig. 6.11. PLIF Experimental Image (Left) Compared Against Particle Tracking Simulation of 8 Elements of a SMX™ plus Static Mixer at a Reynolds Number of 7.48

6.5 | Conclusions and Next Steps

The drawbacks of both passive scalar and traditional particle The drawbacks of both passive scalar and traditional particle tracking laminar static mixing models have been explored. The former suffers from extensive numerical diffusion, which, with currently available hardware, presents as unrealistically high levels of mixing and striation breakdown. The latter has only allowed binary mixing analysis, and the Lagrangian point nature of the outputs makes it hard to compare with fluid volume-based experimental testing. The work presented here demonstrates the effectiveness of a new form of particle tracking that adds particle differentiation with minimal but present particle mass. By sampling the particles as they cross the outlet boundary, a location and frequency heatmap is developed that simulates Eulerian fluid volume results and therefore leads to an output that visually matches PLIF experimentation.

The vast number of particles required to build this image and the reintroduction of particle mass make these simulations very computationally intensive—in the order of days—but not so long that they are untenable. The required cell count and particle count need to be sufficient for independence; however, these are coupled variables, and

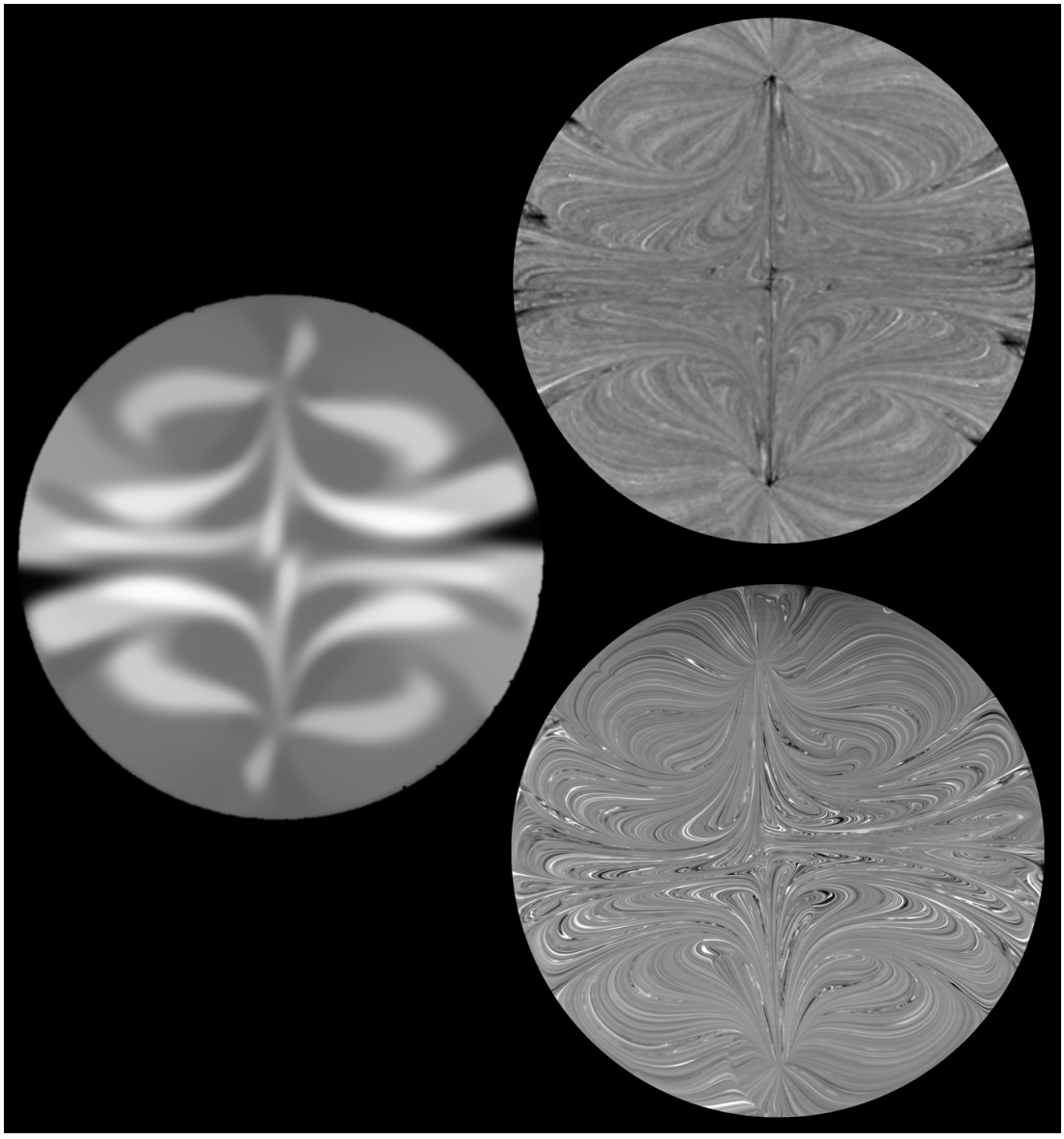


Fig. 6.12. 3 Element Passive Scalar Simulation (Left) Compared Against 8 Element PLIF Experimental Image (Bottom Right) and an 8 Element Particle Tracking Simulation (Top Right) of a CALGAVIN Static plus Static Mixer at a Reynolds Number of 7.36

without extensive experimentation, the most efficient combination is not clear. Further to this, the particle and cell count needed for mesh independence is not fixed. The more mixed the output is, the more cells are needed to saturate the image. There is then a trade-off required between conducting independence studies for all tests and having such a large safety margin for all tests that computational cost is severe.

The method itself should be rheology-independent and allow mixing analysis of non-Newtonian fluids, assuming the fluid models themselves are accurate. The next work should explore and expand on these simulations at multiple Reynolds numbers and insert lengths to map any quantitative mixing trends to experimental results. The key aspect to note is that the CFD experiments are still at an order of magnitude lower resolution compared with the PLIF results (approximately 230 cells across the diameter versus 1800), and any quantitative comparison would require the PLIF results to be downsampled. Extensive mesh independence studies should also be conducted to develop guidelines for the ratios of cells to particles and the minimum acceptable amounts for different expected mixing levels, to save on computational time.

CHAPTER 7

Conclusions

Mixing is a fundamental unit operation in chemical processes, especially when handling viscous substances, where achieving a specific state of 'mixedness' is crucial. Any lack of comprehensive understanding and quantification of mixing processes has historically led to inefficiencies, overdesign, and significant economic losses in the industry. Traditional methods for assessing mixing, such as Planar Laser-Induced Fluorescence (PLIF), while providing high-resolution insights, are constrained by their destructive nature and the associated costs and time limitations.

This research set out to address these challenges by developing a novel, continuous, and non-destructive PLIF methodology, enabling efficient evaluation and optimisation of static mixer designs without incurring fluid wastage. By integrating an activated carbon-based filtration system into the test facility, continuous PLIF testing was achieved by adsorbing the Rhodamine 6G tracer compound from the spent test fluid and recycling the glycerol test fluid back into the loop—eliminating the waste normally seen in PLIF testing. Drawing from industrial techniques, the test rig incorporated digital data acquisition and control, enabling remote control of temperature (and by extension viscosity) and mass flow. All parameters were measured by associated meters and automatically recorded to an SQL database. This level of digital integration, combined with remote-addressable pumps, heater/chiller units, and motorised ball valves, allowed the facility to operate autonomously, running test procedures through a pre-programmed state machine and maintaining control with PID algorithms.

The novelty of this thesis lies in the development of what is arguably the most capable continuous PLIF test facility constructed to date. It is capable of generating mixing images of unprecedented quality and detail, enabled by a recirculating filtration loop, highly integrated automated controls, and finely tuned PLIF optics. The result is a system that not only allows high-throughput testing but also maintains temperature and flow consistency over long periods, producing a steady-state image quality that has not been matched in previous PLIF studies—particularly for laminar, viscous flows. Unlike single-pass systems, the looping design allowed tests to be conducted over a continuous range of Reynolds numbers between 0.02 and 120, without the need to change hardware or fluids. The result is a facility that is rapid, repeatable, and scalable.

The data this system has produced is both comprehensive and of high quality. Over 440 tests were performed across three mixer designs, each at multiple lengths and Reynolds numbers, providing the most extensive known dataset on low Reynolds number static mixing performance. Unlike many previous studies that report only 3–6 test points across two or three mixer lengths, this work spans a far broader design and flow space, enabling true trend identification and comparison across both pressure drop and mixing effectiveness.

Mapping static mixer pressure drop tests proved the accuracy and repeatability of the flow properties. Strong correlations of data across differing mass fractions indicated that the online pipe rheometer measured with a high degree of certainty. Accurately measuring the mass fraction during tests conducted on multiple mass fractions of glycerol required highly precise measurements of temperature, mass flow, density, and pressure drop around the system's rheometer. This mass fraction parameter was then used to calculate test viscosity, which in turn was used in the Fanning friction factor calculation.

Concurrent with the energy tests, Rhodamine 6G dye was injected at the inlets of varying static mixers, and comprehensive PLIF imagery was captured at their outlets. The images exhibited high sharpness, resolution, and dynamic range. Quantitative analysis using the coefficient of variance (CoV) and a recently proposed CG Number

demonstrated high consistency. The CG Number proved to be more consistent than CoV, with experimental data showing, on average, 80% less spread around logarithmic linear regression. In addition, the CG Number is notably more human-understandable; for example, a CG Number of 20 would roughly mean that at least 20% of the area is insufficiently mixed. It is less sensitive to experimental errors, such as insufficient amounts of a certain compound, where CoV might not detect discrepancies unless the mean concentration is measured. This suggests that the CG Number successfully combines the simplicity of CoV with the depth provided by more comprehensive methods like areal fraction, therefore addressing a gap in mixing quantification techniques identified in the literature.

Testing below a Reynolds number of 20 produced PLIF images at an exact steady state with no shot-to-shot variation, as proven by the image-by-image variation heatmaps being purely black. As the Reynolds number increased beyond this point, vortices began to form, causing changes in the mixing pattern at the outlet and introducing shot-to-shot variability and, by extension, visible patterns in the heatmap. Interestingly, at the Reynolds numbers tested (up to 120), this had no impact on either the CoV or the CG Number, indicating that the increased chaos had no effect on the overall mixing level. This is likely because the vortices only had enough energy to move regions of fluid and perform macro-mixing but not to induce micro-mixing at the 12 μm spatial resolution of the PLIF system setup.

For the given length of insert, the SMX™ exhibited the best mixing, followed by the SMX™ plus, and then the CALGAVIN static mixer, with each, in order, taking roughly 150 mm, 160 mm, and 215 mm lengths to reach a CoV of 95% at this imaging resolution. However, when instead evaluating by the total pressure drop of the inserts, the order was reversed. This resulted in a different hierarchy for mixing efficiency, with the SMX™ plus leading, followed by the CALGAVIN mixer, and then the SMX™. With these evaluation criteria, the CALGAVIN mixer doubles the Fanning friction factor compared with the SMX™ plus, with the SMX™ exhibiting around 3.5 times that of the

SMX™ plus. These findings highlight the importance of balancing mixing effectiveness with energy efficiency, a challenge noted in the literature where achieving homogeneous mixing often requires weighing trade-offs between performance and energy consumption. It should also be noted that the accuracy of pressure drop readings became limited with short mixing lengths due to low pressure drops below 3 mbar, and therefore became difficult to measure accurately.

Developed concurrently with this work, the novel flux-based particle tracking Computational Fluid Dynamics (CFD) methodology led to mixing simulations that, despite being built on point systems, exhibited graduated ranges beyond the normal binary outputs of traditional particle tracking. This translation of Lagrangian simulations back into Eulerian space enables CFD simulations to truly mirror experimental PLIF testing for the first time while being immune to the numerical diffusion that hinders passive scalar-based techniques. This methodology potentially provides the most representative analysis of laminar static mixing currently available but does, however, have drawbacks. The particle tracking CFD methodology is computationally expensive and time-consuming, with simulations taking as long as eight days to complete. This computational demand presents a practical limitation for rapid prototyping in its current form. The technique also suffers with an inherent difficulty to conduct mesh independence studies due to the coupling of required particle count and mesh size, which likely leads to needlessly fine resolutions further exacerbating the computational expense.

This CFD method, however, is significant because it creates a pathway to fully virtual static mixer design. Its combination with the PLIF rig creates a complete feedback loop where new designs can be prototyped digitally, simulated with high confidence, and then fabricated and validated through continuous PLIF testing. It provides the backbone of a future static mixer development framework that can iterate faster, test more thoroughly, and ultimately produce more efficient designs with fewer physical prototypes.

The overall contribution of this research is the creation of a complete, integrated, and validated workflow for static mixer development. From a completely blank slate, every element of the test facility was conceived, designed, and built by the author—from mechanical components and instrumentation to the control software, optical system, and CFD pipeline. The system provides a uniquely powerful platform for future mixer research and development. The combination of continuous PLIF testing, fine-resolution optical imaging, live viscosity control, automated state-machine operation, and verified CFD simulation forms a novel and comprehensive testing ecosystem that sets a new benchmark in the field.

Due to the confidential nature of this work, multiple static mixer designs were generated and evaluated using this rig and methodology, but neither the geometries nor their associated performance mechanisms can be discussed in this thesis. However, the infrastructure developed here enables rapid iteration and design exploration using experimental data in ways not previously possible. This research enables the future—where generative design algorithms, trained on validated mixing metrics, can begin to automate the invention of the next generation of mixing technology.

The global static mixer industry presents significant business potential, valued at $493 million (IndustryARC, 2019). By achieving the objectives set out at the beginning of this research, this facility can provide a competitive advantage to static mixer manufacturers, offering clear benefits in cost savings, faster prototyping, and enhanced precision in performance data. In addition to this, the granularity of data gained through this method will allow engineers to design applications with greater confidence and less over-design, potentially reducing costs and improving efficiency.

CHAPTER 8

Further Work

The most obvious first direction for future work would involve either increasing the flow velocity or further decreasing the viscosity of the test fluid, or both, to extend the Reynolds number range of the test facility and provide insight into the threshold point at which increasing the Reynolds number improves mixing. Achieving higher Reynolds numbers could involve experimenting with alternative fluids or adjusting the system to enable higher flow rates. This could be achieved by using further diluted glycerol or implementing a parallel, higher flow rate pump with the capacity to switch between it and the original. The latter approach would maintain the original large range of operational conditions while still extending the top end. It would be necessary, however, to extend the calming sections for Reynolds numbers above 200 to maintain the required hydrodynamic entrance length.

A notable limitation of the current pressure measurement setup is the low pressure drop (less than 3 mbar) observed at the highest temperatures, lowest flow rates, and shortest mixer lengths. Further decreasing the mass fraction of glycerol would compound this issue and result in pressure drops that are unmeasurable on the current rig. Addressing this would require proportionally calculating the pressure drop of short static mixer sections from tests on the full-length sections—a reasonable approach due to the proven proportionality. Alternatively, a more sensitive pressure transducer could be integrated (3 mbar is, however, a very low value), or potentially validated CFD simulation could be used.

The test rig, in its current form, is largely suitable only for high-shear mixers and is unable to test low-shear mixers to complete mixing. To address this, future work could lengthen the test section to accommodate longer static mixer sections, thereby expanding the testing capacity of the facility. This would also help identify the exact point where low-shear mixers become more efficient. Incorporating modular test section lengths while keeping and extending the linear rail carriage system could allow for flexibility in testing mixers of varying lengths. Another area of interest is exploring non-Newtonian fluids, such as shear-thinning Carboxymethyl cellulose (CMC) or Carbopol, both of which are optically clear and were used in studies by Alberini et al. (2014). This would extend the test rig's industrial applicability.

Since the CALGAVIN mixer outperforms the SMX™, producing it at a competitive price compared to the SMX™ plus could allow it to compete in the market against the still-patented competitor. The data from this testing can be used to iterate the first-generation static mixer design from CALGAVIN. Utilising PLIF to identify the physical areas of poor mixing will enable rapid testing of iterated prototypes. Future work could focus on optimising the CALGAVIN mixer design for both mixing efficiency and pressure drop, potentially leading to a superior product in both performance and cost.

Combining the novel flux-based particle tracking CFD methodology with experimental testing from the PLIF facility allows for rapid prototyping of static mixer designs—first by testing slight variations in computational space before fabricating the most promising designs and validating them experimentally. Future research needs to explore further into finding the optimal balance between mesh size and particle count for maximum efficiency - reducing processing time. After this, more comprehensive testing is required to assess if the methodology is sensitive enough for examining the subtle mixing changes that small iterative modifications would exhibit. Studies will also need to explore the implications of applying this technique to non-Newtonian fluids. There are also potential complications arising from the pseudo-turbulence observed at

Reynolds numbers above 20. Laminar simulation may no longer be suitable at this inflexion point and will likely, and unfortunately, require exploring transitional flow simulation.

There is also potential for integrating emerging technologies like generative design into the CFD methodology. This new application of CFD is well-suited to testing generative designs of static mixers, which could lead to innovative mixer geometries without the need for human input.

Bibliography

Alberini, F., Simmons, M. J. H., Ingram, A., & Stitt, E. H. (2014). Assessment of different methods of analysis to characterise the mixing of shear-thinning fluids in a Kenics KM static mixer using PLIF. *Chemical Engineering Science*, *112*, 152–169.

Albright, L. (Ed.). (2008). *Albright's Chemical Engineering Handbook*. CRC Press.

Armeniades, C. D., Johnson, W. C., & Thomas, R. (1966). *Mixing device* (U.S. pat. No. 3286992A).

Aubin, J., Fletcher, D. F., & Xuereb, C. (2005). Design of micromixers using CFD modelling. *Chemical Engineering Science*, *60*(8), 2503–2516.

Baj, P., Bruce, P. J. K., & Buxton, O. R. H. (2016). On a PLIF quantification methodology in a nonlinear dye response regime. *Experiments in Fluids*, *57*(6), 106.

Bakker, A., LaRoche, R., & Marshall, E. (1998). Laminar Flow in Static Mixer with Helical Elements.

Barnes, H. A., Hutton, J. F., & Walters, K. (1989). *An Introduction to Rheology*. Elsevier.

Batchelor, G. K. (2000). *An Introduction to Fluid Dynamics*. Cambridge University Press.

Bergman, T. L. (2011). *Fundamentals of Heat and Mass Transfer*. John Wiley & Sons.

Bird, R. (1961). Transport phenomena, R. B. Bird, W. E. Stewart, and E. N. Lightfoot, John Wiley and Sons, Inc., New York (1960). 780 pages. $11.50. *AIChE Journal*, *7*(2), 5J–6J.

Brown, D. A. R., Jones, P. N., Middleton, J. C., Papadopoulos, G., & Arik, E. B. (2003). Experimental Methods. In *Handbook of Industrial Mixing* (pp. 145–256). John Wiley & Sons, Ltd.

Clifford, M. J., Simmons, K. A., Roberts, J., & Truscot, T. D. (2006). Computational fluid dynamics modelling of a static mixer. *Proceedings of the Institution of Mechanical Engineers, Part C: Journal of Mechanical Engineering Science*, *220*(3), 325–332.

Danckwerts, P. V. (1952). The definition and measurement of some characteristics of mixtures. *Applied Scientific Research, Section A*, *3*(4), 279–296.

DOE Fundamentals Handbook: Thermodynamics, Heat Transfer, and Fluid Flow, Volume 3 (DOE-HDBK-1012/3-92). (1992). USDOE, Washington, DC (United States).

Everitt, B. S., & Skrondal, A. (2010). *The Cambridge Dictionary of Statistics*. Cambridge University Press.

Forte, G., Albano, A., Simmons, M. J. H., Stitt, H. E., Brunazzi, E., & Alberini, F. (2019). Assessing Blending of Non-Newtonian Fluids in Static Mixers by Planar Laser-Induced Fluorescence and Electrical Resistance Tomography. *Chemical Engineering & Technology*, *42*(8), 1602–1610.

Gayen, N., Swamy, S., Hari, S., & Sonawane, S. H. (2024). Laminar mixing of Newtonian and non-Newtonian fluids in SMX static mixer. *The Canadian Journal of Chemical Engineering*, *102*(8), 2768–2785.

Hirschberg, S., Koubek, R., F.Moser, & Schöck, J. (2009). An improvement of the Sulzer SMX static mixer significantly reducing the pressure drop. *Chemical Engineering Research and Design*, *87*(4), 524–532.

Hobbs, D. M., & Muzzio, F. J. (1998). Optimization of a static mixer using dynamical systems techniques. *Chemical Engineering Science*, *53*(18), 3199–3213.

IndustryARC. (2019). *Static Mixer Market* (Market Analysis).

Joaquim Jr., C. F., Reynol, A., Cekinski, E., Seckler, M. M., & Nunhez, J. R. (2011). Development of static mixers for miscible fluids in laminar flow with the use of computational fluid dynamics (CFD). *The Canadian Journal of Chemical Engineering*, *89*(4), 734–744.

Kim, Y., Nematollahi, O., Kim, H. D., & Kim, K. C. (2021). Quantitative visualization of the mixing characteristics of a multilayer static mixer by planar laser-induced fluorescence. *Journal of Visualization*, *24*(4), 671–681.

Kolmogorov, A. (1941). The Local Structure of Turbulence in Incompressible Viscous Fluid for Very Large Reynolds' Numbers. *Akademiia Nauk SSSR Doklady*, *30*, 301–305

ADS Bibcode: 1941DoSSR..30..301K.

Kukukova, A., Aubin, J., & Kresta, S. M. (2009). A new definition of mixing and segregation: Three dimensions of a key process variable. *Chemical Engineering Research and Design*, *87*(4), 633–647.

Lehwald, A., Thévenin, D., & Zähringer, K. (2010). Quantifying macro-mixing and micro-mixing in a static mixer using two-tracer laser-induced fluorescence. *Experiments in Fluids*, *48*(5), 823–836.

Lemenand, T., Della Valle, D., Zellouf, Y., & Peerhossaini, H. (2003). Droplets formation in turbulent mixing of two immiscible fluids in a new type of static mixer. *International Journal of Multiphase Flow*, *29*(5), 813–840.

Meijer, H. E. H., Singh, M. K., & Anderson, P. D. (2012). On the performance of static mixers: A quantitative comparison. *Progress in Polymer Science*, *37*(10), 1333–1349.

Migliozzi, S., Mazzei, L., & Angeli, P. (2021). Viscoelastic flow instabilities in static mixers: Onset and effect on the mixing efficiency. *Physics of Fluids*, *33*(1), 013104.

Moghaddam, S. (2023). Effect of Non-Newtonian Fluid on Mixing Quality and Pressure Drop in Several Static Mixers: A Numerical Study. *Iranian Journal of Science and Technology, Transactions of Mechanical Engineering*, *47*(4), 1585–1597.

Nienow, A. W., Harnby, N., & Edwards, M. F. (1992). Chapter 1 - Introduction to mixing problems. In N. Harnby, M. F. Edwards, & A. W. Nienow (Eds.), *Mixing in the Process Industries* (pp. 1–24). Butterworth-Heinemann.

Nyande, B. W., Mathew Thomas, K., & Lakerveld, R. (2021). CFD Analysis of a Kenics Static Mixer with a Low Pressure Drop under Laminar Flow Conditions. *Industrial & Engineering Chemistry Research*, *60*(14), 5264–5277.

Paglianti, A. (2008). Recent Innovations in Turbulent Mixing with Static Elements. *Recent Patents on Chemical Engineering*, *1*(1), 80–87.

Pust, O., Strand, T., Mathys, P., & Rütti, A. (2006). Quantification of Laminar Mixing Performance using Laser-Induced Fluorescence.

Rafiee, M., Bakalisa, S., Fryer, P. J., & Ingram, A. (2011). Study of laminar mixing in kenics static mixer by using Positron Emission Particle Tracking (PEPT). *Procedia Food Science*, *1*, 678–684.

Rauwendaal, C. (1991). *Mixing in Polymer Processing*. CRC Press.

Reynolds, O. (1883). XXIX. An experimental investigation of the circumstances which determine whether the motion of water shall be direct or sinuous, and of the law of resistance in parallel channels. *Philosophical Transactions of the Royal Society of London*, *174*, 935–982.

Richardson, L. F. (1922). Weather prediction by numerical process. By Lewis F. Richardson. Cambridge (University Press), 1922. 4°. Pp. xii + 236. 30s.net. *Quarterly Journal of the Royal Meteorological Society*, *48*(203), 282–284.

Shen, B., Zhan, X., Sun, Z., He, Y., Long, J., & Li, X. (2022). PIV experiments and CFD simulations of liquid–liquid mixing in a planetary centrifugal mixer (PCM). *Chemical Engineering Science*, *259*, 117764.

Soman, S. (2016). Study of Effects of Design Modification in Static Mixer Geometry and its Applications.

Streeter, V. L., & Wylie, E. B. (1975). *Fluid Mechanics*. McGraw-Hill.

Thakur, R. K., Vial, Ch., Nigam, K. D. P., Nauman, E. B., & Djelveh, G. (2003). Static Mixers in the Process Industries—A Review. *Chemical Engineering Research and Design*, *81*(7), 787–826.

Volk, A., & Kähler, C. J. (2018). Density model for aqueous glycerol solutions. *Experiments in Fluids*, *59*(5), 75.

Wadley, R., & Dawson, M. K. (2005). LIF measurements of blending in static mixers in the turbulent and transitional flow regimes. *Chemical Engineering Science*, *60*(8), 2469–2478.

White, F. M. (2011). *Fluid Mechanics*. McGraw Hill.

Zalc, J. M., Szalai, E. S., Muzzio, F. J., & Jaffer, S. (2002). Characterization of flow and mixing in an SMX static mixer. *AIChE Journal*, *48*(3), 427–436.

Zare, R. N. (2012). My Life with LIF: A Personal Account of Developing Laser-Induced Fluorescence. *Annual Review of Analytical Chemistry*, *5*(1), 1–14.